A thesis submitted to the
Mathematical, Physical and Life Sciences Division
for the degree of Doctor of Philosophy in the
University of Oxford Hilary Term, 2009

Evaluating forcings in an ensemble of paleo-climate models

Helene Østlie Muri
Linacre College
Atmospheric, Oceanic and Planetary Physics
University of Oxford

Evaluating forcings in an ensemble of paleo-climate models

Helene Østlie Muri
Linacre College, University of Oxford

Submitted for the degree of Doctor of Philosophy, Hilary Term 2009

ABSTRACT

This thesis presents the initial results from climate*prediction*.net's paleo-experiments. A grand ensemble of paleo-climate models was successfully designed and executed using this distributed computing approach. The physical parameters, initial conditions and boundary conditions were perturbed in two sets of experiments distributed to the general public. The paleo - focus period is the mid-Holocene, i.e. ∼6000 years before present (6kyBP), due to its relative climatic stability and the abundance of geological evidence. Attempting to simulate climates that were substantially different from today provides an opportunity to evaluate model skill. A set of robust 6kyBP climatological features were established to benchmark the climate model against in order to assess the model's abilities.

Two experiments were distributed: in the first experiment the boundary conditions in the 6kyBP models took on the standard Paleoclimate Modelling Intercomparison Project (PMIP) values with altered orbital configuration as the main forcing on the climate. In a second experiment the local boundary conditions in Eastern North America (ENA) were also perturbed in the 6kyBP models to include an expanded Hudson Bay and land ice. The results highlight strengths and weaknesses in the model and stresses the importance of high quality paleo-observations.

The models simulate the broad-scale features of the mid-Holocene climate reasonably well, though the model performance decreases when the benchmarks are inspected more closely. A relationship between the climate sensitivity, i.e. the equilibrium temperature response to doubling of pre-industrial CO_2 concentrations, and the 6kyBP East Asian monsoonal moisture budget is found. This provides a climate sensitivity range of 2.5-6.1°C.

The ENA boundary condition experiment concludes that the perturbations brought the climate models to a closer agreement with the geological records.

A sensitivity experiment perturbing the North African vegetation cover emphasises the importance of vegetation feedbacks in relation to the 6kyBP northwards expansion of the monsoon.

Acknowledgements

I am grateful for all the hard work the CPDN team has put into this project, in particular Tolu Aina and Milo Thurston. Sincere gratitude is also felt for all the volunteers out there having lent their computing resources to the purposes of this experiment.

ECMWF ERA-40 reanalysis data used in this study have been provided by ECMWF.

Thank you to Dr. Tamsin Edwards and the paleo-QUMP team for providing the 6kyBP ancillary files including the ice sheet and the new land sea mask in addition to interesting discussions.

This project was funded by the Natural Environmental Research Council and Det Kongelig Selskap for Norges Vel (The Royal Norwegian Society for Development). The Royal Meteorological Society and Linacre College have also generously supported conference attendances.

I would also like to thank my supervisors for their support and inspiration: Myles Allen, Gideon Henderson and Paul Valdes.

Finally I must thank my parents, Simon and Lassebasse for moral support, believing in me and providing me with due distractions when needed.

Contents

Chapter 1

Introduction

1.1 Project definition and motivation

Climate modelling is key to predicting future climates and to understand mechanisms of climatic change. It is required that such models are thoroughly tested to assess our confidence in their abilities, and to identify model aspects in need of improvement. Records of past climates provide a unique testing ground for climate models, including model response skill to changes in forcing. Most current General Circulation Models (GCMs) are capable of simulating the broad–scale patterns of the present day climate correctly. This does not necessarily mean that the models are able to simulate future climates, however. Paleo-climates do not provide a direct analogue for future climates, but do include a number of periods where the climatic changes relative to present day were as large as potential future changes due to an increase in greenhouse gases (Crowley and North, 1991). Paleo-model comparisons with geological evidence provide an objective measure of model robustness to such large changes in climate. This is why frameworks like PMIP (Paleoclimate Modelling Intercomparison Project), Palaeo–QUMP (Quantifying Uncertainties in Model Prediction) and this project are of importance.

Even if, according to the IPCC (Covey et al., 2001), our confidence in the models' ability to predict future change has improved, there are still discrepancies between observations and model results and uncertainties related to the fundamental aspects of the parametrisation schemes and representation of feedbacks. It is necessary to evaluate how reliable the models are and whether the complexity levels are sufficient to represent the possible range of climatic responses to changes in forcing.

This project involves exploring model response to forcing. A forcing can be explained as something that perturbs the radiative equilibrium of the climate system. Forcing mechanisms of the climate system can be divided into two groups: internal and external. External causes mean that the climate is being forced by factors outside of the system, such as the Milankovitch Cycle, as explained in **Section 3.4.1**. The concentrations of green house gases, GHGs, such as carbon dioxide and methane, change following the ice ages. On long timescales, of e.g. 10,000 years, this is an internal forcing mechanism. On shorter time scales, however, of say 20 years, this forcing becomes external because small changes in climate have a minimal effect on e.g. fossil fuel burning. Climate forcings are further described in **Chapter 3**. In this project we are trying to improve our understanding of the mechanisms of climate change by examining such changes in the past. We are aiming to provide a framework for the evaluation of the climate models to see if they are able to simulate climates that were different from today. This will improve our confidence in the models' projections for future climates.

Climate sensitivity can be defined in several ways, here it is defined as the equilibrium temperature response to doubling of pre-industrial carbon dioxide concentrations and it offers a simple metric of global warming. The estimates of climate sensitivity have been centred on 1.5–4.5K since the earliest studies and it persists in the latest IPCC (Intergovernmental Panel on Climate Change) assessment, with a best estimate of 3K

(Solomon et al., 2007) (**Figure 1.1**). The concept of climate sensitivity is a useful metric translating atmospheric CO_2 concentrations to warming. There are fundamental difficulties in ruling out the higher values of climate sensitivity due to the uncertainties in forcing and the physics of the response. Climate sensitivity is dependent on many parameters mainly in relation to atmospheric processes. Different sensitivities in the GCMs can be obtained by perturbing the atmospheric parameters, as seen in e.g. Stainforth et al. (2005) and Murphy et al. (2004). The large uncertainty in the estimates of climate sensitivity poses a problem when attempting to plan for and adapt to future changes in the climate. This motivates our efforts to attempt to constrain the estimates of sensitivity.

A lot of the work on constraining sensitivity using the past has been done with simple climate models (see Edwards et al. (2008) for a review of this work). A lot of the sensitivity studies have focused on the Last Glacial Maximum due to the large climate signal. It is easy to read too much information into such results and there is a need to redo the work with more complex GCMs. By looking at more data and the data in more detail alongside more complex models we get a more complicated picture and there is a less obvious constraint on sensitivity from the geological past.

It is important that we understand the complex climate models as they are being used for the prediction of future climates and to advise policy makers. If important decisions are being made on the grounds of GCM results, it is vital that we improve our understanding of their behaviour and establish how confident we are about the model results. Changing the forcing in a widely used GCM and testing output against paleo–observations provides one way to achieve such improvement.

Any GCM is only as good as the boundary conditions that are imposed on it. These include sea–surface temperatures (SSTs), carbon dioxide concentrations, land – sea

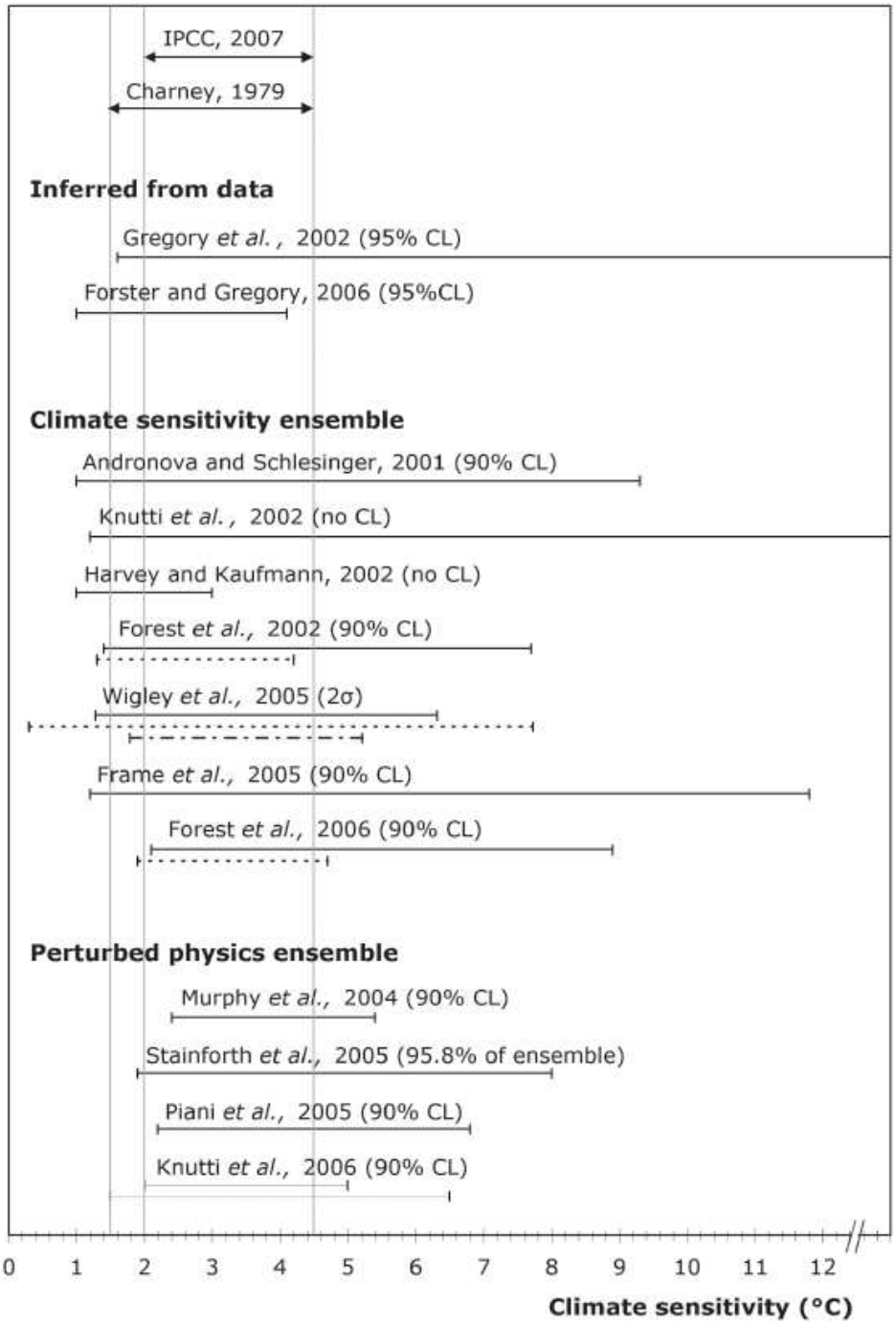

Figure 1.1: Climate sensitivity estimates based on constraints from modern climatic data (from Edwards et al. (2008)). Three bins are shown here: direct inference of climate sensitivity from data, climate sensitivity ensembles and perturbed physics ensembles. Wigley et al. (2005) used data from three volcanic eruptions. Three of the perturbed physics sensitivity estimates are based on climate*prediction*.net data and all four of the perturbed physics ensembles use the same GCM and may be influenced by biases in the underlying model.

mask, surface albedo, land surface properties and orbital variations, i.e. the limits within which the climate system operates. In this project the boundary conditions are perturbed. The principle of perturbing boundary conditions is to keep the conditions as realistic as possible and to omit key elements to see which are important. In the first experiment the boundary condition perturbation is based on proxy reconstructions of past conditions. A subsequent experiment entails an unrealistically large perturbation to investigate feedbacks in the climate system.

1.2 The mid-Holocene

In this study the models are tested under the mid-Holocene conditions, i.e. those of ∼6000 years before present (6kyBP). The experiment is designed to test the model response to changes in insolation: a seasonal and latitudinal redistribution of the incoming solar radiation at the top of the atmosphere due to the orbital cyclicity (Berger, 1978). The Holocene, the last ∼10,000 years, is marked by a relative climatic stability compared to the preceding glacial period which featured fast and large transitions between warm and cold conditions. The mid-Holocene is an attractive period to try to model because several of the boundary conditions (e.g. orbital forcing, sea level, trace gas concentrations and land ice extensions) are known through paleo-observations. Another factor that makes this period appealing from a modelling point of view, is that the atmospheric trace gas levels stabilised to pre-industrial levels during the early Holocene.

The mid-Holocene was chosen as one of the PMIP (see **Section 1.3.1**) focus periods due to the abundance of available paleo-data giving evidence of regional climates significantly different from today (Wright et al., 1993). The external forcing from orbital changes can be accurately prescribed and global quality controlled data synthesis are

available, e.g. the BIOME 6000 pollen and macro-fossil data records and the Global Lake Status Data Base (Harrison, 1989). Regional 6kyBP climatic features can be deduced from a wide range of geological records, both biotic and abiotic (Qin et al., 1998). It is a period of paleo–data abundance with well – dated records yielding information on regional to global scale climatic features. The mid-Holocene climate is further described in **Chapter 4**.

The attempt to simulate the geological past allows us to evaluate model responses to climatic changes. The aim is to compare the climate response of a GCM ensemble to paleo-data to discriminate, where possible, between realistic and unrealistic responses. Attempting to simulate climates that were substantially different from today provides an opportunity to evaluate model skill.

1.3 Related research

1.3.1 The Paleoclimate Modelling Intercomparison Project

The most comprehensive attempt to compare climate models with paleo–data is the Paleoclimate Modelling Intercomparison Project. It is a long standing initiative coordinating paleo-climate modelling activities. Their work form an essential backdrop to the work presented in this thesis. As for my project, PMIP seeks to investigate mechanisms of climatic change, the GCMs ability to simulate climates different from today and to identify feedback mechanisms of the climate system (Braconnot and Harrison, 2008). PMIP has made significant contributions to the last IPCC assessment reports promoting the understanding of past climate changes as a necessity for predictions of future change.

Nineteen modelling groups part–took in the PMIP mid-Holocene experiments. The

boundary conditions were identical in all the GCMs used and deliberately simple. The SSTs and land surface conditions were kept at present day conditions due to the lack of comprehensive data (Valdes, 2000). Harrison et al. (1998) presented some PMIP results regarding model predicted 6kyBP vegetation changes and Joussaume et al. (1999) published a global summary of 6kyBP climatic changes. More than 100 PMIP related articles have been published over the years. Each of the 18 PMIP models were simulated with the following equilibrium phases; one with present-day forcing, and one phase with mid-Holocene orbital configuration (Joussaume et al., 1999).

PMIP also defined a second experiment focusing on the Last Glacial Maximum (LGM), i.e. ∼21kyBP. This period was chosen to be omitted for this project due to the more extensive boundary condition changes needed for this type of experiment and these are associated with more uncertainties than for 6kyBP. It would have been rather time consuming to incorporate these changes into the climate*prediction*.net distribution package. It is also not ideal to use a slab model, as used in this project, for the LGM simulations, as it has been found that this poses a rather large constraint on the model simulations (Valdes, 2000). The slab model is a simplified ocean model consisting only of a thin mixed layer mimicking the upper oceanic heat transport and is described in **Section 3.3**.

The PMIP project has developed from the first phase, where atmosphere–only GCMs were used, into a second phase launched in 2002 using fully coupled atmosphere–ocean models and some simulations with atmosphere–ocean–vegetation models. The second phase is hence able to address the importance of the various feedbacks through these dynamically coupled GCMs (Harrison et al., 2002; Crucifix et al., 2005).

PMIP is currently developing an interest in new focus periods like the early Holocene

and the last glacial inception. Additionally the project is developing new forward modelling techniques based on paleo–data for the use in model evaluation and is encouraging the paleo–observation community to collect new data syntheses, especially of high resolution indicators (Braconnot and Harrison, 2008). Furthermore PMIP has developed a "Science and Implementation Plan" preparing for the next IPCC report. (The outline of the plan is available on the PMIP2 website http://pmip2.lsce.ipsl.fr/).

1.3.2 QUEST PalaeoQUMP

PalaeoQUMP (Quantifying Uncertainties in Model Prediction) is a QUEST (Quantifying and Understanding the Earth System) initiative aiming to constrain climate sensitivity using the geological past. The focus periods are again the LGM and the mid-Holocene. PalaeoQUMP is a continuation of the QUMP (Quantifying Uncertainties in Model Prediction) project, described in Murphy et al. (2004), where the effects of perturbing the physical parameters on climate sensitivity in an ensemble of the HadCM3 model were investigated. Murphy et al. (2004) found a climate sensitivity range of 2.5–5.5°C, as seen in **Figure 1.1**. The same set of parameter perturbation combinations is used in PalaeoQUMP in the search of paleo–constraints on climate sensitivity. The QUMP ensemble size is of 53 members, whilst the CPDN ensemble size is of ∼23,700 HadCM3 simulations and more than 290,000 HadSM3 model simulations have been completed. It has been found for both the probability density functions of climate sensitivity found in Murphy et al. (2004) and Stainforth et al. (2005) that the results are sensitive to sampling strategy in the physical parameter space.

The PalaeoQUMP model runs have not been completed at the time of writing, though it will be of great interest in due course to see how the results from this project compares to the the PalaeoQUMP results. More information on PalaeoQUMP can be

found at: http://www.bridge.bris.ac.uk/projects/PalaeoQUMP/index.html.

1.4 Testing models in a paleo–framework

Comparing models to proxy data is a challenge. Edwards et al. (2008) point out the less than optimal use of existing paleo-climatic records. One of the short comings lie in the lack of use of all the available paleo-data and paleo-climate reconstructions. It is preferable to compare model results directly to the data rather that paleo-climatic reconstructions. Edwards et al. (2008) suggest that for the field to move forward, the current range of paleo-climate model ensembles need to be extended. This view reinforces the rationale for this project. Presently more data are being added to the databases, in particular the pollen database. These expanded data sets will accommodate for more robust benchmarking of climate models in the future.

Model validations can be done with qualitative comparisons to mapped paleo – observations or quantitative comparisons to reconstructed changes in e.g. precipitation rate and temperature. Various methods exist for checking the models against the geological records, i.e. map – map comparison, regional averages and site – by – site comparisons.

Using quality – controlled global paleo–environmental synthesis maps to constrain the predicted range for climate sensitivity of climate models is a relatively new activity. Here one of the aims is to look for constraints on the uncertainty in climate sensitivity by using paleo–data and benchmarking model performance with our knowledge of the the mid-Holocene climate. At such a time-scale the climate signal is strong and regionally coherent in response to large and well-known changes in climate forcing.

Paleoclimate modelling provides an opportunity to investigate how the Earth's cli-

mate have responded to certain forcings and feedbacks in the past and how they may affect future climates. The results can be compared to a number of paleo-data sets.

1.5 Climate feedbacks

In allowing the meteorology in climate models to change during boundary condition [1] experiments, feedbacks operating in the climate system are likely to enhance or reduce the effect of the forcing itself. A forcing can be defined as a mechanism that makes the climate change by altering the global energy balance. Climate forcing mechanisms can for instance be fluctuations in the Earth's orbit, variations in ocean circulation and changes in the Earth's atmospheric composition. Houghton et al. (2001) defines a climate feedback as "an interaction mechanism between processes in the climate system, which is the result of an initial process triggering a change in a second process that in turn influences the initial one. A positive feedback intensifies the original process, and a negative feedback reduces it". Several feedback mechanisms operate in model sensitivity experiments.

The main feedbacks in GCMs, as identified by Colman (2003) are from water vapour, clouds, atmospheric lapse rate, and ice/snow albedo changes. The largest contributor is the water vapour, inducing a positive feedback in all 12 GCMs investigated by Colman (2003). The most uncertain feedback is due to clouds. The representation of feedbacks in the models induce a large range in uncertainty in the global mean surface temperature response to a forcing, e.g. doubling of carbon dioxide concentrations. Hansen et al. (2005) point out that feedbacks are highly model dependent and represented by parametrised processes making them an important contributor to model uncertainty. Feedbacks from ice and vegetation changes are investigated in

[1] Boundary condition changes imply that an external forcing has been applied to the model

this project, as seen in **Chapter 6** and **Chapter 7**.

Radiative forcing is the net change in incoming and outgoing radiation at the tropopause after the stratosphere has reached a new thermal equilibrium. The stratosphere reaches equilibrium much faster (time-scale of months) than the troposphere. The surface – troposphere system is slower, with time-scales of typically decades (Hansen et al., 1997), mainly due to the thermal inertia if the ocean. It is an externally imposed forcing that perturbs the energy balance of the Earth (Solomon et al., 2007). An increase in radiative forcing, ΔF, from e.g. an increase in GHGs or changes in the incoming solar radiation, scales with the surface temperature change, ΔT, and leads to an increase in the climate system's heat flux ΔQ, such that:

$$\Delta Q = \Delta F - \lambda \Delta T. \tag{1.1}$$

The heat is mainly taken up by the ocean. The outgoing long–wave radiation changes resulting from the change in forcing is affected by climate feedbacks (Knutti and Hegerl, 2008). The climate feedback parameter λ $[Wm^{-2}K^{-1}]$ is defined as the ratio of forcing to equilibrium temperature change, $\lambda = \Delta F/\Delta T$. The inverse, $S' = 1/\lambda = \Delta T/\Delta F$, is the climate sensitivity parameter. In this basic model the equilibrium temperature change is proportional to the radiative forcing, and forcing is independent of ΔT (to the first order). The total feedback is the sum of all independent feedbacks (Hansen et al., 1984), e.g. changes in albedo, water vapour, clouds, etc. Boer and Yu (2003); Senior and Mitchell (2000); Hargreaves et al. (2007) found however, that certain feedbacks change with the climate state and the linear feedback term $\lambda \Delta T$ is therefore only valid for surface temperature changes of a few degrees (Knutti and Hegerl, 2008). The simple energy balance model (**Equation 1.1**) is further evaluated in **Chapter 2**.

1.6 Aims

The aim of this thesis is to make use of the climate*prediction*.net distributed computing approach to address issues relevant to global change. This "perturbed physics ensemble" varies the parameters that affect the physics in the model within ranges that are thought to be realistic (Stainforth et al., 2005; Murphy et al., 2004). The climate*prediction*.net project is described in **Section 3.2**. Ensembles are a powerful tool to explore model sensitivity and each member takes on its own climate sensitivity value. A selection of models, or parameter combinations, are used to attempt to simulate the climate of the mid-Holocene. The model selection work was done by Sanderson et al. (2008). The simulations will be compared to paleo-climate observations.

The aims of this study are listed here:

- A target of this thesis is to establish a set of robust climatic features of the mid-Holocene. Various reconstructions based on paleo–observations are used to identify a number of distinctive 6kyBP climate patterns for the use of GCM benchmarking. Quantitative benchmarks are established where possible.

- To design and develop a grand ensemble of climate models and distribute this via climate*prediction*.net (CPDN). Each model will contain a calibration, control, mid-Holocene and a $2\times[CO_2]$ phase. It is intended to provide the paleo-community with the results from this ensemble and make it publicly available through the CPDN results portal.

- It will then be evaluated how well the paleo-ensemble compares to the mid-Holocene climate features as previously identified. I.e. how well can we model past climates? And can the mid-Holocene climate provide a constraint on climate sensitivity in the CPDN ensemble? To answer the latter, correlations

between observables and climate sensitivity are searched for.

- The importance and impacts of the model boundary conditions are also explored in this project. It is aimed to construct a distributed experiment where the boundary conditions are perturbed. This involves expanding Hudson Bay in the model's land – sea mask and including land ice in Eastern North America which was lingering on since the LGM. This experiment is then tested against local paleo-observations to see if the boundary condition perturbations improve the models representation of the meso-scale climate conditions.

1.7 Thesis structure

First the basic physics of climate change are looked into (Chapter 2) with an evaluation of the energy balance model equation. Despite its simplicity the equation illustrates some of the basic concepts arising in the study of the physics of the Earth's climate and its response to external forcing. Chapter 3 introduces the methods undertaken in this work, including background information on how climate*prediction*.net works and technical details of the GCM in question. The paleo–boundary conditions are also described, including the PMIP settings and the new boundary conditions chosen for one of the experiments. The models chosen for this study is further explained along with the ensemble design and the CPDN distribution process.

The fourth chapter outlines the paleo–observational benchmarks. First the main paleo–environmental synthesis maps are described, as most of the benchmarks are based on these. Then six model benchmarks are listed, ranked in an order of confidence in their robustness. The chapter describes the data the benchmarks are based on and makes suggestions as to how to compare the models with the data. Both map – map comparisons and quantitative comparison methods are suggested, where pos-

sible, for each climatic feature of the mid-Holocene. Paleo–environmental data from Eastern North America (ENA) are described for the comparison of model results from the experiment including the new and improved paleo – boundary conditions.

Chapter 5 evaluates the results from the first part of the distributed ensemble, where the models have been forced with the mid-Holocene boundary conditions of an altered orbital configuration and reduced methane concentrations, according to the PMIP standard. The ensemble is benchmarked against the set of 6kyBP climatic features as described in Chapter 4. A model case study is carried out where the results from the best performing ensemble member is investigated and it's parameter settings listed.

Chapter 6 goes on to assess the ensemble response to the new refined paleo–boundary conditions where the Laurentide ice sheet has been added to the model and the land – sea mask has been altered expanding Hudson Bay. The local impact of these changes are described and the ensemble mean is compared to the ENA observations discussed in Chapter 4.

Chapter 7 presents a sensitivity study performed in–house, where the vegetation in the model is perturbed. This is to investigate the importance of vegetation feedbacks upon the northwards expansion of the West African monsoon during the mid-Holocene in the model. Shortcomings in the the models' representation of the mid-Holocene African monsoon was found in Chapter 5 and this was the motivation for this experiment.

Chapter 8 contains a general discussion of the thesis and the main conclusions resulting from this project are outlined in Chapter 9. Future work is also suggested.

Chapter 2

Physical overview

In order to be able to simulate future climates, a model estimating the response to changes in forcing is needed. These models can vary greatly in complexity, from the basic Energy Balance Model (Equation 1.1) to the highly complex General Circulation Models (GCMs) (**Section 3.3**). I.e. these models range from a single partial differential equation to full atmosphere-ocean GCMs, which resolve many aspects of the Earth system, e.g. land surface processes, clouds and atmospheric chemistry. There are natural advantages and disadvantages using the different models, as an increase in complexity leads to an increase in computational costs and perhaps less readily interpretable results.

Firstly, as it is important that we understand the concept of radiative forcing, it's relation to climate sensitivity and it's impact on surface temperatures, the basic energy balance model is investigated. Then climate modelling of the more complex kind is looked into.

2.1 Radiative forcing and the global energy budget

The global energy budget is the balance between the amount of energy through solar radiation entering the climate system and the amount of energy leaving the system (illustrated in **Figure 2.1**). Around 30% of the incoming short-wave radiation is reflected or scattered back to space as a result of the Earth's albedo. The remaining 70% is absorbed by the atmosphere and the surface and radiated back through long-wave infrared radiation (Kiehl and Trenberth, 1997).

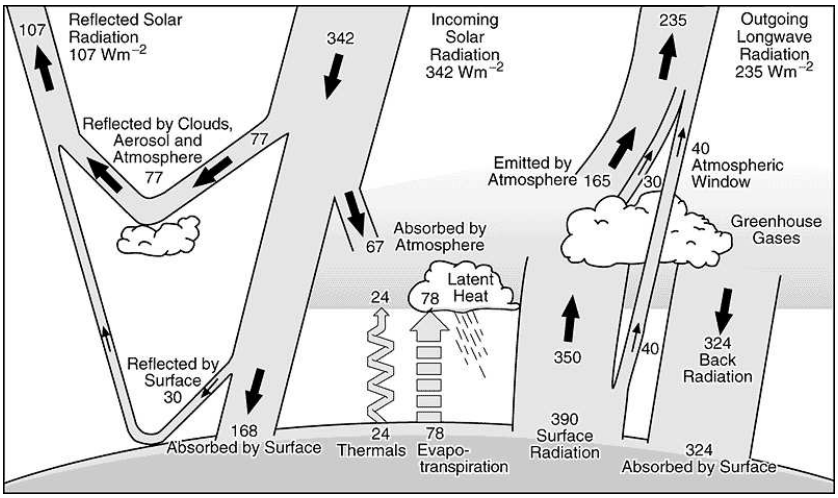

Figure 2.1: The Earth's global annual mean radiation budget [Wm^{-2}]. ∼49% of the incoming solar radiation is absorbed by the surface. That heat is re-emitted to the atmosphere as sensible heat, latent heat and thermal infrared radiation. The major part of this heat is absorbed by the atmosphere, re-emitting it both up and down. Radiation from cloud tops and atmospheric regions that are colder than the surface are lost to space. Some of the energy stays in the climate system. This is what drives the Greenhouse Effect (from Kiehl and Trenberth (1997)).

The amount of energy radiated by the Sun or Earth, assuming they are perfect emitters i.e. black bodies, can be expressed by Stefan-Boltzmann's Law:

$$E = \epsilon \sigma T^4, \tag{2.1}$$

where the Stefan–Boltzmann constant is: $\sigma = 5.6704 \times 10^{-8} W s^{-1} m^{-2} K^{-4}$, and the emissivity, ϵ, is 1 for a perfect black body. The irradiance, E, has the units of $W m^{-2}$. It states that the total energy radiated per unit surface area per unit time is proportional to the fourth power of the temperature of the black body. There is a significant difference between the incoming solar radiation and outgoing terrestrial radiation, affecting the climate system. GHGs affect the amount of radiation that the Earth is able to absorb and emit. The energy emitted by the Sun, i.e. the solar constant, assuming the Sun is a black body:

$$S = E_{Sun} \left(\frac{R_{Sun}}{R_{orbit}} \right)^2 = 1557 W m^2, \tag{2.2}$$

where E_{Sun} is the energy emitted by the Sun and R_{Sun} and R_{orbit} are the radius of the Sun and the radius from the Sun to the Earth's orbit respectively. The amount of energy received at the Earth depends on the size of the Earth and the amount reflected back to space:

$$E_{in} = \pi r_{Earth}^2 S(1 - \alpha). \tag{2.3}$$

r_{Earth} is the radius of the Earth, S is the Solar constant and α is the albedo of the Earth (typically of 0.3).

Now treating the Earth as a black body radiator, the total energy emitted from the entire surface area of the Earth becomes:

$$E_{out} = \left(4\pi r_{Earth}^2 \right) \left(\sigma T^4 \right). \tag{2.4}$$

Hence the energy balance between the incoming solar radiation and the outgoing radiation becomes:

$$\pi r_{Earth}^2 S(1 - \alpha) = 4\pi r_{Earth}^2 \left(\sigma T^4 \right)$$

$$\frac{S}{4}(1-\alpha) = \sigma T^4. \tag{2.5}$$

Illustrating GHGs: energy balance equation at the TOA:

$$\frac{S}{4} = \sigma T_{atmos}^4 = \sigma T_e^4, \tag{2.6}$$

where T_{atmos} is the atmospheric temperature and T_e is the emission temperature. The energy balance for either atmosphere or surface can be used to determine the surface temperature in equilibrium, when absorbed energy = emitted energy:

$$\begin{aligned} atmosphere : \sigma T_s^4 &= 2\sigma T_{atmos}^4, \\ surface : \frac{S}{4}(1-\alpha) + \sigma T_{atmos}^4 &= \sigma T_s^4. \end{aligned} \tag{2.7}$$

This requires that $T_s^4 = 2T_e^4$. T_s is the surface temperature.

Now considering climate sensitivity and feedbacks, as the climate system, including the surface temperatures, can change when a perturbation or forcing is applied:

$$\frac{dT_s}{dS} = \frac{\delta T_s}{\delta S} + \sum_{i=1}^{N} \frac{\delta T_s}{\delta x_i}\frac{dx_i}{dS}. \tag{2.8}$$

The first fraction, $\frac{\delta T_s}{\delta S}$, represents the direct effect of the solar constant change on surface temperature, whilst the second term represents the sum of all feedbacks associated with each climate variable x.

Now let the emitted energy from the Earth be an unknown function of the surface temperature, $E(T_s)$. R is the net radiation, which is 0 in equilibrium:

$$R = \frac{S}{4}(1-\alpha(T_s)) - E(T_s) = 0 \tag{2.9}$$

Let the equilibrium climate be forced by a perturbation F, e.g. $2\times CO_2$, to the energy balance. Using the chain rule to express the change in net radiation to the perturbed forcing:

$$\frac{dR}{dF} = \frac{\delta R}{\delta F} + \frac{\delta R}{\delta T_s}\frac{dT_s}{dF} = 0. \tag{2.10}$$

The total derivative of the net radiation must be 0 in going from one equilibrium state to another. Equation 2.10 is therefore rearranged to express the total change in temperature for a particular forcing F:

$$\frac{dT_s}{dF} = \frac{-\frac{\delta R}{\delta F}}{\frac{\delta R}{\delta T_s}} = -\left(\frac{\delta R}{\delta T_s}\right)^{-1} = \left(S\frac{\delta \alpha}{\delta T_s} + \frac{\delta F}{\delta T_s}\right) = \lambda. \tag{2.11}$$

This relates the magnitude of the global mean temperature response to an external forcing and we arrive at Equation 1.1 first introduced in **Section 1.5**:

$$F = \lambda \Delta T. \tag{2.12}$$

λ is the so-called feedback parameter $[Wm^{-2}K^{-1}]$, representing a combination of possible feedback processes in the climate system. It quantifies how the net inward heat flux, Q, varies with temperature. If Q increases with temperature, λ is negative and tends to enhance temperature perturbations, i.e. corresponding to a positive feedback. If, say, Q decreases with temperature, λ is positive and tends to dampen temperature perturbations (negative feedback). F, the radiative forcing, is defined as the change in net downward heat flux at the tropopause due to an external forcing after the stratosphere has returned to equilibrium (Shine et al., 1995).

Considering a simplified version of the real and complex climate system in the form of an energy balance model allows us to identify some important basic properties of the real system. Possible changes in the climate due to changes in radiative fluxes may

also be explored. Changes in the radiation can result from changes in greenhouse gas concentrations, aerosols, albedo changes or changes in the solar "constant".

CO_2 acts as a climate forcing through changing the radiative properties of the atmosphere and increasing the ability absorb thermal infra-red, long wave, radiation. It is a so-called greenhouse gas (GHG). More radiative heat is trapped in the Earth system and increases the climate system's ability to absorb energy. The direct radiative impacts of long lived GHGs, i.e. CO_2 and CH_4, are relatively well understood. The impact of other forcings are a lot less straight forward, however.

The radiative effects of aerosols are a lot less well understood (Anderson et al., 2003). They can have both a direct and indirect radiative effect. This forcing agent is thought to have a net cooling effect on the climate, however (Haywood et al., 2000; Yu et al., 2006). Aerosols can change the radiative properties of the atmosphere through changing the cloud albedo. Aerosols act as cloud condensation nucleis (CCNs), as these small particles facilitate for droplet condensation leading to a lot of smaller droplets rather than fewer and larger ones. This way the clouds become brighter and more solar radiation is reflected back into space (Houghton et al., 2001).

The influence of the anthropogenic Earth surface albedo changes can also act a forcing on the climate. Deforestration and agricultural activity is thought to increase the albedo (Betts, 2001), whilst soot depostion onto ice and snow acts to warm the climate through reducing the reflectivity of the surface (Hansen and Nazarenko, 2004). The severity of these effects are uncertain and under debate.

Considering the surface heat fluxes, a balance between the amount of incident solar radiation and the radiative cooling to space is obtained. A change in one of these will result in changes to the other until equilibrium is re-established. Such an exter-

nal change, or radiative forcing (F), must balance with the change in global mean temperature, ΔT. Considering the global energy budget out of equilibrium, the rate of heat uptake, $\frac{d\Delta Q}{dt}$, of the Earth must be taken into account. ΔQ is the change in energy compared to the system's heat content:

$$F = \lambda \Delta T + \frac{d\Delta Q}{dt}. \tag{2.13}$$

The deep ocean has the largest heat store capacity in the climate system with the ability to store as much as 1000 times the heat capacity of the atmosphere. Making the approximation that the ocean is a surface mixed layer in thermal contact with the atmosphere, with a heat capacity proportional to changes in the air temperature at the surface, the rate of the heat uptake of the whole climate system, $\frac{d\Delta Q}{dt}$, is approximately equal to the rate of oceanic heat uptake. The appropriate amount of ocean to include, however, is of $\sim$0.7. Further assuming that the rate of the ocean heat uptake can be expressed by the heat capacity of the global oceans per unit surface area, C, times the rate of change of surface air temperature, $\frac{d\Delta T}{dt}$:

$$\frac{d\Delta Q}{dt} = C\frac{d\Delta T}{dt}. \tag{2.14}$$

Substituting this into equation 2.13 and rearranging, the following is obtained:

$$C\frac{d\Delta T}{dt} = F - \lambda \Delta T. \tag{2.15}$$

The radiative forcing concept is useful for climate change research when it is possible to distinguish between the forcing, feedback and climate response. This is possible when working with GCMs and e.g. the $2\times CO_2$ experiment.

2.1.1 Constant forcing

Considering the case when a constant radiative forcing, $F = F_c$ is applied to the climate system, e.g. an instantaneous doubling of CO_2:

$$C\frac{d\Delta T}{dt} = F_c - \lambda \Delta T. \tag{2.16}$$

We can't simply work out λ as C is uncertain, though observations of the SST range and ocean heat content changes over the past 40 years or so exist. A more fundamental problem is that we don't know F. Greenhouse gases are not the only external factor affecting climate over the past century, but also land – use changes, ozone levels, volcanic eruptions, aerosols from sulphate emissions and changes in the output from the Sun.

Equation 2.16 may be solved as a first order linear differential equation for the deviation of the global mean temperature from its equilibrium value using an integrating factor of $e^{t/\tau}$ to obtain the following solution:

$$\Delta T = \frac{F_c}{\lambda}\left(1 - e^{-\frac{\lambda t}{C}}\right). \tag{2.17}$$

The response time of the climate system can in this case be expressed by $\tau = C/\lambda$. Hence a large heat capacity or a low feedback parameter will take a long time to reach a new equilibrium after the forcing has been applied. The feedback factor, λ does not scale linearly with ΔT (**Figure 2.2**) making it difficult to constrain climate sensitivity,

$$S = \frac{F_c}{\lambda}. \tag{2.18}$$

The figure (2.2) is the predicted response by this simplified energy balance model after a forcing of $2\times CO_2$ has been applied to the Earth system. It shows λ versus the

resulting change in surface temperatures ΔT, i.e. climate sensitivity. The physics of the response and uncertainties in forcing means it is fundamentally difficult to rule out high sensitivity values resulting from doubling of carbon dioxide concentrations (Knutti and Hegerl, 2008).

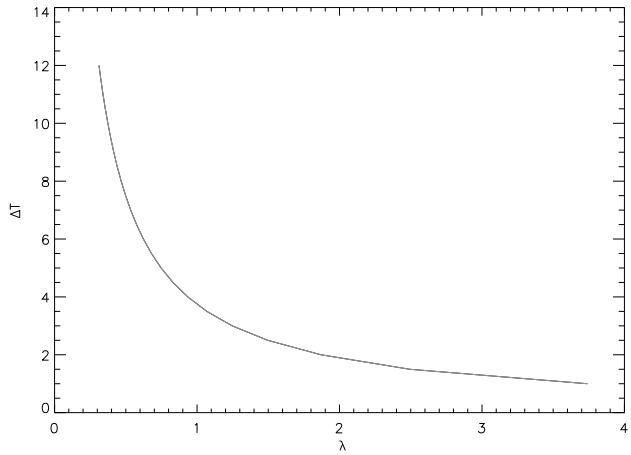

Figure 2.2: The feedback parameter, λ, versus surface temperature change for a doubling of pre-industrial CO_2 forcing, as predicted by the energy balance model. The ocean heat capacity is assumed to be $2.1 \times 10^7 JK^{-1}m^{-2}$.

From the simple equation (equation 2.16) it is seen that equilibrium temperature increase is proportional to the radiative forcing and can be seen as a function of the current CO_2 relative to the pre-industrial CO_2: $\Delta T = S \ln(CO_2/CO_{2,t=pre-ind})/\ln 2$ (Knutti and Hegerl, 2008).

A doubling of the pre-industrial CO_2 concentrations is equivalent to a radiative forcing of about $3.7 \mathrm{Wm}^{-2}$ (Forster, 2007). The heat content is an uncertain issue in the slab model, where it is assumed to be $C\frac{dT}{dy} \propto C$, a constant. This brings up the issue that the results from PMIP and this ensemble are somewhat uncertain, based on the assumption of the ocean heat content, which is not allowed to vary or change in the simple slab ocean.

2.1.2 Seasonal cycle

The orbital forcing on the global annual mean climate during the mid-Holocene was small, as later described (**Chapter 3**). There was a seasonal and latitudinal redistribution of the incoming solar radiation at the top of the atmosphere, however (Berger, 1978). The seasonal cycle in surface heat flux per unit area can be represented by a sinusoidal function (**Figure 2.3**). The heat flux per unit area is considered to see a local seasonal cycle. The forcing can thus be expressed by:

$F = F_0 \sin(\omega t + \phi)$.

F_0 is the amplitude of the oscillation of the heat flux downwards through the atmosphere due to the seasonal cycle. $\omega = 2\pi f$ where f is the frequency of the seasonal cycle and ϕ is the phase factor (constant). Equation 2.13 then becomes:

$$C\frac{d\Delta T}{dt} = F_0 \sin(\omega t + \phi) - \lambda \Delta T. \tag{2.19}$$

Solutions for ΔT can be sought using an integrating factor and integrating by parts. Multiplying through with an integrating factor of $e^{\frac{\lambda t}{C}}$, the following is obtained:

$$\Delta T e^{\frac{\lambda t}{C}} = \int e^{\frac{\lambda t}{C}} \frac{F_0}{C} \sin(\omega t + \phi) dt. \tag{2.20}$$

Integrating by parts twice gives:

$$\begin{aligned} \Delta T e^{\frac{\lambda t}{C}} &= \frac{F_0}{\omega C} e^{\frac{\lambda t}{C}} \cos(\omega t + \phi) \\ &+ \frac{F_0 \lambda}{\omega C^2} \left(e^{\frac{\lambda t}{C}} \frac{F_0}{\omega} \sin(\omega t + \phi) - \frac{\lambda}{\omega C} \int e^{\frac{\lambda t}{C}} \sin(\omega t + \phi) dt \right). \end{aligned} \tag{2.21}$$

Equating equations 2.20 and 2.21, rearranging and then substituting back into equation 2.20, followed by dividing through by $e^{\frac{\lambda t}{C}}$ finally provides the solution of:

$$\Delta T = \frac{F_0 C\omega}{C^2\omega^2 + \lambda^2}\left(\frac{\lambda}{C\omega}\sin(\omega t + \phi) - \cos(\omega t + \phi)\right). \tag{2.22}$$

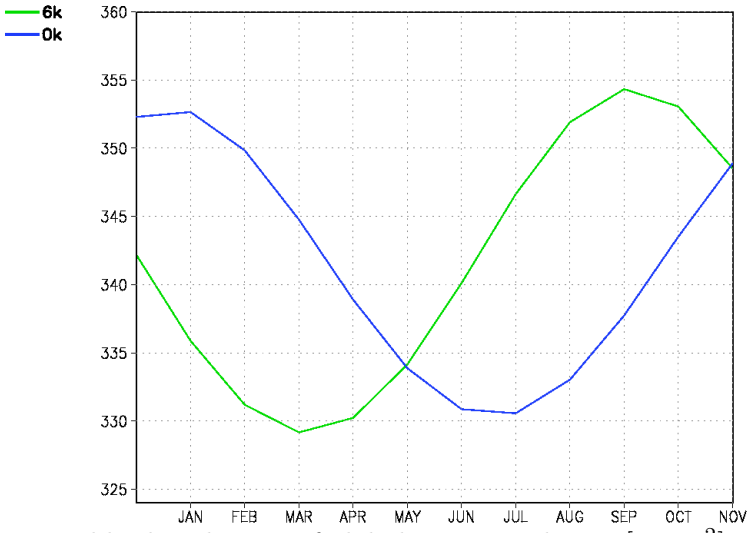

Figure 2.3: The monthly distribution of global mean insolation [Wm^{-2}] at 6kyBP (green) and at present (blue).

Over the duration of a year, $\Delta T = 0$ (eqn 2.22), and the $\frac{\lambda}{C\omega}\sin(\omega t+\phi)$ and $\cos(\omega t+\phi)$ terms are balanced out.

Looking at Equation 2.22, it is obvious that for small values of λ, i.e. $\lambda \to 0$, the cosine term becomes the dominant term. For the case when the feedback parameter is very large, i.e. $\lambda \to \infty$, the sine term dominates over the cosine term. This illustrates how λ contributes to determine the seasonal variations in surface temperatures through time. As a cosine wave is a phase shifted sine wave, i.e. $\cos\phi = \sin\left(\phi + \frac{\pi}{2}\right)$, we see how seasonal shifts in temperatures, as in e.g. the mid-Holocene climate, arise from Equation 2.22.

2.2 Modelling the climate system

Away from the very basic, but illustrative energy balance model, we have the complex general circulation models. These attempt to include more of the intricate processes of the real climate system. To evaluate more aspects of the climate response to changes in forcings, the AOGCMs (Atmosphere–Ocean General Circulation Models) need to be used. These type of models have been evolving and in use for more than 40 years (Smagorinsky et al., 1965).

AGCMs, the atmospheric part, may include various components such as atmospheric chemistry and land surface models. The Earth's surface is discretised into grid boxes, or grid cells or alternatively spherical harmonics. Each grid box has prognostic variables such as temperature, atmospheric pressure, etc. Diagnostic variables are calculated from these prognostics. The equations of fluid motion are integrated forward in time deriving the evolution of the prognostics and the climate state.

The AGCM contains a radiation code, which is most often divided into two components: the longwave and shortwave, representing the terrestrial infra-red radiation and solar shortwave radiation respectively. This part of the model code calculates the amount of radiation absorbed and emitted by each atmospheric layer in the model. The calculation is often done twice, including and emitting the effects of clouds on the radiation budget, hence estimating the "clear-sky" and "cloudy" fluxes.

With regards to the oceanic component of the GCM, it can be represented by the use of a so-called thermodynamic "slab" ocean, or of course a full oceanic circulation model. The slab model is described in **Section 3.3.1**. It is vertically isothermal and represents the upper mixed layer of the ocean, with the equivalent heat capacity. The full oceanic GCM is, similarly to the atmosphere, discretised both vertically and

horizontally, resolving the transport of fluid and heat. Both generally contain a sea ice model.

Numerous processes, both in the atmosphere and ocean, occur at scales smaller than that of the model grid. These processes are therefore parametrised so they can be accounted for in the integration. Grid scale diagnostics are related to the sub–grid scale processes through parametrisation schemes. Cloud cover, land–surface processes and convection are all parametrised. These parametrisations all contain uncertainty. Each parameter has a range of realistic values, derived from observations of the true climate system. The use of an inappropriate parameter value or physical model may cause a systematic bias in the simulated climate. There is an uncertainty in the model response due to the uncertainty and inaccuracy in the representation of the model physics.

Uncertainties in GCM predicted climate response to a certain forcing arise from two major sources: boundary conditions and model response. Stott and Kettleborough (2002) found through a process called "optimal fingerprinting" that the dominant uncertainties over the next 30–40 years were from the model response, rather than the initial conditions or forcing scenario. This study highlights the importance of not only representing the actual uncertainty in the model predictions due to the model physics, but also improving the model physics themselves.

Model parameters can be tuned to best represent the underlying physics of the present and past climates. This might not hold for future predictions, however. An additional problem is that the effect of multiple parameter perturbations on the large scale climate cannot be predicted without performing the actual model simulation. The solution to this problem is to perform simulations covering all possible ranges and combinations of parameter values and check the results with observations to reduce

the uncertainties in the parameter values (Smith, 2002). Exploring the full parameter space requires substantial amounts of computing resources, however. Every combination of parameter perturbations must be simulated since one cannot assume that the effects combine linearly. The computational resources required increase exponentially with the number of parameters in question (Allen et al., 2000).

Chapter 3

Tools and Method

3.1 Introduction

This chapter describes the methods and tools used in the project, starting with climate*prediction*.net, the model used, paleo-boundary conditions and how they are decided and the distribution design, including the models chosen for the study. So far, the CPDN method for the atmosphere–slab model experiments has been to use three phases, including a calibration, control and $2\times CO_2$ phase. Here (**Section 3.2.2**) it is described how this method has been edited in this project to include four phases, i.e. a paleo-phase has been added.

3.2 Climate*prediction*.net

The motivation behind the climate*prediction*.net project is that climate change and our response to it are issues of global importance. There is a wide agreement within the climate science community that the Earth is likely to continue to warm over the coming century. Climate*prediction*.net (CPDN) is trying to address the crucial question of how much. It is the world's largest computer – based climate modelling

experiment where each participant can download a unique version of a GCM and it will run as a background process making use of available CPUs. The data is returned to the CPDN database via the Internet, when the GCM run has completed. The distributed computing project makes use of thousands of standard public or home computers to run climate model simulations and has got ∼50,000 volunteers at any one time. The experiment has now passed more than 43 million model years simulated (June, 2009) and is a unique tool for investigating model behaviour.

CPDN is a perturbed physics ensemble of GCMs, i.e. it takes one climate model and make changes to the physical parameters in it. These parameters arise from the need to parametrise physical processes that occur on sub–grid scales and to quantify poorly understood physical parameters. The parameters perturbed are typically in the cloud scheme, as there are large uncertainties in the behaviour of various cloud properties. Additionally, perturbations are made to the initial conditions and the model parameters to explore all viable combinations in order to find the possible range of the climate's response to $2\times[CO_2]$. Stainforth et al. (2005) found that the single perturbations with the largest influence on climate sensitivity are the entrainment coefficient, critical relative humidity and the ice fall speed. (See http://climateprediction.net for more information). The CPDN ensemble approach contrasts with the multi-model approach, e.g. the Coupled Model Intercomparison Project (CMIP) and PMIP, where several different GCMs are compared.

Figure 3.1 shows the frequency distribution of simulated climate sensitivity from the climate*prediction*.net ensemble (Stainforth et al., 2005). The black curve shows the result from 2578 slab models, the red curve represents all the models, except those with perturbations to the cloud-to-rain conversion factor, whilst the blue shows all model version apart from those with perturbations to the entrainment coefficient. Most sen-

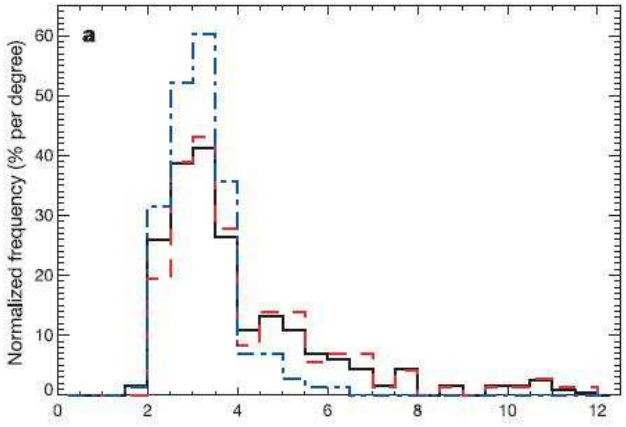

Figure 3.1: The frequency distribution of simulated climate sensitivity using all model versions (black), all model versions except those with perturbations to the cloud-to-rain conversion threshold (red), and all model versions except those with perturbations to the entrainment coefficient (blue) (Stainforth et al., 2005).

sitivities cluster around 3.4 K, which corresponds to the value for the unperturbed model, i.e. the model with the default parameter values. This figure indicates that the parameters you choose to perturb in your ensemble determines the shape of your frequency distribution. See **Appendix A** for a definition of the various parameters and **Appendix B** for the default values of the parameters.

3.2.1 The CPDN HadSM3 three–phase procedure

The usual CPDN HadSM3 procedure involves taking one model with a certain combination of parameter values and run it with three phases, i.e. each simulation includes three different phases: a calibration phase (model years December 1810 – November 1825), followed by a control phase where the CO_2 concentrations are kept at a pre-industrial level of 280ppm (model years December 1826 – November 1840), and a final phase during which the pre-industrial [CO_2] is doubled to 560ppm (model years December 2050 – November 2065). In the calibration step, the SSTs are artificially kept at a steady level and the heat needed for this is calculated and applied to the following phases. In the control step, the SSTs are varying according to how much

energy the ocean receives and emits. This is assumed to be of equivalent magnitude as in Phase 1, hence the application of the heat flux convergence extracted from the first phase. The temperatures of the atmosphere should therefore remain stable in the control run, unless the energy balance at the TOA has been altered. **Figure 3.2** illustrates the three model phases used in the original CPDN HadSM3 ensemble.

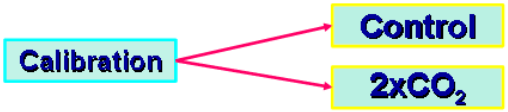

Figure 3.2: The different model phases used in the original CPDN HadSM3 ensemble, including the calibration-, control- and $2\times[CO_2]$ phases. The end climate of the calibration phase is used as the starting climate of the two follow-on phases.

As the new forcing is applied in the third and final phase, the atmosphere should eventually adjust to a new stable equilibrium climate. This perturbed physics method is a way of testing which combination of parameters that work. We are seeking combinations that produce climate scenarios that are realistic, i.e. no snowball Earth scenarios or boiling oceans. The parameters represent the approximations and assumptions needed to be made in the model. These parameters can hold a range of realistic values. The climate sensitivity can be deduced by comparing the global average surface temperatures from the control and $2\times CO_2$ phases. The average over the last eight years of the model run is used to find the former. To find the predicted equilibrium temperature, equation 2.17 is revisited. The change in temperature is fitted to the exponential expression (c.f. (Stainforth et al., 2005)):

$$\Delta T(t) = \Delta T_{2\times CO2}(1 - e^{-t/\tau}). \tag{3.1}$$

This provides a $T_{2\times CO2}$ estimate that allows for the uncertainty in the response time scale, τ.

3.2.2 The new HadSM3 four–phase procedure.

In this project the distribution code has been changed to incorporate a fourth phase where a paleo-forcing is applied to the model. The first step is to investigate the effect on the modelled climate by altering the Earth's orbital parameters. The obliquity was increased from the current value of 23.446° to 24.105°, representing 6kyBP. In addition, the eccentricity is changed to the 6kyBP value of 0.018682 compared to the current value of 0.016724. The angular precession takes a value of 0.87° in the 6kyBP simulations and 102.04° in the control and $2\times[CO_2]$ scenarios. The mid-Holocene orbital parameters are given by Berger (1978) and are shown in **Table 2.1** in addition to the present day values. The impact of increasing the obliquity to 6kyBP values is to increase the amount of incoming solar radiation at high latitudes, whilst changing the longitude of perihelion redistributes the seasonal distribution of insolation. The changes made to the eccentricity here have comparably little impact.

Boundary Conditions:			
	Obliquity	Eccentricity	Precession
0kyBP	23.446°	0.016724	102.04°
6kyBP	24.105°	0.018682	0.87°

Table 3.1: The Milankovitch boundary conditions for the 6kyBP and 0kyBP simulations. The solar constant is 1365 Wm^{-2}. These boundary conditions follow the PMIP standard (see e.g. Joussaume et al. (1999)).

The main change in incoming solar radiation at 6kyBP was due to the displacement of the longitude of perihelion (Berger, 1978). The orbital configuration then intensifies (weakens) the seasonal distribution of the incoming solar radiation in the northern (southern) hemisphere, by about 5%. This is illustrated in **Figure 3.3**, which shows the zonally averaged differences in insolation [Wm^{-2}] at the TOA between the mid-Holocene and present throughout the year. The Milankovitch Cycles are further described in **Section 3.4.1**.

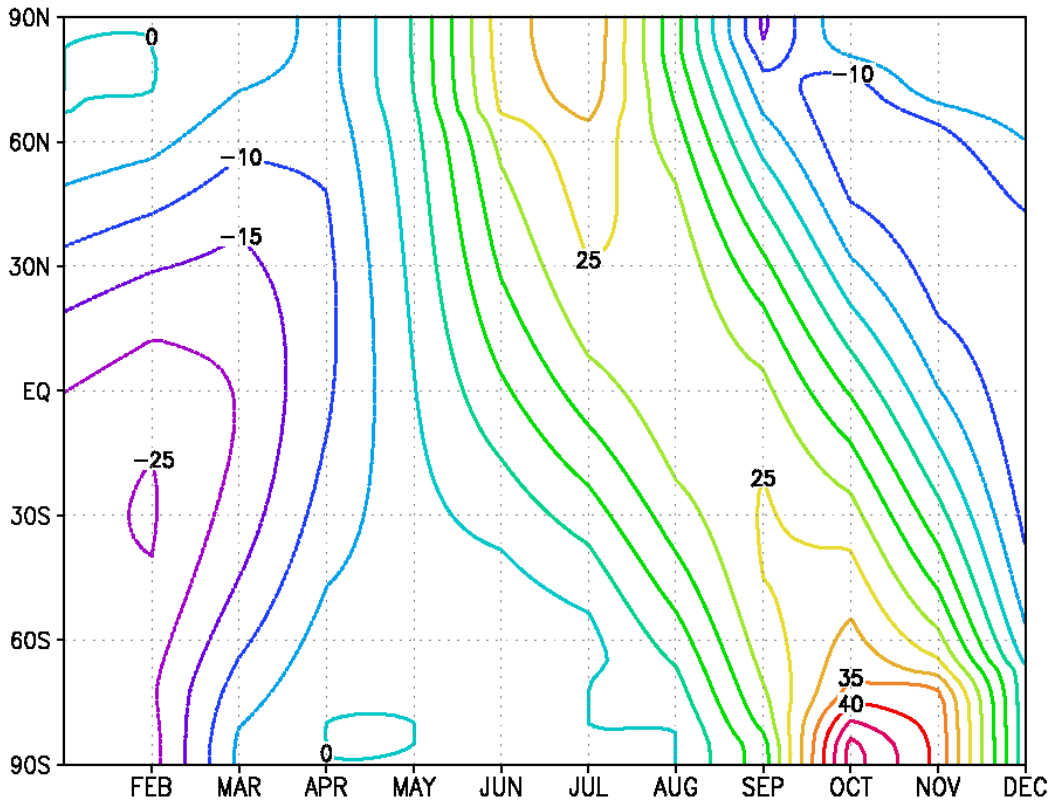

Figure 3.3: The latitude – month distribution of the differences in insolation [Wm^{-2}] between 6kyBP and 0kyBP.

In addition to alter the orbital configuration to represent the mid-Holocene, as described earlier, the methane, CH_4, concentrations are reduced somewhat from 700ppb to 650ppb. This is in line with the PMIP (Paleoclimate Modelling Inter comparison Project) standard for 6kyBP boundary conditions. The methane concentrations are derived from ice core data (Raynaud et al., 1993).

The output from the last eight years of the run is compared to a pre-industrial control run. The data are averaged over the last eight years of the simulation in order to ensure that a stabilised climate is sampled. Due to the lower heat content of the slab compared to a full ocean circulation model the model takes a shorter time to reach equilibrium after the forcing has been applied at the beginning of the simulation.

After the calibration step, there is the usual control step, but in this experiment an

additional model run is performed, were the orbital forcing of the Mid-Holocene is applied to the models. These phases are also followed by a $2\times[CO_2]$ forced stage. The control, 6kyBP and $2\times[CO_2]$ phases are initialised from the end climate of the calibration integration. The different phases are illustrated in **Figure 3.4**.

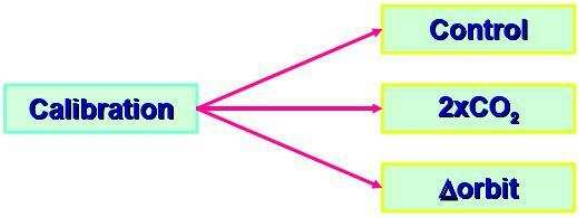

Figure 3.4: The different model phases used in this project, including the calibration-, control-, $2\times[CO_2]$ and the mid-Holocene phase with altered orbital configuration. The end climate of the calibration phase is used as the starting climate of the three follow-on phases.

3.3 The Model

The Met Office Unified Model is a state-of-the-art General Circulation Model (GCM). Here HadSM3 is used, which is the atmospheric component of the model, i.e. HadAM3, in combination with a mixed layer slab ocean. The horizontal grid consists of an Arakawa B grid with a 2.5° latitude × 3.75° longitude resolution and there are 19 vertical levels in the atmosphere (Stainforth et al., 2005). The vertical levels use hybrid coordinates and each time step is of 30 minutes. The vegetation is kept fixed at modern conditions in the model. The equations governing the atmosphere are the quasi-hydrostatic versions of the full primitive Navier–Stokes equations, and include the Coriolis force.

Due to the resolution of the climate model certain processes need to be parametrized. These parametrisations are not true representations of the real world but they represent important processes of the climate system. They are subject to uncertainty and can pose a large effect on the climate in any given model. The parameters are per-

turbed within a known range of realistic values. The schemes that are parametrized in the model include the radiation, clouds, precipitation (large scale and convective), convection, gravity wave drag, advection, diffusion and boundary layer processes (Pope et al., 2000).

Atmospheric momentum, mass, angular momentum and water content are conserved within the model away from source and sink regions. The boundary layer in the model consists of five layers and uses a turbulent mixing scheme where the mixing is calculated from local turbulent fluxes. Roughness length is used to represent the various surface types including orographic drag effects.

Known biases in the model, improved from the earlier HadAM2 version of the model though still not fully resolved, include too high pressure at high latitudes, cold biases at the tropopause in high latitude summers and in the storm tracks as found in a study by Stratton (1999). Another bias in the model is the too strong Hadley and Walker cells.

3.3.1 The slab ocean and ice component

The slab ocean model consists of a 50m deep vertically isothermal and static mixed layer ocean. This accounts for the upper oceanic seasonal storage of heat (Jackson and Broccoli, 2003). Oceanic heat transport by currents is simulated by additional sources and sinks of heat in the mixed layer. These flux adjustments are functions of latitude, longitude in addition to season, but has no inter-annual variability. A TOA (Top Of the Atmosphere) radiative imbalance of about $1.2\mathrm{Wm}^{-2}$ is considered to be reasonable for a completely adjusted model, according to Stainforth et al. (2005). Modern day climate simulations are the basis for determining the magnitude of the heat flux adjustments. The sea ice amount and SSTs are prescribed, in order to find

the heat needed to maintain that state. In an equilibrium state, the globally averaged heat flux adjustments tend to zero. For each simulation, there is a calibration phase where the heat flux convergence is calculated. In this phase, the SSTs are kept fixed, whereas in the following control run, the SSTs are allowed to vary. The SSTs vary in accordance to the atmosphere–ocean heat flux (Stainforth et al., 2005). The advantage of using a slab model, as opposed to a full ocean general circulation model, is that it is computationally cost effective and a long spin – up phase is avoided. Meehl (2004) suggest that the atmospheric model is dominant in determining the equilibrium response based on work done with several AOGCMs.

The simple slab ocean incorporates a zero layer sea ice model with thermodynamics and a basic representation of sea ice dynamics (Gordon et al., 2000). The slab ocean allows for no dynamical response within the ocean but allows atmospheric forcings to change the distribution of SSTs. This lack of dynamical oceanic response has the benefit of rapid equilibrium conversion within few years. The sea ice model is able to respond to forcing through the ice–albedo feedback mechanism (Curry et al., 1995). The surface temperature change in response to e.g. a doubling of CO_2 would be underestimated in the model (i.e. lower) if the important ice–albedo feedback was not included in the model. Rind et al. (1995) and Ingram et al. (1989) evaluate the issues with the simplified sea ice representation.

A simple climatology of ocean surface currents is used to advect sea ice. Where the sea ice is thicker than 4.0m the resistance of ice to convergence sets the current to be zero. In a fully coupled atmosphere – ocean GCM, snow that falls into the sea cause a latent cooling of temperatures due to the melting snow. This changes the heat fluxes into the ice, where snow falls into open ocean next to sea ice. This process is simplified in the slab ocean, however, as grid cells containing ice have fixed SSTs. The snow is distributed over existing ice and snowfall over the open water is

not considered, affecting the conversion of sea water into ice. If a region becomes filled with sea ice and the heat convergence does not allow for this, the model ignores the heat convergence values in the relevant grid boxes as calculated in the calibration phase. The SST and sea ice climatologies are based on the GISST (Global Ice and Sea Surface Temperature) 3.1 and 2.2 data sets available at BADC (British Atmospheric Data Centre) provided by the Met. Office. GISST contains grid information on the monthly mean global sea surface temperatures from 1871 to 2003. Statistical methods were used to derive a global coverage in areas where no data is available (Rayner et al., 1996). The sea ice data originate from various sources, including passive microwave data from satellites and digitized sea ice charts (Rayner et al., 2003).

The obvious advantage of the slab model is that it is fast and many more model runs can be performed. The model integration is so much quicker to complete than for HadCM3, making it a more appropriate tool for a D.Phil project due to the natural time-constraints that implies. The slab model is also considerably more popular to download by the volunteers than the full AOGCM. It is a priority for CPDN to keep the users that we already have and to keep them motivated to stay connected to the CPDN project we aim to provide them with the quick slab model to download. The HadCM3 model with its long spin–up phase is a lot less popular and is often reserved for the more serious and long–term BOINC users. It is realised that in using the slab model instead of the full ocean circulation model, there is a risk that the climatic response to the mid-Holocene forcing is less realistic and that oceanic feedbacks are underestimated.

3.3.2 The vegetation module

The vegetation is kept fixed at modern settings in the original CPDN slab model ensemble. In order to use the Hadley Centre's dynamic vegetation scheme, TRIFFID

(Top–down Representation of Interactive Foliage and Flora Including Dynamics) (Cox et al., 2001), with the model a different land surface scheme than the one incorporated in the CPDN set–up has to be used. Currently CPDN is using MOSES (Met Office Surface Exchange Scheme) 1, whilst the MOSES 2 scheme has to be used in order to dynamically couple the model to the TRIFFID vegetation module. Moses 2 is an enhancement of Moses 1 with hydrology and boundary layer scheme modifications, including a new ice scheme in radiation and radiatively active anvils in convection (Essery et al., 2003). MOSES 2 calculates certain values that are exported to TRIFFID. Updating the land surface scheme and including the global dynamic vegetation model in the CPDN set–up would involve too much time and effort, hence the already existing set–up is used for this distribution. An offline vegetation model, e.g. BIOME4, could be used on the model results instead. It calculates biomes based on the climatology resulting from a GCM and this biome map can be directly compared to observations, i.e. BIOME 6000.

As seen in the BIOME 6000 data there are some differences between the modern and 6kyBP vegetation. The vegetation differences in the tropics would have an impact on the local water recycling, if included in the simulations. The more moisture demanding vegetation at 6kyBP facilitates for stronger convection through enhance moisture supply to the atmosphere through evapotranspirational processes. In the middle latitudes the differences in the 6kyBP albedo would be of importance. Neglecting to include for these changes in the model makes the simulations less realistic. But on the other hand, circularity issues are avoided and the model results can be compared to the BIOME 6000 data. This data is essential for the benchmarking of the model results.

3.4 Paleo – boundary conditions

Perturbing the boundary conditions imply that a forcing has been applied to the model. The external forcing may be changes in greenhouse gases or changes in the insolation due to orbital cyclicity. The forcing agent might result in a climatic response of e.g. changes in temperature. The application of different boundary conditions may cause the effect of the perturbed physics parameters to be stronger or yield a wider response range. This "boundary value problem" is predictability of the second kind which is how strong perturbations force the climate system to respond (Collins and Allen, 2002).

This section outlines the paleo-boundary conditions for the 6kyBP model, beyond the orbital settings, and the motivation behind these choices.

3.4.1 Milankovitch Cycles

As introduced in **Section 3.2.2**, Milankovitch Cycles is the name for the effect of the alterations in the Earth's orbital motion on the climate. The theory is named after Milankovitch, who formalised the theory (Hays et al., 1976). The Milankovitch theory was developed by Adhémar, Croll and Milankovitch. Initially their theories were difficult to verify due to lack of reliable observations.

The ∼100,000 year ice age cycle is a result of the variations in the axial tilt, eccentricity and precession of the Earth's orbit. The changes in the motion and orientation of the Earth changes the amount of solar radiation reaching the Earth, i.e. the solar forcing.

Obliquity (Axial tilt): The angle of the axis of the Earth's tilt varies with respect to the plane of the Earth's orbit. The Earth's obliquity ranges from 22.25–

24.5° and back again over ∼41,000 years, as indicated in **Figure 3.5** (Imbrie et al., 1993). The current obliquity is of 23.446°. The amplitude of the seasonal cycle in incoming radiation at the TOA increases as the tilt increases. At the maximum tilt of 24.5°, the seasonal temperatures become more extreme: the winter temperatures are colder and the summers warmer than for a state with a smaller tilt. The cooler summers at small obliquity values are thought promote the initiation of ice ages.

Precession (Wobble): Precession is the change in the Earth's axis of rotation relative to the fixed stars. It is due to the tidal forces from the Moon and the Sun on the Earth associated with the non–perfect spherical shape of the Earth, i.e. the Earth is an oblate spheroid bulging at the equator caused by the centrifugal force of the Earth's rotation. The precession of the orbit leads to a ∼26,000 year cycle in the equinoxes. When the axis is aligned such that it points towards the Sun during perihelion when the Earth is the closest to the Sun in the orbit, one hemisphere has a larger amplitude in the seasons, whilst the other has milder seasons.

Eccentricity (Orbital shape): The shape of the Earth's orbit around the Sun is an ellipse. The eccentricity is the degree of how much the ellipse departs from being perfectly circular. The eccentricity ranges from 0.005 (closest to circular orbit) to 0.058 and the mean eccentricity is of 0.028. At the most elliptical orbit, the TOA incoming solar radiation (insolation) is about 23% more at perihelion (closest approach to the Sun) than at aphelion (the largest distance from the Sun). The eccentricity of the Earth's orbit varies due to the gravitational impacts of Saturn and Jupiter. Perihelion is presently 3^{rd} of January and aphelion 4^{th} of July.

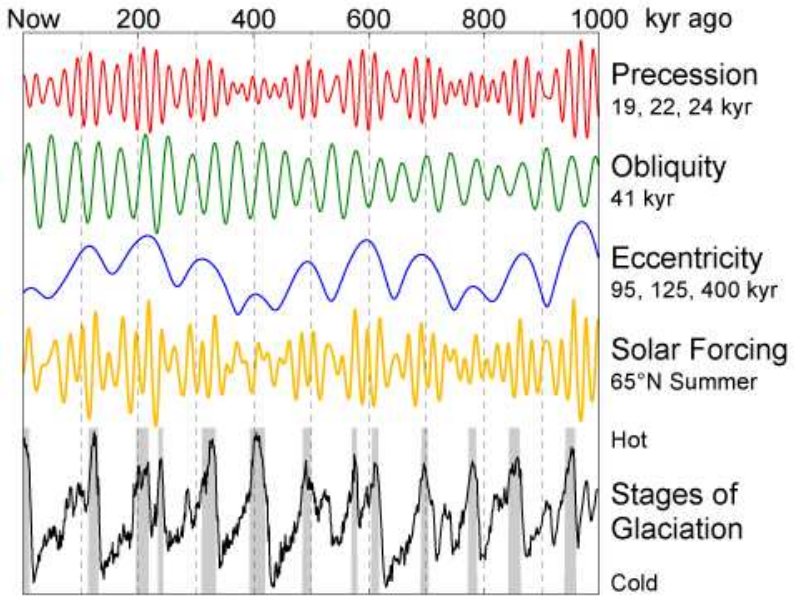

Figure 3.5: The Milankovitch Cycles (Imbrie et al., 1993).

Globally the largest differences in insolation between 6kyBP and present happens in winter and summer. In the Northern Hemisphere the differences are the largest in June and July, with the differences being somewhat bigger at high latitudes (**Figure 3.6**). From this we would expect the 6kyBP NH summer to be warmer than present, and somewhat colder in winter, though less so. The insolation has a sinusoidal behaviour with larger amplitude at high latitudes, with a slight phase shift at 6kyBP. At the equator the wave number is two.

3.4.2 Ice Sheets

The last global deglaciation event was the LGM (Last Glacial Maximum), ∼21,000 years ago. This ended the last 100kyr ice age cycle. The thickness of the ice sheets dating back to the LGM has only been poorly constrained until recently. This has been done by applying equilibrium glaciological models of continental ice sheet formation. In such models, a combination of the isostatic adjustment and ice mechanical modelling–based methodologies have been applied to make a major advance (Peltier,

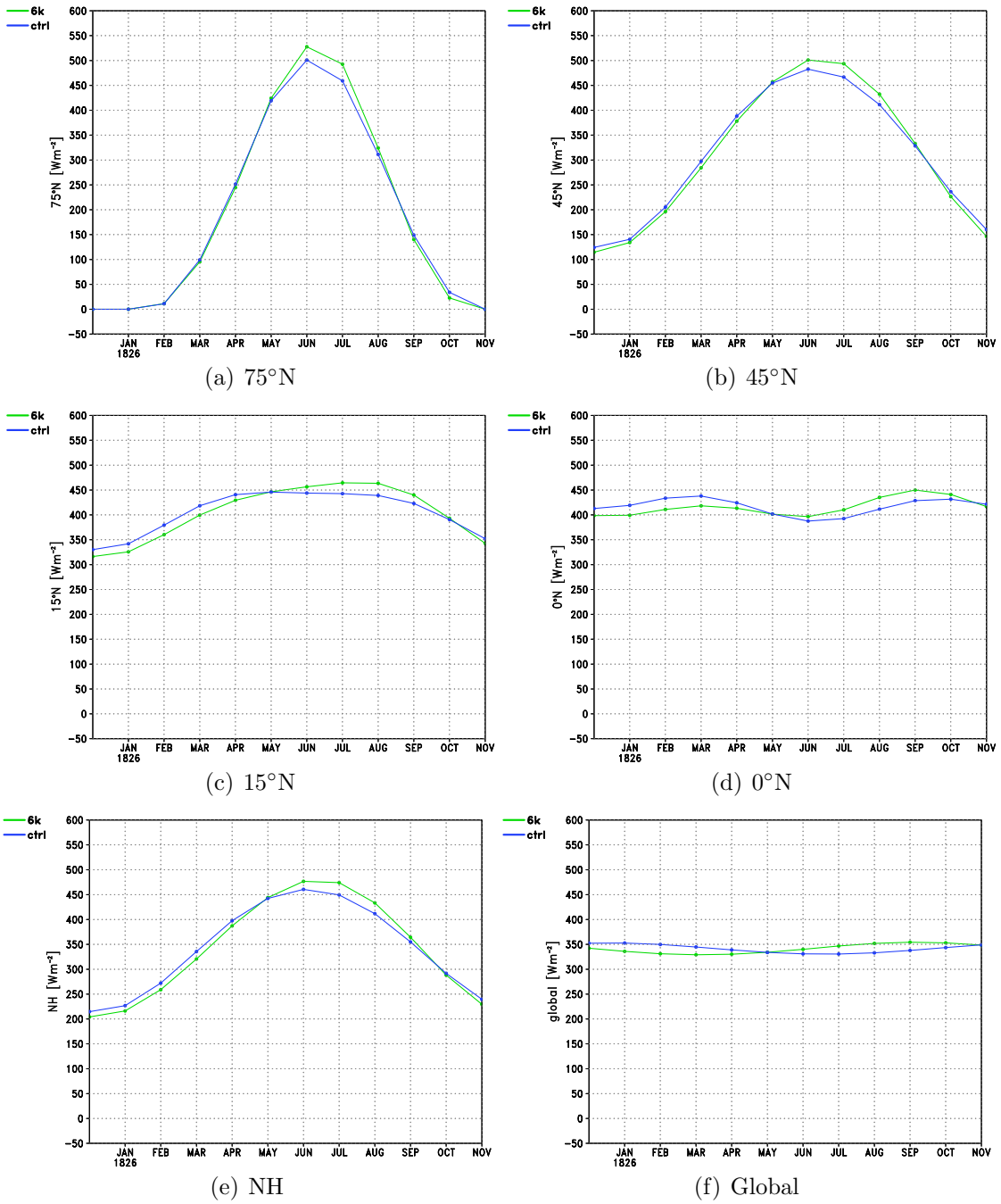

(a) 75°N (b) 45°N

(c) 15°N (d) 0°N

(e) NH (f) Global

Figure 3.6: The incoming solar radiation at the top of the atmosphere at 75°N, 45°N, 15°N, equator, NH and globally [Wm^{-2}]. Green is the 6kyBP insolation and blue the present day.

2004). This modelling technique now serves as a tool to develop surface boundary conditions for coupled atmosphere ocean GCMs exploring past climates.

Although climates were as temperate or somewhat warmer than at present in the early

Holocene – mid-Holocene, large amounts of land ice remained in eastern Canada because it had not had enough time to totally melt away. As the ice retreated rapidly and cooled the local climate, the ice masses exposed a rim of new land (Taylor et al., 1997). After it took time for the forest to recolonise. In Alaska too, the present forest cover had not yet returned fully, with ongoing ecological succession (Taylor et al., 1997). Most other areas, however, had somewhat similar vegetation cover to the present. In the early Holocene the Laurentide ice sheet was still large enough to have a significant downwind cooling effect.

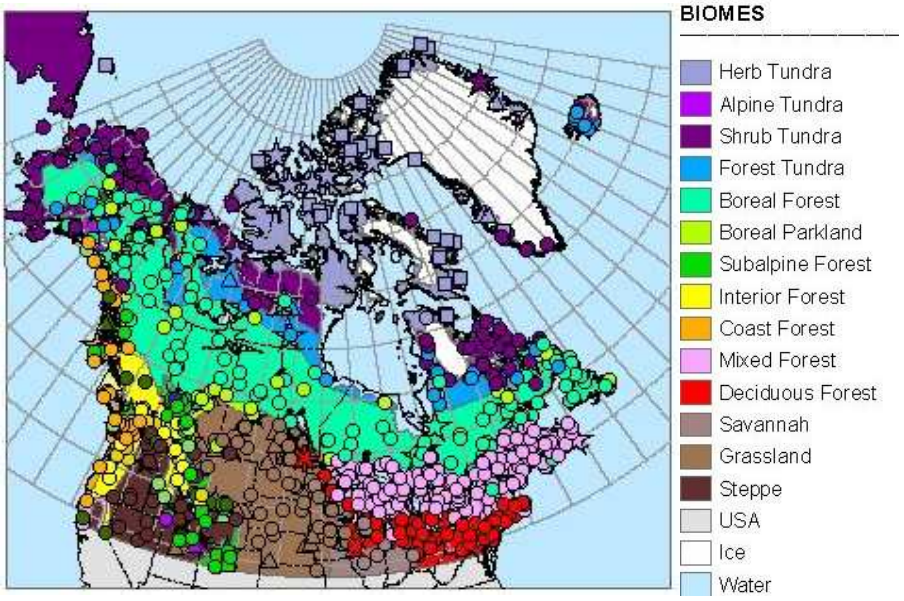

Figure 3.7: A map showing the 6kyBP paleo-environments from North America (map from the Geological Survey of Canada, based on the work of Dyke et al. (2003)). Note the larger Hudson bay area and the remnants of the Laurentide ice sheet. The dots, squares and stars indicate proxy sites: pollen, macrofossil and mammal. The shaded contours show the distribution of terrestrial biomes based on the proxy data from the region. The purple and blue colours represent tundra, green boreal forest, pink mixed forest and brown grassland. Each observation site is indicated.

The map (**Figure 3.7**) is from the Geological Survey of Canada and shows the 6kyBP conditions of North America; note the larger Hudson Bay and regions of ice on Baffin Island and in Québec. This is the remnants of the Laurentide ice sheet.

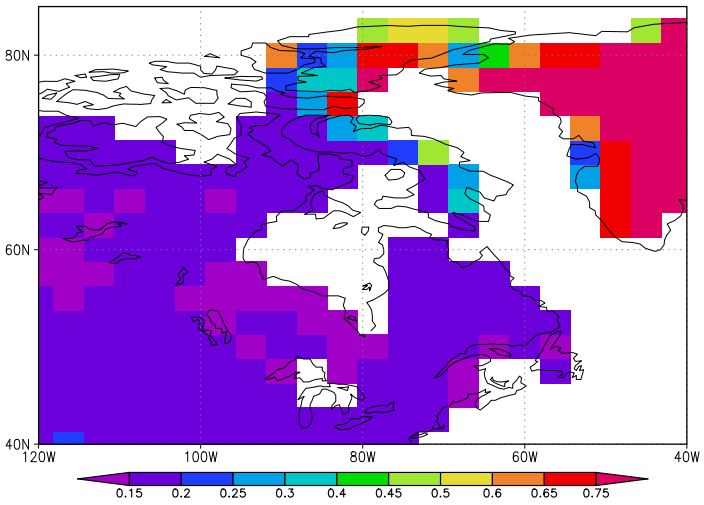

(a) 0kyBP

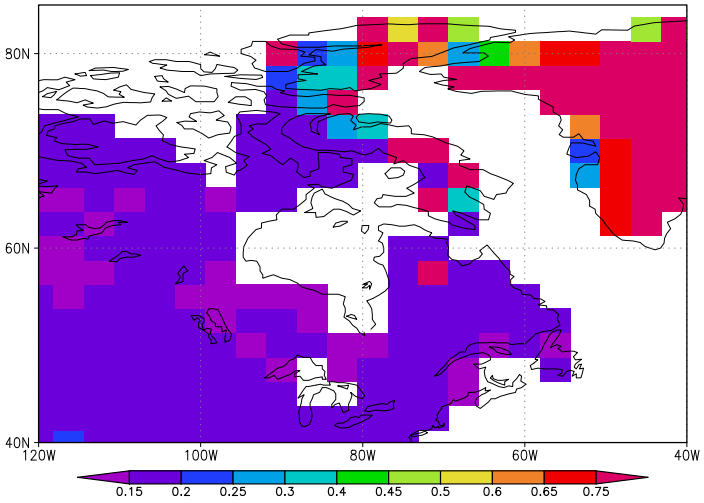

(b) 6kyBP

Figure 3.8: The old (a) and the new (b) ancillary files for the model, here showing the snow free surface albedo. The new ancillary files has been constructed based on the work of Dyke et al. (2003).

No modelling efforts to date have included the 6kyBP Laurentide ice sheet or the difference in the coastlines of Eastern North America (ENA) which result from the isostatic depression by the ice and perhaps as a result the modelling community has struggled to simulate the local Eastern North American 6kyBP climate. This encouraged the QUEST project PalaeoQUMP to create new ancillary files for the mid-Holocene time slice, i.e. model files describing the boundary conditions. As a part of my project I have included these new boundary conditions and in an attempt

to capture a more valid representation of the ENA local climate in our models. The present day and new 6kyBP model land – sea mask and snow free surface albedo are seen in **Figure 3.8**. Five land points have become sea in the new ancillary file and eleven grid boxes now contain ice, e.g. the albedo has been increased to make the surface more reflective. The model file describing the vegetation distribution also contains other fields than just the snow free surface albedo. The changes made to these are shown in **Appendix C**. The vegetation is kept fixed in the model, as explained in **Section 3.3.2**.

3.4.3 The Baltic Sea

The Baltic Sea was extended during the Holocene, which is shown in both data from e.g. Uscinowicz et al. (2000) and in the ICE-5G model (Peltier, 2004). The land was still lowered after the recent ice sheet retreat. The ice model results for the surface elevation [m] are seen in **Figure 3.9**, with the 6kyBP results in (a) and 0kyBP results in (b). The largest differences occur in grid boxes that are already sea in the model's land – sea mask due to the coarser GCM resolution, and no changes are made to the boundary conditions in this region.

3.5 The models chosen for the study

Around 100 models are focused on in this project. The models were chosen based on work by Sanderson et al. (2008). A climate model emulator was developed using artificial neural network techniques and trained with data from 4000 CPDN models to emulate the response of the climate model output. These emulated ensemble members were used to look for models closest to observations within each 0.1K bin of sensitivity found within the original CPDN ensemble. The method allowed the

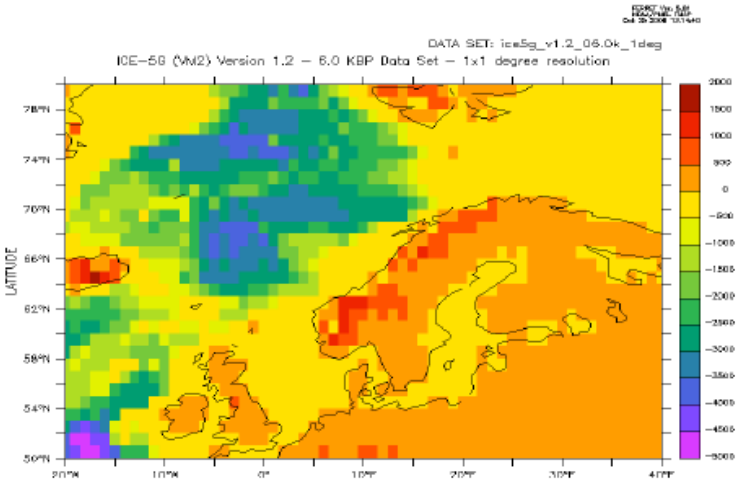

(a) 6kyBP

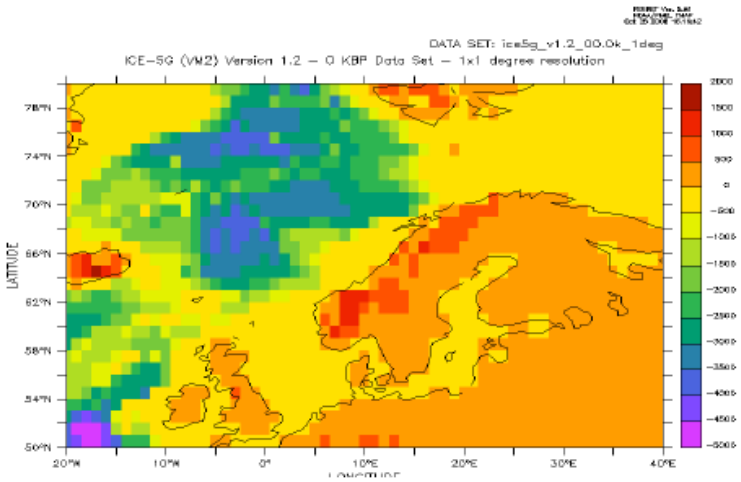

(b) 0kyBP

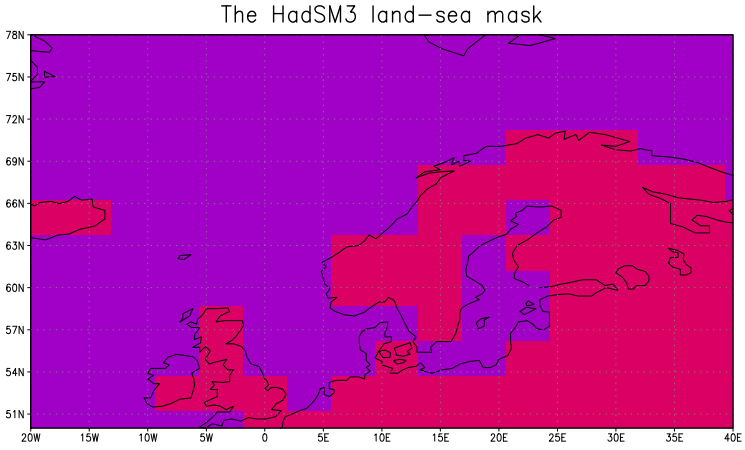

(c) land-sea mask

Figure 3.9: The ICE-5G (VM2) Version 1.2 results showing surface elevation [m] for the Baltic region for (a) 6kyBP and (b) 0kyBP. (c) shows the HadSM3 land-sea mask.

CPDN team to explore the model parameter space more than in the original CPDN ensemble. The CPDN method so far has been to choose 2 – 3 values for each parameter and investigate the model response to combining various perturbed parameters. These perturbations represent the extremes of the range of the uncertainty in the parameter value. Sanderson et al. (2008) found the parameter changes necessary to achieve a wide range of climate sensitivity whilst minimising the deviation from the observations.

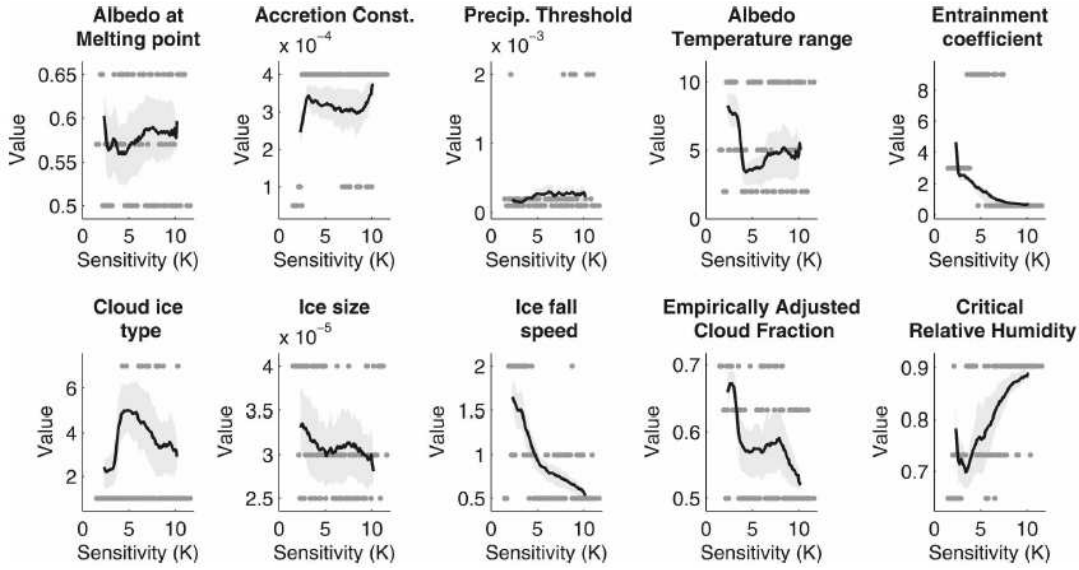

Figure 3.10: The black line shows the mean parameter value from the 100 best performing emulated models in each 0.1K sensitivity bin. The grey shading indicated the 10–90th range of the 100 best models (Sanderson et al., 2008). The grey dots show the parameter value for the best performing model in each bin (if one exists) from the original CPDN ensemble. The average parameter values from the 100 emulated models are used in this project.

The modern observations the models have been tested against is the temperature and precipitation data from the NCEP (National Centers for Environmental Prediction) reanalysis data and the radiative data from the ERBE (NASA's Earth Radiation Budget Experiment) data-set. JJA and DJF seasonal means, in addition to annual means of temperature, precipitation and radiation model data were tested against the observations.

After the artificial neural network had been trained and verified, a Monte–Carlo parameter perturbation experiment was performed and an ensemble of many order of magnitude greater than the original CPDN data-set was emulated (1 million members). The ensemble sampled the parameter space densely, hence allowing Sanderson et al. (2008) to find the best performing models, as judged by observational constraints, in different 0.1K climate sensitivity bins. Given that we do not know the behaviour of models in the unsampled parameter space, the neural network is designed to give a smooth transition between the model responses at the known parameter values. This set of models were used in this project.

Figure 3.10 shows the sensitivity value versus the parameter settings for the chosen models for my ensemble. The black line shows the mean parameter value for the 100 best performing models within the ensemble in each 0.1K sensitivity bin. The grey shading indicates the 10 – 90^{th} range of the 100 best performing models. The dark grey dots show the parameter value for the best model in the bin from the original ensemble, if one exists. By evaluating the input parameters for the most likely models in each sensitivity bin, we can find the parameter perturbations needed in order to achieve the best models at different climate sensitivities. The optimal parameter settings required for a given sensitivity whilst making each model as close to observations as possible is predicted (**Figure 3.10**). For more information on how the models were selected see Sanderson et al. (2008).

3.6 Ensemble design

The model used is HadSM3 (**Section 3.3**). The 4–phase procedure as outlined in **Section 3.2.2** is applied to the 100 best performing models from Sanderson et al.

(2008). In the mid-Holocene phase of the experiment, the boundary conditions are changed by lowering the methane concentrations and by altering the orbital configuration (Table 2.1). This allows us to tease out the model response to this forcing. The results from the models will be compared to observations of the mid-Holocene climate. Such model validations can be done by qualitative comparison to mapped paleo-observations, or by quantitative comparison to reconstructed changes in temperature and the moisture budget. The next chapter (**Chapter 4**) proposes a method for validating the model results against a list of observational benchmarks.

In a second experiment, the same 100 models are re-run with a different set-up. This time the models will be distributed including for the different coastline, or land – sea mask, and the Laurentide ice sheet. The land – sea mask has to be the same in all the four phases, as a slab ocean model is being used and calculating heat flux values in the calibration phase that are applied to the slab ocean in the remaining three phases. For this purpose the land – sea mask needs to be the same in all four phases. In the mid-Holocene phase in this part of the experiment, the Laurentide ice sheet is included and the eleven grid boxes are set to ice, as explained in **Section 3.4.2**. This way the models might simulate a more realistic local climate in ENA. The ensemble design for this part, comparative to **Figure 3.4**, is illustrated in **Figure 3.11**.

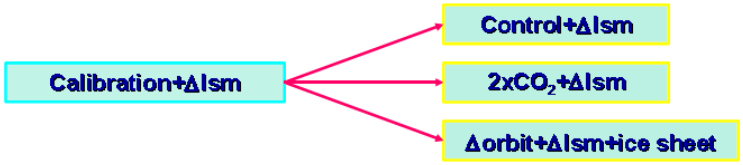

Figure 3.11: The different model phases used in the second experiment, including the calibration-, control-, $2\times[CO_2]$ and altered orbital configuration phases. In the mid-Holocene phase the $[CH_4]$ is reduced, orbital configuration changed, the land – sea mask changed and the Laurentide ice sheet included for. The land – sea mask is the same in all the phases.

3.6.1 Distribution process

The distribution process consists of three phases as described in this section. There are two test phases before the models are finally launched via the main website. Volunteers are encouraged to log on to the project's website and download the model.

Alpha – test: Firstly the models were alpha tested. This involved setting up the models as work units and creating namelists for each set of parameters. The model source code had to be adjusted to incorporate the four phases (**Figure 3.4** and **3.11**), as opposed to the usual CPDN three phases. The models were then sent out to the Oxford University computing cluster to check the model code is working and producing physically sensible results.

Beta – test: After having proved that the new 4–phase process was functioning, there was the beta test. The model work units were made available to the public via a separate website to climate*prediction*.net (http://cpdnbeta.oerc.ox.ac.uk). This is to test that the whole downloading and uploading process is working and check that the model executable runs on new versions of operating systems. Each computer downloads a unique version of the model. It runs on the host computer and trickles back results regularly and the final batch of the results are returned to the CPDN servers when the model run of 60 years (the 4 × 15–year long phases) has completed.

CPDN launch: When it has been assured that all processes function as they should and that the results are looking sensible, the models are released from the main climate*prediction*.net website and the results of the models are returned to the project database.

The download – upload procedure is illustrated in **Figure 3.12**. This project's home-page is located at http://www.climateprediction.net/science/hadsm3mh.php (Link

valid September 2008). After the full ensemble has been returned to the project servers, the results are freely available to download from http://results.cpdn.org. In this way we provide the research community with invaluable resources.

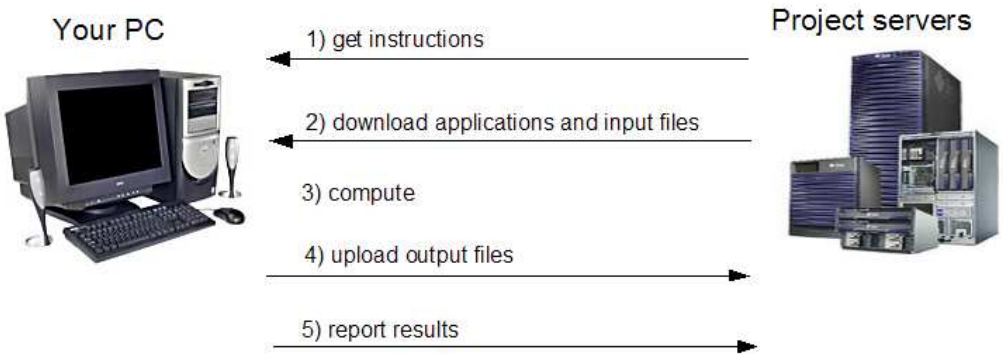

Figure 3.12: A simple illustration of how the process of downloading and uploading the CPDN models work (http://climate*prediction*.net).

Climate*prediction*.net uses a platform called BOINC, i.e. the Berkeley Open Infrastructure for Network Computing. Many aspects of the BOINC platform makes it user friendly allowing download and maintenance times to be kept at a minimum. The downloaded BOINC package contains the four following modules:

1. The client: the interface between the remote servers, local package and the user.

2. Experimental control: this controls the shut down and restart of the model as the user switches the computer off and on. It also handles the post processing of the integration results which is returned to the project servers.

3. Visualisation: the graphical interface allowing the user to follow the model integration in real time. The diagnostics viewable include surface pressure, temperatures, precipitation and clouds.

4. Model: the model executable containing the model source code and ancillary files.

The recommended system requirements is 600 MBytes of available disc space, 256MBytes of RAM and hardware with 800MHz capabilities minimum. The model is available for Linux, Windows and Mac. On the average desktop computer the simulation of the full four phases of a total of 60 model years would take around 3–4 weeks.

The initial conditions (dtheta) in the model are also perturbed with ten different values ($0.03 \leq \Delta\theta \leq 0.09$). This is to sample the uncertainty in the starting climate in the model. So each set of parameters, one model, is sent out in combination with ten various dtheta values to produce a sub-sample of model variability averaging out noise and quantifying sampling uncertainty. Changing the initial conditions does not involve changing the model physics or the boundary conditions. Several models can be run with different initial conditions and this group of models provide an insight into the range of responses associated with an individual physics perturbation. Perturbing the initial conditions tend to give diverging short term forecasts, though for long term climate forecasts the signal is reduced over the long term time averaging (Collins and Allen, 2002; Palmer, 2000). This is known as predictability of the first kind. The results of the ten models with the same parameter values but different initial conditions are averaged. The ensemble size therefore becomes of $\sim$2000 and is the world largest 6kyBP perturbed physics paleo–ensemble.

Not all the model integrations distributed provide reliable results. Models are not included in the analysis if

– The simulation contains contaminated data in associations with "over–clocking", or overworking the processor, or data loss due to computers loosing internet connection or being switched off during critical data upload times.

– The modelled climate is drifting. Models with a drift of more than 0.02K/year in the control phase is deemed unstable (Stainforth et al., 2005).

3.7 Summary

This chapter describes how the already existing CPDN tool has been developed to suit the needs in this project, by altering the source code to include four phases instead of the three phases used so far in the CPDN slab experiments. The fourth phase added is the paleo–phase, where the model is forced with mid-Holocene settings. The distribution has been designed to make use of a selection of 100 models (see Sanderson et al. (2008)) covering the full range of sensitivity values found in the original CPDN ensemble. These models will be used in two set of runs, à four phases:

- In the first part of the distribution, each model will consist of four phases, each of 15 years; a calibration, control, $2\times[CO_2]$ and a 6kyBP phase. Here the 6kyBP phase is forced with reduced methane concentrations and most importantly an altered orbital configuration.

- In the second part of the distributed experiment, the same 100 models are sent out again, only this time there are some changes to the boundary conditions in the 6kyBP phase. The models are run with four phases as in the first experiment and in the mid-Holocene phase, the land – sea mask is changed around Hudson Bay and the remnants of the Laurentide ice sheet is included in Eastern North America. The land–sea mask changes were applied to all four phases due to the heat convergence calculations done in the calibration phase.

After α and β –testing the models, they are distributed on the climate*prediction*.net website for public download. The results are eventually uploaded onto the project servers for analysis and made publicly available via the project's results portal.

Chapter 4

Paleo-observational benchmarks

This chapter proposes a method for validating GCMs against paleo-observations for the mid-Holocene. Six benchmarks are listed, which describe well - established characteristics of the mid-Holocene climate. Various studies agree on these climatologies for the period. Here, a global set of features are established to provide a framework for testing the models. Paleo-environmental data provide qualitative and semi–quantitative evidence of climatic change and stability.

There are other data available from 6kyBP, but some are non-conclusive about the direction of the signal or the magnitude of change. E.g. there is the MOTIF (Model Obervations to Test clImate Feedbacks) data (Kim and Schneider, 2004) of 6kyBP North Atlantic sea surface temperatures. That compilation however, based on alkenone and foraminiferal records, shows SSTs in disagreement with each other in certain regions, e.g. opposite sign of change in SSTs at the same site. See **Section 4.4** for a description of rejected benchmarks.

The first section covers a summary of the global monsoon systems of 6kyBP. The two most substantial databases are briefly introduced, as most of the six benchmarks listed are featured in these global maps. One section has been devoted to valida-

tions methods of ENA (Eastern North America). This benchmark is not proposed as a routine, unless modellers are including the 6kyBP Laurentide ice sheet in their simulations. An evaluation of uncertainties arising from the paleo-records is found in **Section 8.4**.

4.1 The main paleo–data sets

Liu et al. (2004) make use of two global data sets, the Global Lake Status Data Base (GLSDB) and BIOME 6000, to investigate the moisture budgets of the six monsoon systems during the mid-Holocene. The BIOME 6000 data consists of pollen and plant-macro fossils that have been radiocarbon dated and a global vegetation map has been created based on this information (Prentice et al., 1996, 2000). The Global Lake Status Data Base contains geomorphic and biostratigraphic evidence of changes in lake extents (Kohfeld and Harrison, 2000). See **sections 4.1.1** and **4.1.2** for more information about these two essential data sets.

PAM is defined as Plant Available Moisture, i.e. it is a measure of the moisture

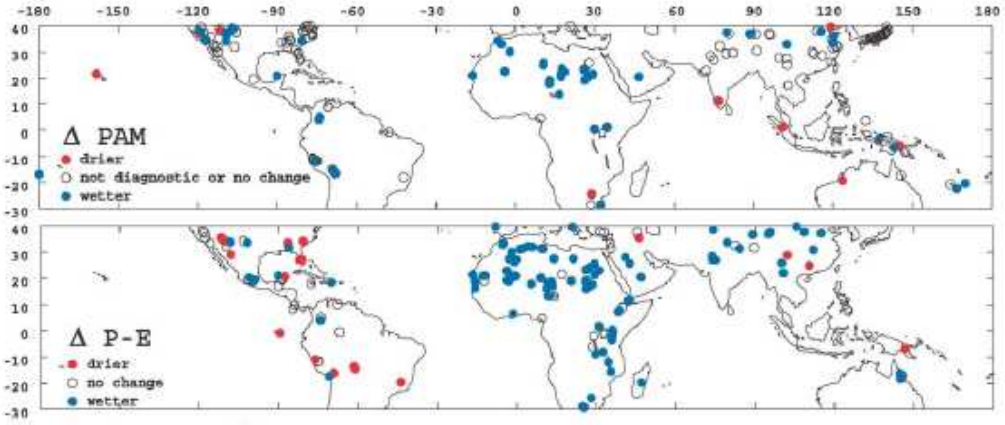

Figure 4.1: Changes in PAM and regional aridity at 6kyBP (Liu et al., 2004). The top panel is drawn from information from BIOME 6000 and the bottom panel from GLSDB (Liu et al., 2004).

availability during the growing season. In areas where cold temperatures inhibit plant growth for part of the year, PAM is used to represent the water balance during the half year over summer (Liu et al., 2004). In the tropics, PAM reflects the water balance over the whole year, as temperatures is not a limitation on plant growth. The constructed picture of changes in PAM at 6kyBP is shown in **Figure 4.1**. In the NH (Northern Hemisphere) monsoon areas the lake and vegetation information agree on the pattern of change in the mid-Holocene. From this it can be inferred that a large increase in the monsoon precipitation, i.e. summer rainfall, dominated the annual signal at 6kyBP.

4.1.1 BIOME 6000

Information on vegetation distribution changes can be derived from pollen and macro fossil data. These dated sediments can provide spatially extensive coverage. The BIOME 6000 project is an on-going project attempting to compile an extensive reconstruction of the vegetation patterns of the mid-Holocene and Last Glacial Maximum (LGM) (Prentice et al., 2000). Biomes are defined as broad physiognomic vegetation classes. According to Prentice et al. (2000), climate induced vegetation changes modify the effects of radiative forcing on climate. The paleo-vegetation maps can be used to evaluate modelling experiments and help design representative sensitivity experiments.

The top panel in **Figure 4.2** displays the present day vegetation pattern, the middle the mid-Holocene vegetation, whilst the bottom panels shows the LGM vegetation pattern. The vegetation is divided into 9 different mega biomes in these BIOME 6000 plots. A mega biome is simply several similar vegetation types grouped as one broader unit. This re-definition of the biomes is due to the fact that most vegetation models computes only a certain number of plant functional types and therefore discri-

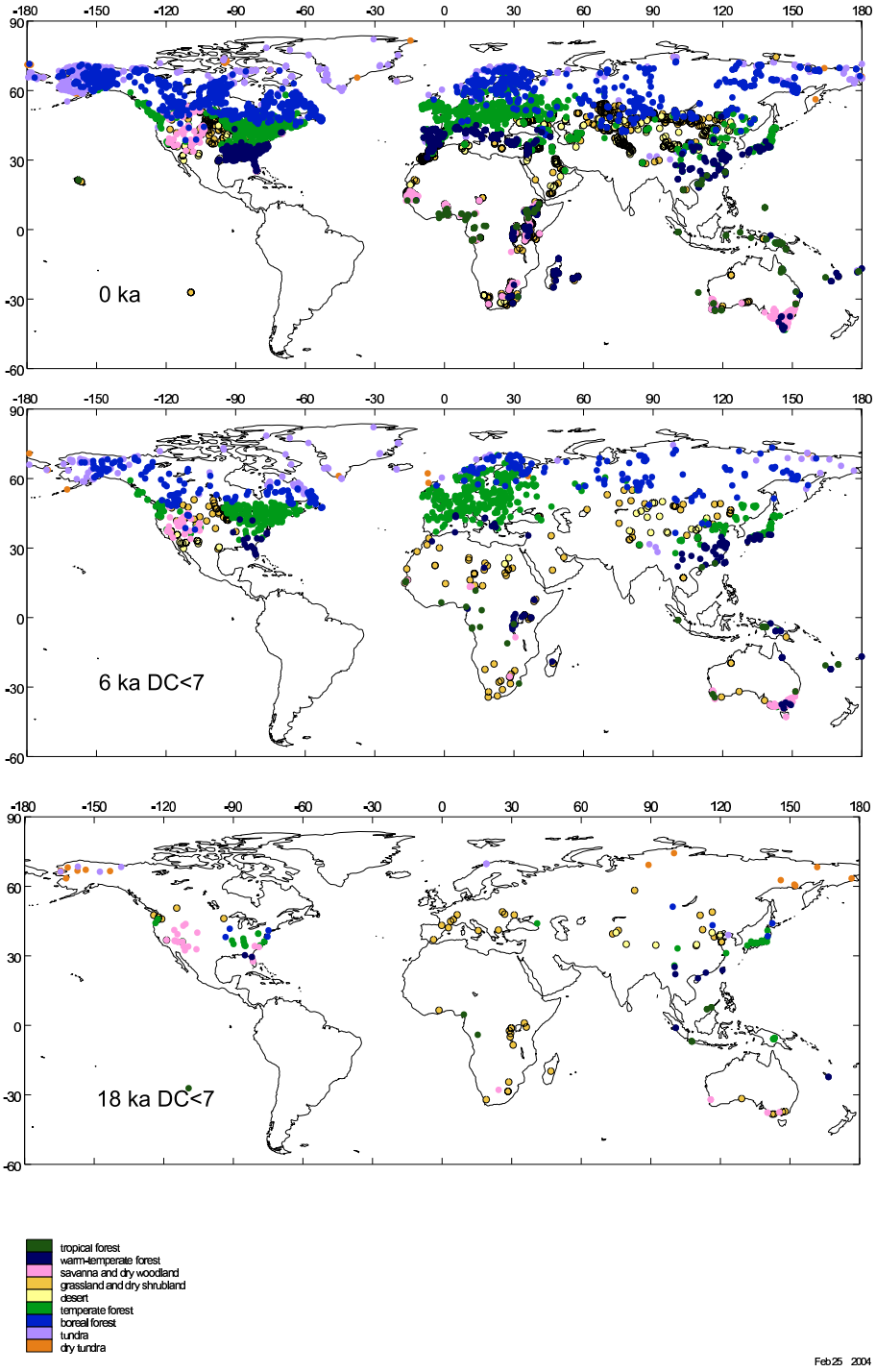

Figure 4.2: BIOME 6000 results. The panel shows the vegetation pattern of present day, 6kyBP and 18kyBP (Prentice et al., 2000; Harrison et al., 2001; Bigelow et al., 2003; Pickett et al., 2004). The colour coding is as follows: dark green - tropical forest, dark blue - warm-temperate forest, pink - savanna and dry woodland, dark yellow - grassland and dry shrubland, pale yellow - desert, green - temperate forest, blue - boreal forest, purple - tundra and orange - dry tundra.

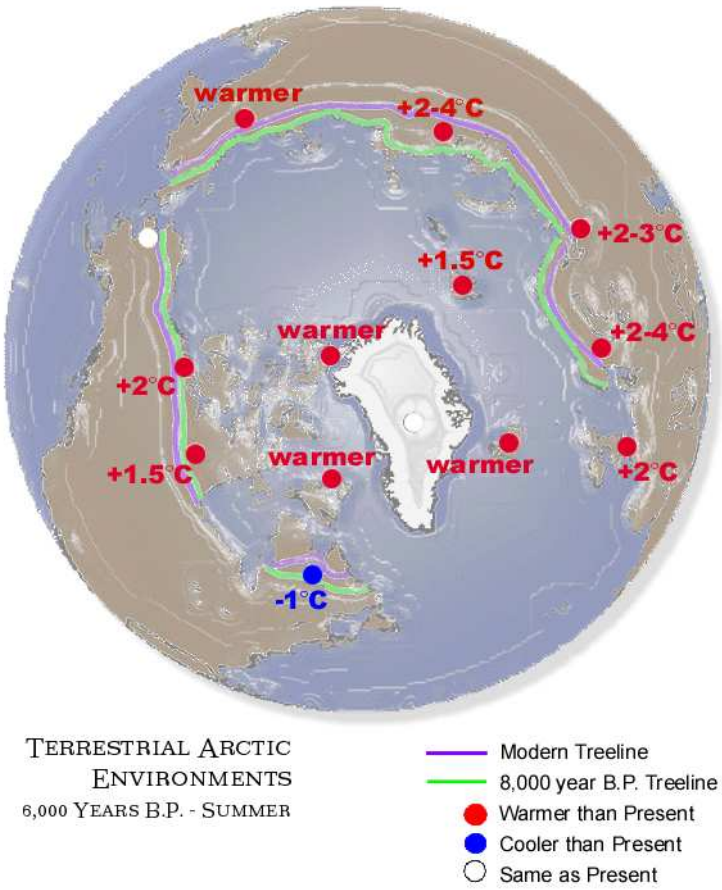

Figure 4.3: The Arctic terrestrial conditions (Kerwin et al., 1999). The Arctic summer was warmer, up to 2–4°C in regions, during the mid-Holocene. ENA however, was ∼1°C cooler.

minate between fewer biomes. Where the Laurentide ice sheet was present at 6kyBP in eastern Canada, as described in **Section 3.4.2**, the tree line was 200km further south as seen in **Figure 4.3** and found in the BIOME 6000 data (Kerwin et al., 1999), (Prentice et al., 2000; Harrison et al., 2001; Bigelow et al., 2003; Pickett et al., 2004).

Figure 4.3 shows the terrestrial Arctic summer environments of the mid-Holocene. The 8kyBP treeline is shown in green, whilst the present day treeline is in purple. The white dots indicate regions where the temperatures were the same as present, the blue dot in Eastern North America, ENA, cooler and the red dots where it was warmer than present at 6kyBP. Much of the Arctic was warmer than present during

summer, leading to a higher number of GDD (Growing Degree Days) for boreal forest (Kerwin et al., 1999).

Northern temperate forest was expanded significantly more than the boreal forest at 6kyBP relative to today (**Figure 4.2**). Both warmer summers and warmer winters, are needed to explain this kind of magnitude of the expansion in this region (Prentice et al., 2000). In addition, a longer growing season with warmer temperatures are needed for this biome to expand. In Europe the temperate deciduous forest border was both further north and south. Regions that were more arid at 6kyBP, were covered in steppe as opposed to present forest (**Figure 4.4**). Forest biomes flourished during the Mid-Holocene in the present day steppe areas of south eastern Europe and Central Asia. The areas observed to be wetter due to the enhanced monsoon flows at 6kyBP had more moisture demanding vegetation; inland China had extended forest biomes and the Sahara had more of a Sahelian flora (Jolly et al., 1998a,b).

4.1.2 Global Lake Status Data Base

The Global Lake Status Data Base (GLSDB) is another global effort to gather information on past climates from lake sediment cores including geomorphic and biostratigraphic data. Again the periods of concentration were the Last Glacial Maximum (LGM) and the mid-Holocene. **Figure 4.4** shows global maps indicating regions where the local water balance was wetter, more arid or the same during these periods (Kohfeld and Harrison, 2000; Harrison et al., 2003; Yu et al., 2001). Precipitation minus evaporation changes results in fluctuations in water levels in lake basins, particularly in closed lakes.

Conditions were wetter than present at 6kyBP across northern Africa, the Arabian Peninsula, Northern India. This is a signal of an expansion of the African and Asian

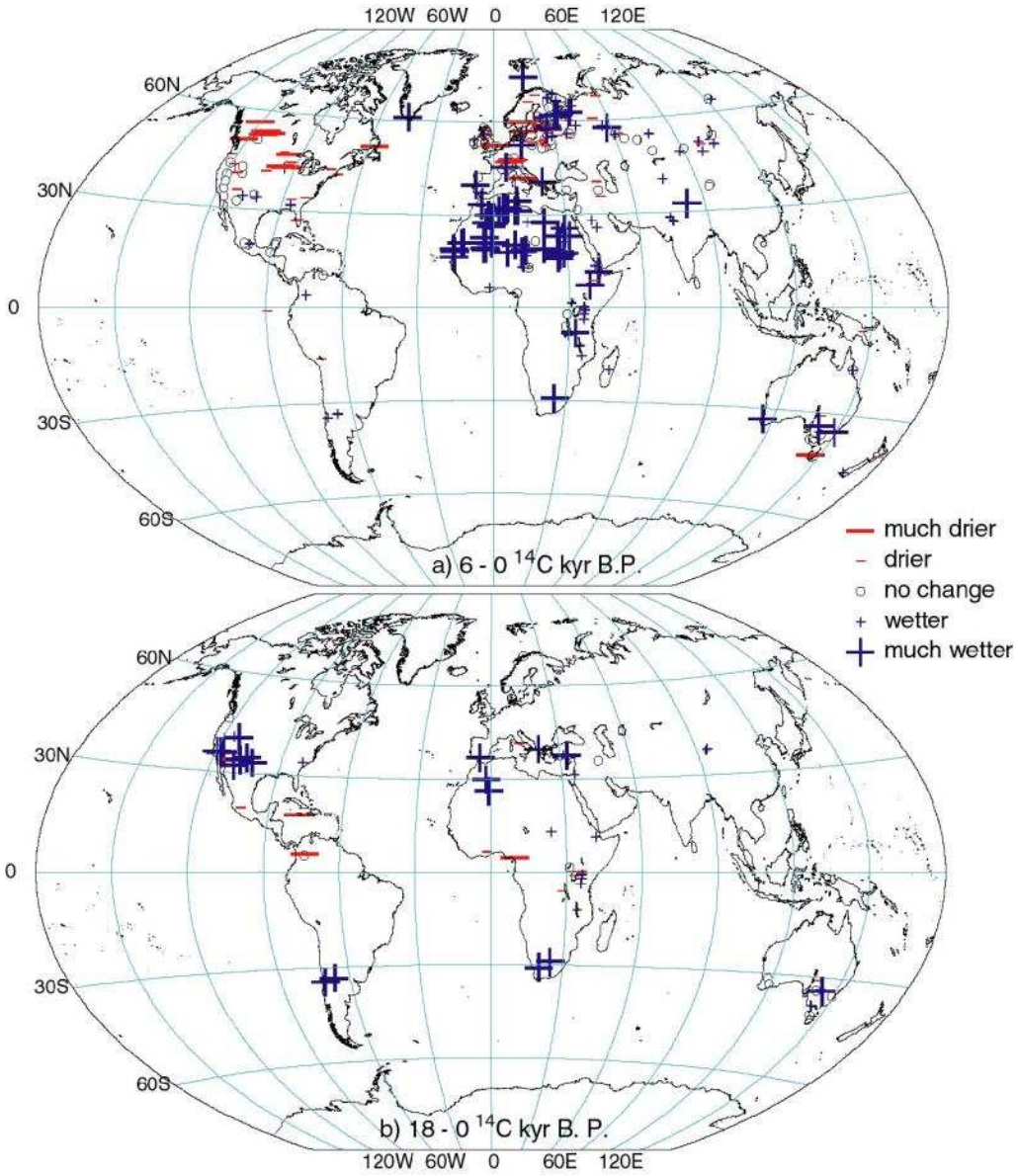

Figure 4.4: Global Lake Status Data Base. The maps shows changes in the water balance compared to presently during a) the mid-Holocene and b) 18kyrBP (Kohfeld and Harrison, 2000; Harrison et al., 2003; Yu et al., 2001).

monsoons. Conditions were somewhat wetter in the southern hemispheric middle latitudes, in addition to the Mediterranean areas. North America's interior and western and central Europe was drier during the mid-Holocene than present.

Changes in lake status can give information on changes in the regional water balance integrated over the whole year (Cheddadi et al., 1997). Variations in continental and

regional aridity and moisture can be derived from fluctuations in water levels (Smith and Street-Perrott, 1983). Changes in the moisture budget can especially have an impact on closed lakes. The present mean position of major features (e.g. the ITCZ) can be directly related to the spatial distribution and extent of such lakes (Street-Perrott and Harrison, 1985). Lake level variations and regional water budget reconstructions can be used to test GCM experiments (Harrison, 1989).

Evidence of increases in precipitation can be seen in lakes by an increase in certain minerals that have been transported to the lake through drainage channels (Kirby et al., 2004). Mineral rich deposits in the lake cores are hence signifying a period with increases in precipitation minus evaporation and higher lake levels. Fluvial input is strongly related to the moisture budget and increases in the mineralogy deposits indicate a stronger inflow or through–flow in a lake (Haberzettl et al., 2007). Closed lakes present the most easily detectable signals of P–E changes, then lakes with inflow channels, and when considering lakes with an incoming and outgoing drainage system lake map modelling for the specific lake is needed to investigate past P–E changes.

Changes in lake height, Δh, can be represented by:

$$\Delta h = P + R - S - E. \tag{4.1}$$

P is precipitation directly onto the lake, R is runoff into the lake from the sides (depending on local geography) and in– and outflow from rivers, S represents the seepage, i.e. most lakes leek through ground water outflow (usually a very small term), E is the evaporation (Larson et al., 2007). The terms are in units of depth averaged over the relevant area. This equations is different for every lake, depending on local geography, including river routing. The evaporation is affected by atmospheric temperature, humidity, winds and temperature of the lake water. For a lake with a

stable water level; $R = P - E$ (Weisse and Oestreicher, 2001).

4.2 The Benchmarks

The BIOME 6000, GLSDB and other data sets are used to derive 6 benchmarks, which any successful model of 6kyBP climate should be able to simulate.

4.2.1 Benchmark 1: The European latitudinal temperature gradient

Mid-Holocene paleo-observations show a mean annual warming of the European high latitudes and a cooling in southern parts, the Iberian peninsula and the Mediterranean coastline in particular, compared to the present. This pattern is also true for the winter season with the winter temperatures 1–3°C warmer than present in the far northern and northeastern parts of Europe and 2–4°C cooler in the vicinity of the Mediterranean (Cheddadi et al., 1997). The modern pollen analogue technique constrained with lake-level data has been used to create climatological maps of Europe at 6kyBP in work done by Cheddadi et al. (1997). A map of the reconstructed temperature anomaly of the coldest month is shown in **Figure 4.5**.

The statistical inverse modelling technique used to obtain this map is the same general approach as widely used by the paleo-climate community. The proxy data, here pollen data, has been used to infer temperature anomalies which can be directly compared to the GCM simulations. Lake level data has been used by Cheddadi et al. (1997) as a constraint on the modern pollen analogue selection. Corrections have been made for bias due to upward pollen transport in high altitude sampling sites and a topographically sensitive interpolation method was used to construct the anomaly map.

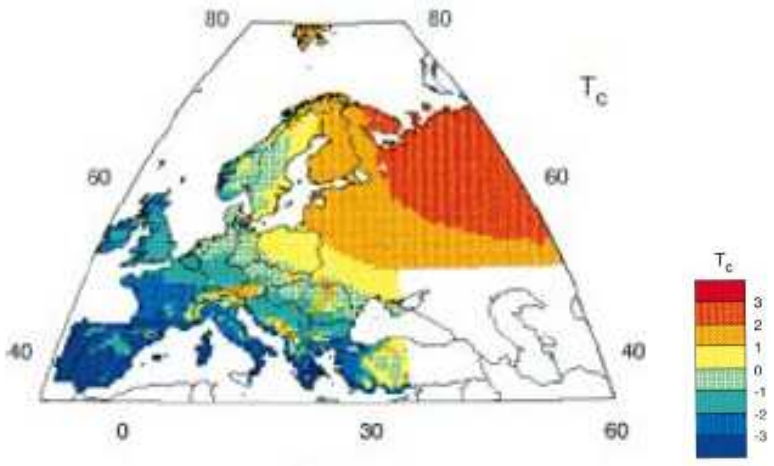

Figure 4.5: *Benchmark 1-* The constrained analogue reconstruction of European temperature differences of the coldest month between 6kyBP and present (Cheddadi et al., 1997).

The inferred winter temperature anomaly patterns are consistent with the findings of Prentice et al. (1996) and Huntley and Prentice (1993). **Figure 4.5** is a spatially coherent, quantitative estimate of the 6kyBP winter temperature anomalies and can be directly compared to the model results. Ideally the models should simulate both the pattern and the magnitude correctly. As the forward modelling might induce further uncertainties to the observations, one might perhaps have a higher confidence in the pattern than the magnitudes. Hence a model capturing a cooling in the southwest and warming in the northeast does have some skill even if the magnitudes are not correct c.f. Cheddadi et al. (1997).

4.2.2 Benchmark 2: Expansion of the North African Monsoon

Perhaps one of the most prominent features of the mid-Holocene climate is the expansion of the North African Monsoon at the time (**Figure 4.1**). This is evident in both the GLSDB and BIOME 6000 data. Joussaume et al. (1999) estimated using inverse forward modelling techniques that in order to maintain the observed 6kyBP

steppe as far as 23°N, an increase in precipitation of 200–300mm/year compared to present is needed. Hoelzmann et al. (1998) found from the GLSDB that lakes covered around 6% of the total land area of northern-Africa between 10–30°N. Presently the same region is covered with ≤0.6% lakes. The vegetation and lake evidence combined suggest that the observed changes were driven by an increase in the summer precipitation from the monsoon resulting in an year round increase in the moisture budget (Liu et al., 2004).

Hoelzmann et al. (1998) created a data-set based on various paleo-observations de-

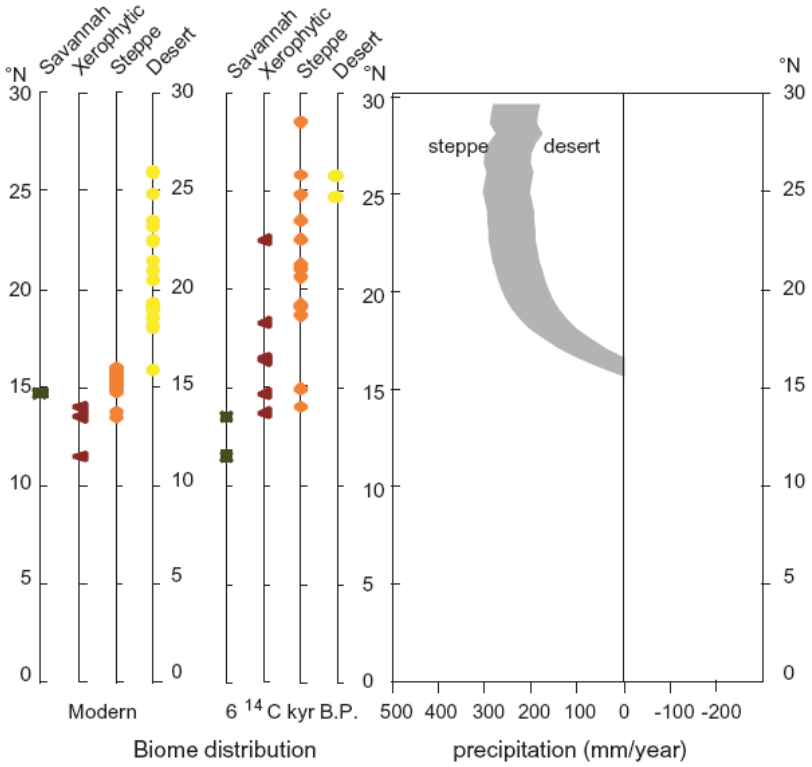

Figure 4.6: *Benchmark 2*- The African 6k Land Surface Conditions Data (Hoelzmann et al., 1998), including information on the annual precipitation excess needed for steppe to dominate over desert at these latitudes [mm/year] panel on the right). The modern and mid-Holocene distribution of biomes zonally averaged is shown. Four biomes are considered here; desert, steppe, xerophytic woods and savannah. Data has been zonally averaged between 10–30°N over Northern Africa and the Middle East.

scribing the land-surface conditions at 6kyBP across the Arabian Peninsula and

northern Africa; 10–30°N and 17°W–60°E. The data are on a 1×1° grid displaying information about the percentage of each grid cell filled by a certain type of surface characteristics; e.g. open lakes, wetlands, flow direction of major drainage channels and vegetation types. The vegetation types include savannah, steppe, tropical deciduous forest, xerophytic woods and shrubs, and tropical montane evergreen forest. This gridded data set can be compared to model simulated surface conditions.

It is evident that the more moisture demanding biomes existed up to 10° further north during the mid-Holocene (**Figure 4.6**). Also, the Saharan southern desert boarder was 10° further north; at 25°N. Steppe covered a much larger region and was found across 13–28°N, as opposed to 13–17°N presently.

The panel on the right in **Figure 4.6** shows the zonally averaged annual precipitation rate difference [mm/year] between 6kyBP and 0kyBP needed to explain the observed vegetation changes in the BIOME 6000 data (Joussaume et al., 1999), based on forward–modelling and inverse techniques. The shaded region indicates the upper and lower bounds for excess precipitation needed to sustain grassland. This is based on present day climate limitations of desert and steppe in the paleo-ecological records. Northwards of ∼17°N the mid-Holocene needed as much as 250–300mm/year more precipitation than present to sustain the vegetation observed. This amount of precipitation makes a difference to the vegetation allowing the more moisture demanding steppe biome to dominate over the desert. These estimates are consistent with estimates of the runoff required to maintain the observed increase in lake levels at the time (Coe and Harrison, 2002).

This information can be used to validate climate models. Either by directly comparing the zonally averaged precipitation anomaly to the data, or by running the model results through an offline vegetation model, e.g. BIOME4 and zonally average the

resulting biomes. It should be noted, however, that zonally averaging does not make for optimal use of the available information from the proxy database. The models should capture a 6kyBP excess of 200–300 mm/year in precipitation northwards of ∼17°N. If BIOME4 is used, a 10° northwards shift in the southern desert boarder should be seen in the model results and a 10° northwards expansion of steppe.

4.2.3 Benchmark 3: Expansion of the North American Monsoon

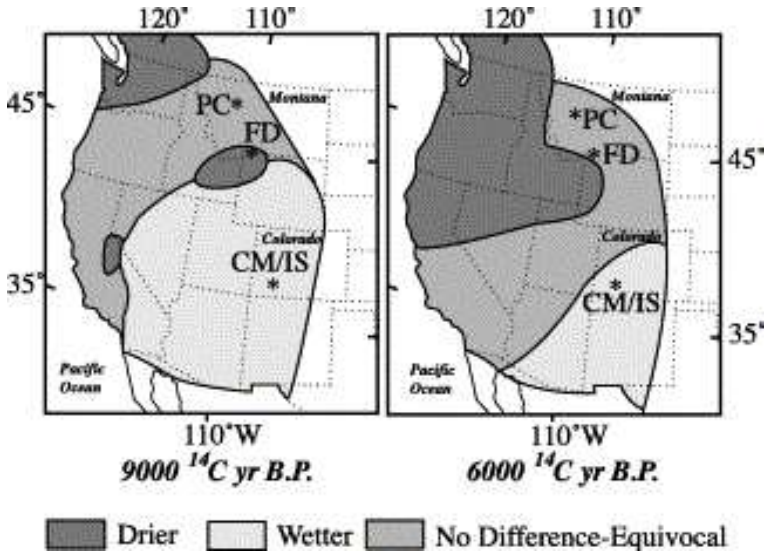

Figure 4.7: *Benchmark 3-* The expansion of the North American Monsoon (Sjostrom et al., 2004). The figure shows which areas were wetter, drier or the same as presently at 9kyBP in the figure on the left and at 6kyBP (figure on the right). The labelled stars indicate ferricrete (a mineral conglomerate) sample sites.

The North American monsoon also experienced changes during the mid-Holocene. Both the vegetation data from BIOME 6000 and the lake data from GLSDB indicate that central America, the American Southwest and northernmost South America experienced wetter conditions. This area was surrounded by a crescent shaped region of increased aridity. This pattern resembles the North American monsoon today during stronger than usual monsoon years. The Pacific northwest, through the interior plains

of southern Canada and the central plains of North America was drier according to the paleo-records (Liu et al., 2004). Harrison et al. (2003) noted that this crescent shaped aridity is also found in data that indicate a reactivation of the dune-systems and increased levels of aeolian activity, i.e. wind driven geological processes, during the mid-Holocene.

This increased aridity in the Great Plains and Rockies is seen in pollen records, aeolian proxy variables in lake cores, and active sand dune migration (Dean et al., 1996). A peak in the aeolian activity around 6kyBP has been noted in observations from Minnesota. Pollen, plant macrofossil data and lake level data provide evidence that the NAM (North American Monsoon) was stronger than today in the Southwest and Southern Rocky Mountains. Isotopic data from the southern Rocky Mountains specifically indicate enhanced summer rainfall. This is indicated in the figure by Sjostrom et al. (2004) (**Figure 4.7**). The increased monsoonal activity was dynamically coupled with increased aridity in southwestern Canada, the northern Great Basin and the upper Great plains of the US to the northeast. This is also seen in the GLSDB (**Figure 4.4**).

This information can be used to look for a change in the ΔP–E budget in the models. We seek to detect a pattern of increased ΔP–E of $\sim$0.75$\pm$0.25mm/day in northernmost South America, Central America and the American Southwest. This should be surrounded by a belt of no change moving over into drier conditions. Here the models need to capture the correct sign of change, i.e. ΔP–E$\leq$ 0.

4.2.4 Benchmark 4: Changes in the East Asian Monsoon

The East Asian Monsoon is the interplay of the convergence of the southerly warm moist air masses and colder and drier northerly airflow from higher latitudes. Ac-

cording to Tao and Chen (1987), the intensity of the summer monsoon over China is governed by the northwards penetration of the monsoonal rainfall belt into the continental interior.

Reconstructions of MAP (Mean Annual total Precipitation) indicate drier or similar conditions in the north and northwest and large parts of China experiencing a positive anomaly in the moisture budget at 6kyBP (Guiot et al., 2008) (**Figure 4.8**). This reconstruction is based on pollen data only, using a mechanic inverse modelling technique. Large circles indicate high significance levels.

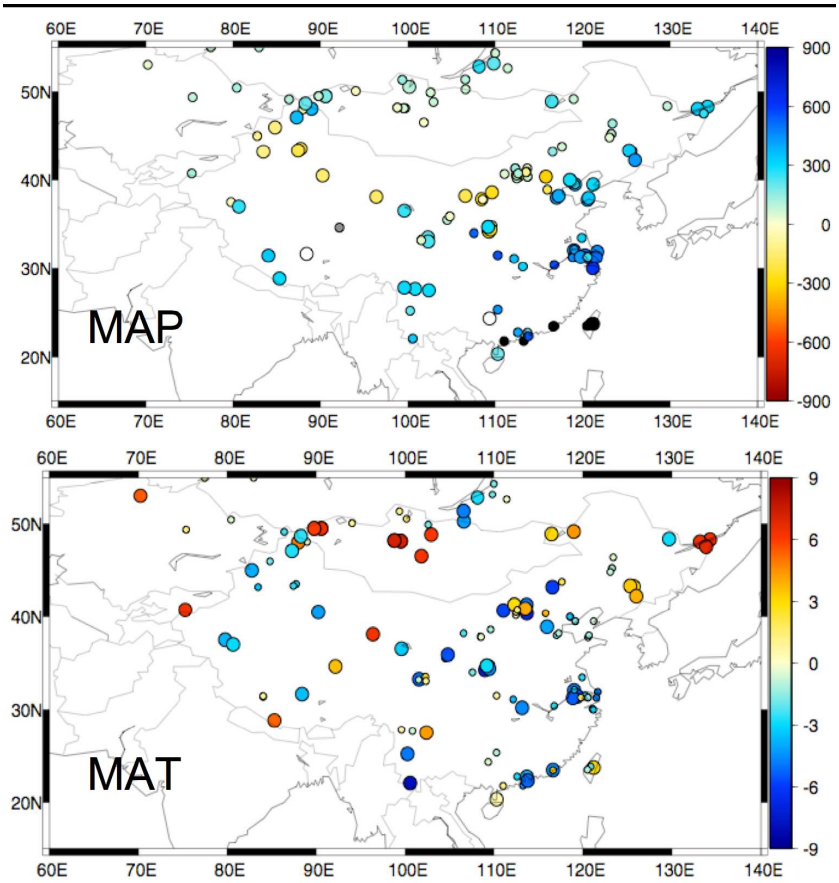

Figure 4.8: *Benchmark 4*- Climate reconstructions of the 6kyBP China (Guiot et al., 2008). Inverse modelling methods were used to construct the maps of mean annual temperature (MAT) as seen in the bottom panel [°C] and total annual precipitation (MAP) [mm/year].

An enhancement of the Asian monsoon is also indicated by coral records from the East China Sea (Morimoto et al., 2007). Stalagmite records provide additional evidence

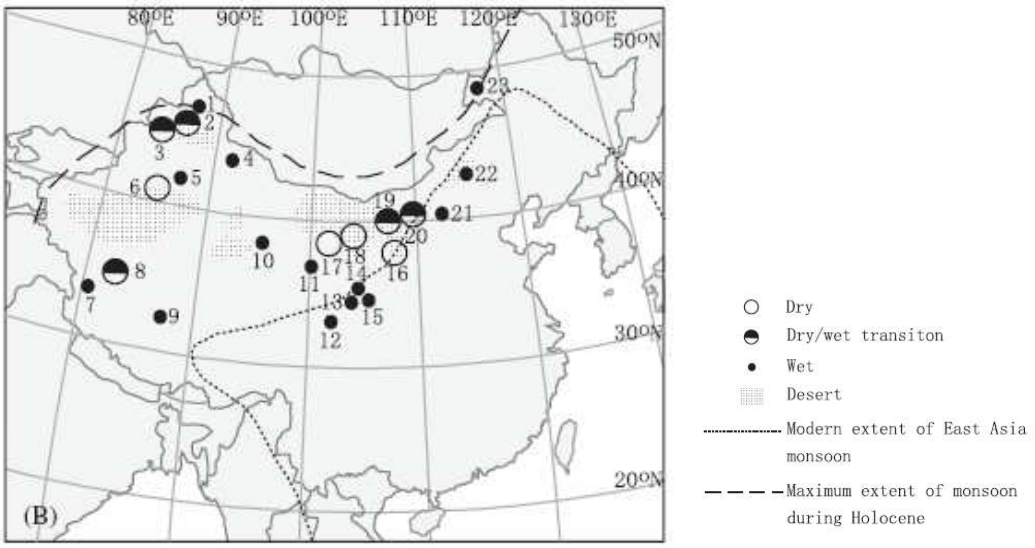

Figure 4.9: *Benchmark 4*- A map of the moisture records from China at 6kyBP (An et al., 2006). The limits of the modern monsoon front, indicated in the dashed line, is from Wright et al. (1993). The long dashed line show the maximum extent of the monsoon during the Holocene. Black dots indicate wetter conditions.

of an increase in rainfall in southern China during the middle Holocene (Hu et al., 2008). Jiang and Liu (2007) found that the monsoon retreated southeastwards during the Holocene and that the summer monsoon front retreated around 400–550km in the period of 6500 – 4500 years B.P. The drying out of northern parts of China started in the early Holocene, as found in various studies, e.g. An et al. (2000); Chen et al. (2003); Jiang et al. (2006).

The Tibetan Plateau and Xinjiang regions were wetter than presently at 6kyBP (An et al., 2006) (**Figure 4.9**). Though the desert, arid and semi-arid regions across China were drier at 6kyBP according to An et al. (2006), whilst the monsoon extended further inland than presently and had a stronger rainfall rate. So in desertous regions the evaporation exceeded the precipitation rate even under these expanded East Asian monsoon conditions.

The mid-Holocene retreat of the Asian Monsoon has been linked to the gradual decrease in the summer solar insolation at the time (An et al., 2000), reducing the

thermal contrast between the land and the ocean and hence reducing the monsoon flow.

Realistic models should capture a spatial pattern of increased precipitation in south-western and southeastern China. The magnitude should be of around +0.75 ± 0.25 mm/day.

4.2.5 Benchmark 5: Central Eurasian moisture budget

Various paleo-observations indicate no major change in the moisture budget across central Eurasia (Tarasov et al., 1998; Prentice et al., 2000). The region was covered in roughly the same amount of steppe as presently during the mid-Holocene, signalling no significant change in the local hydrology (**Figure 4.2**).

Taiga reached its modern range in central and southern Siberia and northern Mongolia during the mid-Holocene (**Figure 4.10**). The steppe biome also encompassed the same area at 6kyBP as at present. Arid conditions north of the Aral Sea (Kazakhstan) and western Mongolia also covered a similar area as presently (Tarasov et al., 1998). Mid-latitudinal former Soviet Union biomes also remain broadly the same presently compared to the mid-Holocene (**Figure 4.11**).

The evidence of steppe covering the same area across central continental Eurasia at the time signifies no major change in the regional water budget. This information is valuable in the process of validating the model simulations. ΔP–E=0 ±50mm/year is what the models should capture in this region.

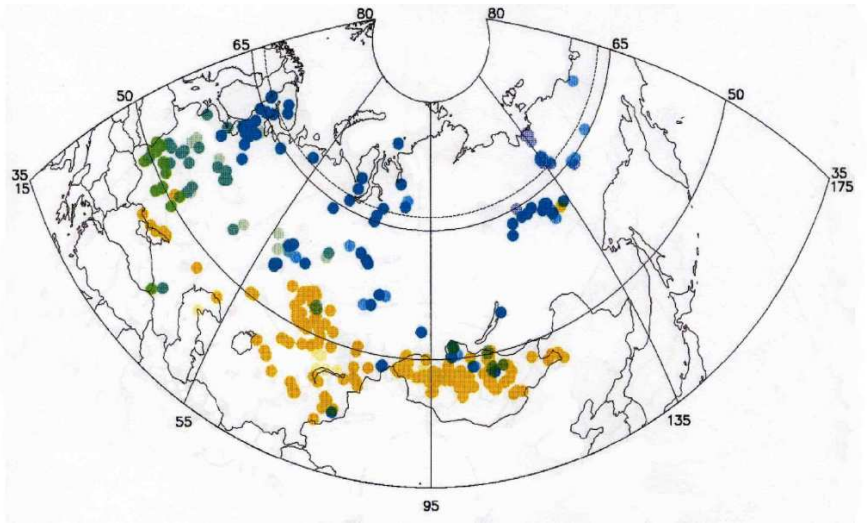

(a) 0k biomes

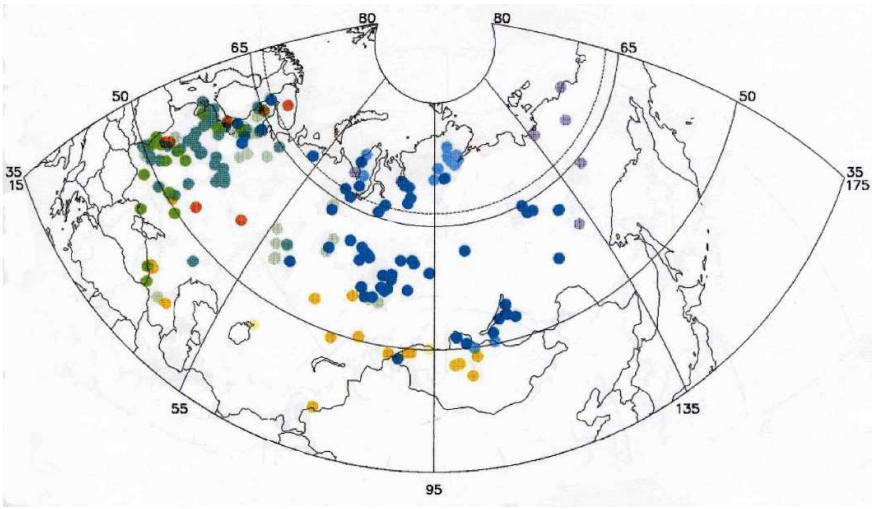

(b) 6k biomes

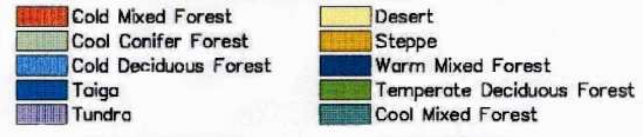

Figure 4.10: *Benchmark 5*- Present day (a) and 6kyBP (b) biome distributions derived from pollen and macrofossil data (Tarasov et al., 1998). Steppe and taiga were the main biomes at 6kyBP, as it still is today at mid-latitudes.

4.2.6 Benchmark 6: Reduction of the South American Monsoon

The more limited spatial data coverage of South America makes comparisons to model simulations more challenging. Data from the region is limited, which makes this a

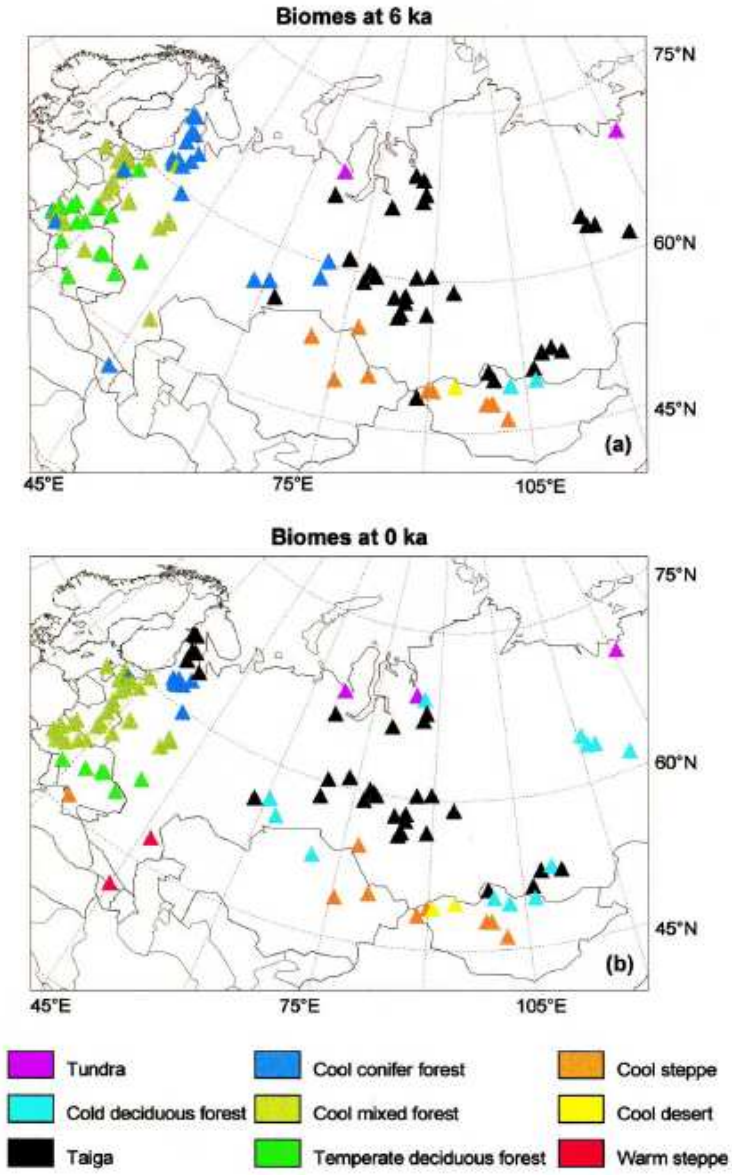

Figure 4.11: *Benchmark 5*- Pollen derived biomes from 6kyBP and 0kyBP (Tarasov et al., 1999). The middle latitudinal biomes are the same for both periods.

weaker constraint on the models compared to the other benchmarks. The paleo-observations from subtropical South America show a rather different picture from the other monsoon regions at the time. There is a consistent signal in the data from southeastern Brazil, where the GLSDB show that the conditions were somewhat drier than today. There is also some stalagamite records supporting this (e.g. Haug et al. (2001); Cruz Jr. et al. (2005)). A drier Amazon basin signal seems to be consistent

with a marine sediment core of the Amazon river discharge (Maslin and Burns, 2000).

The paleo-climatic reconstructions of South America are more geographically diverse than elsewhere, possibly due to the strong climatic influence of the Andes Mountains. Markgraf (1991) synthesised the Holocene paleo-climate for most of South America south of 30°S and found that at 6kyBP climate of the southern Andes shifted towards drier conditions. At low latitudes summer precipitation was higher. Overall, however, the South American moisture budget was reduced compared to present at 6kyBP.

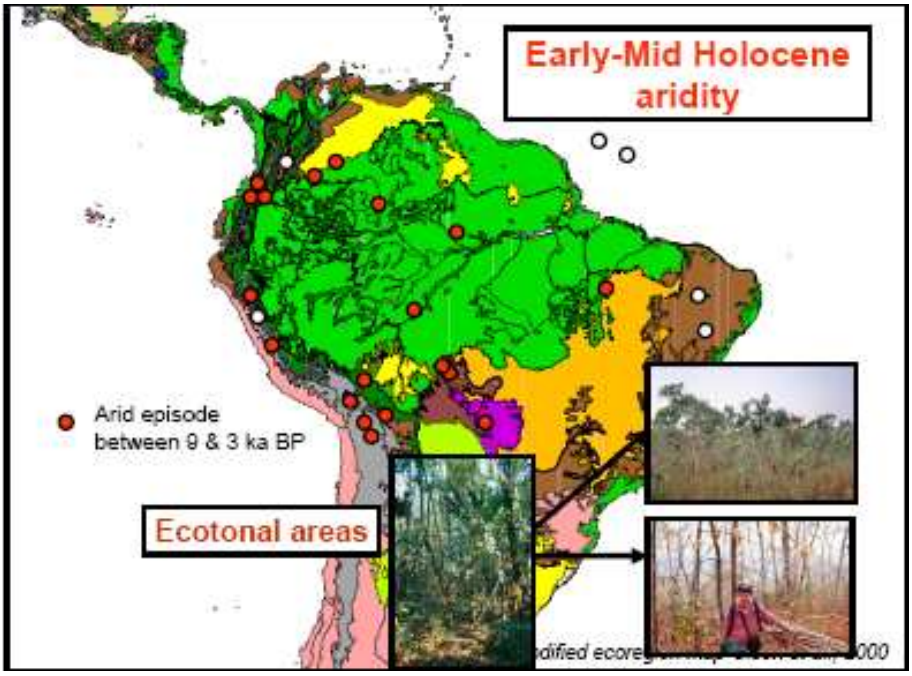

Figure 4.12: *Benchmark 6-* Aridity in the early – mid-Holocene in South America (Mayle, 2007). The red dots are observational sites of drier conditions compared to today, white no change and blue wetter conditions.

Various studies, including Behling and Hooghiemstra (2001); Mayle et al. (2000); Mayle and Power (2008), have found indications that South America was drier than presently. Measurable, but limited ($\leq$15%) reduction of the Amazonian rain forest is observed for the mid-Holocene and the south eastern areas was experiencing intense fires (Behling and Hooghiemstra, 2000, 2001; Mayle et al., 2004). Evidence arise from a multitude of proxies e.g. peak dust concentrations and snow accumulation minima

in Andean ice cores (Thompson et al., 1998), oxygen isotope ratios in lacustrine calcite (Seltzer et al., 2000), and diatom, seismic and geochemical evidence indicating lower lake-levels. The lake levels of Lake Titicaca have been found to have been 85m lower than today (Rowe et al., 2003). This evidence all suggests drier conditions during the middle Holocene. Dry events have been recorded in various paleo-data in tropical South America throughout the past 7,000 years according to Turcq et al. (1998). The red dots in **Figure 4.12** shows proxy data sites with evidence of a dry anomaly during the mid-Holocene (Mayle, 2007).

Realistic 6kyBP model runs should therefore have a drier than present South America, in particular South Brazil, though uncertainties in proxy data does not allow a magnitude to be placed on this drying.

4.3 Benchmarking Eastern North America – the ice sheet experiment

Wohlfahrt et al. (2008) describe the need to run mid-Holocene experiments with inclusion of Laurentide ice sheet remnants to fully understand the complex climate of the region. Their analysis indicates the importance of the ice sheet remnants to make full use of the available pollen vegetation reconstructions from eastern North America. Early Holocene experiments including permanent ice over eastern Canada have shown that the ice has a "non-negligible" effect on the regional climate (Mitchell et al., 1988). The PMIP 2 models simulate a northwards expansion of temperate forest, with a decline in boreal forest as a result of the winter warming. This matches the pollen data, but the northward expansion is overestimated (Wohlfahrt et al., 2008), possibly due to the lack of the inclusion of the Laurentide ice.

Viau et al. (2006) use an extensive collection of fossil pollen records from terrestrial sediments, lakes and bogs to estimate the July temperature changes in North America during the Holocene. The results show a rapid increase in July temperatures in North America at 6kyBP of about 0.3 – 0.4K over ∼200–300 years followed by a more gradual increase of temperatures reaching maximum (the so called HTO – Holocene Thermal Optimum) at around 3kyBP. The broad outline of the Holocene climate indicates a thermal maximum around 6kyBP as ice sheets were no longer a major forcing factor globally (Viau et al., 2006). This is not the case for Eastern North America, however, due to the remnants of the Laurentide ice sheet. Also the surface conditions take some time to recover/ change after the retreat of the ice masses.

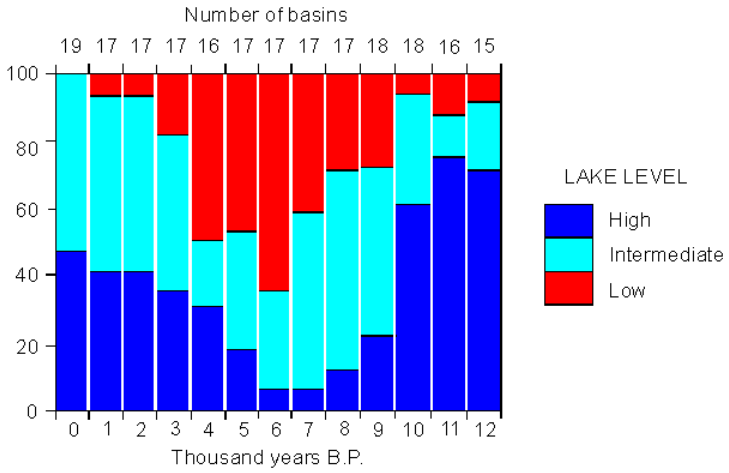

Figure 4.13: Lake level data for eastern North America, showing conditions wetter on average than today during the late glacial period, then becoming rapidly drier after 10kyBP. Maximum aridity occurred at 6kyBP. The return to wetter conditions occurred gradually, with lake levels similar to today by 2kyBP (after Harrison (1989)).

Pollen and sediment analysis from North American lakes reveal significant variations in the climate during the Holocene. The main factors causing these changes are the retreat of the Laurentide ice sheet and the orbitally induced changes in insolation. These forcings lead to changes in the regional climate and in turn caused the changes in vegetation and regional water budgets. The lake-level data, determined by sediment core analysis and mapping paleo-shorelines, from Maine and eastern North

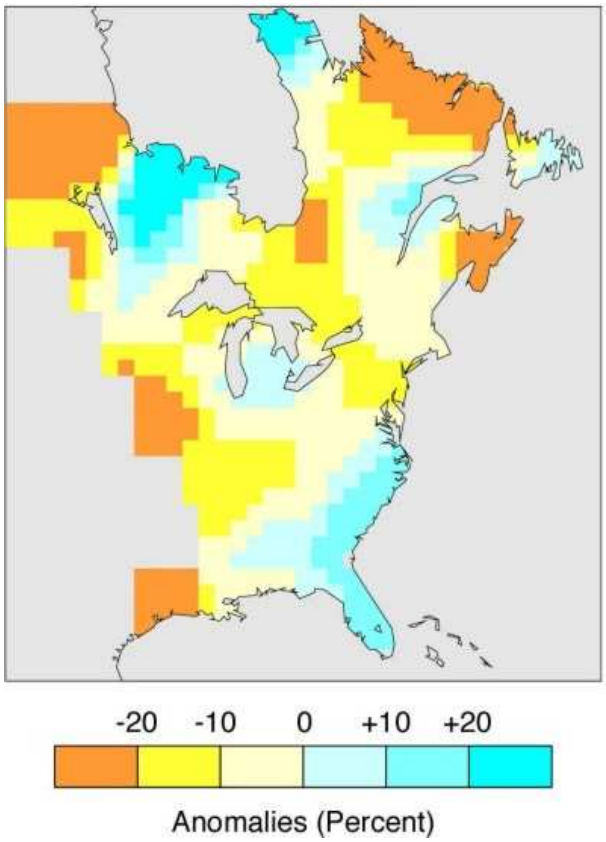

Figure 4.14: Percentage change in 6kyBP mean annual precipitation compared to presently based on pollen data (after Webb et al. (1993)). Note the 20–30% decrease in precipitation in the Labrador area.

America show that conditions were on average wetter than today during the late glacial period, then became rapidly dryer after 10kyBP, with a maximum aridity, indicated by low lake levels, occurring at 6kyBP (**Figure 4.13**). There was a gradual development into wetter conditions and the lake levels reached similar levels to today by 2kyBP (Harrison, 1989). Filby et al. (2002) found that the simulated 6kyBP lake levels were mostly affected by a decrease in winter precipitation rather than an increase in the temperatures, as they used a hydrological model to simulate regional lake level changes.

Figure 4.15 shows the zonally averaged observed changes in four vegetation types across eastern North America (60–90°W; 40–55°N) (Wohlfahrt et al., 2008) based on

pollen and macro–fossil data from PAIN (Pan Arctic INitiative) and BIOME 6000. Cool mixed forest and cool evergreen needle-leaf forest grows further north today by 5–7°. The observations show a southwards migration of the tree–line and a southwards expansion of tundra, a symptom of the local changes in growing – degree – days.

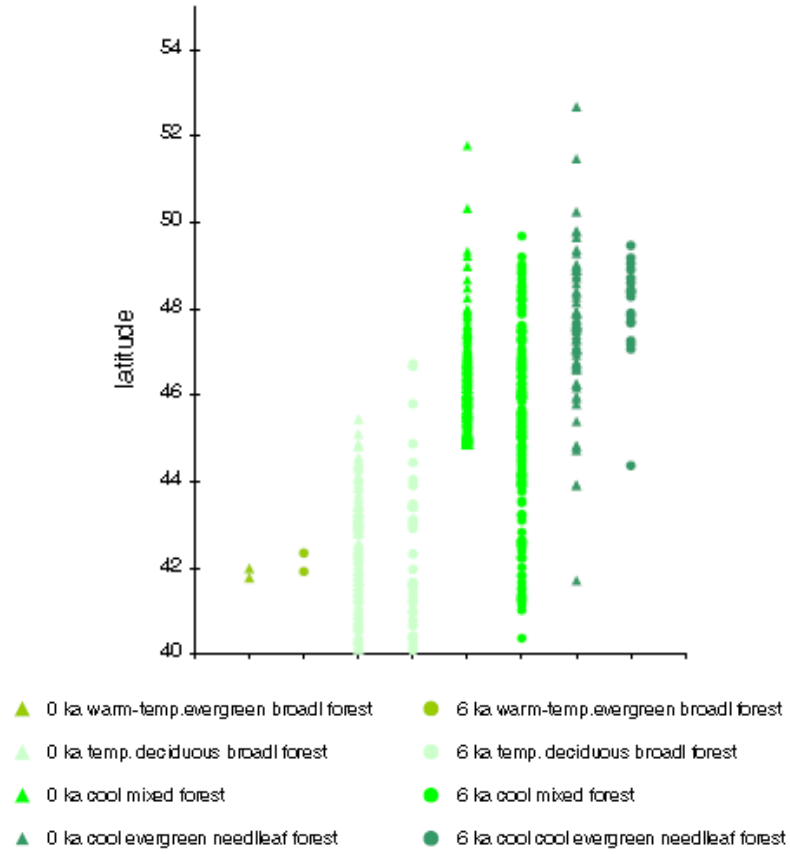

Figure 4.15: Zonally averaged biomes across ENA (Wohlfahrt et al., 2008). Note the 6kyBP southwards contraction of cool forests compared to presently.

If a vegetation model is used, realistic model simulations should show a contraction of the cool evergreen needleleaf forest and a southwards shift of the cool mixed forest, as seen in Wohlfahrt et al. (2008). Kerwin et al. (1999) show how the ENA summer temperatures were 1°C cooler at 6kyBP compared to today, whilst the rest of the Arctic was mostly warmer. **Figure 4.14** shows the percentage changes in precipitation during the mid-Holocene compared to presently (after Webb et al. (1993)). It

shows a pollen – climate response surface based on 60 fossil pollen data sites. The pollen data has been checked against evidence of water level fluctuations (Webb et al., 1993). The models including for the expanded Hudson Bay and Laurentide ice sheet should simulate a regional cooling and drying in ENA.

4.4 Unused potential benchmarks

This section briefly describes other mid-Holocene observational benchmarks that are of interest, though not used in this project.

4.4.1 Arctic treeline changes

During the mid-Holocene the Arctic forest – tundra border was further north than present in Europe (Prentice et al., 1996), western and central Siberia (Texier et al., 1997), (Tarasov et al., 1998) and in the Mackenzie Delta region (**Figure 4.3**). Where the Laurentide ice sheet was present at 6kyBP in eastern Canada, the treeline was around 200km further south, as seen in **Figure 4.3** and found in the PAIN and BIOME 6000 data (Kerwin et al., 1999; Bigelow et al., 2003; Harrison et al., 2001; Pickett et al., 2004). This paleo-information can be used in two ways; the model results can be fed into the offline vegetation model BIOME4. This way we can see if the treeline is shifted further northwards in Siberia and further south in ENA (Québec/ Labrador). This would be a quantitative comparison, though not a direct one, as the modeled climate goes through another model to give us the result and more uncertainties arise this way. The other way of inspecting this observed change is to calculate the GDD and look for an increase in the mid-Holocene phase compared to the control.

The robustness of this benchmark can be questioned as it is based on pollen data only and a change of 200km is comparatively small, keeping in mind that wind-borne pollen can travel large distances.

4.4.2 East African moisture budget increase

According to the Global Lake Status Data Base the eastern coast of Africa's lakes had higher water levels than presently (**Figure 4.4**) (Kohfeld and Harrison, 2000; Harrison et al., 2003; Yu et al., 2001). Evidence of increased 6kyBP precipitation levels has also been found in several peat bog sequences in equatorial East Africa (e.g. Beuning and Russell (2004)) and oxygen isotope data from Mounts Kilimanjaro (Thompson et al., 2002) and Kenya (Barker et al., 2001). The precipitation changes in east Africa were not as substantial as in northern Africa (Peyron et al., 2006). In the region of 28 – 31°E and 0 – 10°S various reconstruction techniques (e.g. PFT method and best analogues method) have yielded an annual precipitation increase of up 300mm/year in eastern Africa, whilst in Sahara and Sahel the same methods found twice that increase at 6kyBP.

This benchmark is not used here due to time constraints and as efforts are are being focused on the northern climates on this continent. It has also been suggested that GCMs are not able to simulate the 6kyBP increase in east African precipitation due to the underestimation of the topography in the models, i.e. the Mitumba Mountains, including Kilimanjaro, are too low in the models (Peyron et al., 2006). This underestimation means that the monsoon flow is not affected enough by topography and the monsoon flow would penetrate too far to the east over the oceans.

4.4.3 Reduction of the Amazonian rain forest

Measurable but limited ($\sim 15\%$) reduction of the Amazonian rain forest is observed for the mid-Holocene (Behling and Hooghiemstra, 2000; Mayle et al., 2004; Behling and Hooghiemstra, 2001). This is seen in pollen and isotopic data.

This feature is neglected in this study due to the overlap with the benchmark regarding the reduction in the South American Monsoon and due to the small magnitude of change and that no vegetation model is used in this project.

4.4.4 North Atlantic SSTs

A data base of changes in 6kyBP sea surface temperatures compared to present has been compiled and contains 17 alkenone records, as previously compiled by the GHOST project (Global Holocene Spatial and Temporal climate variability) (Kim and Schneider, 2004) and 12 foraminiferal records. From a few cores in the record both alkenone and foraminiferal data have been derived. For the foraminiferal data two SST estimates exist derived from two different transfer function techniques, i.e. maximum likelihood and modern analogue technique, to illustrate the magnitude of differences that can result from the choice of calculation method. The statistical error is close to ± 1°C (Kim and Schneider, 2004), which is of comparable magnitude to, or larger than, the 6kyBP SST changes in places. This benchmark is not used due to the large uncertainties in the observations and because the data disagree on the sign of change in certain locations. Additionally, the sediment cores are typically extracted around coastlines and islands, which are not that well represented in the model due to the resolution. Some SST observations are from locations that are represented as land in the model.

4.5 Summary

A set of robust features of the mid-Holocene climate have been identified. Modellers should routinely check their GCMs against these. The characteristics are largely agreed upon by the paleo-community and cover various, observation rich parts of the globe. The two largest data–bases, GLSDB and BIOME 6000, have been introduced in this chapter, as the majority of the benchmarks are partly, if not entirely based on these global networks. Two methods for testing the models against the six 6kyBP climate patterns have been proposed: visual map–map comparisons and area–averages. For the model ensemble presented in the rest of this thesis I have used the following seven benchmarks:

1. European winter temperature anomaly of a 2–4K warming in the northeast and 1–3K cooling in the southwest.

2. Expansion of the North African Monsoon with a 6kyBP precipitation excess of 200–300mm/year as a zonal average north of $\sim$17°N.

3. An increase in the East Asian Monsoon of 0.75$\pm$0.25mm/day in southwest China.

4. No major changes in the moisture budget across mid–latitudinal Eurasia.

5. An increase in the North American Monsoon with a crescent shaped region of an increase in the moisture budget of 0.75$\pm$0.25mm/day extended to 30–35°N surrounded by a region of no change, then an increase in aridity.

6. Drier conditions in South America

7. Cooler and drier conditions in Eastern North America; a regional summer cooling of –1K and a 10–30% reduction in precipitation in Québec and Labrador.

The limitations of the paleo–environmental data include limited spatial coverage and incomplete understanding on how records reflect climate. This can give rise to apparent disagreement between data types, which is why a set of robust features are identified. The paleo–record sample distribution can slightly bias temperature reconstructions by over-weighting certain regions, which is something to keep in mind when dealing with the paleo–observations (Viau et al., 2006).

Chapter 5

Evaluation of the First Ensemble Results

This chapter presents the initial results from the first ensemble experiment where the 6kyBP models have been forced with an altered orbital configuration, as described in **Section 3.6**. The models were distributed to volunteers and the results from the 100 models are analysed in the following chapter and validated after the method described in **Chapter 4**. Firstly the ensemble's control models are checked against the ERA–40 reanalysis data. The ensemble response in terms of climatological means and standard deviations is then assessed, before the ability of the various model runs to meet the six benchmarks are evaluated. The differences between the 6kyBP and control models are plotted as the proxy data indicate how past climates differed from the modern climate and not what the past climates were like explicitly. The ensemble standard deviation is also shown to illustrate the variations across the ensemble due to the parameter perturbations. Regarding the sub-ensembles of initial condition perturbations, the CPDN method is to take models with the same atmospheric parameter values and different initial condition values and average them to represent one model (or one set or parameter values/ perturbations) in the rest of the analysis.

For each 6kyBP climatic feature each models' results have been plotted, but only the ensemble mean and standard deviation are printed here. A model case study of the best performing model is also presented in this chapter.

The full ensemble had not been returned at the time of analysis. 70% of the returned models are used in the analysis presented in this chapter containing no duplicates to avoid over-representing any models. The models that had been successfully returned to the database and their sensitivity values as found from the $2\times[CO_2]$ phase are plotted against each other in **Figure 5.1**. Model number is plotted against its corresponding sensitivity value.

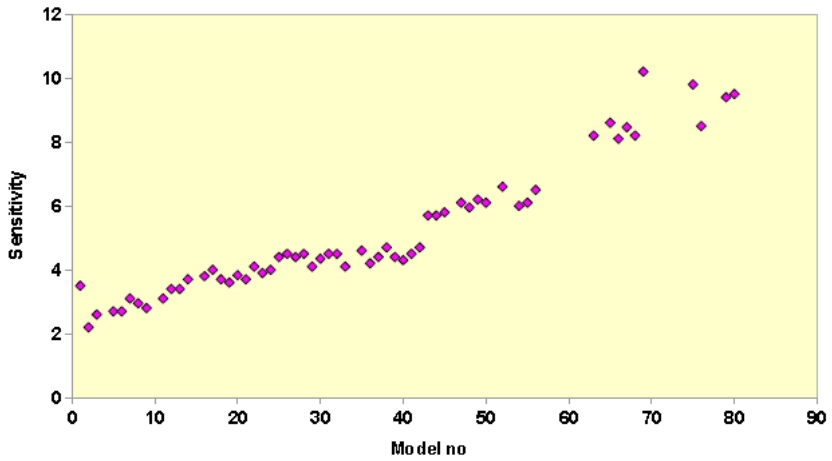

Figure 5.1: The sensitivity values corresponding to each model in the ensemble. Model number is plotted against its corresponding sensitivity value as found by comparing the $2\times[CO_2]$ model phases to their control runs. This is the set of parameter combinations derived in Sanderson et al. (2008).

These parameter settings were, as explained in **Section 3.5**, were found to produce the climates that are closest to modern observations in each 0.1K sensitivity bin. Here the validity of Sanderson et al. (2008)'s artificial neural network is tested and it is seen from the plot that the models do lie in a quasi-straight line. The linear regression has a correlation coefficient of 0.92. Model 1 is the model with the default parameter values after the CPDN standard. This model has a climate sensitivity

of 3.6K. The climate sensitivity values found in the ensemble is plotted against the sensitivity values derived from the artificial neural network in Sanderson et al. (2008) (**Figure 5.2**).

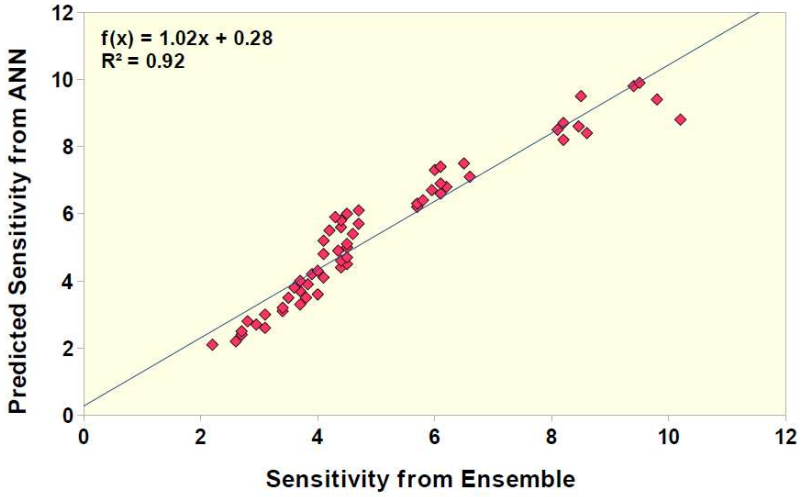

Figure 5.2: The sensitivity values as found in this ensemble versus the sensitivity values from the Artificial Neural Network (ANN) developed by Sanderson et al. (2008).

5.1 Comparing the control runs with reanalysis data

Firstly the ensemble mean control simulations are compared against the reanalysis data from ECMWF, i.e. the ERA–40 Atlas, using observations from 1979–2001 as this period contains the highest quality and density of observations. The control runs were thoroughly checked against observations, including the ERBE data and the NCEP/NCAR reanalysis data, in work by Sanderson et al. (2008). This is why the ensemble is here only briefly checked against modern observations to test that the results are sensible enough for further analysis. The ERA–40 Atlas is provided by the combined model and analysis approach of the data–assimilation system where external information from observations and boundary conditions are incorporated.

There are some known issues with this data set, however, due to the spin-up methods used (Troccoli and Kållberg, 2004). There is a shortcoming in the humidity scheme used in the assimilation system resulting in too strong precipitation, according to Troccoli and Kållberg (2004). This is particularly an issue over the tropical ocean and for the period succeeding 1991 compared to independent observations. The reason for this overestimation is due to a fundamental issue with the moisture variational analysis in areas with a high observational density. The onset of the satellite era brought this on with the sudden relative abundance of atmospheric humidity observations. The largest discrepancies in the data set is found in the ITCZ, i.e. $\pm 30^{\circ}$ latitude. The differences between the ERA-40 and GPCP (Global Precipitation Climatology Project) data are of $\sim$2–7mm/day over the tropical oceans (Troccoli and Kållberg, 2004). The precipitation is also overestimated in the ERA-40 data over Africa of $\sim$5mm/day between 10°S and 10°N.

The ensemble annual mean air temperature at 1.5m from the control runs compares well to the 2m air temperatures from ERA–40 (**Figure 5.3**). E.g. both the 0 and 25°C modelled isotherms follow the reanalysis data closely. Though in Finland and the neighbouring far northwestern corner of Russia the 0°C isotherm is $\sim 2^{\circ}$ too far south in the HadSM3 ensemble. The winter temperatures in the ensemble of control models match the reanalysis data well in this region, however (not shown).

The reanalysis temperatures are from 2m above the surface, whilst the HadSM3 data are from 1.5m. This difference of 0.5m could mean that the modeled temperatures are somewhat warmer than the reanalysis data, though this is possibly offset by the fact that the control run temperatures are pre–industrial and the reanalysis data use observations from 1979–2001.

The ensemble annual mean total precipitation rate shows similar behaviour to the

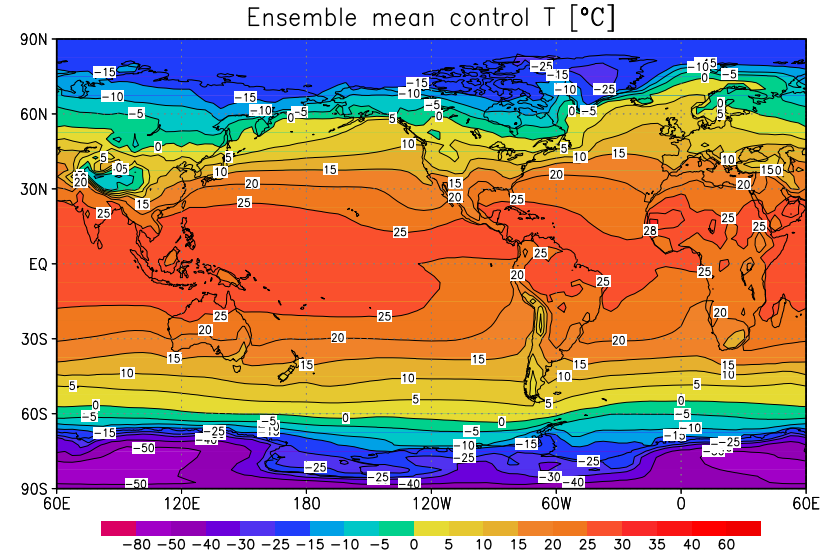

(a) control

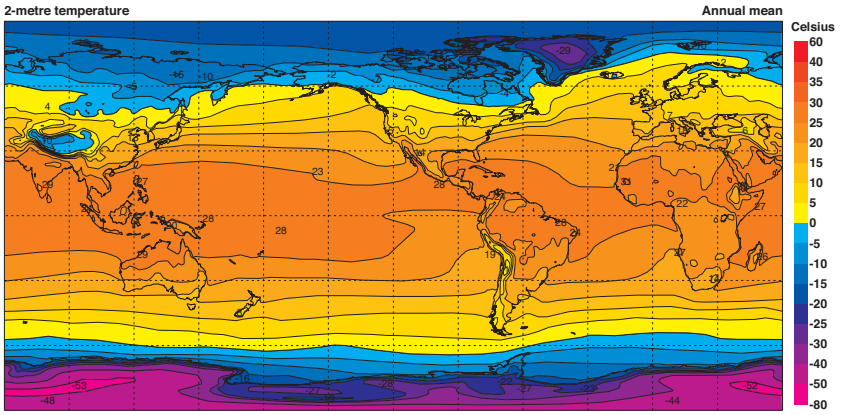

(b) ERA–40

Figure 5.3: (a) The ensemble annual mean surface (1.5m) air temperature from the control runs, i.e. pre–industrial, and (b) the 2m annual mean air temperature from the ERA–40 reanalysis from the period of 1979–2001.

ERA–40 Atlas (**Figure 5.4**) with the shape and magnitude of the storm track precipitation and the placement of the ITCZ. The ensemble mean maximum precipitation peaks are somewhat lower than ERA-40, however, in Indonesia and Central America. The precipitation rate in ERA-40 is overestimated in this region, however, with as much as 7–10mm/day in Indonesia (Troccoli and Kållberg, 2004). The summer (JJA) rainfall is well modelled compared to the ERA–40 data as well (not shown). The overall effort from the control models is deemed satisfactory for the purposes of

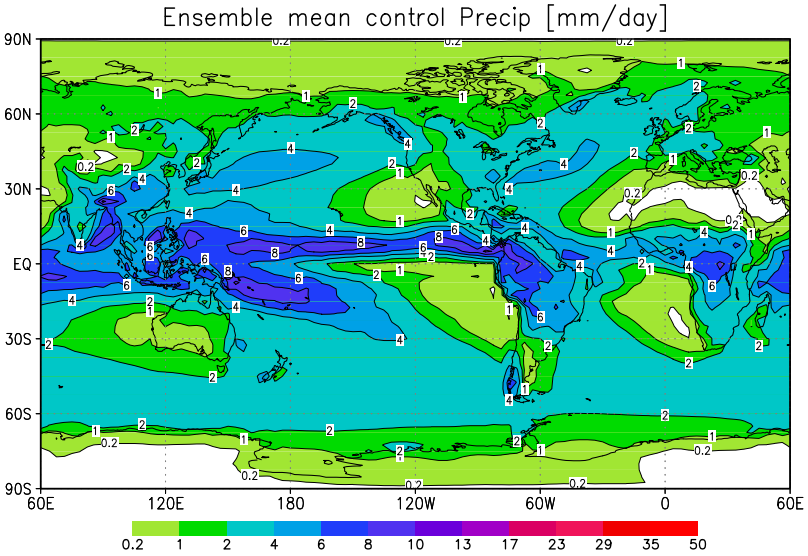

(a) control

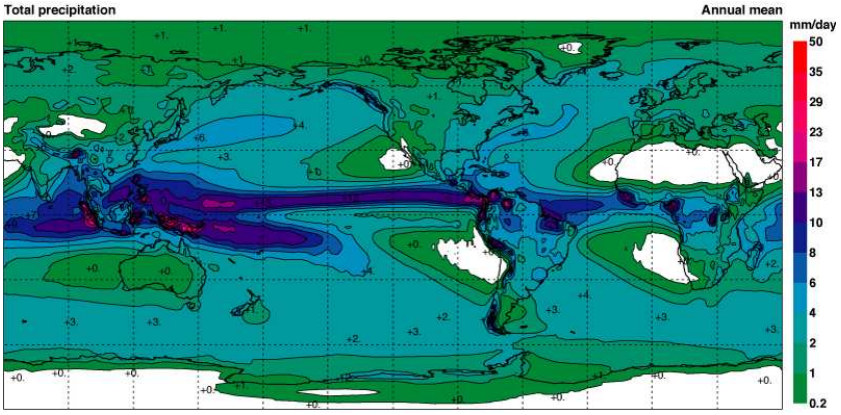

(b) ERA–40

Figure 5.4: The ensemble annual mean control precipitation rate [mm/day] and the total annual precipitation from the ERA–40 reanalysis from the period of 1979–2001.

this study.

The modelled control annual mean evaporation minus precipitation rate is in good agreement with the reanalysis data, in particular over the oceans, though less so than precipitation (**Figure 5.5**). Over land there are some small magnitude discrepancies in central north America, southern south America and Australia. The modelled control JJA E–P budget (not shown) coincides well with the ERA–40 data, including the monsoon regions of interest in this study.

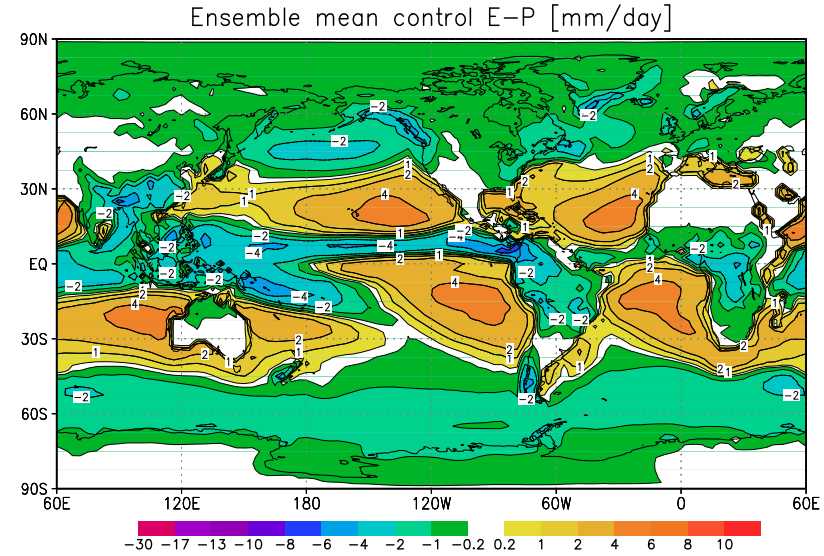

(a) control

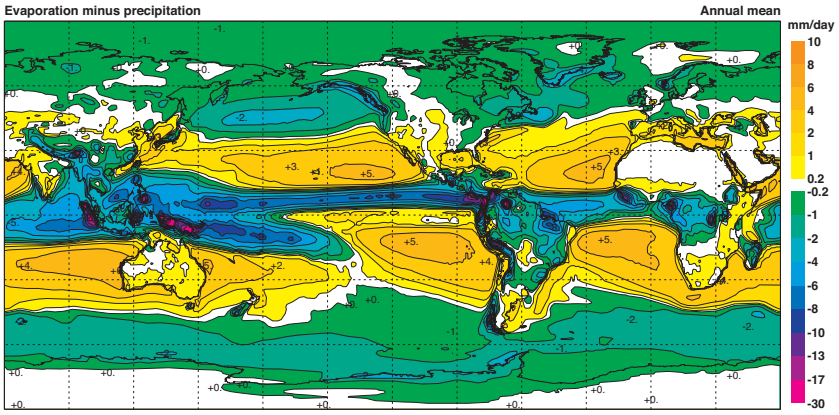

(b) ERA–40

Figure 5.5: The ensemble annual mean evaporation minus precipitation [mm/day] from the control runs, i.e. pre–industrial, and from the ERA–40 reanalysis from the period of 1979–2001.

5.2 Ensemble results

The change in the orbital configuration results in an ensemble mean warming in high latitudes, the Arctic in particular, where the annual average displays a warming up to 3°C (**Figure 5.6(a)**). In the sub-tropics, the temperatures are cooler over land, by as much as 2°C in places, where there is an increase in the cloud amount due to the intensification of the monsoons. Annually there is a decrease of 0.5–1Wm^{-2} at the latitude band of ±30° in the insolation due to the change in the orbital configuration.

These responses are expected due to the increase insolation, and similar results have been observed in the PMIP ensemble (Braconnot et al., 2007b). North of 60°N there is an annual insolation increase of 2–4Wm^{-2}.

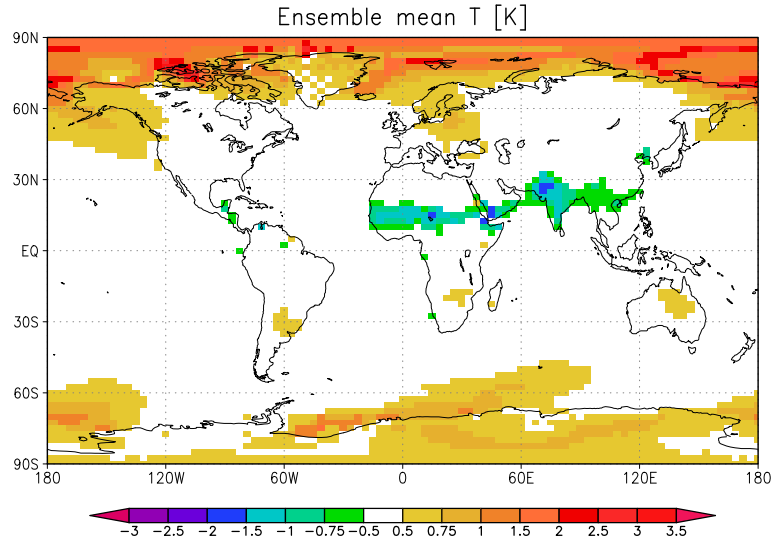

(a) ΔT Annual

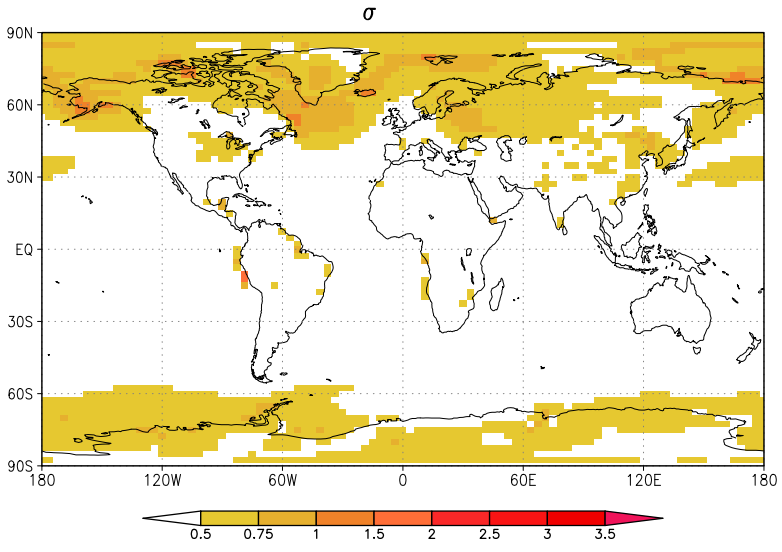

(b) σ

Figure 5.6: The ensemble annual mean surface (1.5m) air temperature change (i.e. 6kyBP–control) and the corresponding standard deviation.

The largest variations in temperature between the model runs in the ensemble are found at high latitudes, where the standard deviation reaches 1°C in places (**Figure 5.6(b)**). The inter-ensemble standard deviation gives an idea of the mod-

elling uncertainties resulting from the parametrisation in the models. It does not reflect uncertainties due to the imposed boundary conditions, however. Standard deviations smaller than the mean change gives us some confidence in the model predicted changes.

The ensemble simulates an amplification of the seasonal cycle in the NH surface temperatures, with the strong continental 6kyBP warming during boreal summer (**Figure 5.7(a)**) and an continental cooling during DJF. Northwards of ∼20°N there is an increase of more than 20Wm^{-2} in the summer at 6kyBP resulting in the observed warming in the models. The maximum warming is found over Eurasia, the Middle East and Eastern Europe. The DJF continental cooling has a maximum within the subtropics where the change in insolation has the largest effect. This contributes to strengthen the winter monsoon. In DJF there is a 12–20Wm^{-2} reduction in the insolation southwards 30°N encouraging the continental cooling. The colder NH winter continents results in an amplification of the precipitation over the ocean and a slight drying over the continent (**Figure 5.9**).

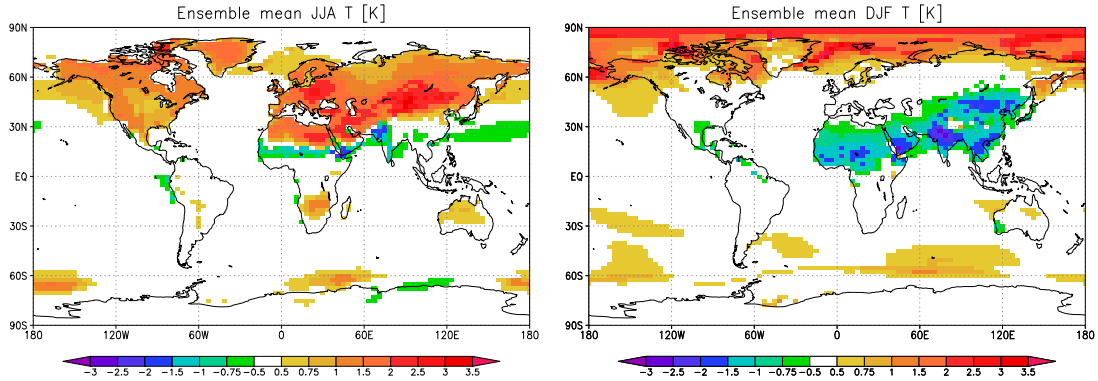

(a) ΔT JJA (b) ΔT DJF

Figure 5.7: The ensemble mean temperature anomalies in boreal summer and winter.

The ensemble is characterised by large changes in the hydrological cycle in the tropics (**Figure 5.8(a)**). There is an annual northwards shift in the ITCZ (Inter Tropical Convergence Zone), except in Asia, where there is a southwards shift. The intensifi-

cation in the Indian Monsoon, can be seen in the annual anomaly. The increase in cloud cover from the intensified monsoons and the increase in the evaporation rate both contribute to lower the air temperatures. In parts of the North Pacific, there is an annual reduction in the rainfall rate anomaly. The standard deviation is up to

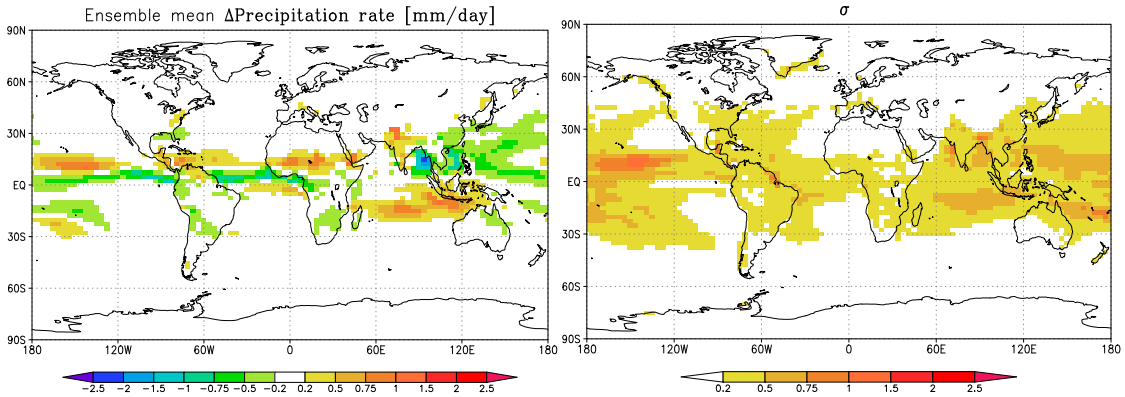

(a) ΔP Annual (b) σ

Figure 5.8: The ensemble mean annual precipitation rate anomaly [mm/day] and the standard deviation.

1.5mm/day and there is some variation across the ensemble in terms of the spatial precipitation rate anomaly pattern (**Figure 5.8(b)**). This is to be expected, as precipitation is a noisy field. The largest spread between the models is found across the $\pm 30^{\circ}$ latitude belt where the rainfall is predominantly convective and the ITCZ is a governing climatic feature.

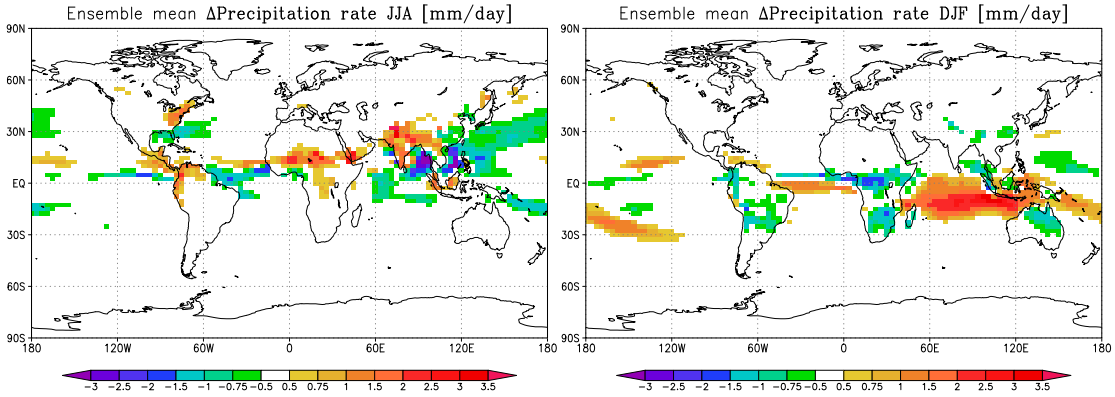

(a) ΔP JJA (b) ΔP DJF

Figure 5.9: The ensemble mean precipitation rate anomalies in boreal summer and winter.

Figure 5.10 shows 6k–control global mean temperature [K] and precipitation rate

[mm/day] time–series. There is a decrease in the precipitation rate during northern summer and an increase during boreal winter globally. The largest increase in temperatures is during the boreal autumn and the largest decrease is during spring, indicating the shift in the 6kyBP seasons. The changes in the longitude of the perihelion results in an increased length of the polar nights and the periods of Arctic midnight sunshine. A more of a two–seasonality is seen in the 6kyBP simulations with rather brief intermediate warmth seasons. As the orbital configuration is changed in the 6kyBP models, the insolation is reduced for a longer period of time in the NH winter and equally increased for longer during summer. There is a lag of about two months between the peaks in the change in insolation and the maximum and minimum in the temperature differences, which is probably due to the heat content of the climate system. The minimum and maximum changes in the insolation at 6kyBP compared to present were in February and August with a magnitude of $\pm 18 \mathrm{Wm}^{-2}$.

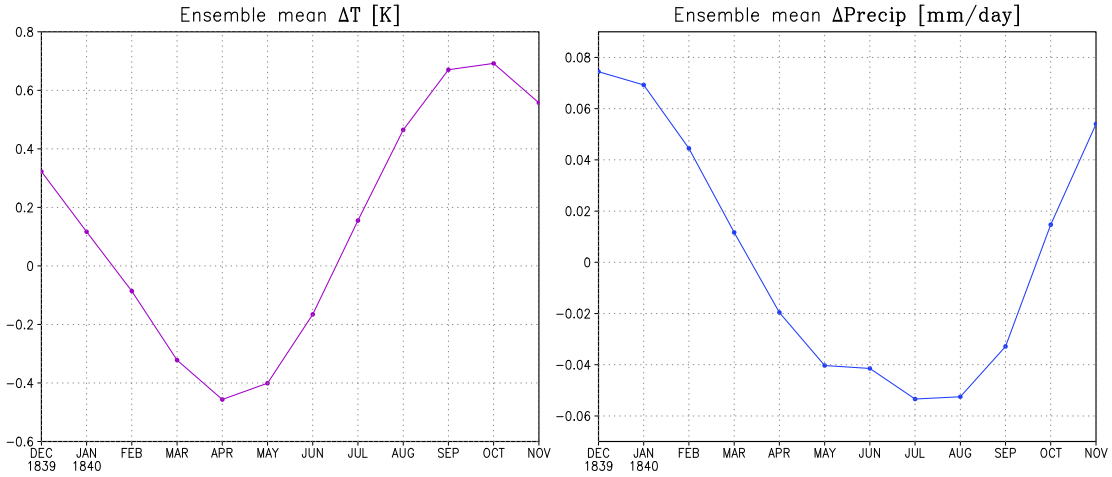

(a) ΔTemperature (b) ΔPrecipitation

Figure 5.10: Time–series of the ensemble global monthly mean temperature [K] and precipitation rate [mm/day] anomalies.

The continental summer warming favours the deepening of the thermal low pressure cells over land, intensifying the low level advection of moist air from the tropical seas to the continent resulting in enhanced monsoons at 6kyBP. The ensemble mean

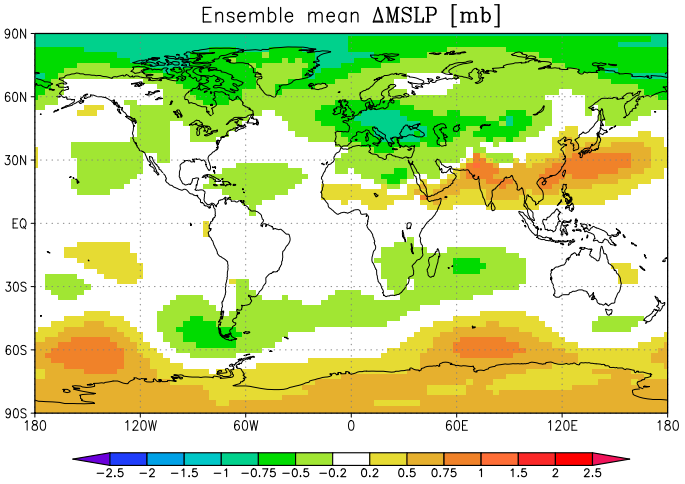

Figure 5.11: The ensemble annual mean surface pressure difference (6ka–control) [mb].

surface pressure response to the 6kyBP forcing, indicates deepening of the continental lows in the NH (**Figure 5.11**). Tropical – subtropical pressure is somewhat heightened in the monsoon regions.

The low sensitivity models simulate the highest precipitation rates (∼3mm/day). The 4–6.5K sensitivity models (model no. 30–60) all simulate a precipitation rate of about 2.8mm/day. The low sensitivity models simulate a slightly higher precipitation rate in the control models compared to the mid-Holocene ones, whilst the opposite is true for the highest sensitivity models (**Figure 5.12**). The higher end sensitivity models predict a positive change in 6kyBP NH annual temperatures, whilst the lower sensitivity models show a small decrease. The R^2 value is here of 0.52 (at the 95% confidence level as used throughout the thesis). There is a higher correlation between the 6k–control global annual mean temperature difference (a) and climate sensitivity than the precipitation difference (d), suggesting that the seasonal forcing is potentially more effective on temperature than precipitation. The control models and the 6kyBP models display a similar pattern in the amplitude of the seasonal cycle in surface temperatures in the NH versus sensitivity (**Figure 5.12(c)**). The 6kyBP models have a ∼0.3K larger JJA–DJF difference, however. The lower end sensitivity models

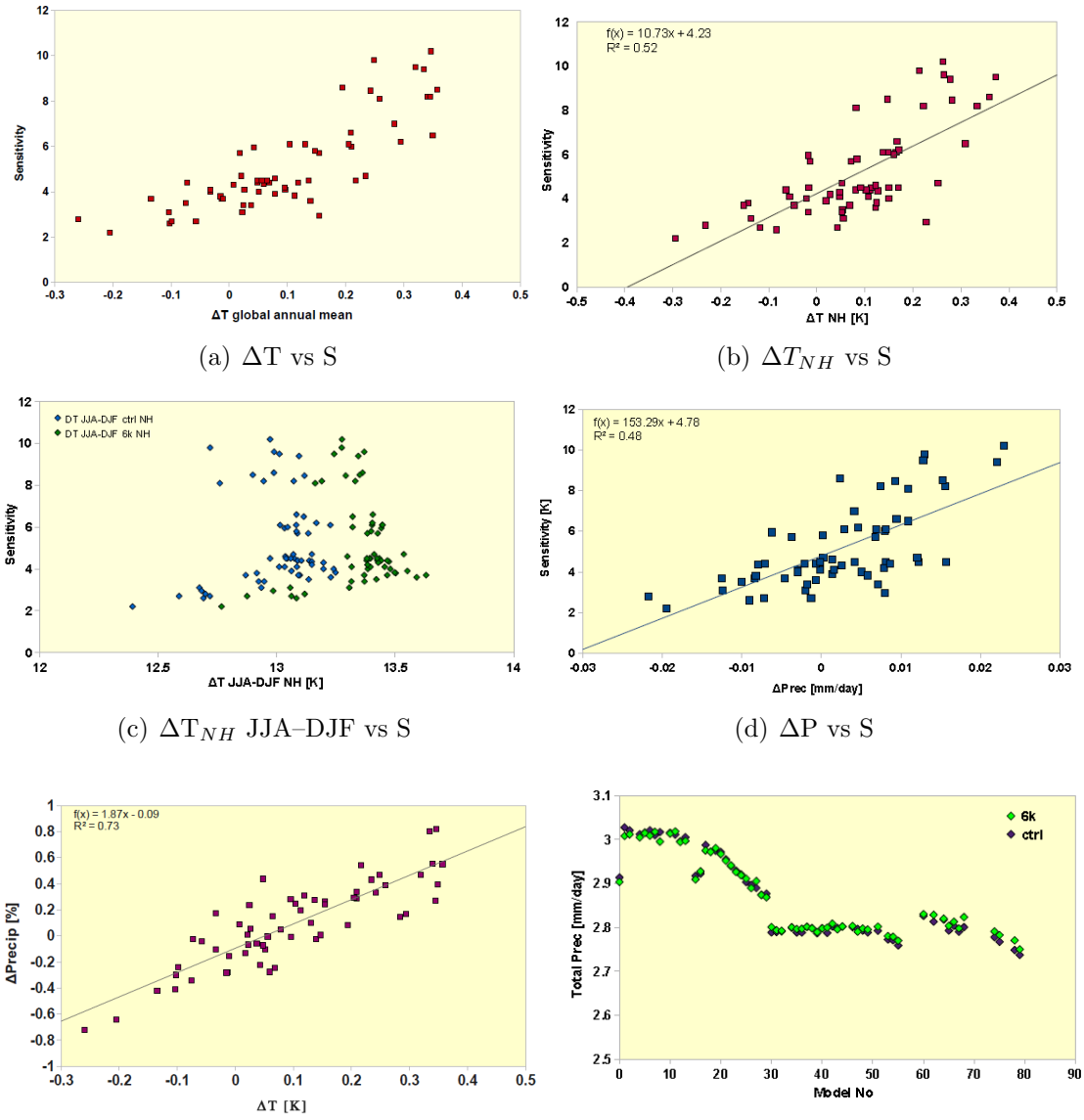

(a) ΔT vs S

(b) ΔT_{NH} vs S

(c) ΔT_{NH} JJA–DJF vs S

(d) ΔP vs S

(e) ΔT vs ΔP

(f) Model no. vs P

Figure 5.12: Scatter plots of the ensemble, each dot represents a model. (a) shows the global annual mean temperature difference between the 6kyBP and control models versus the corresponding sensitivity value, (b) shows the 6kyBP–control temperature difference in the Northern Hemisphere versus sensitivity. (c) shows the seasonal temperature differences in the NH (JJA–DJF) for the control models (blue diamonds) and the 6kyBP models (green) versus sensitivity. The ERA-40 reanalysis data offers a value of 11.9°C. (d) shows the same as (a) only for precipitation rate [mm/day]. The low end sensitivity models simulate a slight reduction in precipitation in the 6kyBP models whilst the high sensitivity models simulate an increase. (e) shows the temperature anomaly [K] versus the precipitation anomaly [%]. The black line shows the best–fit (least squares) linear relationship. The R^2 value is 0.73. Finally (f) shows the total precipitation rate [mm/day] in the 6kyBP and control models. The green diamonds are the 6kyBP models and the blue the control.

simulate a wider range of seasonal amplitudes, the mid – higher en sensitivity models simulate a narrower range. An amplification of the seasonal cycle is expected from our knowledge of the orbital configuration changes. As seen in **Chapter 2**, the 6kyBP climate was forced by higher insolation in boreal summer and lower in winter (globally). The magnitude of change was larger in summer than winter (**Figure 3.6**). It is the change in the precessional forcing that amplifies the seasonal cycle.

5.3 Benchmark 1 results

The mid-Holocene winter experienced a warm anomaly in the north east and a cold anomaly in the south west, as described in **Chapter 4.2.1** (Cheddadi et al., 1997).

Figure 5.13 shows the mean temperature difference (6k–control) of the coldest month

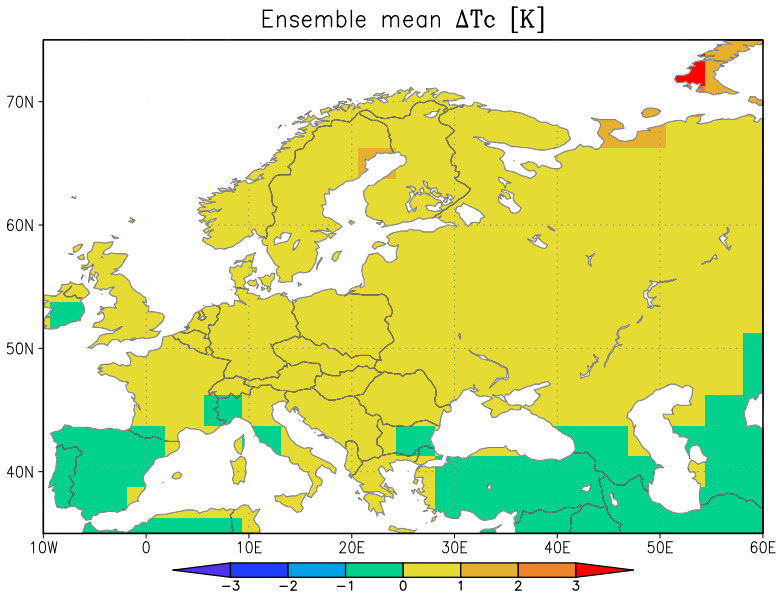

Figure 5.13: The ensemble mean temperature anomaly of the coldest month, using the same colour–scale as used in Cheddadi et al. (1997) for ease of comparison.

for the whole ensemble. The coldest month is January in both the control and the mid-Holocene models. The 6kyBP February temperatures are very close to the January ones, so an average of these two months could also be used. This can be compared

to **Figure 4.5** (Cheddadi et al., 1997) in **Chapter 4**. The ensemble mean displays a warming in northern Europe and cooling in far southern areas (**Figure 5.13**), as the geological evidence does. The magnitude of change is not strong enough, however in the model, and the 0°C isotherm is too far south. The ensemble mean temperature anomaly is generally up to 1°C warmer in central to northern Europe, which is an underestimation of 1–2°C compared to the paleo-records. The ensemble mean temperature anomaly in Iberia is of –1°C, i.e. a 1–3°C underestimation compared to Cheddadi et al. (1997). The ensemble has some skill with regards to this benchmark, as the sign of change is correct, though the magnitudes are underestimated.

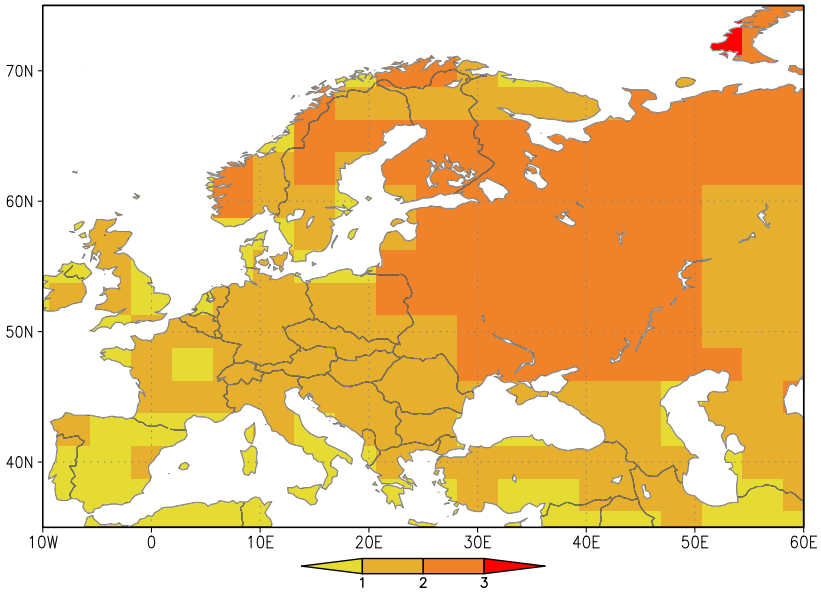

Figure 5.14: The ensemble standard deviation of the temperature anomaly of the coldest month.

The largest temperature variability within the ensemble is found in eastern–northeastern Europe, of 2–3°C (**Figure 5.14**). For this benchmark a wide variety of behaviour was found in the ensemble. Some of the models in the ensemble were found to mirror the paleo-data almost perfectly, whilst other members displayed the opposite pattern with a cooling in the north and warming in the south. It is useful to have found ensemble members capable of modelling this climatic feature. The parameter perturbation

combinations, can be focused on in more detail if it is wanted to e.g. investigate model behaviour and climate dynamics for this region. The Cheddadi data-set is widely used in the paleo community and here I have the opportunity to identify what atmospheric parameters govern the model's ability to simulate the meso-scale paleo-climate most accurately.

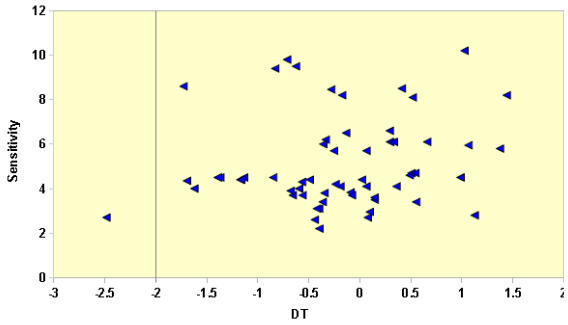

(a) Iberia

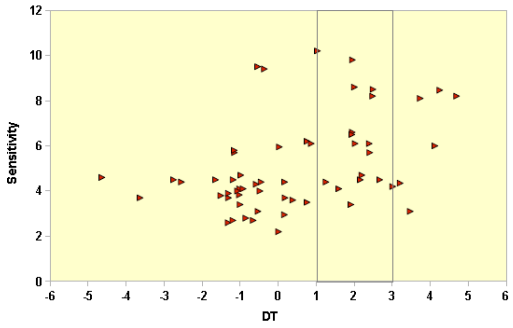

(b) Northeastern Europe

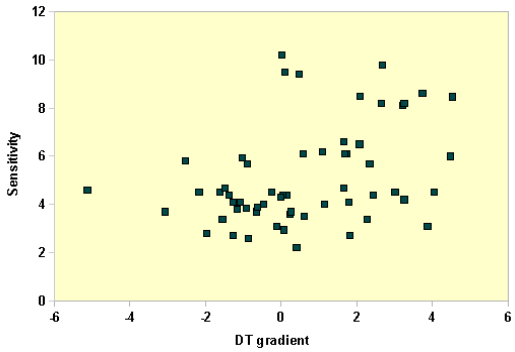

(c) Gradient

Figure 5.15: (a) The temperature difference between the 6kyBP and 0kyBP models in Iberia (33–43°N and -10–1°W) (b) Northern Europe (58–68°N, 40–55°W) versus the corresponding sensitivity values [K]. (c) shows the temperature gradient, i.e. (b)–(a), versus sensitivity.

In **Figure 5.15(a)** the temperature anomaly across Iberia for each ensemble member has been plotted against the corresponding sensitivity value. The proxy data indicate a winter cooling during the mid-Holocene of -2 – -4°C. In the ensemble, there is only one model capturing the correct magnitude in this selected region, namely Model 5 with a sensitivity of 2.7K. Geological evidence suggest a warming of 2–3°C in the selected northeastern European region. A number of models with sensitivities up

to ∼10K are within the observational limits in this region. **Figure 5.15(c)** shows the NE–SW gradient in temperature versus the sensitivity, i.e. figure (b) minus (a) and only one model, Model 29 with a sensitivity of 4.35K, simulates this difference correctly. The gradient according to the observations is of 5–7°C.

The results indicate the importance of the atmospheric parameter choices in the model for this benchmark, i.e. the modeled European temperatures are dependent on the parameter values. Some models simulated this 6kyBP feature almost perfectly, indicating that it is OK to use a slab model. Though it could be speculated that the ensemble mean would have behaved more accurately if a full ocean circulation had been used and the impact of the AMOC (Atlantic Meridional Overturning Circulation) had been included.

5.4 Benchmark 2 results

This section describes the results of the ensemble relative to the North African Monsoon expansion benchmark (described in **Section 4.2.2**). The model and data have been zonally averaged across Northern Africa and are compared with the precipitation needed at that latitude to sustain steppe vegetation (**Figure 5.16**). The spread in the ensemble decreases with latitude. In the Sahel, there is an ensemble variability of ∼300mm/year. The maximum peak in rainfall at 6kyBP is found at 12.5 – 15°N, which is too far south relative to observations suggesting high rainfall rates from 15–30°N. The models are too dry at these latitudes. Most likely this is due to the Hadley Cell in the model subsiding in this region. Looking at the Global Lake Status Data Base (**Figure 4.4**) one might speculate that the Hadley Cell subsided in the then drier southern and central Europe at 6kyBP. The models do rightly predict a northwards extension of the North African Monsoon during the mid-Holocene,

though they underestimate the full northward expansion.

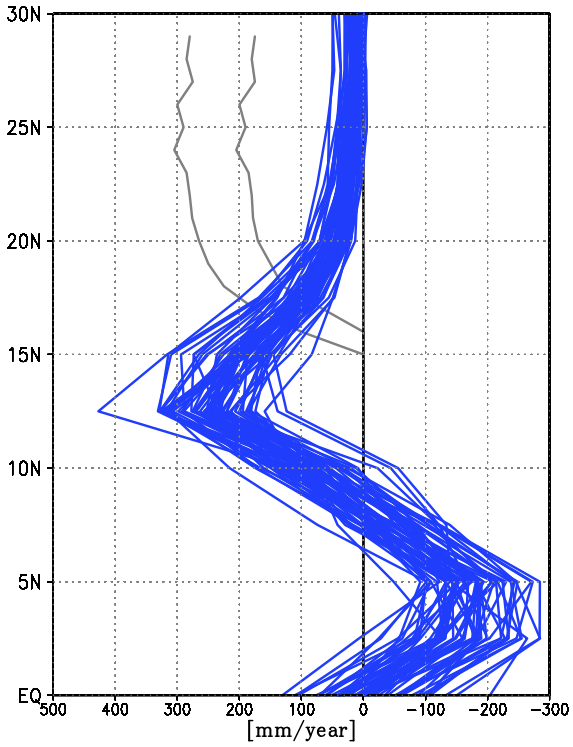

Figure 5.16: The zonally averaged precipitation rate [mm/year] difference across northern Africa (20°W – 30°E). Each curve represent an individual ensemble member and the grey lines indicate the upper and lower limit on the excess precipitation required to maintain steppe vegetation as opposed to present day desert (from Joussaume et al. (1999)).

There is no apparent link between the annual precipitation difference (6k–present) and climate sensitivity in this region (**Figure 5.17**).

5.5 Benchmark 3 results

With this benchmark the models' ability to capture the expansion of the North American Monsoon during the mid-Holocene is tested. The feature to look for is a crescent shaped region of increased monsoon flow surrounded by no change, then an increase in aridity (see **Section 4.2.3**).

The average North American ΔP–E (Precipitation minus Evaporation) anomaly across

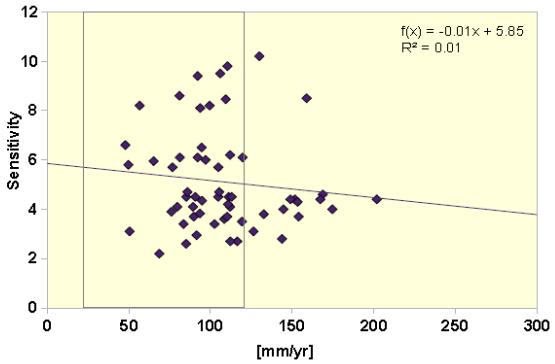

Figure 5.17: The annual mean precipitation rate difference at 17°N across northern Africa versus climate sensitivity. The grey lines indicate the precipitation change in the region at 6kyBP. The purple line is the regression curve with an R^2 value of 0.01. I.e. there is no relationship between the precipitation difference and climate sensitivity.

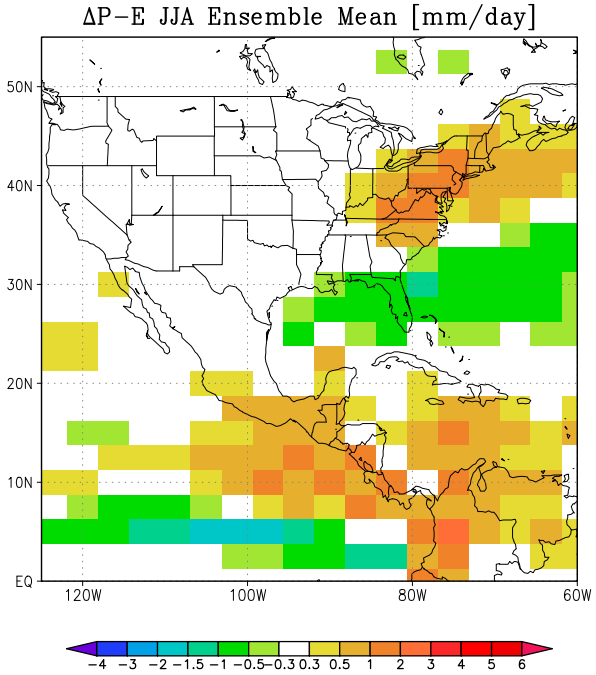

Figure 5.18: The ensemble mean JJA moisture budget anomaly across North America [mm/day]. The data show an expansion of the North American Monsoon at 6kyBP, surrounded by an increase in aridity.

the whole ensemble is shown in **Figure 5.18**. The ensemble does simulate an enhancement in the mid-Holocene moisture budget compared to the control southwards of 20°N, though again monsoon flow expansion does not reach northwards enough compared to the paleo-observations. The order of magnitude of change, where any

change is observed in the ensemble, is correctly modelled by the ensemble mean of 0.5–1mm/day, reaching 2mm/day in regions. Most of North America is modelled to have seen no changes in the moisture budget at 6kyBP. Instead drier conditions were experienced in parts of the interior of the continent during the summer season.

The largest variability in P–E within the ensemble is found in southern and eastern areas (**Figure 5.19**). Still, none of the models capture the full northwards extent of the enhancement of the monsoon at 6kyBP.

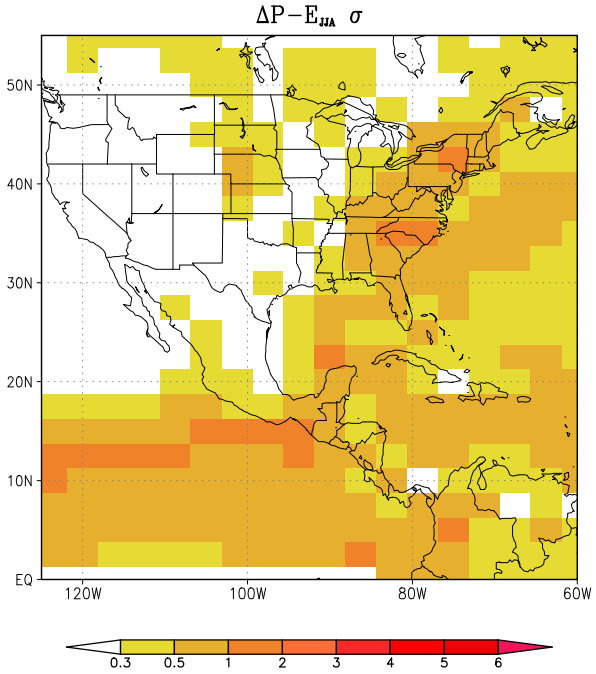

Figure 5.19: The standard deviation of the JJA P–E change between the 6yBP and control models in the ensemble.

The ΔP–E anomaly [mm/day] for a selected region of the North American Monsoon (15–18.5°N; 103–88°E) versus each models' sensitivity value is shown in the following scatter plot (**Figure 5.20**). This region was selected as it is over land and in an area where the ensemble mean fits the paleo-observations. There is little point in testing the model skill in a region where it has none. About half of the ensemble members lie within the observational range of 0.75±0.25mm/day, including models

with a sensitivity of ∼10K.

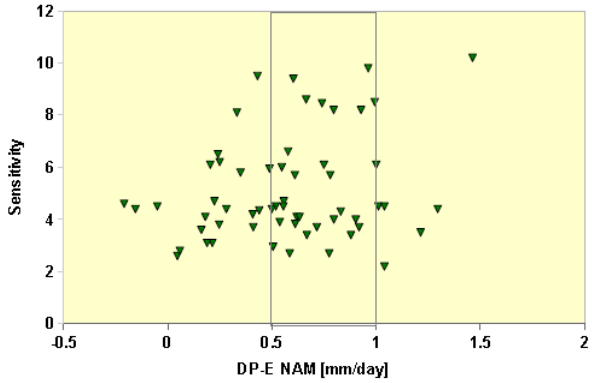

Figure 5.20: The ensemble JJA P–E moisture budget anomaly from a selected region of North America [mm/day] versus the corresponding climate sensitivity for each model. The paleo-observations indicate an increase of 0.75±0.25mm/day.

5.6 Benchmark 4 results

This benchmark considers the models' performance regarding the East Asian Monsoon. The ensemble mean correctly captures an increase in the Indian monsoon precipitation, though the area of increase in southwestern China is underestimated. Pollen data show an increase in southeastern China, where the ensemble mean predicts a decrease in annual mean precipitation (**Figure 5.21**). The same pattern is seen in the CCM3, FOAM and HadCM3 PMIP2 models. Oceanic feedbacks are thought to reduce the precipitation over SE China (Liu et al., 2004). The NW Pacific warm pool becomes even warmer in the mid-Holocene model, leading to stronger convection and more precipitation over sea, i.e. the precipitation is reduced over land and shifted eastwards. The standard deviation of the annual precipitation rate difference is seen in **Figure 5.22**. There is a lot of variability across the region among the ensemble, particularly in eastern and southern parts.

Looking at the JJA seasonal mean, a similar picture to the annual mean precipitation

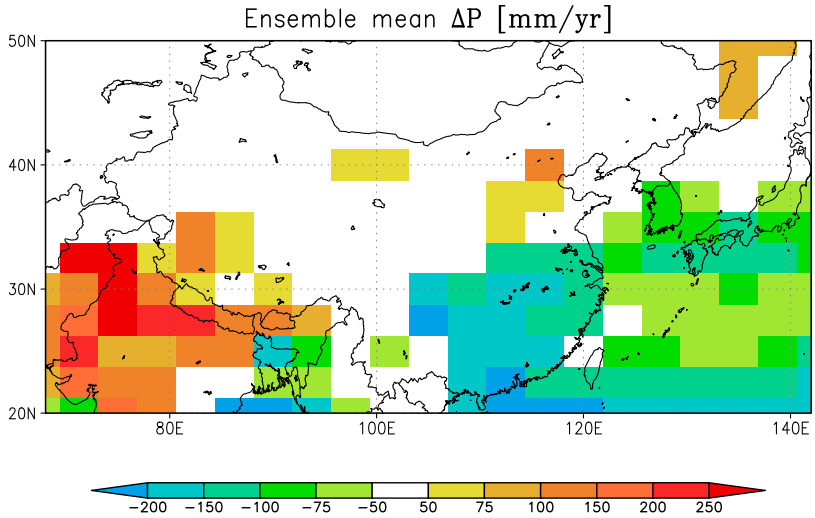

Figure 5.21: The ensemble mean annual precipitation rate anomaly across Asia [mm/year] (6kyBP–control). The paleo-records indicate an expansion in the monsoon at 6kyBP.

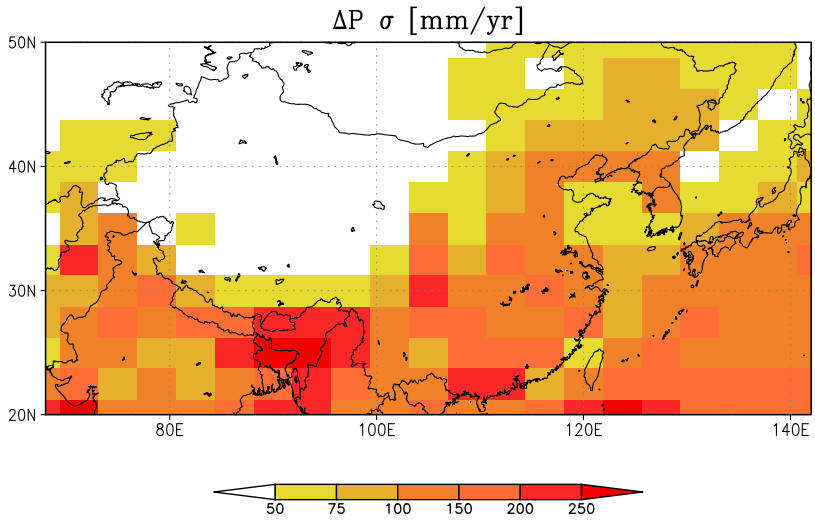

Figure 5.22: The standard deviation of ensemble mean annual precipitation rate anomaly across Asia [mm/year].

is seen (**Figure 5.23**). The strong summer monsoons dominate the annual precipitation pattern, as expected. Western parts of China is experiencing stronger monsoonal precipitation, whilst eastern parts sees less precipitation.

The models produce an increase in the 6kyBP JJA moisture budget (**Figure 5.24(a)**). A similar picture is seen in the moisture budget as in the precipitation rate anomalies. The ensemble mean matches the Guiot et al. (2008) data from 70–110°E with

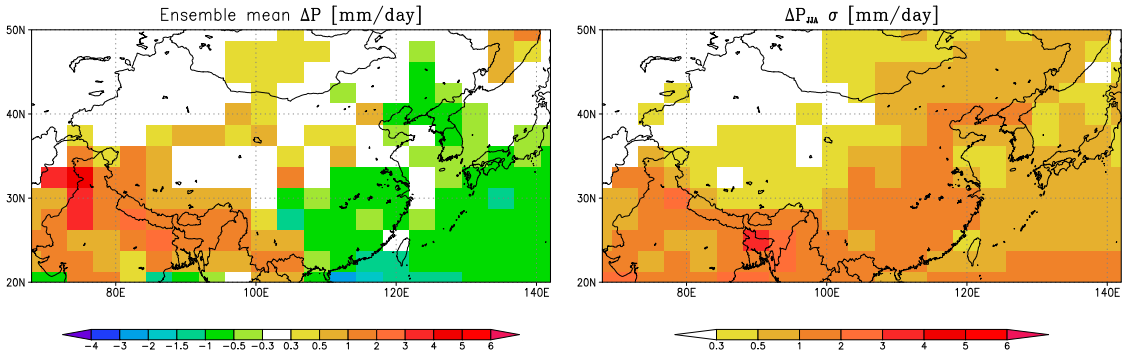

(a) ΔP JJA (b) ΔP JJA σ

Figure 5.23: (a) The ensemble mean JJA precipitation rate difference (6k–control) across Asia [mm/day] and its corresponding standard deviation (b).

an increase of 0.5–1mm/day, up to 2mm/day in places. East of this the ensemble suggests a mid-Holocene drying of 0.5–1mm/day, whilst data suggest some drying or no difference along the coast and otherwise wetter conditions in this area. The standard deviation of the ensemble mean Asian monsoon anomaly [mm/day] is shown in **Figure 5.24(b)**. As seen in the figure there is a lot of variability across the ensemble with a standard deviation of up to 3mm/day in some regions.

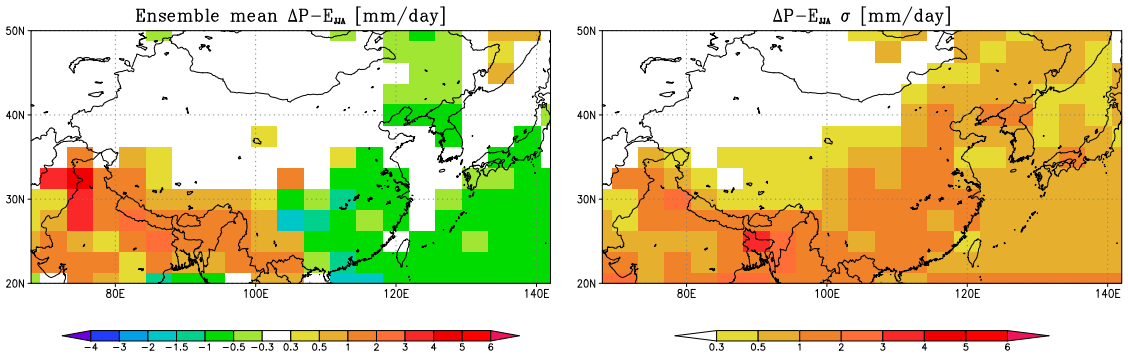

(a) ΔP–E JJA (b) σ JJA

Figure 5.24: (a) The ensemble mean JJA moisture budget difference (6k–control) across Asia [mm/day] and its corresponding standard deviation (b).

ΔP–E for a selected region in China (22–32°N; 98–102°E), where the paleo-records show evidence of a stronger monsoon during the mid-Holocene, versus the climate sensitivity for each model is seen in **Figure 5.25**. This region was chosen based on density of paleo-records and the high confidence levels in the observations. For this

region there seems to be a relationship where high sensitivity models underestimate the increase in the moisture budget at 6kyBP. The majority of the 8–10K sensitivity models simulate a decrease, where the observations suggest a +0.5–1mm/day increase. This method places an upper limit on climate sensitivity of 6.1K. The two high sensitivity models, with sensitivities of 8.6 and 8.2K, that lie close to the observations on the lower and upper bounds respectively, can be ruled out due to their low entrainment coefficient values. This plot highlights the importance of sampling and the need to sample the sensitivity and parameter space as densely as possible. The parameter space needs to be sampled as much as possible in order to find all viable combinations of parameter perturbations for the 6kyBP climate. This is to see what ranges of sensitivity values these models correspond to, in order to reduce the uncertainties associated with this metric.

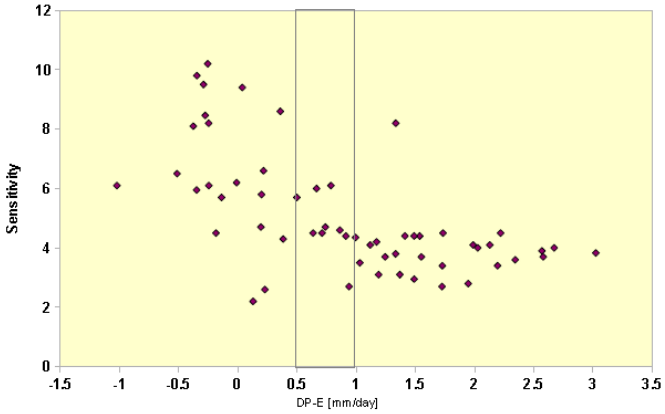

Figure 5.25: The ensemble JJA moisture budget anomaly across Asia [mm/day] versus the models' corresponding sensitivity values [K]. The R^2 value is of 0.4. The models should capture a 0.75±0.25mm/day increase.

The moisture budget anomaly versus the inverse of climate sensitivity is seen in **Figure 5.26**. This plot could be used to create a Piani et al. (2005) – style transfer function and use the resulting feedback parameter as a predictor of climate sensitivity and generate a probability density function. This is intended to be attempted in future work.

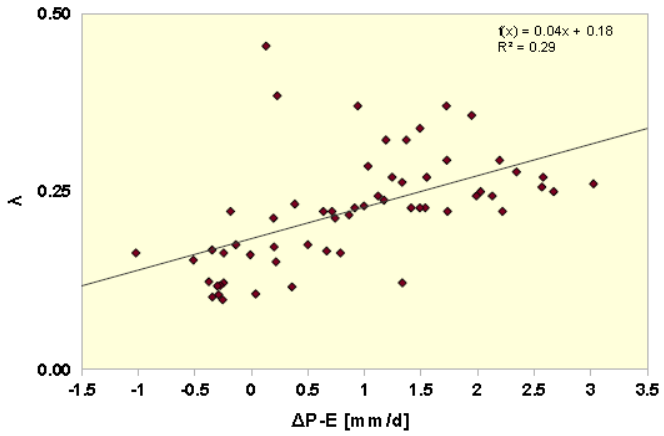

Figure 5.26: The ensemble JJA moisture budget anomaly across Asia [mm/day] versus lambda, the feedback parameter. The models should capture a 0.75±0.25mm/day increase. The linear regression curve has an accuracy of $R^2 = 0.29$.

5.7 Benchmark 5 results

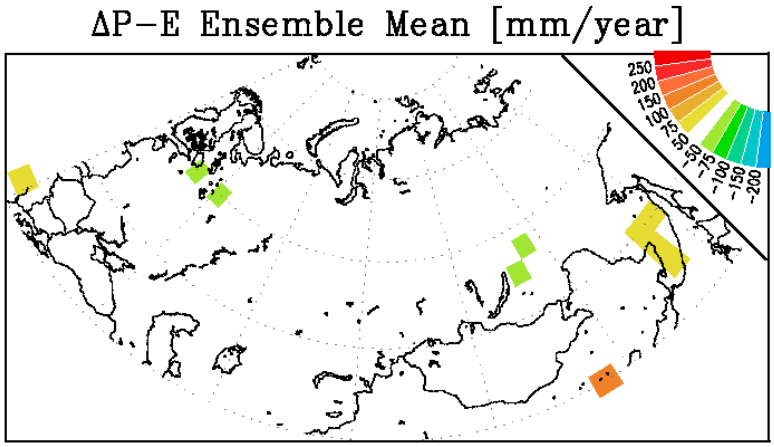

Figure 5.27: The ensemble mean annual moisture budget (P–E) anomaly (6k–control) across Eurasia [mm/year]. It is a north polar stereographic map projection covering 40–80°N and 20–150°E. The paleo-observations show no major changes.

The geological evidence from the mid-Holocene show no major change in the moisture budget across mid-latitudinal Eurasia compared to present (as described in **Chapter 4.2.5**).

Eurasia is relatively dry presently, as it was during the mid-Holocene. The ensemble mean predicts no changes in the 6kyBP simulations (**Figure 5.27**), indicating the

models' ability to keep dry regimes dry.

It is seen that there is little variations in the moisture simulations across the ensemble (**Figure 5.28**), except in southeastern parts, which is influenced by the Asian Monsoon. Across mid-latitudes, the standard deviation is of 50–75mm/year in far eastern Eurasia and zero elsewhere.

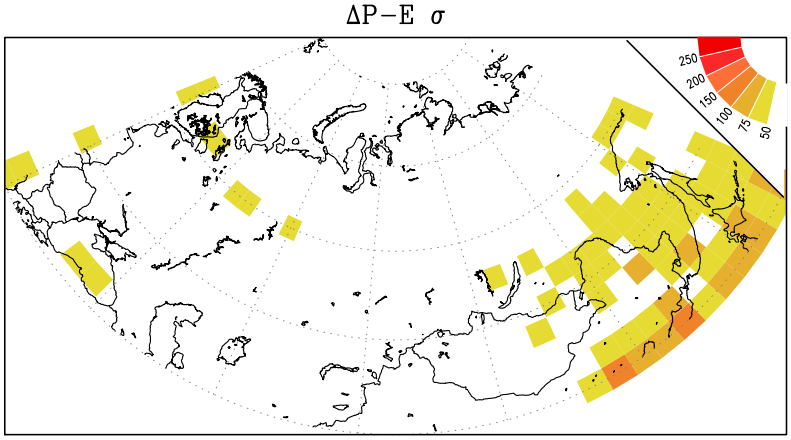

Figure 5.28: The standard deviation of the ensemble mean annual moisture budget anomaly across Eurasia [mm/year].

The difference in the ΔP–E [mm/year] budget between 42.5–47.5°N across Eurasia plotted against sensitivity is shown in scatter **plot 5.29**. Each dot denotes a model from the ensemble. All the models fit the observations of no change and no upper limit on climate sensitivity is found.

5.8 Benchmark 6 results

Here the modelled South American Monsoon moisture conditions are evaluated. A variety of paleo-observations give evidence of a reduction in the monsoon at 6kyBP (see **Section 4.2.6**).

The ensemble mean result is mainly a 6kyBP reduction in P–E south of 10°S. Atlantic

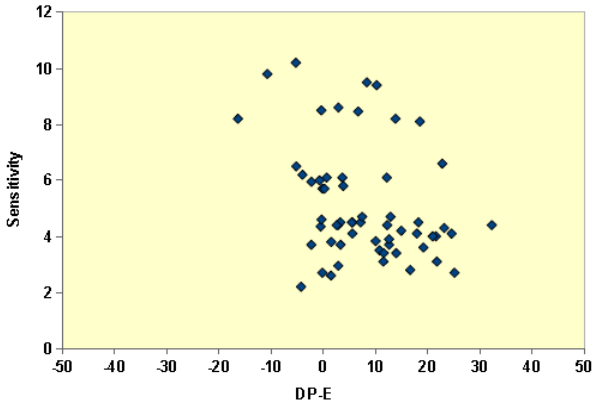

Figure 5.29: The ensemble mean annual moisture budget anomaly [mm/year] across Eurasian mid-latitudes versus sensitivity. The geological records indicate no major change.

coastal areas see no change or an increase of 0.5–1mm/day, whilst in southern parts there's a reduction of up to –1.5mm/day (**Figure 5.30**).

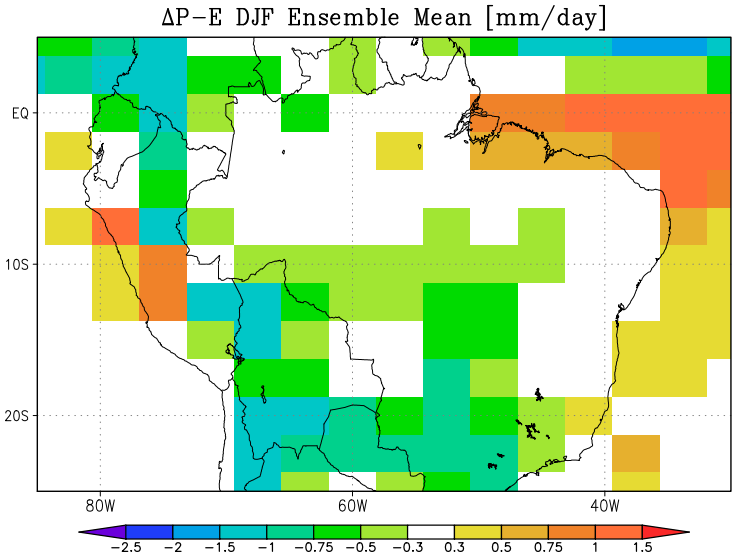

Figure 5.30: The ensemble mean DJF moisture budget (P–E) anomaly in South America [mm/day].

The standard deviation reaches 1–1.5mm/day south of 12°S (**Figure 5.31**). North of this it is smaller; 0.3–0.75mm/day. As precipitation is a noisy field, it is not unexpected that rainy regions are associated with large standard deviations.

Figure 5.32 is a scatter plot of the South American ΔP–E [mm/day] DJF anomaly

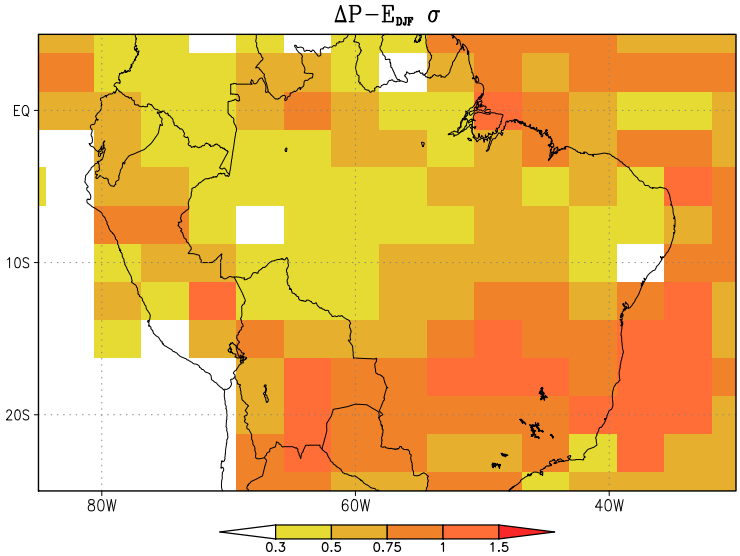

Figure 5.31: The standard deviation of the ensemble mean DJF moisture budget anomaly in South America [mm/day].

from a selected region (15–25°S; -55– -45°E) versus each model's corresponding sensitivity value. This region was selected due to a higher confidence in the paleo-data here. There is no obvious relationship between the ΔP–E budget and the climate sensitivity in this region and the majority of the models correctly simulate dryer conditions. Some of the models simulate a drying of up to 2mm/day, or 720mm/year. This magnitude may be rather large and one might speculate that if the mid-Holocene was that much drier than present, there would be a stronger signature in the paleo-records. A reduction of 0.5–1mm/day seems more reasonable, and around a third of the ensemble simulates this magnitude, including high sensitivity models.

5.9 Model Skill Assessment

Having considered all the six benchmarks, it is found that none of the models simulate the North African Monsoon correctly. Evaluating the ensemble's performance regarding the five other benchmarks, one of the members capture the remaining five mid-Holocene climatic features; Model 29 with a climate sensitivity of 4.4K, four of

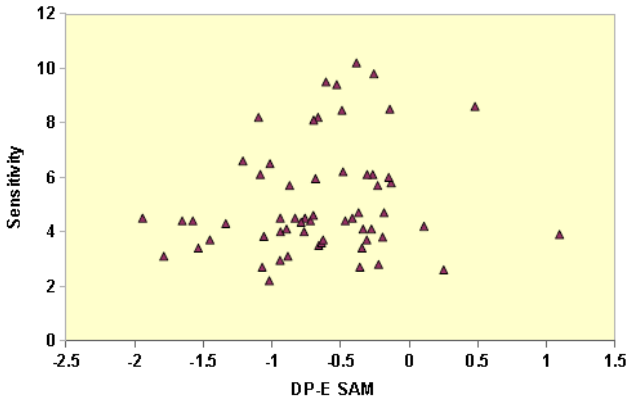

Figure 5.32: The DJF moisture budget (P–E) anomaly (6kyBP–control) for a selected region in South America [mm/day] versus climate sensitivity for each ensemble member.

the models correctly simulate four out of the six benchmarks, whilst 30 models capture three, 19 models capture two and six models simulate one only. All members of the ensemble correctly simulate the Eurasian moisture budget. **Figure 5.33** shows the model number versus sensitivity. Model 1 is the one with unperturbed parameter values. The majority of the ensemble feature half of the benchmarks, including sensitivities up to 9.4K. The models that simulate the right magnitude of change in the NAM also simulate a reasonable drying of the South American Monsoon.

The models passing 1 – 3 out of the 6 benchmarks have an average sensitivity of around 5K (**Figure 5.34**). 6.25K is the average sensitivity for the models capturing 4 and 4.35 for the one model passing 5 out of 6 benchmarks.

The number of models fitting each benchmark are shown below:

- BM 1: NE: 16, SW: 1, Gradient: 1
- BM 2: 0
- BM 3: 34
- BM 4: 9

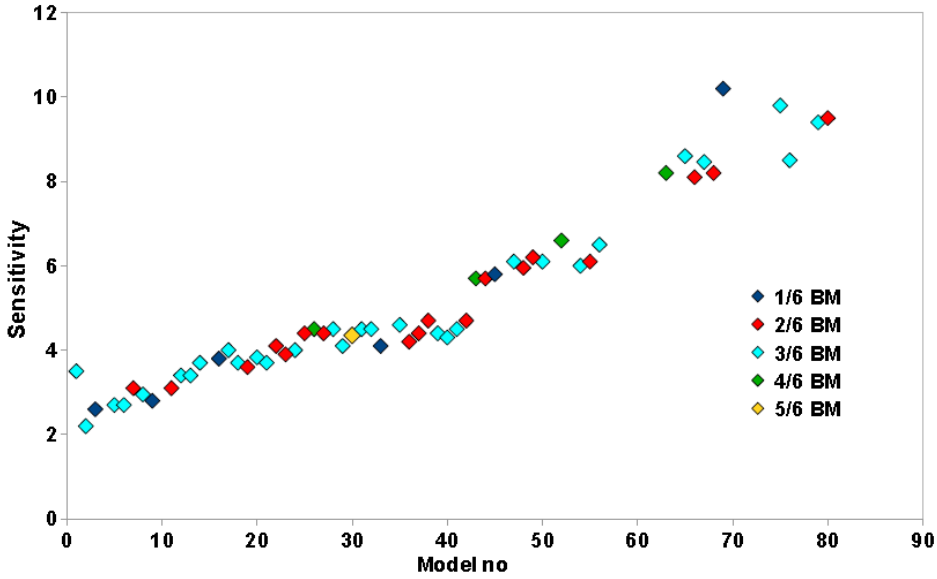

Figure 5.33: Model number versus sensitivity. Blue dots capture 1 out of 6 benchmarks, red 2, turquoise 3, green 4 and yellow 5. Turquoise models simulate the no change in the 6kyBP moisture budget correctly. Only four models simulate four climatic features right (sensitivities of 4.5–8.1K). Model 1 is the standard HadSM3 model.

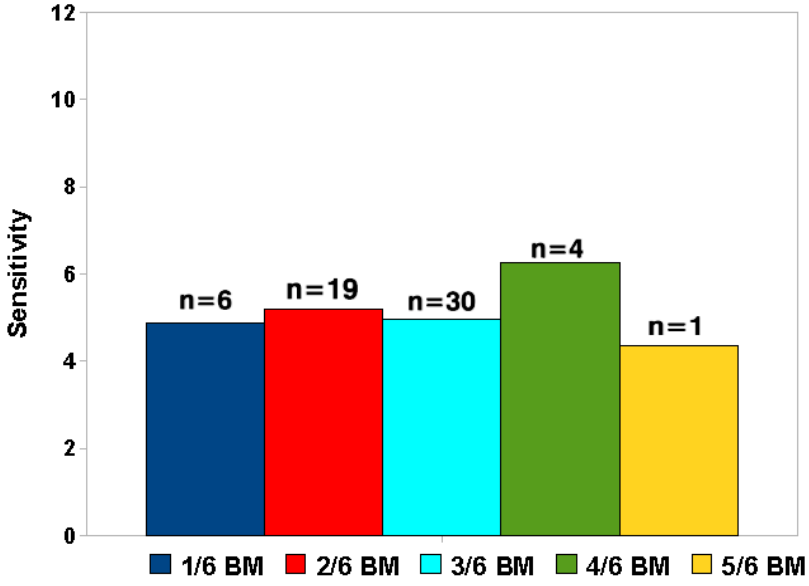

Figure 5.34: The average sensitivity of the models in each category of benchmark fit. The histogram has the same colour coding as in Figure 5.33. The models passing 1–3 benchmarks have an average sensitivity of ∼5K. The figure also indicates how many models fall into each category.

- BM 5: 60 (all models)
- BM 6: 33, out of 28 in -0.5– -1mm/day bin and 5 -1 – -1.5mm/day.

5.9.1 Model 29 Case Study

One model fits five of the six paleo–climatic benchmarks when using area averages to compare the paleo-records. All models underestimate the northwards expansion of the North African monsoon for the mid-Holocene. **Figure 5.35** shows Model 29's representation of five climatic features of the mid-Holocene. Considering Benchmark 1, the magnitude of the temperature gradient is correctly simulated and the north-eastern European temperature is of 3.2K, whilst the Iberian temperature anomaly is of –1.7K, fitting the Cheddadi et al. (1997) data well. Model 29 does capture the magnitude of the expansion of the North American monsoon correctly, though as for the North African Monsoon, the northwards extension is underestimated **(b)**. The northwards stretching pattern of an increase, surrounded by no change then a drying of the moisture budget fits the picture presented by Sjostrom et al. (2004) relatively well. The model overestimates the area of drying and shows more of a westwards shift in the monsoon, rather than an expansion in both southeastern and southwestern China **(c)**. The magnitude of change in southeastern areas is reasonable, however. Along 45°N in Eurasia no changes in the ΔP–E budget is seen in the results **(d)**. According to the paleo-records the South American Monsoon was reduced at 6kyBP. **(e)** shows the results from Model 29. The average reduction in the moisture budget in the region of 15–25°S and -55– -45°E is –0.8mm/day during the summer season.

Figure 5.36 shows the annual mean temperature [K], precipitation rate [mm/day], moisture [mm/day] and surface pressure [mb] anomalies in Model 29. The orbital

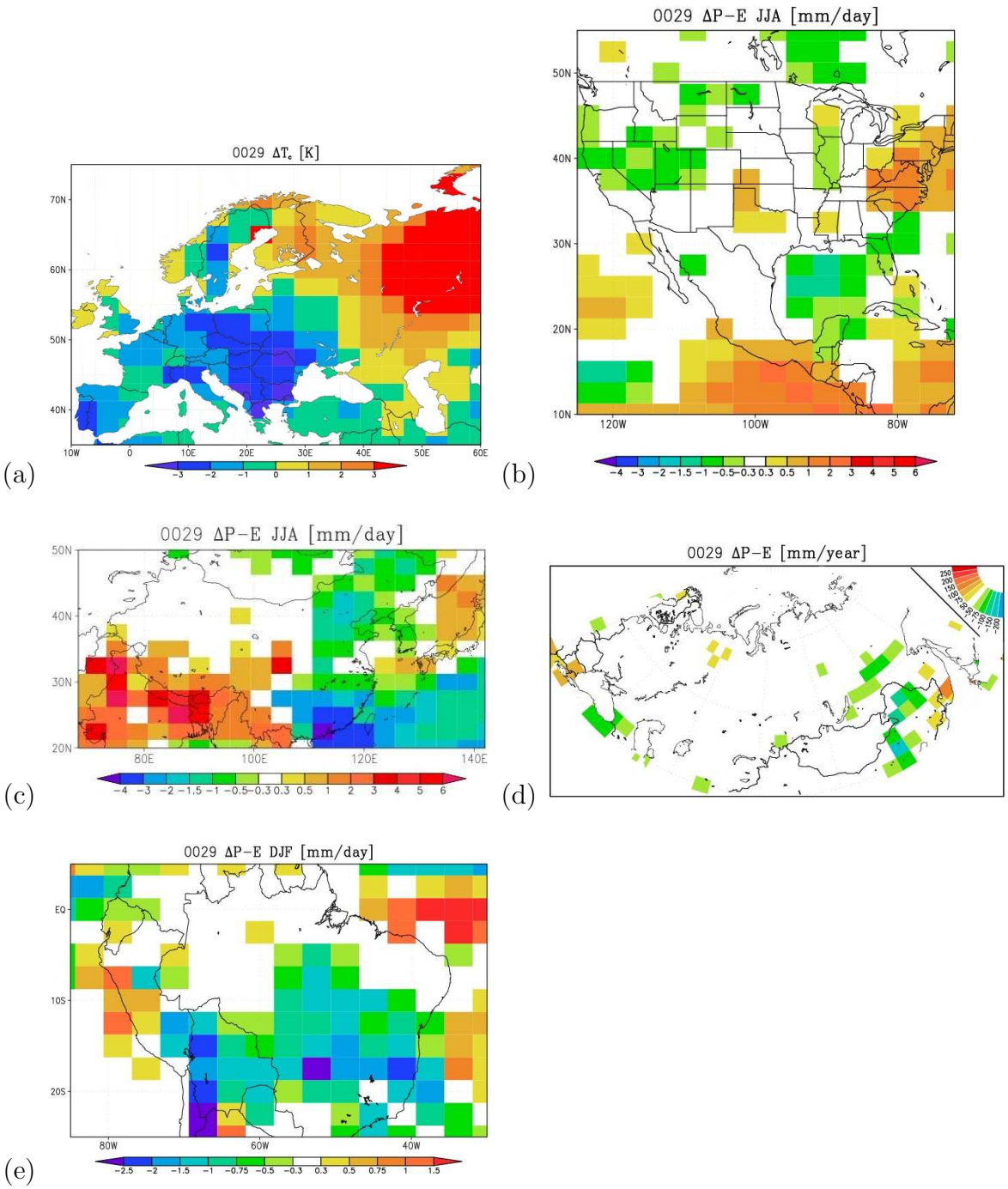

Figure 5.35: Model 29 was found to match the 6kyBP paleo–observations most closely, simulating five out of the six benchmarks correctly. None of the models simulate a northwards enough expansion of the North African Monsoon (Benchmark 2). **(a)** shows the winter temperature gradient across Europe. The results regarding the North American Monsoon is seen in **(b)**. **(c)** illustrates the mid-Holocene changes in the East Asian Monsoon. In **(d)** the annual mean 6kyBP Eurasian moisture budget according to this model is reviewed. **(e)** shows the DJF moisture budget anomaly in South America.

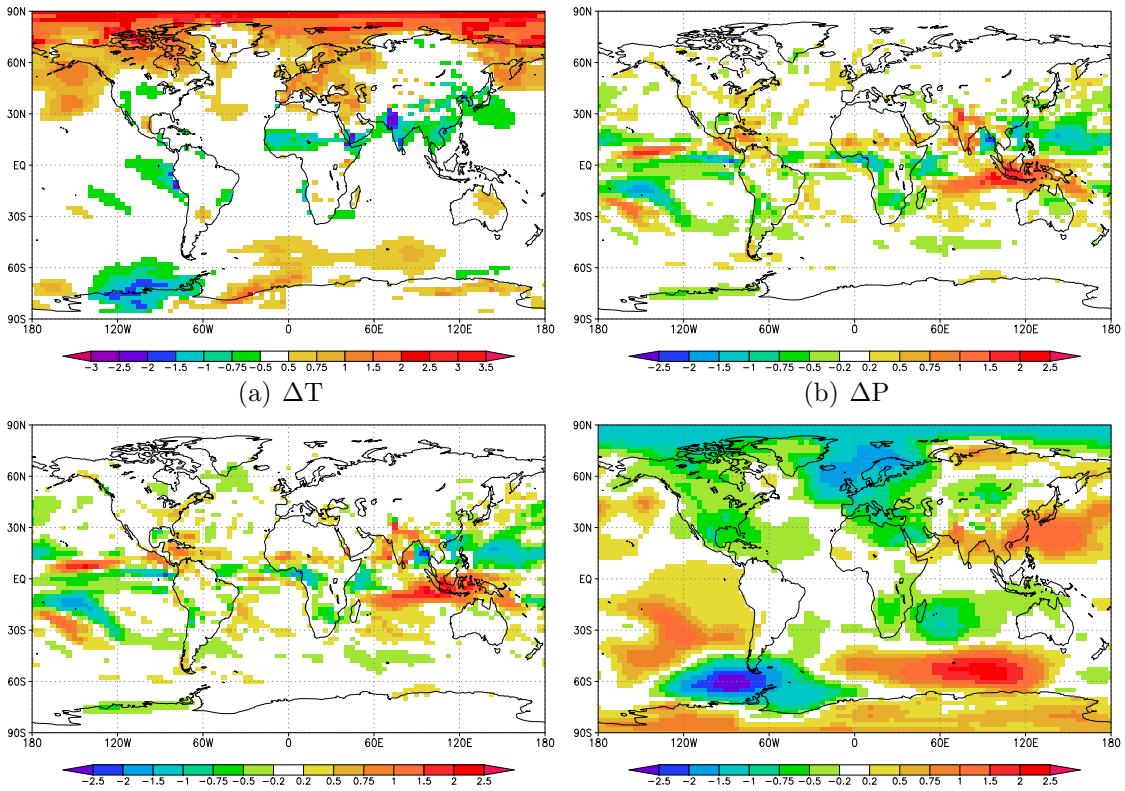

(a) ΔT (b) ΔP

(c) ΔP–E (d) ΔPressure

Figure 5.36: Model 29's simulation of the annual mean temperature [K], precipitation rate [mm/day], precipitation–evaporation [mm/day] and surface pressure [mb] anomalies in the 6kyBP run compared to the control.

Parameter	**Model 29 Value**	**Value Range**
Albedo at melting point	0.589	0.55–0.6
Accretion constant	3.07×10^{-4}	$2.5–3.8\times10^{-4}$
Dtice	4.68	3–8
Entrainment coefficient	2.25	0.3–4.8
Ice size	2.92×10^{-5}	$0.7–3.35\times10^{-5}$
Critical relative humidity	0.821	0.7–0.88
Ice fall speed	0.815	0.55–1.65
Empirically adjusted cloud fraction	0.554	0.515–0.675

Table 5.1: The atmospheric parameter values for Model 29. The range of the values found in my ensemble is also shown in the above table. The CPDN ensemble used 3 different values per parameter (see Figure 3.10). The unperturbed values can be seen in Table B.

forcing results in a warming in the Arctic in accordance with geological reconstructions (Kerwin et al., 1999). Expectantly, low latitude 6kyBP land surface temperatures are reduced as a result of the increase in cloud cover associated with stronger monsoon

circulations. The North Atlantic storm tracks are intensified in the mid-Holocene model, with a reduction of 2mb in the surface pressure. This is associated with a slight increase in precipitation. A deepening of the Eurasian continental low is seen in **(d)**. This accompanied by an intensification of the Pacific subtropical high leads to a larger pressure gradient and an increase in the offshore winds, suppressing precipitation over eastern China. The surface pressure over Indonesia is somewhat lowered accompanied by an increase in the water balance associated with the intensification of the winter monsoon. The Southern Hemisphere is dominated by a dipolar pattern, of a lowering of the pressure west of the Drake passage and higher pressure between 60–120°E.

The atmospheric parameter values for this model is seen in **Table 5.1**. The temperature range of ice albedo variation, dtice, takes on a value between the standard value and the low one. Alpham, the albedo at the melting point, is close to the standard value. The critical relative humidity holds the standard value in this model run. The entrainment coefficient is between the standard and low values. Low values of this parameter have been found to have a large impact on the climate in the models and also on climate sensitivity (Sanderson et al., 2007). A reduction in this parameter in the convection scheme has been found to moisten the upper tropical troposphere introducing potential for convective feedbacks with increasing surface temperatures (Sanderson et al., 2007). On warming, an increase in the relative humidity at high altitudes causes an exaggerated clear sky green house effect. The ice fall speed in the clouds has a value close to the standard in this model. A reduction in this parameter can lead to a global increase in cloud cover and humidity. It has been found that this parameter along with the entrainment coefficient and empirically adjusted cloud fraction all have the potential to cause the largest climatic feedbacks affecting the climate sensitivity. They can lead to very high sensitivity values, but also unrealistic climates (Sanderson et al., 2007).

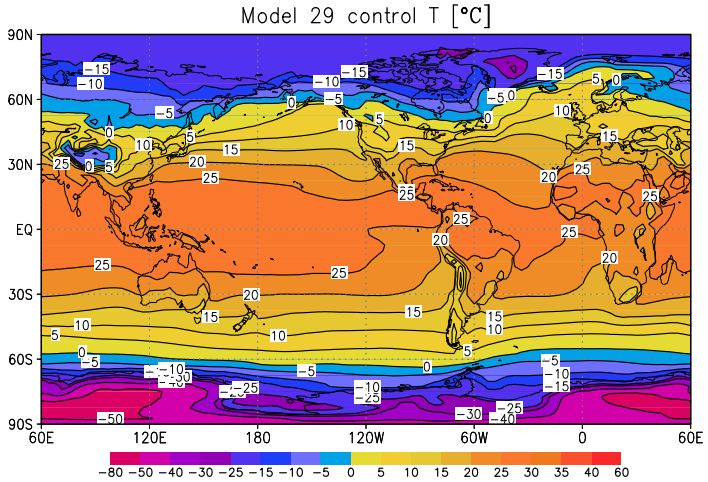

Figure 5.37: Model 29's simulation of the annual mean temperature [°C] in the control model to compare with the ERA-40 Atlas.

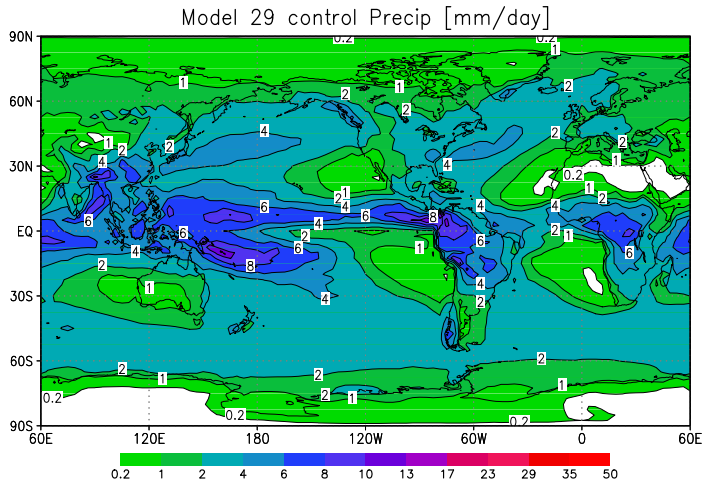

Figure 5.38: Model 29's simulation of the annual mean precipitation [mm/day] in the control model.

Comparing the control model (**Figures 5.37, 5.38, 5.39**) to the ERA-40 Atlas (**Figures 5.3(b), 5.4(b), 5.5(b)**) reveals that Model 29 also does a decent job of simulating the modern climate. The annual mean temperatures are in close agreement with ERA-40, though again as for the ensemble mean, the 0° isotherm is slightly too far south in the model at 50–60°E and 60–70°N, i.e. Fennoscandia and northwestern Russia. The general precipitation pattern is sensibly simulated by the model, though the magnitudes are somewhat underestimates in the monsoonal regions of the ITCZ,

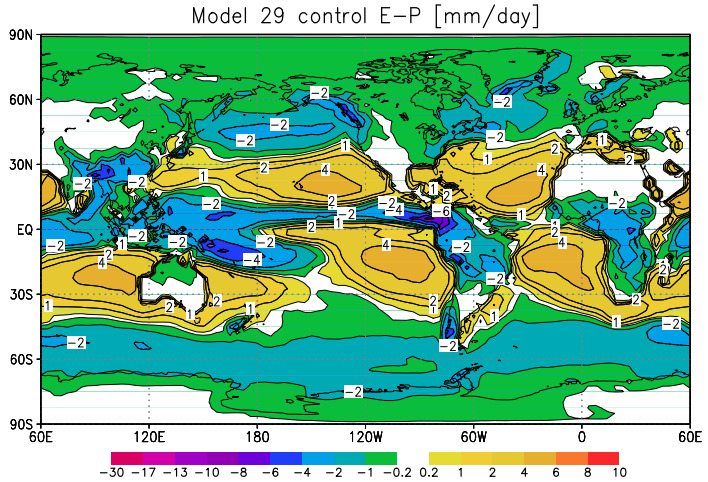

Figure 5.39: Model 29's simulation of the annual mean evaporation minus precipitation [mm/day].

i.e. Central America and parts of South East Asia compared to the reanalysis data. Though the ERA-40 data is known to posses a wet bias in the tropics (Troccoli and Kållberg, 2004). The storm tracks are well simulated in Model 29. The E–P budget is correctly modelled in the subtropical high pressure cells over the oceans. The largest discrepancies are found over land over Australia, Asia and USA, as the regions are modelled to be wetter than in the ERA-40 Atlas. The shape of the ITCZ region is reasonably captured in Model 29. From this basic comparison it is concluded that Model 29 not only simulates the mid-Holocene well, but also the modern conditions.

5.10 Summary

It has been found that the ensemble underestimates the magnitudes of temperature changes in Europe at 6kyBP, though it does simulate the correct sign of change. The shape of the zero degree isothermal is correct, but the placement is too far south. The ensemble underestimates the northwards extent of the North African Monsoon, but does capture the 200–300mm/year needed in excess precipitation in order to sustain steppe, as opposed to present day desert, in northern Africa and the Middle East.

None of the ensemble members manage to simulate the full northwards expansion of the North American Monsoon. The ensemble mean does produce an increase in the moisture budget of the right magnitude in the southern regions. The East Asian Monsoon also saw an expansion at 6kyBP in southern and eastern China. The ensemble simulates a westwards shift of this monsoon, rather than an increase across the whole of southern China, possibly due to oceanic feedbacks. Selecting a region with a high confidence in the paleo-data and plotting the moisture budget anomaly against sensitivity provides a lower constraint of 2.5K and an upper constraint on climate sensitivity of 6.1K. The whole ensemble successfully simulates no major changes in the moisture budget across mid-latitudinal Eurasia. And finally the majority of the ensemble members simulate a reduction in the available moisture in South America.

A count has been made finding that only one of the ensemble members encapsulates five out of the six mid-Holocene climate features. This model has a sensitivity of 4.35K and the details of this simulations have been described. Middle to low values of the physical parameters govern this models climate indicating a suitable parameter combination for the mid-Holocene climate.

It has been demonstrated that some of the large changes in the mid-Holocene climate cannot be simulated with the slab model. Feedbacks associated with the ocean, vegetation and the land–surface need to be considered. Testing the models against this set of 6kyBP climatic changes provides an opportunity to evaluate the model skill. A failure to capture either of these robust features should be considered as an opportunity to improve the models. It also provides information on which parameter perturbation combinations are valid in perturbed physics ensembles.

Chapter 6

Results from the ENA ice sheet experiment

6.1 Introduction

In this chapter, the effects of including the new 6kyBP paleo-boundary conditions of an expanded Hudson Bay and the remnant Laurentide ice sheet are evaluated. As described in **Section 3.2.2**, the models were distributed on climate*prediction*.net with a four phase set–up. In the first experiment, the mid-Holocene phase used the standard PMIP 1 paleo–boundary conditions of altered orbital configuration and somewhat reduced methane concentrations, whilst in the second experiment the paleo–phase also included an expanded Hudson Bay and the remnants of the Laurentide ice sheet. The boundary conditions were kept the same as in the first 6kyBP experiment, apart from these 16 grid boxes with new ice and ocean. I.e. the vegetation was again kept fixed at 20^{th} Century conditions. The heat fluxes were calculated by the same method as usual (**Section 3.2.1**). The same set of parameter perturbations were used in both experiments, those of Sanderson et al. (2008), as explained in **Chapter 3**.

The reason for this focus region is the abundance of paleo-observation and the mismatch between GCM simulations and the proxies so far. The full ensemble is not analysed here, due to time constraints, but will be published at a later date. About 40% of the ensemble had been returned at the time of analysis. The model number and the corresponding climate sensitivity value is shown in **Figure 6.1**. The models used in this analysis represent the full range of climate sensitivity values in the ensemble.

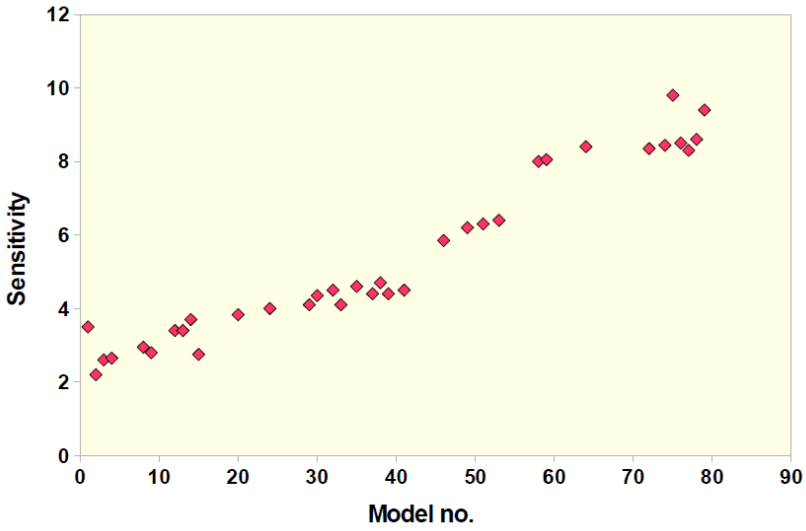

Figure 6.1: Model number versus climate sensitivity for the models used in the analysis in this chapter, c.f. Figure 5.1.

6.2 Results

The first check is to see if the ensemble mean climatological 6kyBP response on global scales is sensible. The effects of the ice sheet and LSM changes are then investigated, by first seeing if there is much of a climatic response outside of Eastern North America, followed by a focus on the regional response in the climate due to the boundary condition changes.

Figure 6.2 shows the annual mean temperatures difference and the corresponding standard deviation. The plots show the 6kyBP models with ice and different LSM (Land – Sea Mask) minus the corresponding control simulation from the models returned from the ensemble. It is seen that the temperatures are cooler above the ice sheet, elsewhere the ensemble mean response is similar to that of the simulations without the ice sheet and change in LSM. I.e. there is a 6kyBP warming at high latitudes and cooling over land in monsoon regions.

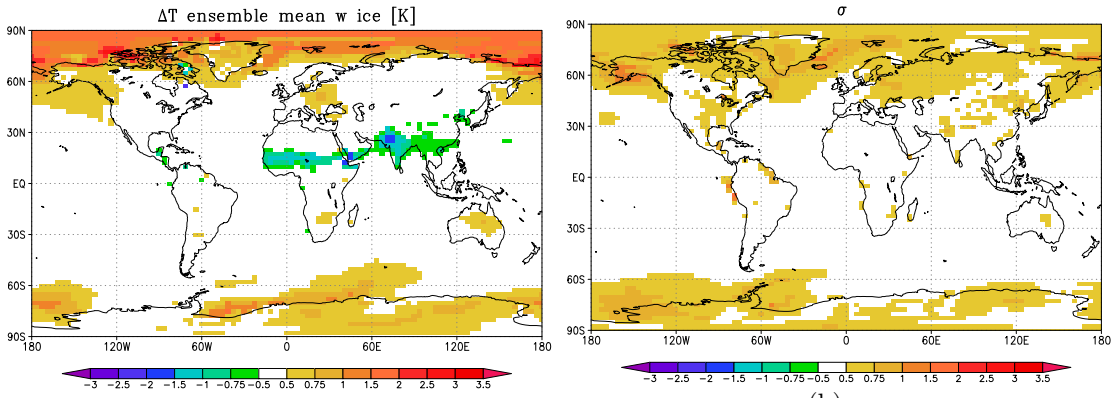

(a) Annual ΔT (b) σ

Figure 6.2: The ensemble mean temperature differences between the 6kyBP model with ice sheet and changed LSM and the control model with changed LSM. (a) is the difference in annual mean temperatures and (b) is the corresponding standard deviation.

During boreal winter, DJF, the ensemble mean temperature response to the forcing is again similar to that seen in **Chapter 5**, with colder tropical, sub-tropical and mid-latitudinal continents and a warming in the Arctic. Only in the 6kyBP simulation with ice, there is a cooling over the added ice in Québec (**Figure 6.3**).

The temperature difference in March – April – May shows a continental cooling during the mid-Holocene due to the longer NH winter season. The strongest cooling is again found over the ice sheet in Québec.

During boreal summer, there is again a localised cooling over the five southernmost grid boxes with ice in ENA. The orbital forcing results in a strong NH continental

warming, though the warming in North America is reduced compared to the first ensemble run without the ice sheet and changed LSM.

The poles are modelled to have been warmer during the mid-Holocene during the boreal autumn (**Figure 6.3**). The Arctic is warmer due to the extended summer due to the change in the orbital forcing and the thinning of the sea ice and reduction in extent (not shown). Again the temperatures over five grid boxes with ice are colder in the 6kyBP runs.

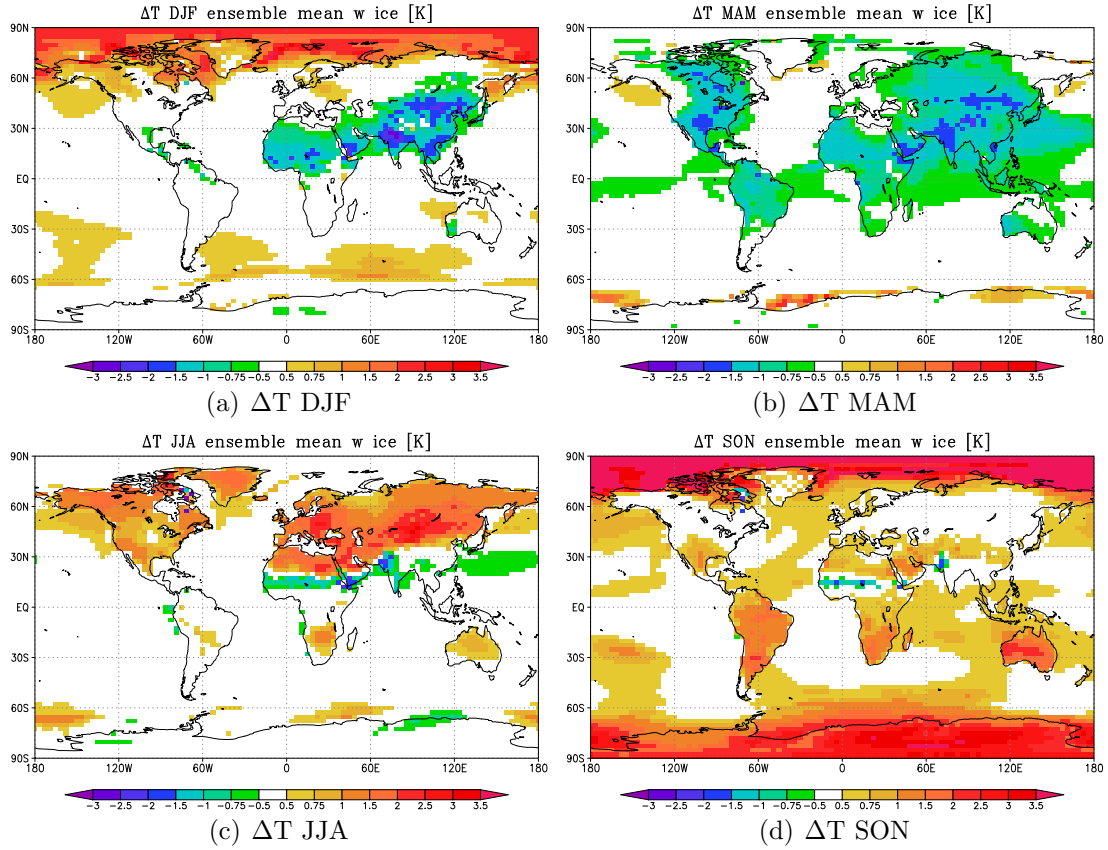

(a) ΔT DJF (b) ΔT MAM

(c) ΔT JJA (d) ΔT SON

Figure 6.3: The seasonal mean 6kyBP temperature anomalies (6k–control) from the ensemble including the ice sheet. Hudson Bay is expanded in both the 6kyBP and control phases.

The annual mean precipitation rate anomaly from the 6kice minus control simulations shows a reduction of 0.2–0.5mm/day over the ice sheet in Québec and no changes

elsewhere in the ensemble mean compared to the anomaly from the ensemble with the standard 6kyBP boundary conditions (**Figures 6.4(a), 5.8(a)**). No changes in precipitation rate between the mid-Holocene ice run and the control in ENA during DJF and SON, whilst a reduction of up to 1mm/day is seen in ENA during JJA (not shown).

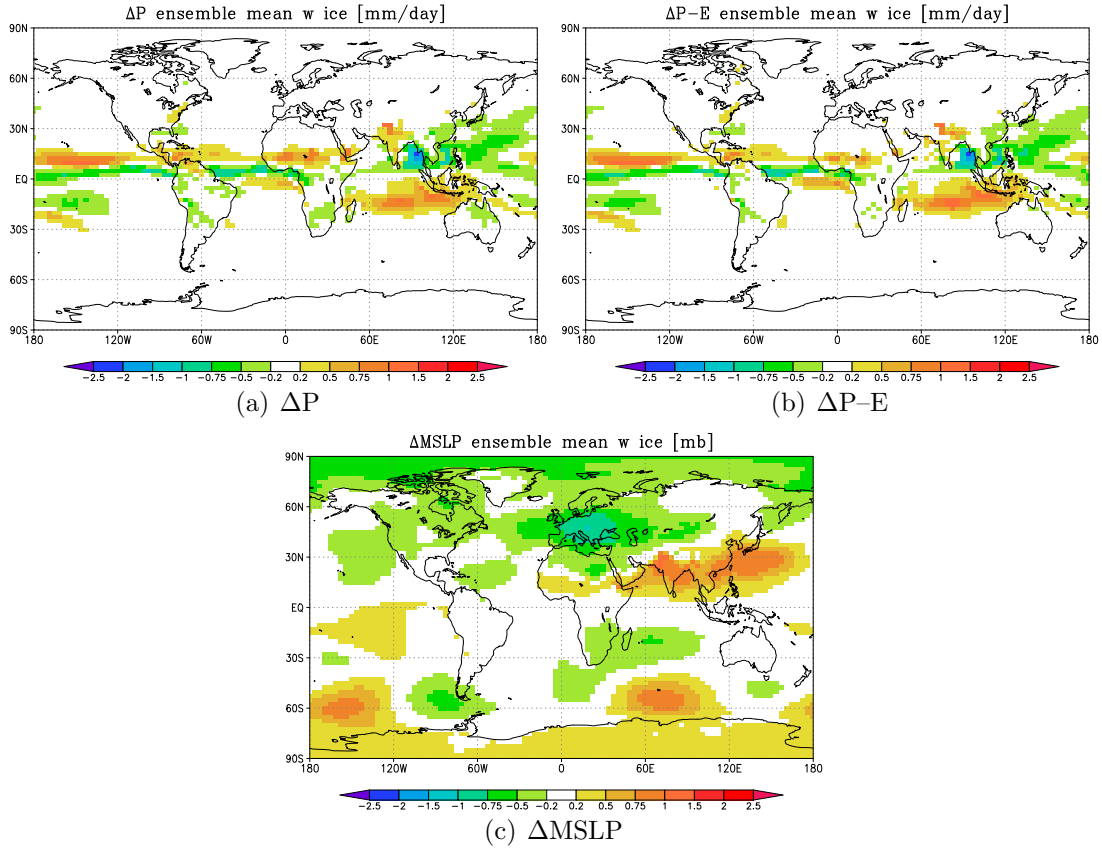

(a) ΔP (b) ΔP–E

(c) ΔMSLP

Figure 6.4: The ensemble annual mean (a) precipitation rate [mm/day] (b) moisture budget [mm/day] and (c) surface pressure [mb] anomalies between the 6kyBP models with ice and the controls. Hudson Bay is expanded in both the 6kyBP and control models.

Annually, there is an increase in the ensemble mean moisture budget of 0.2–0.5mm/day over three of the grid boxes with ice in the 6kyBP models (**Figure 6.4(b)**). There is no change in ΔP–E in ENA during DJF, but during boreal summer, there is a reduction surrounding Hudson Bay and an increase of up to 1mm/day above the ice sheet. During MAM there is a small increase in the moisture budget over the southernmost grid box with ice and no change elsewhere in the mid-Holocene models compared to

the controls. There is also an increase of 0.2–0.5mm/day in ΔP–E over three of the grid boxes with ice in SON. Only the annual mean difference is shown here.

The ensemble annual mean sea level pressure (MSLP) difference [mb] (**Figure 6.4(c)**) shows the same general pattern as seen in the first ensemble, with a deepening of the continental pressure cells and a heightening of the pressure over Antarctica and the monsoon belt in the 6kyBP runs. In the experiment including for the ice sheet, however, there is no negative pressure anomaly over Greenland and Siberia/ northeastern Eurasia, as was seen in the 6kyBP model with standard PMIP boundary conditions. The DJF pressure anomaly shows a lowering of the surface pressure during DJF in ENA (not shown). There is also a JJA negative pressure anomaly in ENA in both experiments, the anomaly is reduced in the ice sheet experiment.

Annually there is a cooling over seven of the grid boxes with ice in the 6kyBP models with ice compared to the 6kyBP models with the standard boundary conditions (**Figure 6.5**). There is positive temperature anomaly across most of Hudson Bay during SON and DJF due to the expanded sea mask and the increase in thermal heat capacity. The Arctic oceans is also simulated as warmer in the ensemble including the ice and new LSM. This could be due to a reduction in sea ice extent and thickness. During MAM there is a localised cooling in the Hudson Bay Lowlands, possibly due to sea ice cooling the air temperatures. During boreal summer the combination of the expanded sea and ice results in a local cooling signal. This reduction in the continental summer heating reduces the growing – degree – days facilitating tundra growth, rather than the temperate forest that the PMIP Hadley Centre models overestimate regionally in ENA (Wohlfahrt et al., 2008). The PMIP Hadley models were run with fixed 20^{th} Century vegetation and the model results were run through the BIOME4 vegetation model.

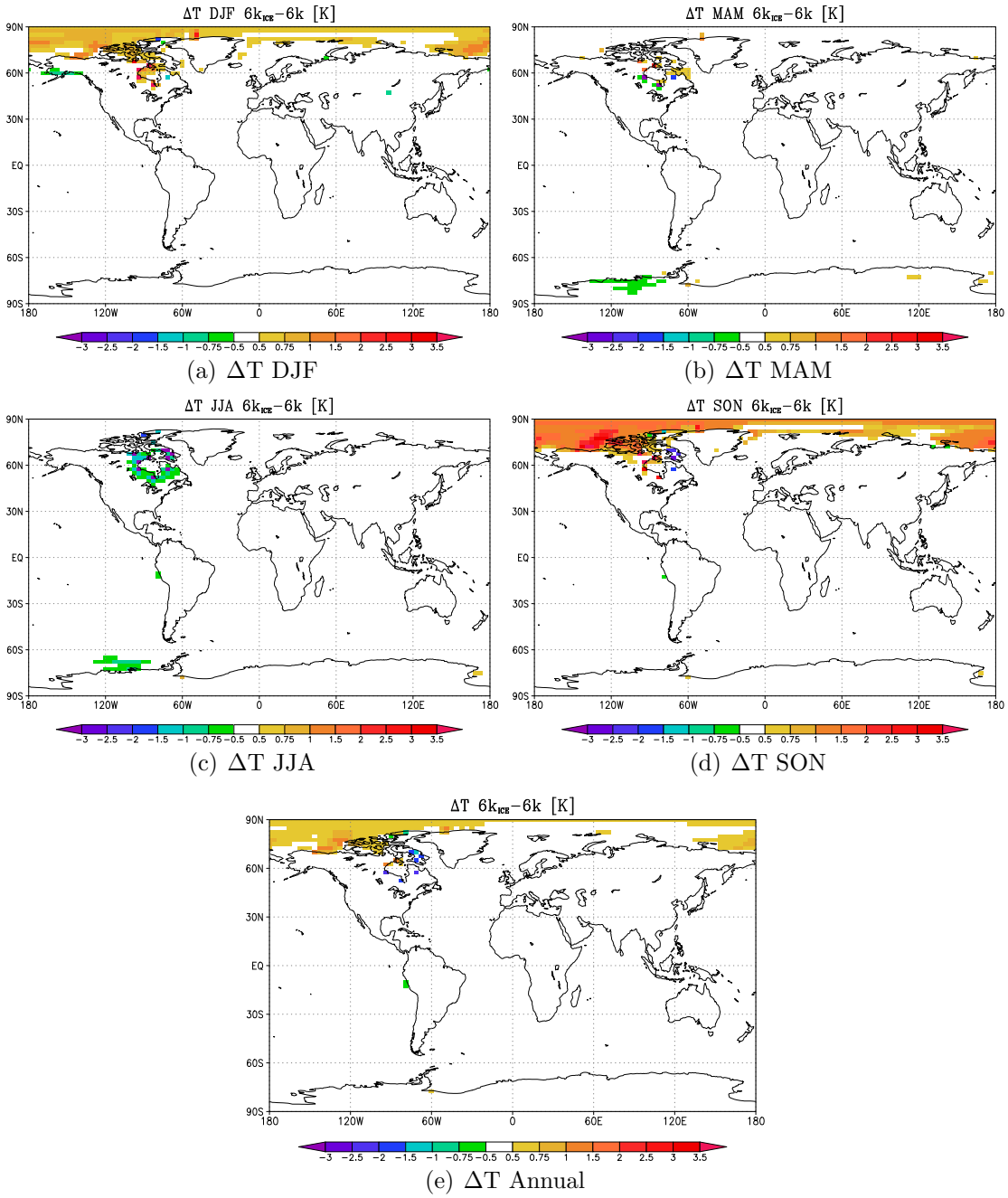

(a) ΔT DJF

(b) ΔT MAM

(c) ΔT JJA

(d) ΔT SON

(e) ΔT Annual

Figure 6.5: The ensemble mean seasonal and annual temperature differences between the 6kyBP model with ice and new LSM and the 6kyBP model without.

Figure 6.6 shows the ensemble mean temperature differences between the (6kice-control)–(6k-control) anomalies, i.e. the difference in the temperature anomalies from the two ensembles over Eastern North America. The direct effect of the eleven grid boxes with ice is a localised cooling of the surface air temperatures above the ice,

with the largest changes in the boreal summer and autumn.

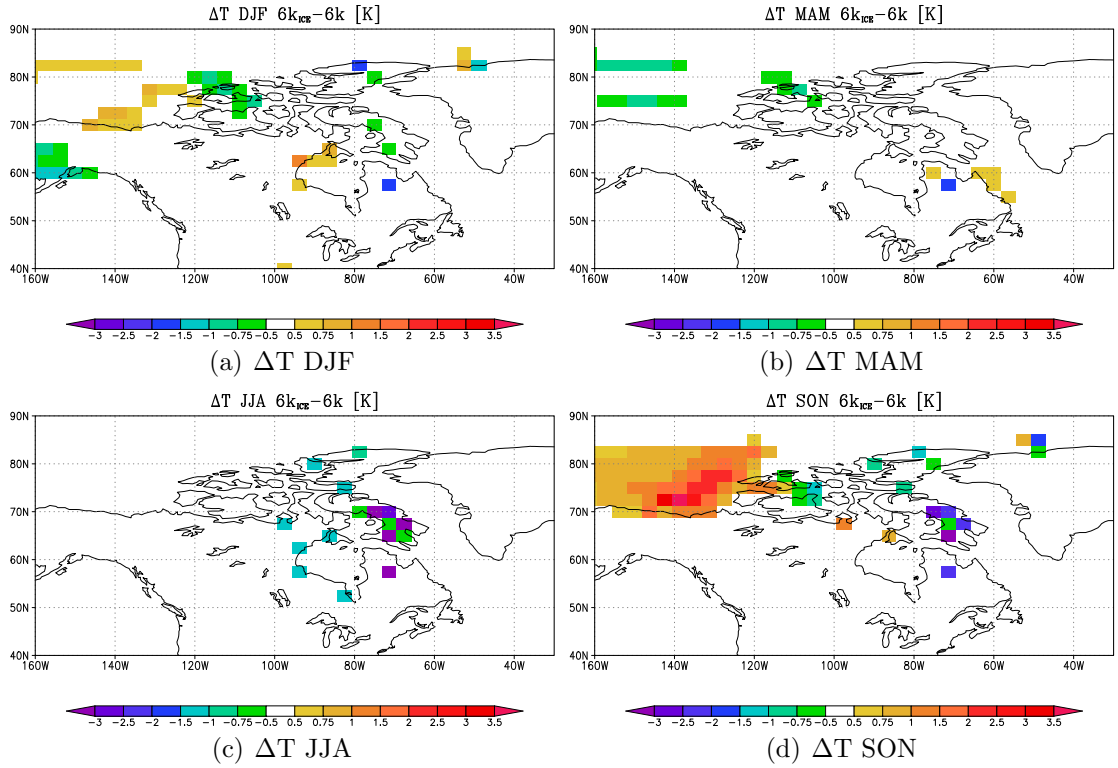

(a) ΔT DJF (b) ΔT MAM

(c) ΔT JJA (d) ΔT SON

Figure 6.6: The seasonal temperature differences between the 6k–control anomalies from the two ensembles; (6kice-control) minus (6k-control).

Focusing further on the regional differences in the simulations between the 6kyBP ensemble with ice and the 6kyBP ensemble without (**Figure 6.7**), it is seen that that the annual changes in mean sea level pressure (MSLP) are minimal, though there is a slight heightening of the pressure regionally of up to 0.3mb. This is mainly directly above the grid boxes with changes, where the air above is cooled by the new surface cover, encouraging sinking of the air and hence an increase in the pressure. The annual pattern is dominated by the changes seen in JJA, where there is an increase of 1.5mb in ENA (not shown). This is slightly offset by a lowering of the DJF pressure (not shown). The surface temperatures are cooler in JJA in the whole region, and warmer in the winter due to the expanded sea mask in DJF, with only a cooling over three of the grid boxes with added ice. Looking at the annual ΔP–E differences

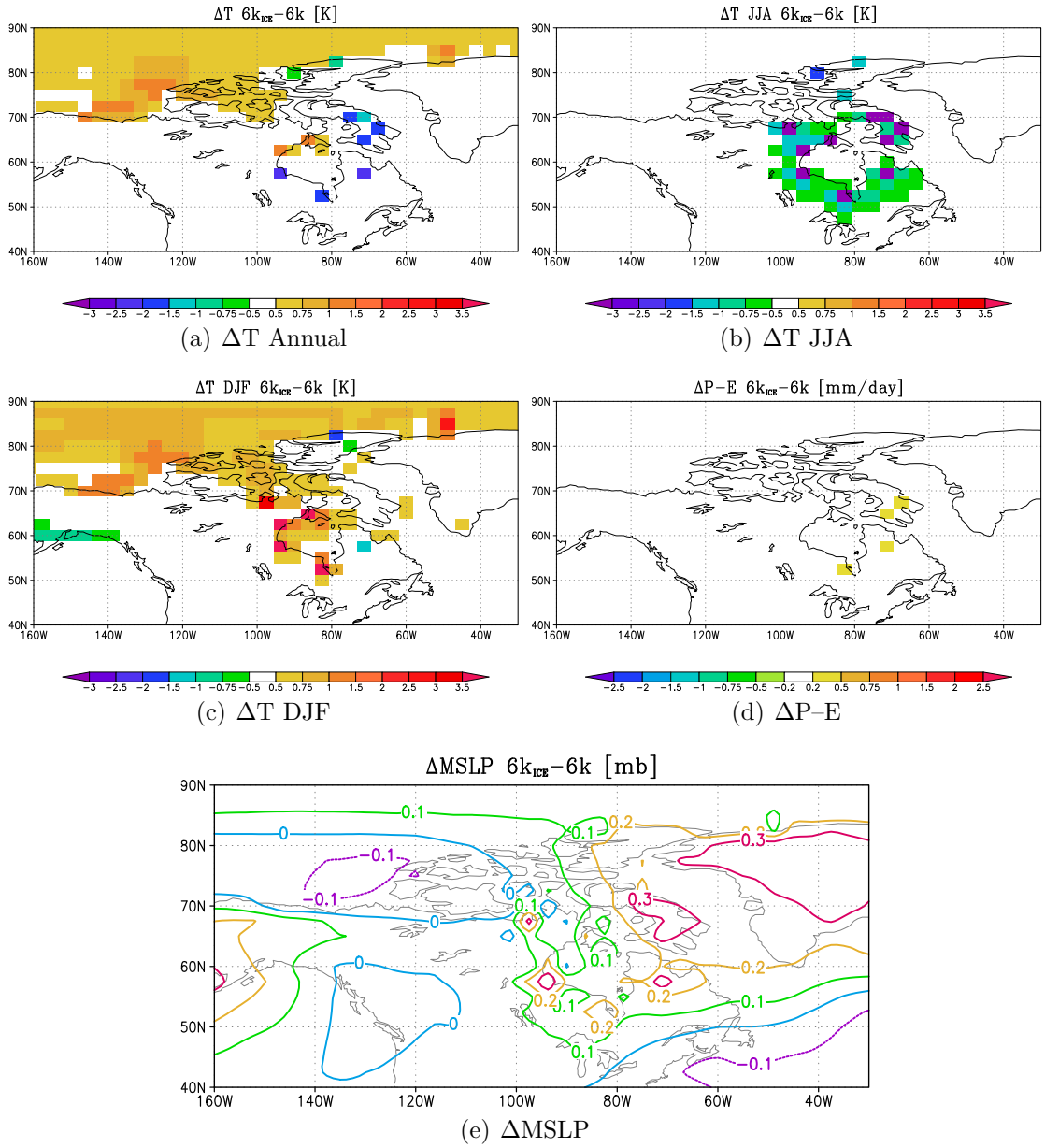

(a) ΔT Annual (b) ΔT JJA

(c) ΔT DJF (d) ΔP–E

(e) ΔMSLP

Figure 6.7: The annual mean, JJA and DJF temperature differences between the 6kyBP ensemble with ice and the 6kyBP ensemble without extra land ice. The annual mean ΔP–E and and surface pressure differences are also shown.

between the two ensembles, there are hardly any differences (**Figure 6.7(d)**); there are only four grid boxes where the 6kyBP ensemble with ice has a positive anomaly.

The observations after Webb et al. (1993) show a decrease in annual mean precipitation of 10–30% in Labrador and Québec at 6kyBP, whilst the ensemble with ice simulate a decrease of 10–20% (**Figure 6.8**). The ensemble simulates the right mag-

nitude of change over the ice sheet in Québec of -10 – -20%. The observations show an increase in the precipitation on the Coastal Plain, as does the ensemble. The ensembles overestimates the area with the positive anomaly, however. Both ensembles (with and without ice sheet and LSM changes) simulate the positive anomaly to stretch inland past the Appalachian Mountains. The resulting precipitation anomalies are similar in both ensembles and the impact of the inclusion of the ice sheet is evident (**Figure 6.8**). The inclusion of the Laurentide ice sheet has a localised effect of reducing the annual mean precipitation, improving the model response compared to the observations.

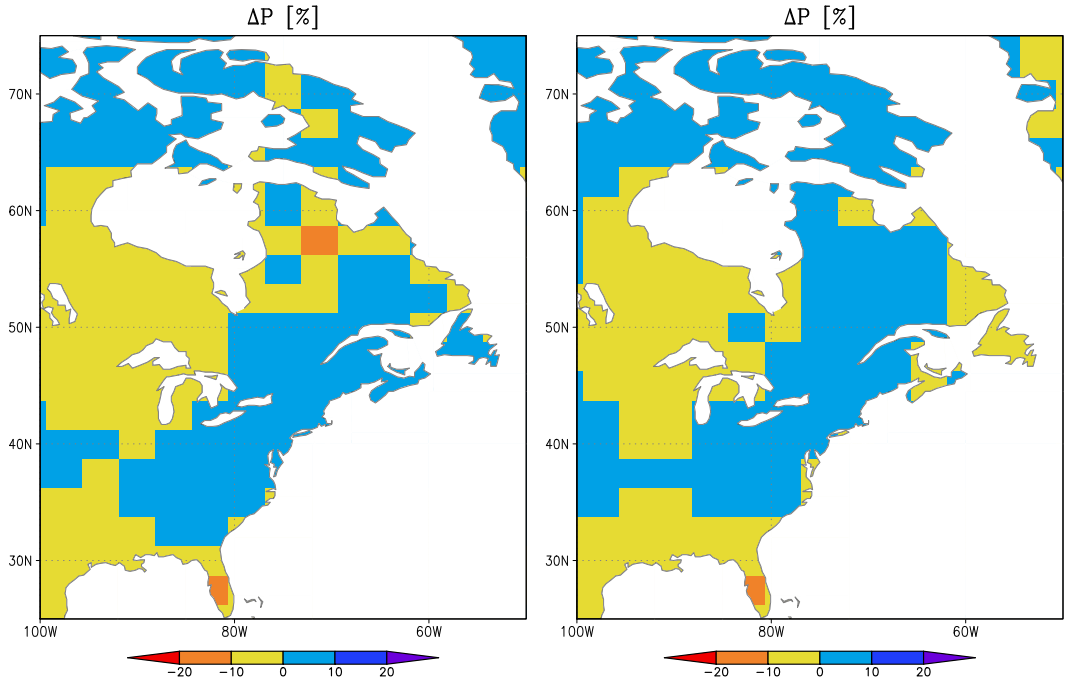

(a) ΔP 6kice–ctrl (b) ΔP 6k–ctrl

Figure 6.8: The ensemble annual mean percentage precipitation differences between the mid-Holocene and control models in (a) the ensemble with the new LSM and ice sheet, (b) the ensemble with standard PMIP boundary conditions in the 6kyBP model. The colour scale is as in Figure 4.14 by Webb et al. (1993).

6.2.1 ENA Growing Degree Days

Growing-degree-days is a bioclimatic variable and an expression for the heat requirement for plant growth. Plants grow in a cumulative stepwise manner and they are dependant on the local climate, in particular temperature. GDD accumulations involve the accumulated amount of heat required for a plant of to flourish. GDD accumulates faster as the days get hotter. GDD is a heat unit and it is calculated by taking the average of the daily maximum and minimum temperatures compared to a base temperature, i.e. $\bar{T}$–T_{base}. The baseline temperature is determined by the lifecycle of the plant of interest. Maximum temperature is usually capped at 30°C as temperatures higher than this does not make the plants grow any faster. The threshold for trees is of 5°C and for non–woody plants it is of 0°C (Wohlfahrt et al., 2008). Every degree the mean temperature is higher than the baseline temperature turns into a growing degree day.

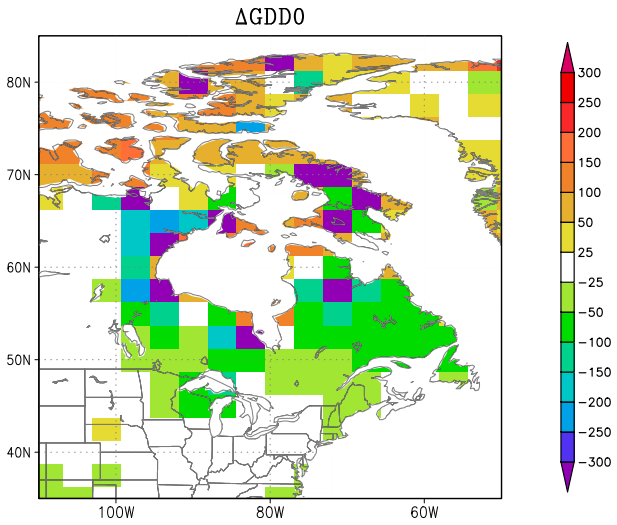

Figure 6.9: The ensemble mean GDD0 (i.e. using 0°C as baseline temperature) anomaly from the ice sheet experiment compared to the ensemble of standard 6kyBP models. Growing degree days are a measure of both temperature and length of the growing season and represents a limit on plant growth.

The PAIN and BIOME 6000 observations suggest that tundra existed further south than presently in eastern Canada, indicating a local reduction in the growing–degree–

days. The northwards expansion of temperate forest seen elsewhere during the mid-Holocene was most likely inhibited in ENA by the Laurentide ice sheet. The northwards shift in the tree–line seen at 6kyBP in e.g. northern Eurasia is a result of the increase in the summer temperatures, a direct effect of the changes in the orbital parameters, and the length of the summer season, an indirect effect due to the ocean feedbacks. The simulated GDD is much higher in the 6kyBP simulations compared to the control. A local reduction in GDD0 and GDD5 is seen in ENA in the ensemble including the ice sheet. **Figure 6.9** shows the ensemble mean difference in growing degree days with a temperature base line of 0°C between the 6kyBP simulations with ice and the 6kyBP simulation with the standard boundary conditions.

The results have not been run through BIOME4, but one might speculate that this localised reduction in growing degree days would have placed a limitation on the plant growth. By knowing the mean temperature and rainfall of a region, especially with information on the seasonality and variability, the plant types, and animal for that matter, can be fairly accurately predicted (biogeography). A reduction in 6kyBP cool evergreen needle-leaf forest and cool mixed forest would be the result of a reduction in GDD, as the conditions become more favourable for cooler vegetation types like tundra. Between 50–60°N, there is a reduction in GDD0 by 50-100 °C–days. The tundra climate is characterised by cold winter, short summers and growing seasons of <60 days, in addition to low rainfall rates (200mm/year), though with melting snow in the summer (Burroughs, 1999). The taiga vegetation requires about 300-850mm/year in precipitation and sustains cold winters and relatively warm summers. The reduction in the 6kyBP precipitation, summer temperatures and growing season in ENA in the model experiment with ice, all facilitate for a southwards shift in the tundra – taiga border.

6.3 Summary and concluding remarks

The effect on the climate of changing the orbital parameters, expanding the Hudson Bay and including the 6kyBP Laurentide ice sheet has been investigated with a perturbed physics ensemble using an atmospheric GCM coupled to a mixed layer ocean. It is seen that incorporating these new boundary conditions results in a closer agreement with the paleo-data locally in eastern North America, with little or no change elsewhere. There is an annual reduction in precipitation and growing–degree–days, fitting Webb et al. (1993) and the pollen data from the PAIN and BIOME 6000 (Prentice et al., 2000; Harrison et al., 2001; Bigelow et al., 2003; Pickett et al., 2004) better. Modelling groups investigating the 6kyBP North American vegetation distribution should therefore in the future incorporate these new boundary conditions.

The increase in the summer insolation and the warmer September SSTs extends the mid-Holocene growing season. The PMIP models, via offline vegetation modelling with BIOME4, have been found to underestimate the local extent of tundra in ENA (Wohlfahrt et al., 2008). I.e. the local ENA 6kyBP cooler and drier climate has not been captured by the GCMs due to shortcomings in the boundary condition designs. This has been improved with this ensemble experiment. The inclusion of the more accurate paleo–boundary conditions results in a closer match to the geological evidence. A further extension of this analysis would be to run the ensemble results through the vegetation model BIOME4 after Kaplan (2001) and do a ENA biome count to compare with the PAIN and BIOME 6000 pollen data. The localised reduction in growing – degree – days and precipitation should contribute to a more accurate vegetation cover with an expansion of tundra compared to presently and a contraction of cool mixed fore and and evergreen needle forest, i.e. a southwards displacement of the tree–line.

Chapter 7

Perturbing the North African vegetation

7.1 Introduction

As seen in **Chapter 5** the models grossly underestimate the northwards expansion of the 6kyBP North African Monsoon. Orbital forcing alone is not sufficient to explain the changes in the 6kyBP monsoons. Feedbacks, associated with e.g. SSTs and vegetation cover, may need to be included in order to explain the observed northwards expansion. A step towards a better understanding of the respective roles of oceans and land surfaces is to design sensitivity studies with prescribed forcings. To see if the model can be forced out of the North African dry regime, the vegetation ancillary file is altered. North Africa is set to be covered in rain forest, which is an unrealistic assumption, because there is no evidence of any rain forest in the region during the mid-Holocene. Sahara was covered in Sahelian vegetation of grassland and xerophytic woods and shrubs at 6kyBP. But to tease out a larger signal from

the model, the vegetation is more drastically changed to that of the Amazonian rain forest. This experiment is therefore a sensitivity test rather than a realistic assessment of past conditions. The changes made to the vegetation ancillary file can be seen in **Appendix D**. This simple experiment was designed after the results from the distributed experiment was returned and analysed. The ensemble method was not used for this project and only a single model run was performed in-house. It is a sensitivity experiment, hence the simple design.

Various model experiments have indicated that the monsoons are sensitive to changes in the land surface, e.g. vegetation (Kutzbach et al., 1996; Street-Perrott et al., 1990; Claussen, 1997; Texier et al., 1997), lakes and wetlands (Coe and Bonan, 1997; Broström et al., 1998). The PMIP 2 coupled ocean – atmosphere – vegetation simulations allowed the African monsoon to penetrate further north (Braconnot et al., 2007a).

The monsoon is driven by the land–sea temperature contrasts. The onshore winds are advected from the colder oceans onto the warmer continents, i.e. the pressure gradient drives it through the high pressure over the ocean and low pressure over land. The main source of water vapour for the African monsoon is the tropical Atlantic and Gulf of Guinea (Cadet and Houston, 1984).

Vegetation has the potential to affect climate through the albedo effect. Tropical rain forest has an albedo of 13%, grassland 20%, whilst desert has an albedo as high as 40% (Huber et al., 2001). Vegetation can also alter the transfer of heat, momentum, and moisture between the surface and the atmosphere and thus affect the atmospheric circulation. (Claussen, 1994) show that for semi-arid Africa, if the

region was initially vegetated, there continued to be enough precipitation to support the vegetation, through local water recycling. If the region was initially unvegetated, the precipitation continued to be weak and vegetation was not able to grow. Thus the vegetation distribution has the potential to affect climate.

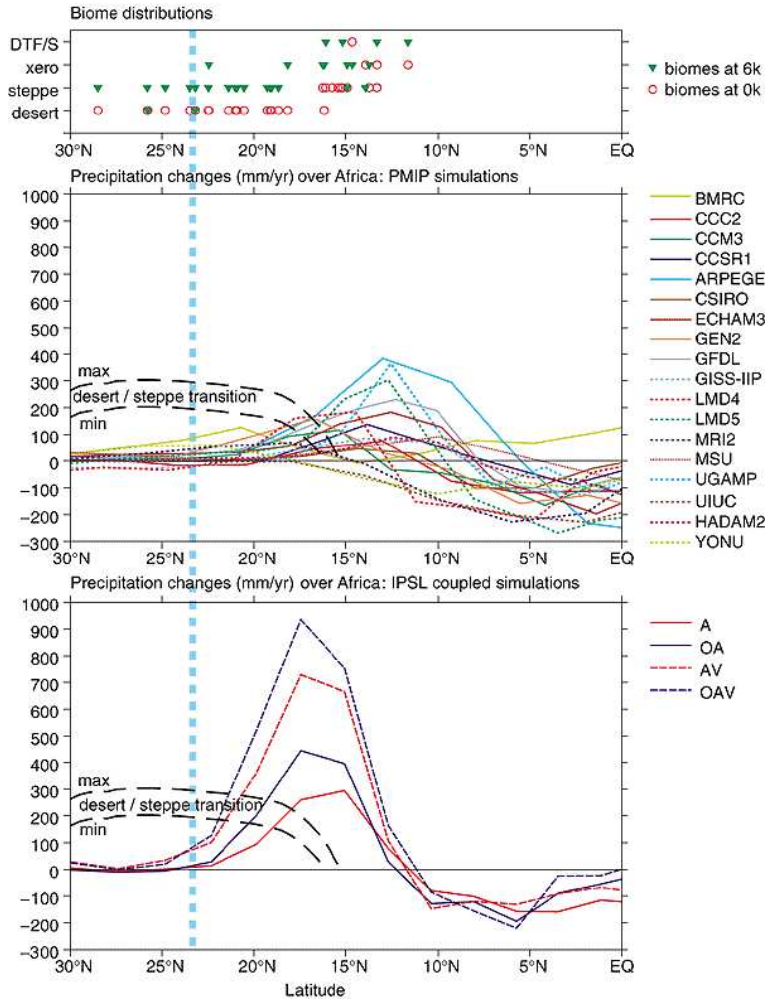

Figure 7.1: The zonally averaged annual mean precipitation anomaly from each of the PMIP ensemble members (middle panel) (Covey et al., 2001). The bottom panel shows the results from simulations with the IPSL model, coupling the atmospheric component to the ocean (OA), to dynamic vegetation (AV) and a combination of the two (OAV). The dashed lines indicate the excess precipitation needed to favor steppe over desert. The top panel is the 6kyBP and 0kyBP biome distribution of 4 biomes.

Figure 7.1 shows the zonally averaged 6kyBP annual mean precipitation anomaly across northern Africa from the PMIP 1 ensemble from Covey et al. (2001). It is seen that all ensemble members underestimate the northwards expansion of the monsoonal rain at 6kyBP. Some of the models simulate the right magnitude of 200–300mm/year, though as in the ensemble results presented in **Chapter 5**, the max precipitation peak is too far south. This deficiency in the models encouraged this sensitivity experiment.

7.2 Experimental set–up

The simulations were carried out using the HadSM3 keeping the vegetation fixed. One control pre-industrial simulation was performed, in addition to one standard 6kyBP simulation where the only changes to the model is the orbital configuration and reduced methane concentrations. In a third simulation, the 6kyBP model now contains a new vegetational forcing, i.e. the vegetation parameters were set to represent rain forest across northern Africa and the Middle East. The standard HadSM3 parameter values were used for the experiment. Orbital parameters for the control and all 6kyBP simulations follow the PMIP convention as described in **Chapter 3** and Joussaume and Taylor (1995). Differences between the standard 6kyBP and 6kyBP with perturbed vegetation simulations quantify the sensitivity of the simulated mid-Holocene climate to changes in the vegetation.

This experiment is a stand-alone experiment and was not included in the CPDN ensemble. The models were run in–house on a single processor computer as a complimentary sensitivity test of the model after the revelation of the model–observational mismatch in this region in the CPDN ensemble.

7.3 Results from perturbing the vegetation

The ECMWF (European Centre for Medium Range Weather Forecasts) reanalysis data set, the ERA-40 Atlas, is used to check the climate of the control simulation used in this experiment. The ERA-40 data is of a 2.5° grid resolution and the observations cover the period of 1979–2001. The ERA-40 annual mean total precipitation [mm/day] is shown in **Figure 7.2**, whilst the results from the control run is mapped in **Figure 7.3**. It is seen that the HadSM3 control model simulates the main features of the global precipitation patterns rather well, including the placement of the ITCZ and the storm tracks. The precipitation pattern across Africa is also in close agreement with the reanalysis data. Between ∼17–30°N the model overestimates the rainfall by 0.2–1mm/day in parts of northern Africa. The magnitude of the rainfall across the main convective equatorial cell is correctly simulated of 6–8mm/day. Based on the model's ability to simulate modern rainfall, keeping in mind that the simulation is pre-industrial and the reanalysis data present day observations, it can be used for this analysis.

The zonally averaged anomaly in the moisture budget is seen in **Figure 7.4** covering Northern Africa and the Middle East between the model forced with the 6kyBP orbital configuration and North African vegetation changes and the default pre-industrial control simulation (blue line). The pink curve represents the default 6kyBP–control ΔP–E in comparison. At 20°N ΔP–E is more than doubled in the run with North Africa covered in rain forest; 56mm/year, compared to 22mm/year in the default mid-Holocene model.

Figure 7.5 shows the zonally averaged differences in precipitation and evaporation

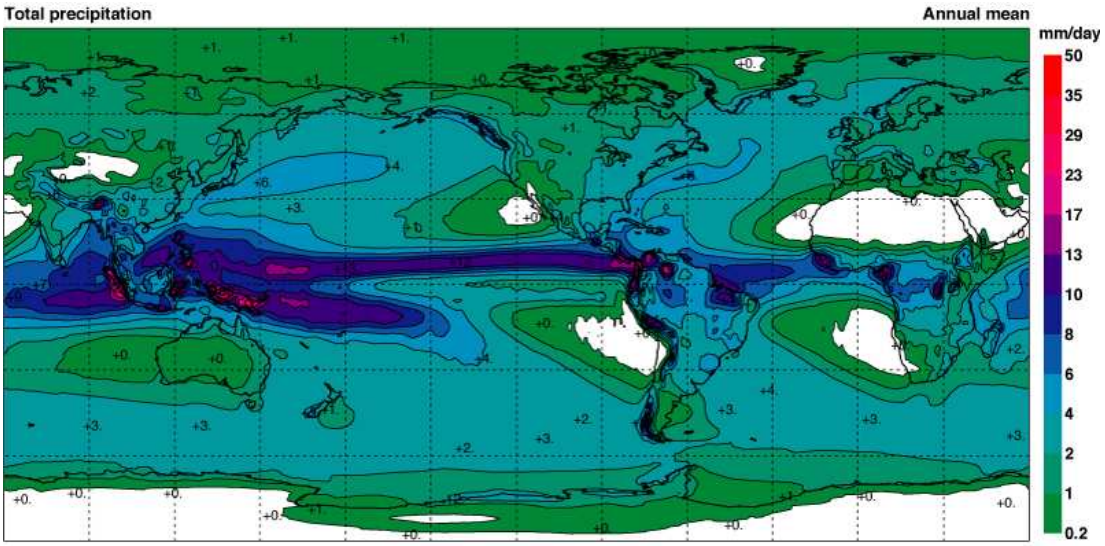

Figure 7.2: The annual mean total precipitation [mm/day] from the ERA-40 Atlas, using reanalysis data from the period 1979 – 2001.

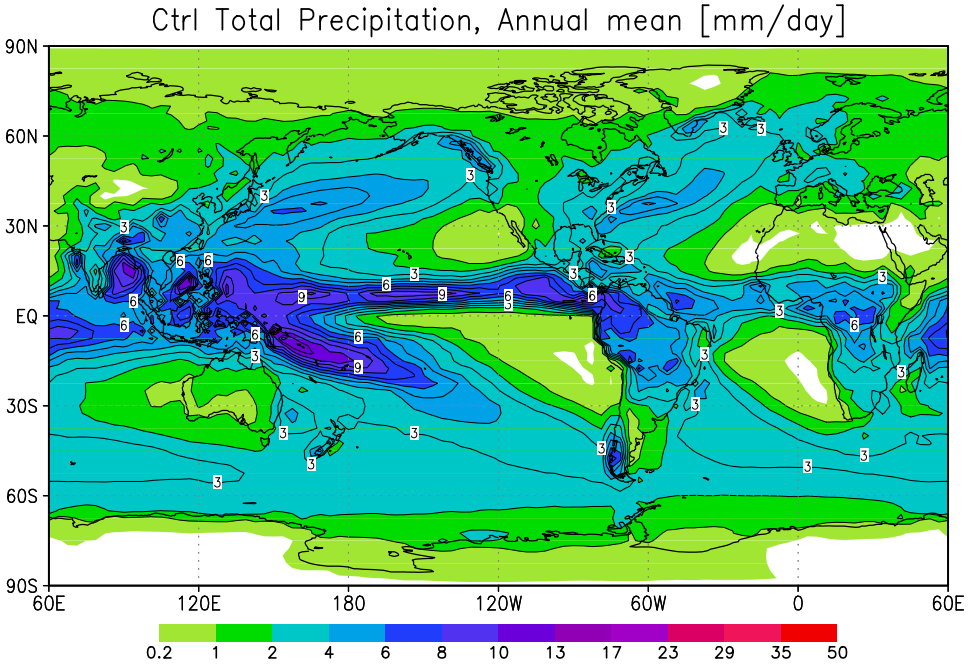

Figure 7.3: The annual mean precipitation rate [mm/day] from the control simulation. The modelled precipitation is in close agreement with the reanalysis data.

rates [mm/year]. The blue and red curves represent the annual precipitation rate and evaporation difference respectively between the 6kyBP model with the Saharan rain

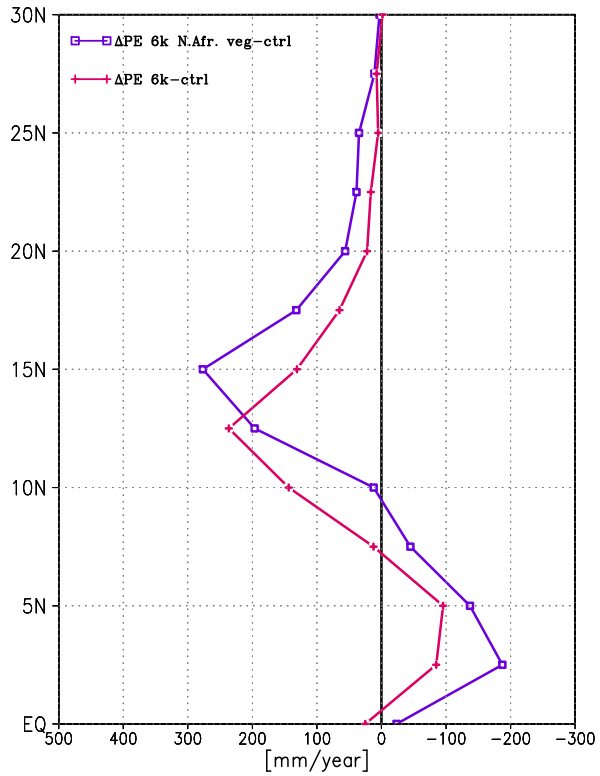

Figure 7.4: The precipitation – evaporation anomaly between the default 6kyBP and control runs (pink line) and a 6kyBP model with rain forest covering North Africa and the control run (blue curve).

forest. The light blue and orange curves represent the same variables for the standard 6kyBP and control models. The maximum peaks are shifted northwards by a couple of gridboxes and increased by over 400mm/year. The evaporation rate is also increased in the perturbed vegetation run by about the same rates as the precipitation. Joussaume et al. (1999) estimated that an increase of 200–300mm/year in 6kyBP precipitation is needed to explain the observed changes in the North African pollen tax between ∼17–30°N. The model with the perturbed vegetation simulates this excess between ∼11–25°N but even these drastic vegetation changes are not enough to cause precipitation increase northwards of this. Comparatively, the standard 6kyBP model simulates an increase of above 200mm/year between 12–17°N.

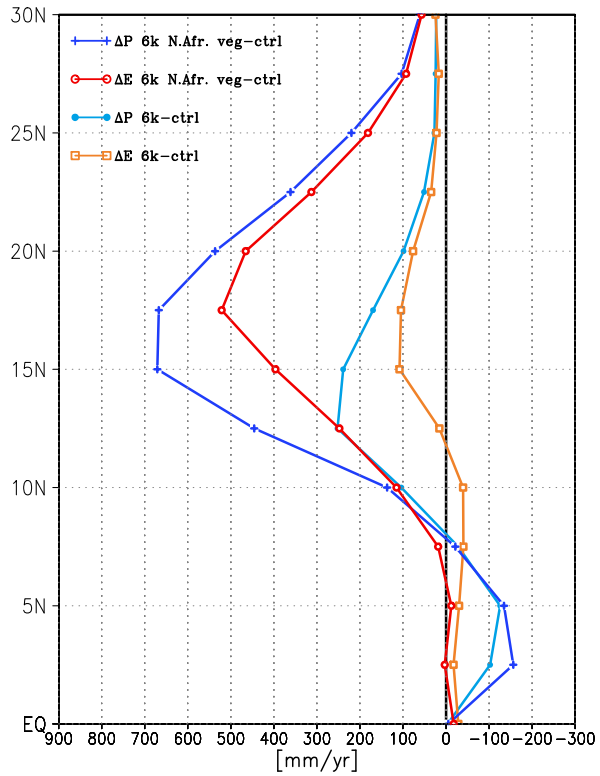

Figure 7.5: The precipitation and evaporation differences between the default 6kyBP and control runs (light blue and orange curves respectively) and a 6kyBP model with rain forest covering North African and the control run (blue and red curves).

The JJA moisture budget anomaly across the region in question is mapped out in **Figure 7.6**. (a) shows the anomaly involving the 6kyBP model with perturbed vegetation, whilst (b) is from the default 6kyBP model minus the control. Positive water budget anomalies cover a larger area in the perturbed vegetation – control, extending up to 25°N in western parts. The maximum peak is shifted and extended northwards.

Figure 7.7 shows the JJA mean temperature differences between the 6kyBP model with North African rain forest and the control model (a) and between the 6kyBP and the control model (b). As expected due to the orbital forcing, the continents warm

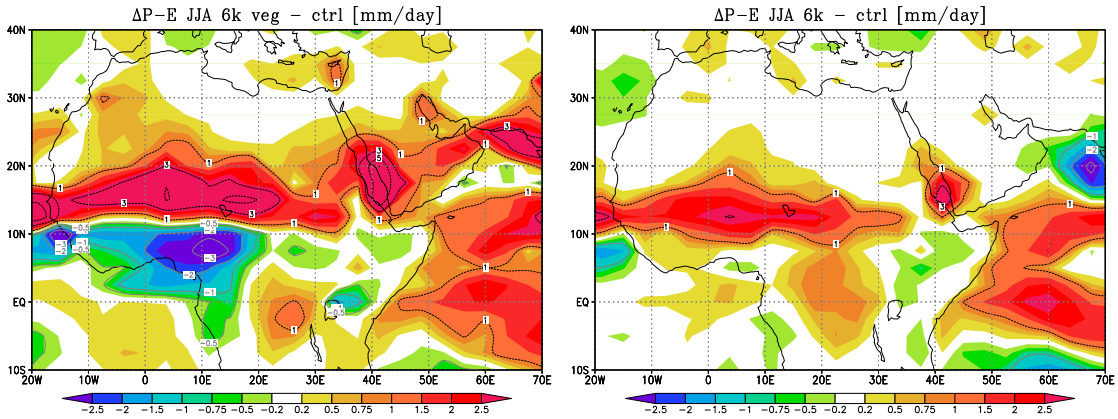

(a) ΔP–E 6k N. Afr. veg. (b) ΔP–E 6k

Figure 7.6: (a) The JJA mean water budget anomaly between the 6kyBP model with North African rain forest and the control model. (b) between the 6kyBP and the control model.

up during boreal summer in the mid-Holocene models compared to the control. The vegetation changes act as a positive feedback and amplify this warming, as seen in (a). The reduction in the surface albedo results in more radiation being absorbed and heating the atmosphere above it rather than being reflected by the ground.

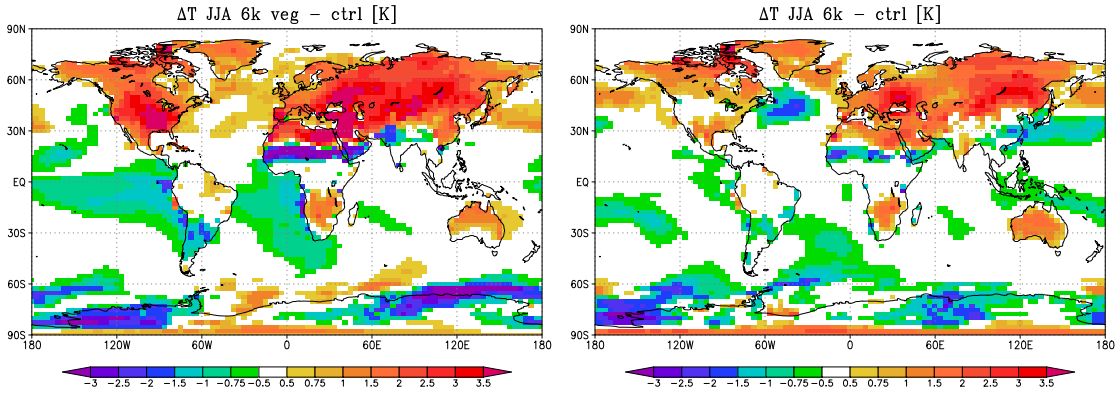

(a) ΔT 6k N. Afr. veg. (b) ΔT 6k

Figure 7.7: (a) The JJA mean temperature difference between the 6kyBP model with North African rain forest and the control model, (b) between the 6kyBP and the control model.

The global patterns of precipitation change are similar in both 6kyBP runs, only am-

plified in the perturbed vegetation simulation (**Figure 7.8**). The ITCZ is enhanced across the tropics.

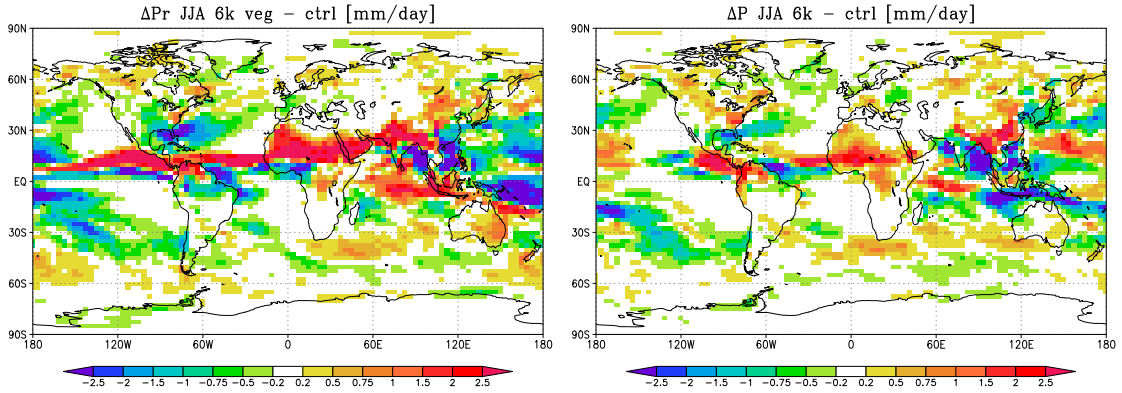

(a) ΔP 6k N. Afr. veg. (b) ΔP 6k

Figure 7.8: (a) The JJA mean precipitation rate difference between the 6kyBP model with North African rain forest and the control model. (b) The difference between the 6kyBP and the control model [mm/day].

The continental lows are deepened in both mid-Holocene simulations, strengthening the monsoon inflow (**Figure 7.9**). The pressure is heightened over the Pacific, elsewhere in the NH, the pressure is lowered in the perturbed vegetation model.

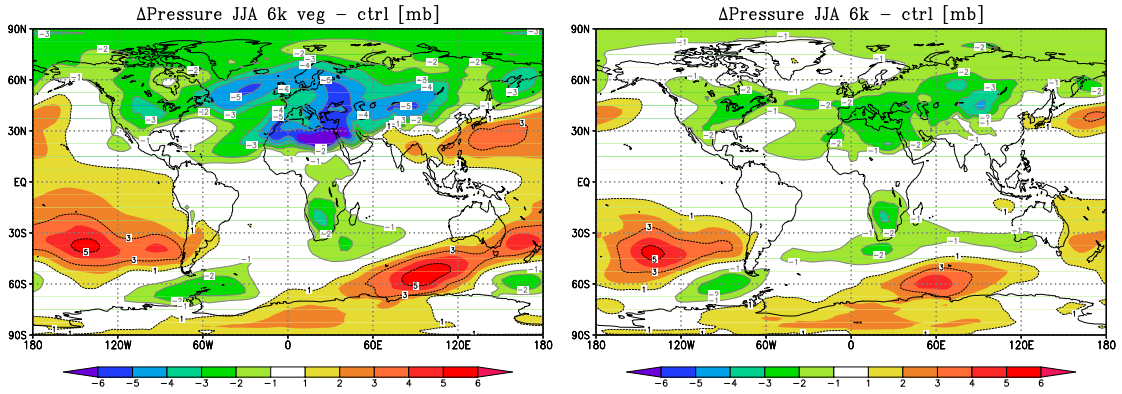

(a) ΔMSLP 6k N. Afr. veg. (b) ΔMSLP 6k

Figure 7.9: (a) The JJA mean surface pressure difference between the 6kyBP model with North African rain forest and the control model. (b) The difference between the 6kyBP and the control model [mb].

The difference in OLR (Outgoing Long wave Radiation at the top of the atmosphere) [Wm^{-2}], the difference in latent heat flux [Wm^{-2}] and total cloud amount in the long wave radiation scheme between the 6kyBP model with the Saharan rain forest and the control run is shown in **Figure 7.10**. The outgoing long wave radiation is strongly reduced in the region with the increase in cloud amount where the monsoons are expanded. The same signal of change is seen in **Figure 7.11**, showing the anomalies from the standard 6kyBP and control models.

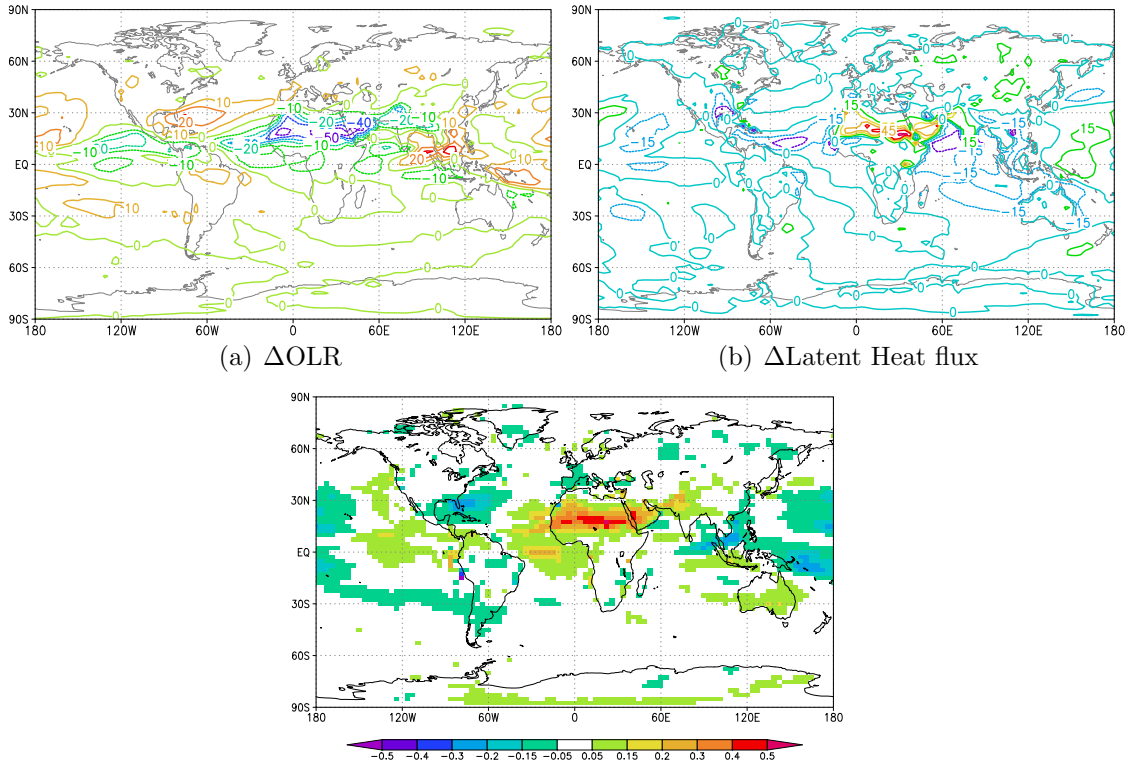

(a) ΔOLR (b) ΔLatent Heat flux

(c) ΔCloud amount

Figure 7.10: (a) The difference in Outgoing Long wave Radiation (OLR) [Wm^{-2}], (b) surface latent heat flux [Wm^{-2}], (c) total cloud amount in the long wave radiation scheme [0-1] between the 6kyBP perturbed vegetation model and the control. As for **Figure 7.11**, the contour interval in (a) is 10Wm^{-2}, (b) 15Wm^{-2} and (c) 0.05.

The Tropical Easterly Jet (TEJ) is strengthened in the 6kyBP model (**Figure 7.12**). The TEJ is related to the summer monsoons in Asia and Africa and usually lasts

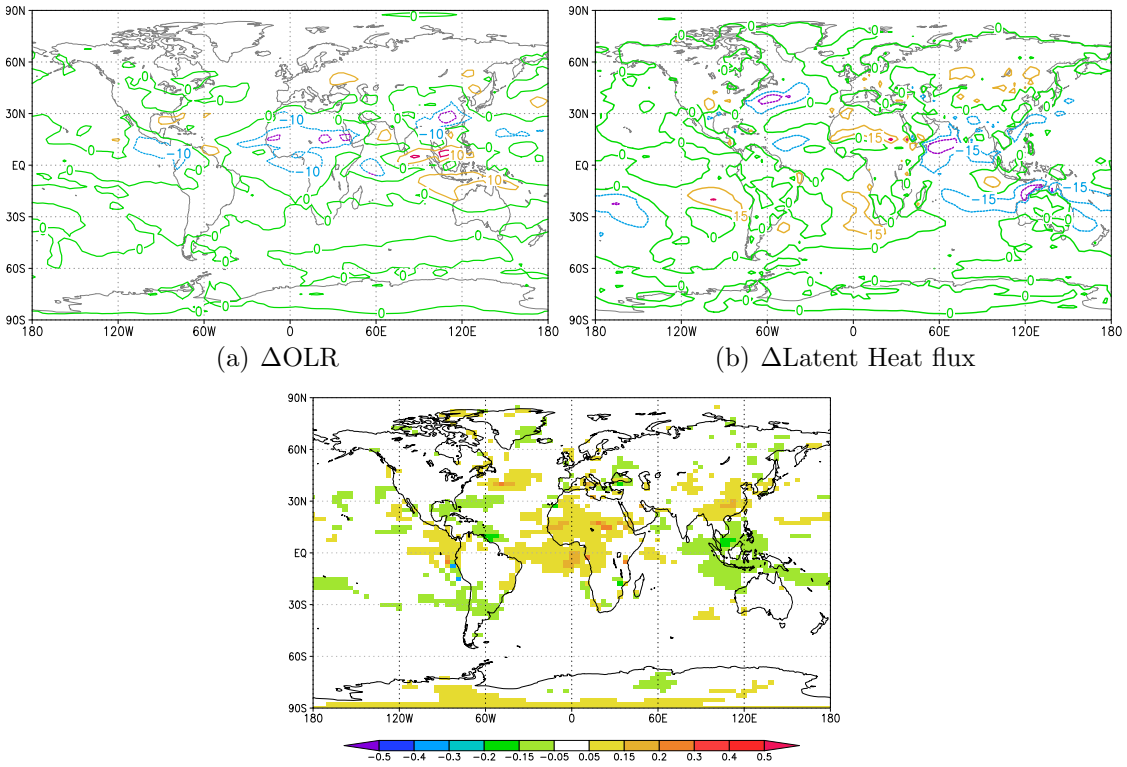

(a) ΔOLR (b) ΔLatent Heat flux

(c) ΔCloud amount

Figure 7.11: (a) The standard 6kyBP anomalies in Outgoing Long wave Radiation (OLR) [Wm^{-2}], (b) surface latent heat flux [Wm^{-2}], (c) total cloud amount in the long wave radiation scheme [0-1].

from June to September. It's source is the Tibetan Plateau and it is accelerated by the continental heating during summer (Raghavan, 1973). A strong jet is associated with higher precipitation. A weakening of the African Easterly Jet (AEJ) centered on ∼650mb and 13°N is seen in **Figure 7.12(a)**. Patricola and Cook (2007) argue that the increased 6kyBP wetness observed in proxy data over North Africa, could partly be due to a collapse or weakening of the African Easterly Jet during the mid-Holocene. The AEJ is currently present due to the contrast in the land surface between the Sahel and Sahara resulting in a strong meridional surface temperature gradient (Cook, 1998). There is an increase in the easterly winds just northwards of the weakening at 15°N, suggesting a possible northwards and upwards shift in the

AEJ, possibly merging with the TEJ at upper levels. These changes in the jets could be related to changes in the temperature structure in the atmosphere above northern Africa (see **Figure 7.14**) due to the increase in the latent heat release. The meridional temperature gradient is increased and the jet is strengthened.

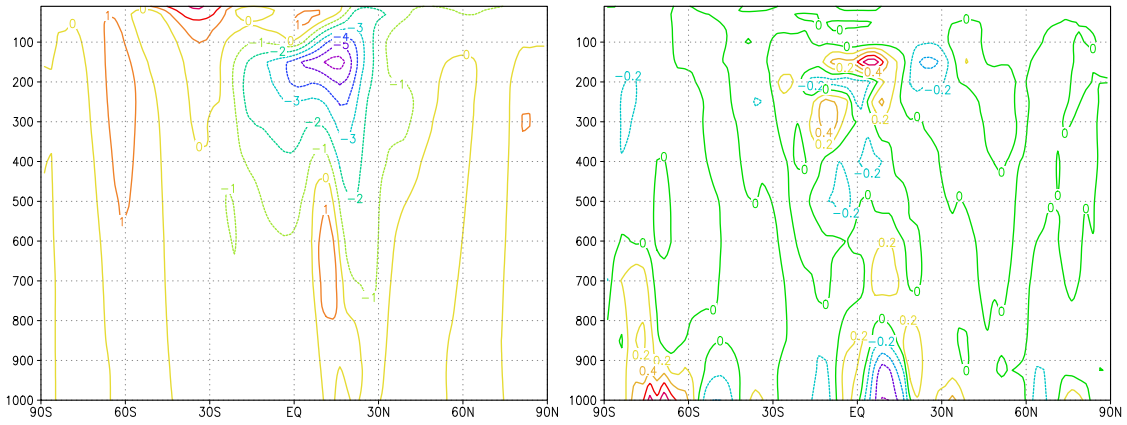

(a) Δu (b) Δv

Figure 7.12: The JJA differences in the zonal averages of the u and v- components of the wind [m/s] between the 6kyBP model with the perturbed vegetation and the control.

The JJA wind component anomalies in the default 6kyBP model compared to the control model is seen in **Figure 7.13**. The patterns are similar to the ones observed in **Figure 7.12** only the magnitudes are smaller. There is a weakening of the NH mid-latitudinal storm tracks in the standard 6kyBP model, not seen in the 6kyBP model with perturbed vegetation. The AEJ is reduced to a smaller region in the standard 6kyBP model run, as the vegetation is kept fixed at pre-industrial conditions. This possibly contributes to prevent the northwards expansion of the monsoon rain.

To sum up; the lower albedo of the rain forest compared to the desert increases the amount of radiation absorbed by the surface. The much larger roughness length of the rain forest increases the sensible and latent heat fluxes. The release of latent heat in the atmosphere amplifies the convection. The establishment of a thermal low over

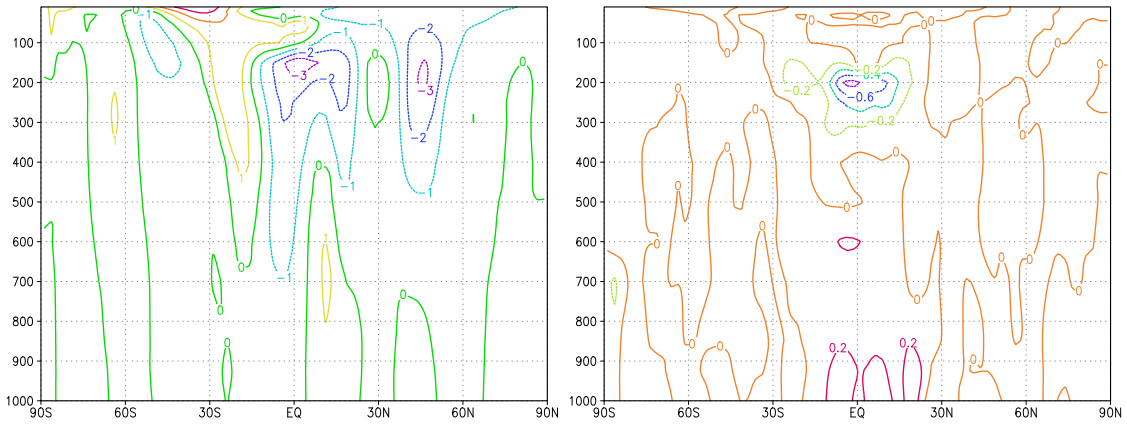

(a) Δu (b) Δv

Figure 7.13: The JJA differences in the u- and v- components of the wind [m/s] between the standard 6kyBP and control runs.

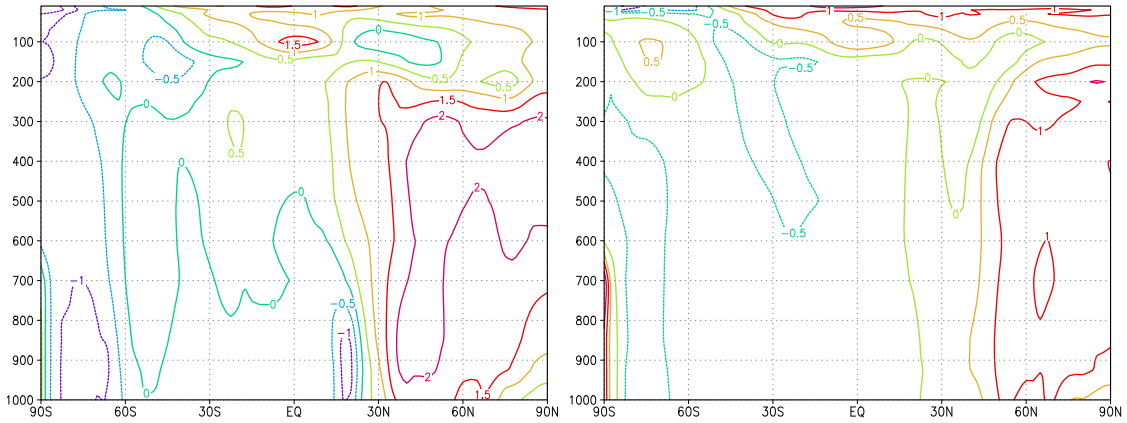

(a) ΔT 6k N. Afr. veg. (b) ΔT 6k

Figure 7.14: The JJA temperature anomalies, latitude versus height, from (a) the 6kyBP model with perturbed vegetation and (b) the standard 6kyBP model.

the continent is accompanied by a pressure and land – sea temperature gradient that is stronger than in the control and standard 6kyBP runs. The atmospheric feedbacks associated with the vegetation perturbation involves an increase in the downward infrared radiation due to the increased cloudiness as seen in **Figure 7.10** and an increase in the net solar heat flux at the surface due to the increase in the albedo. The large amount of rain simulated during the monsoon season is mainly sourced from local evapotranspiration.

The large change in the albedo affects the surface temperatures as more heat is absorbed by the ground. This is partly responsible for the northwards shift in the monsoon trough. This is also affected by the changes in the latent heat and sensible heat fluxes due to the much larger roughness length and decreased resistance to evapotranspiration.

The intensity of the monsoon might be stronger due to interactions between the low–level moisture advection and surface evapotranspiration and the deep convection. The latent heat release from condensation amplifies and sustains the low level convergence.

7.4 Discussion

Results have been presented from sensitivity experiments where the model has been forced with altered vegetation across Northern Africa and the Middle East. This is a single model experiment and the distributed computing approach, as seen in the two first experiments, was not used. The vegetation is kept fixed in the HadSM3 and as seen in **Chapter 5**, the orbital forcing alone is not enough to explain the northwards expansion of the 6kyBP North African monsoon as observed. The pre–industrial vegetation cover in the model was therefore changed to rain forest to investigate the sensitivity of the system to vegetation feedbacks. This increased the water recycling, i.e. both the precipitation and evaporation rates were intensified. The positive anomaly reached further north than in the model simulations performed with pre-industrial vegetation, though still not as far north as 30°N.

The 6kyBP simulation with the perturbed land surface simulates a 5° northwards migration of the ITCZ over Africa. Similar results were found by Broström et al. (1998) in a simulation afforesting the Sahel. The peak in the moisture budget has

been shifted further north compared to the standard 6kyBP simulations. Not only is there an increase in the maximum precipitation rate, but also a widening of the ITCZ belt. The albedo changes induce a warming of the surface temperatures throughout the year.

The water and energy budgets are both modified as a result of the vegetation property changes. Vegetation is more efficient at recycling precipitation through evapotranspiration. The larger latent heat release helps amplifying and sustaining the large scale convection and hence the onshore water vapour advection.

Broström et al. (1998) found in their sensitivity study that including changes in the land surface of increased lakes and wetlands resulted in a small signal comparative to the impact of vegetation changes. Changing the vegetation and the land surface increased the summer precipitation and extended it northwards in their study, but the full northwards expansion were not captured in their experiments with the CCM3 either.

To conclude, the vegetation–included albedo and moisture flux changes increase the simulated precipitation and the maximum peak is shifted northwards. The northwards extension in precipitation is still not northwards enough compared to the paleo–indications as seen in Hoelzmann et al. (1998). This could possibly be due to the subtropical high, the sinking part of the Hadley Cell, being situated too far south in the model. The GLSDB (Global Lake Status Data Base) indicate that southern Europe was drier during the mid-Holocene, possibly inferring this as the latitude of the subsiding part of the Hadley Cell at the time (**Figure 4.4**).

Chapter 8

Summary and General Discussion

Understanding the processes and mechanisms of past change can be aided by the use of climate models. Paleo-climate modelling is also key to understanding climate change and to test the models used for future predictions. The geological past offers a unique opportunity to examine climate sensitivity when the climate was different compared to the present, thus the signal-to-noise ratio is improved compared to the instrumental records (Edwards et al., 2008).

The use of climate reconstructions from paleo–observations can provide a constraint on the ability of a model to realistically simulate observed changes in paleo-climates. Even though the use of paleo-climate observations have not yet reduced the uncertainty in our estimates of the climate sensitivity, these studies have reinforced our understanding that climate sensitivity is affected by the type of forcing (Hansen et al., 1997; Joshi et al., 2003). The uncertainties in the past forcings are larger than the recent change in forcings. This could be a contributing factor to the failure of the paleo-studies in reducing the uncertainty in the climate sensitivity estimates. It could also reflect the non–optimal use of paleo–observations. Uncertainties also arise

from assuming that feedbacks contain the same behaviour in a $2\times[CO_2]$ climate as in present and past climates. Paleo-evidence may assist however in reducing uncertainties around climate sensitivity, for instance if more of the available data are used and if the model data are compared to spatially-located data instead of regional averages and if more paleo-reconstructions are created, as identified by Edwards et al. (2008).

Our knowledge of past climates is not complete. There are uncertainties in our understanding of how the atmosphere reacts to external forcing for today's boundary conditions and there are still significant advances to be made with numerical modelling. For the past, we only have imprecise and incomplete information about the boundary conditions. It is important to fully understand the uncertainties in the models caused by uncertainties in the forcings and also from within the model physics. "Whatever anthropogenic climate changes occur in the future, they will be superimposed on a background of natural variability. Therefore, to anticipate future changes, we must understand how and why climates varied in the past" (Bradley, 2006).

Two different methods have been used in this project to compare geological evidence of regional climates at 6kyBP with GCM simulations; map–map comparisons and regional averages. Site–by–site comparison methods have not been used due to the coarse resolution of climate models and it is a less effective measure of model skill. A more powerful tool is the visual examination of mapped climate patterns. This qualitative method makes it possible to evaluate the models' ability to simulate the observed shifts in regional climates and can be applied to data–poor regions. It makes it possible to investigate the underlying mechanisms for climatic change and deficiencies in the models. The visual assessment involves a subjectivity risk, however. A quantitative assessment of the model skill is found by comparing area averaged anoma-

lies to the paleo-observations, where such information is available. This method is sensitive to the delimitation of the area chosen to study and can lead to unrealistic poor assessment of the models.

Neither the model nor the data are good enough to do any better. In many cases we do not trust the paleo-data well enough to give a quantification of change and certainly do not trust a single record. This work work has highlighted the shortcomings of the models, even with the coarse gridding of the data.

The analysis presented here show a systematic model–data comparison approach providing a robust method yielding insight into the underlying mechanisms governing the modeled climates. This two–way method evaluating the six established 6kyBP climate patterns is valid for both perturbed physics ensembles and inter–model ensembles and could provide a standard tool for future paleodata–model comparisons.

8.1 Summary of findings

The larger tilt of the Earth at 6kyBP increase the summer and annual mean insolation in the high latitudes of both hemispheres. The additional change in the precession induces changes in the length of the seasons. The changes in the mid-Holocene simulations reflect the sensitivity of the climate system to changes in the seasonal cycle of insolation driven by these orbital changes. Consistently, there are no significant changes in the global annual mean insolation, and no major changes in the global annual mean temperature or precipitation rate at 6kyBP compared to present. The changes observed are an enhanced seasonal cycle in surface temperatures in the NH and a reduction in the SH.

The largest changes in the mid-Holocene climate results from the change in the seasonal contrast. The land–sea temperature contrast is increased in the 6kyBP simulations compared to the control, the pressure gradient is stronger and the inland penetration of moisture is increased. This results in strengthened monsoons and regions with high precipitation reaching further north in the Northern Hemisphere.

At low latitudes, the summer warming is limited due to the increases in cloud and soil moisture, opposing the pattern seen in mid–latitudes in the models. Various feedback mechanisms modify the local response to the changes in insolation at the TOA. In the Northern Hemisphere, the warming is the largest at high latitudes in the autumn and winter as a result of changes in sea ice.

The location of the change in 6kyBP precipitation in the models is mainly driven by the synoptic scale changes in moisture advection onto the continents. The specific location of the continental warming thus has an impact on the location of the increase in monsoonal precipitation, as it forces the structure of the summer continental thermal lows. The 6kyBP 5% increase in incoming solar radiation at the TOA, or $\sim$20Wm^{-2}, during JJA favours a deepening of the continental thermal lows pushing it further inland. The high summer insolation results in a strong land–sea thermal contrast enhancing the monsoon flows at 6kyBP.

The Asian and African Monsoon are dominant components of tropical climate variability. The latent heat release due to precipitation intensifies the surface low pressure systems and enhances the monsoon circulation. The intensity of the monsoon has been associated with the orographic effects of the Himalayas and the east African highlands, the Eurasian snow cover and ENSO (Kutzbach et al., 1989; Rodwell and

Hoskins, 1995; Dong and Valdes, 1998; Rasmusson and Carpenter, 1983; Yin et al., 2008).

It has been found in this work that the HadSM3 simulates a northwards expansion and increased intensity in the North African and North American monsoons. It underestimates the extent of the northwards expansion of the North African and North American monsoons. The magnitude of the peak in the precipitation increase is of the right order, however. The ensemble simulates an enhancement of the East Asian Monsoon, too, only it is shifted westwards. The geological record show an increase in moisture in the whole of southern China (Guiot et al., 2008). The westward shift in the Asian monsoon could be due to the model placing the west Pacific high pressure centre too far northwest.

Discrepancies between the simulated and observed regional precipitation across northern Africa were a motivation for running new simulations. A sensitivity study was performed where the vegetation ancillary file was modified. Instead of perturbing the surface conditions from modern desert sand to 6kyBP steppe and grassland, as the pollen data indicates, the vegetation was set to be rain forest across the whole of northern Africa and the Middle East. This was to test the relevance of the vegetation feedback in relation to the strength and northwards extension of the monsoon rain. This large and unrealistic vegetational forcing resulted in almost a trebling of the precipitation peak and the positive precipitation anomaly extends further north. The precipitation anomaly holds a value above the estimated 200-300mm/year as far north as 26°N, which is 9° further north than in the model with the pre-industrial vegetation cover. This experiment highlights the importance of vegetation feedbacks in the climate system, at least in these areas.

It seems that HadSM3 is competent at simulating dry climates, as seen in e.g. its treatment of the Eurasian moisture budget. It can be speculated however, that the model keeps dry climates dry and has difficulties in simulating other regimes in these regions. E.g., the models keep far northern Sahara dry even with strong forcing posed upon it. This could be a potential structural shortcoming in the model, emphasising the uncertainties with regards to simulating future unknown climates.

In the second distributed experiment, the local boundary conditions in eastern North America were perturbed in the mid-Holocene phase. All phases were run with an altered land–sea mask where the Hudson Bay was expanded by 5 grid cells. The mid-Holocene phase was forced with the usual change in the orbital configuration, reduced methane concentrations, in addition to the inclusion of the remnants of the Laurentide ice sheet. Eleven grid boxes had their surface properties changes to ice. These changes were based on results from ice sheet modelling by Dyke et al. (1997) and Peltier (2004) and the ancillary file was created by Dr. Tamsin Edwards and the Palaeo-QUMP team. The inclusion of these changes resulted in a change in the regional climate towards a closer agreement with the geological records, including a reduction in temperatures, precipitation and growing – degree days over Québec.

The first distributed experiment design with the PMIP boundary conditions is not a complete simulation for 6kyBP. In particular, the boundary conditions do not include land surface or SST changes. A step towards a more complete simulation was performed in the second distributed experiment.

This work has validated the Artificial Neural Network (ANN) developed by Sanderson et al. (2008). This was done by distributing the models with the parameter combi-

nations derived from the emulator and comparing the actual ensemble's sensitivity values to the predicted ones. It verified that the models produce a climate sensitivity close the the value predicted by the ANN, encouraging the development of this method. Neural networks could become an increasingly important tool in the climate sciences, compensating for the incredible computing power needs of perturbed physics GCM ensembles.

8.2 Climate*prediction*.net as a tool

Climate*prediction*.net serves well as a tool for exploring the climate sensitivity issue. It has the advantage of being able to investigate huge numbers of parameter perturbation combinations, especially in the HadSM3 experiments. The project has an impressive computing power and hopefully the research community can continue to benefit from this for a long time to come.

With respect to paleo-climate studies, ensemble experiments are less relevant. In particular the further back in time you go, when the uncertainties from the geological records become more extensive. It is of more importance to investigate basic climate dynamics in these experiments than the effect of atmospheric parameter perturbations and micro-physics. Climate*prediction*.net is a less attractive tool when interested in simulating past climates that need extensive changes to the distribution package, say where large changes to the boundary conditions are needed, e.g. changes to continents, topography, land ice, surface characteristics or land–sea–mask.

It is however an excellent tool when what you are interested in changing or perturbing is a constant/ parameter in the model distribution package. If it is merely a number

in a list, it can be easily done and large ensembles can be generated.

This specific project has involved both pure paleo-climate and climate sensitivity studies. The CPDN method has been a suitable tool as the mid-Holocene is such recent past that plentiful observations exist and we have a certain confidence in what the 6kyBP climate was like, also down to a regional level. The perturbed physics method has allowed us not only to explore sensitivity – 6kyBP observational relationships, but also to find parameter perturbation combinations that work particularly well when attempting to simulate this period.

8.2.1 Some challenges faced in this project

Changing the distribution package from three– to four phases turned out to be more difficult than expected. Partially because some of the relevant code was written many years ago, when the project was first initiated, by scientists who have now left the project. CPDN's IT specialist managed to sort this out successfully in the end and the four–phase distribution template is ready to be used for future projects.

Another issue arose when tackling the design of the second part of the experiment where more land ice was implemented and the sea mask expanded. For this experiment, separate start dump files had to be created for each of the four phases in the distribution. In order to create the new start dump file, describing the state of the world at the beginning of the model integration, a working installation of the model in-house was needed. The Department has during my three years there undergone major upgrades of the IT systems, in particular the last year. For the majority of my stay, we have unfortunately not had a working installation of the model, due to vari-

ous issues, including servers breaking etc. This made the file creation for my CPDN experiment rather more troublesome. Thanks to patience from the CPDN team, and finally an installation of the Unified Model thanks to Milo Thurston, we managed to reach our goals and execute the ensemble successfully.

The time when the model was not up and running in-house, provided at least an opportunity to explore the available paleo-data more thoroughly and time was spent trying to understand what work and just how much work goes into the derivation of every single proxy data point.

8.3 Some aspects of the model uncertainties

Modelling uncertainties take on a number of forms. There are uncertainties in the model boundary conditions and the approximations made in the models in the physical representation of the climate system. Approximations of the fundamental physical equations are required. These approximations may differ between various GCMs. An advantage of the perturbed physics approach is that you see the effect of the physical parameter perturbations rather than structural biases in the models. Model parameter uncertainties also arise from our lack of knowledge or understanding of processes that exist on sub – grid scales. Resolution is only one of many uncertainty contributors in modelling.

The coupling of the slab model to the atmospheric GCM is an improvement to the atmosphere only models as it predicts SSTs and sea ice extent. It is based on the assumption that the ocean heat transport is prescribed at its present day value. A constraint of the slab is therefore that it cannot simulate e.g. changes in the North

Atlantic thermohaline circulation or changes in equatorial upwelling.

8.4 Uncertainties arising from the paleo–records

Issues to keep in mind when dealing with climate reconstructions from paleo–observations arise from the use of multiple data sources (e.g. pollen, isotopes and noble gas), differing spatial scales from point– to area averages, more than one reconstruction from one site, varying reconstruction techniques (e.g. forward modelling, inverse, constrained analogue, analogue and response surface). Also, most reconstruction are without error bars, as these are difficult to establish. The age models are an additional uncertainty source.

The paleo-record sample distribution can bias temperature reconstructions by over weighting certain regions (Viau et al., 2006). Ambiguities in the dating and interpretation of individual records can be assumed. During the mid-Holocene the response in some paleo-records might be dampened from the scale interactions between orbital and millennial scales because of the response's sensitivity to climate variations (Fisher, 1982). Millennial scale climate variations may be expressed differently or not shown at all in some paleo-records. Viau et al. (2006) therefore suggests that more data is needed to investigate the nature of millennial scale oscillations during the Holocene.

Human disturbances could have been responsible for a decline in forest after 6kyBP (Guiot et al., 2008). Lake level data is therefore more reliable than pollen data in such regions, including e.g. China.

Another aspect to keep in mind when handling pollen data is that certain types of biomes produce more pollen than others and may be overrepresented in the records. The pollen can also be carried large distances by the wind which might contribute to a misrepresentation of biome distributions. Certain types of pollen are lighter and can be more readily carried further distances.

There is a lack of quantitative paleo–reconstructions, though they exist for some regions. We can use our knowledge of the dynamics governing the current climate and make assumptions regarding the magnitude of change during the mid-Holocene. Though the paleo–community should be encouraged to continue to develop information on the quantitative changes in the paleo-climates. Qualitative benchmarks are still useful, especially as a first assessment of the model skill.

8.5 The wider context

PMIP found a relationship between the climate in the control runs and the 6kyBP runs, in which the models that produce a maximum increase in 6kyBP African precipitation furthest to the north are the ones with the northernmost rain–belt in the control run (Joussaume et al., 1999). Furthermore the PMIP 1 ensemble underestimates the expansion of the North African Monsoon at 6kyBP compared to the paleo-environmental observations (Joussaume et al., 1999). Some of the models underestimate the precipitation increase at 23°N by 50% whilst other models do not simulate a precipitation increase this far north at all.

The PMIP 2 simulations, however, produced larger precipitation changes across North Africa than PMIP 1. The increase in the rainfall rate is found to reach further north

and the magnitude is increased in the coupled OA (and OAV) models in the PMIP 2 ensemble compared to the PMIP 1 models. This emphasises the importance of the ocean in enhancing the monsoon flow; there is a build up of warmth in the North Atlantic subtropics and mid-latitudes during summer and a cooling south of the equator, strengthening the cross equatorial flow and maintaining the presence of the ITCZ northwards of equator for a longer duration. The ocean seems to amplify the feedbacks from the hydrological cycle and large–scale dynamics in the tropical regions (Kutzbach and Liu, 1997; Braconnot et al., 2000; Zhao et al., 2007; Braconnot et al., 2007b).

Braconnot et al. (2002) found that even though the insolation forcing at 6kyBP was small, the resulting climatic change cannot be inferred from the control run. This underpins the value of paleo-climatic research and how this provide an independent testing ground for model skill.

Kutzbach and Liu (1997) and Hewitt and Mitchell (1998) ran OAGCM simulations for the mid-Holocene showing that the changes in tropical South America were mostly small and represent an enhancement of the orbital forcing changes only. Compared to the PMIP results, using constant sea – surface temperatures, there were changes of up to 1mm/day, though at rather small spatial scales. Vegetation boundary conditions have been shown to be important for Asia and Africa (see e.g. Claussen (1997)), though it is unclear how important these feedbacks are for the South American climate. The models predict relatively small changes in 6kyBP tropical vegetation on this continent (Harrison et al., 1998; Texier et al., 1997) and the data is unclear with regards to the extent of tropical rain forest decline. In mid-latitudes, the vegetation changes were on a small scale and vegetation has a less direct influence on climate.

As seen in Harrison et al. (1998) the PMIP ensemble simulates an overall drying over the south American continent, as seen in my ensemble. This drying results in more arid vegetation types. Markgraf (1993) suggests that this is consistent with the rather sparse data from this region. Modelling the climate of South America is particularly challenging. The Andes Mountains are high and narrow making them difficult to represent with the GCMs due to resolution issues. This affects the model's capability of modelling changes in the Andes Mountains, in addition to rain shadow effects and the mountainous blocking effect (Valdes, 2000). The climate in the tropical low - lands, including the Amazon Basin, is potentially sensitive to the model's ability to simulate convection, cloud cover and land surface processes.

The models in my ensemble produce a relatively consistent picture of temperature changes, though with larger uncertainty for precipitation. Precipitation processes are all sub – grid scale and sensitive to the model parametrisation. The convection parametrisation is particularly important as it is the main process associated with tropical precipitation.

Cases where the models are not exactly matching the paleo-environmental data, suggest that the effects of the orbital forcing on the mid-Holocene climate are amplified by some other mechanism. According to Tarasov et al. (1999), the effects of the 6kyBP atmospheric circulation changes are underestimated.

Mitchell et al. (1988) performed an ice sheet feedback experiment, simulating the 9kyBP ENA climate including the remnants of the Laurentide ice sheet. It was found that the high latitude warming found in their standard 9k model simulation was substantially reduced, particularly downstream of the ice sheet. In the ice sheet ex-

periment carried out in this study, a localised cooling on and around the ice was also found. The area and magnitude is much smaller compared to Mitchell et al. (1988), mainly due to the different sizes of the ice sheets.

Chapter 9

Conclusions

9.1 Overview and basis for this study

This study has identified aspects of the climate*prediction*.net ensemble that are important in projecting the response of the real world climate system to anthropogenic forcings. The work was motivated by the lack of perturbed physics paleo–ensembles, as identified in the literature. This project attempted to rectify this and has successfully designed and executed the largest paleo–ensemble to date. This section reviews the main questions and conclusions from this study.

9.2 A review of the main questions

The aim of this study was to investigate the climate response to various forcings in a GCM ensemble. The main driving factors behind this work were:

– Establishing a set of robust 6kyBP climatic features for routine model testing.

– Assess how well can we model past climates?

– Evaluation of the impacts and importance of boundary conditions in the models.

– Is there an upper boundary on climate sensitivity to be found in relation to the mid-Holocene climate?

– Provide the paleo–community with a grand ensemble of models.

9.3 Answers to questions

A set of six mid-Holocene features have been established based on a variation of geological evidence. The climate patterns are mainly based on precipitation and moisture budget proxies. One benchmark is based on temperature estimates derived from pollen and lake data. Map–map and area–average comparisons where possible should routinely be used to test the models. The thesis presents a thorough compilation of mid-Holocene data, providing a useful overview of the 6kyBP climate, and a novel approach to benchmarking GCMs.

It has been seen that the GCMs are capable of simulating the broad–scale characteristics of the mid-Holocene climate. There is a certain amount of variability within the ensemble, with some parameter combinations faring better than others. An optimum parameter combination for simulating the 6kyBP climate with the Hadley Centre model has been found. The results highlight not only some of the model's strengths and weaknesses, but also the need for better and more paleo-data, in particular quantitative data.

Forcing the model with the standard PMIP boundary conditions for the mid-Holocene

results in a reasonable ensemble mean response comparative to the geological evidence from this era. Some deficiencies in the modelled representation of the mid-Holocene climate were found, however, in particular, the models underestimate the northwards expansion of the North African monsoon and misrepresent the eastern North American micro-climate. A sensitivity test of the monsoon response to vegetation feedbacks proved the importance of the surface conditions in the model. Changing the boundary conditions in ENA to include the remnants of the Laurentide ice sheet and expand the Hudson Bay resulted in a more representative mid-Holocene climate. The local temperatures and precipitation rates were reduced, comparing more accurately with the paleo–records.

A part of this work has involved searching for an upper boundary on climate sensitivity through a relationship with the mid-Holocene climate. Encouragingly, a relationship was found between area–averaged annual precipitation rates in a region dominated by the East Asian Monsoon and climate sensitivity. An upper limit of 6.1K was found in this observation rich region. The lower bound found here, of 2.5K, is comparable to the lower bounds found in other perturbed physics ensembles (**Figure 1.1**).

The ensemble results are freely available for download via the project's results pages (http://results.cpdn.org), offering an outstanding resource to the research community.

9.4 Implications of the study

A number of studies focus their efforts on one mid-Holocene climate feature, e.g. European temperatures or the Asian or African monsoons. Here it is suggested that more efforts should be made towards testing the GCMs against more than a single

pattern to improve our confidence in the models.

Having found a suitable parameter combination for realistic simulations of the 6kyBP conditions, this can be used as a guideline for future simulations attempting to address questions regarding the 6kyBP climate. The ensemble can also be used to retrieve information on parameter settings resulting in models with e.g. a particularly warm climate, if interested in modelling past warm period. E.g. the default parameter values in HadCM3 do not simulate warm enough conditions for the Eocene and Pliocene climates (Valdes, pers. comm., 2007) (Haywood and Valdes, 2004).

The evident failure to model the full northwards expansion of the North African paleo-monsoon suggests the need to include other feedback mechanisms in the model. Furthermore, the inclusion of more realistic boundary conditions could bring the models to a closer agreement with the geological records. Or possibly the need to review the paleo–evidence more closely. Perhaps plant physiognomics have evolved over the last 6000 years? Though this is less likely on such relatively short time–scales. Or less moisture was needed to sustain perhaps more of a patchy vegetation cover that far north in the Sahara. It certainly suggests the need to revise the forward and inverse modelling techniques used. Another possibility is that the pollen could have been wind born and sourced from elsewhere than the Sahara. Perhaps the idea of an expansion over the whole of North Africa, c.f. the zonal profiles in Joussaume et al. (1999); Hoelzmann et al. (1998), is somewhat simplified. There might have been an increase in the 6kyBP moisture budget throughout western North Africa and less so in the northeast. When not even such a strong boundary condition perturbation (desert changed to rain forest) can kick a model out of the dry regime, one has to not only question the structural soundness of the model, but also our confidence in the

paleo-data.

There is the possibility that the GCMs are underestimating the mid-Holocene SST changes. This could be part of the explanation for the underestimation of the northwards expansion of the monsoons. A reduction in SSTs in the Gulf of Guinea and an increase in SSTs in the North Atlantic, i.e. an anomalous northwards SST gradient, amplifies the 6kyBP North African monsoon (Liu et al., 2004). An increase in this gradient could possibly amplify the monsoon further.

Including the more refined boundary conditions in eastern North America showed that small changes in the boundary conditions can have an important impact on the results. This inclusion is a positive step towards a stronger agreement between the paleo–records and the models, suggesting that new 6kyBP modelling efforts should include these boundary condition changes.

Further investigations into the relationship between the mid-Holocene climate and sensitivity is needed. It would be of interest to see if there is a similar relationship found in other GCMs as that found in this ensemble of high end sensitivity model underestimating and low sensitivity models overestimating the moisture budget anomaly in southwestern China.

Researchers are encouraged to make the most of the large number of simulations made available through the efforts made in this project, including the hard working and dedicated CPDN team and the volunteer participants.

9.5 Future work

The first item on the agenda would be to analyse the full ensemble, as not all models had been returned at the time of analysis for this thesis. This would increase the certainty of the results, although it is considered that the runs analysed here already provide reasonable statistical robustness.

A mid-Holocene vegetation ancillary file could be developed for the model, based on the existing pollen data base. This ancillary file would be suitable for a model set–up run without interactive vegetation scheme. This would impose a circularity issue however, if the model results are benchmarked against pollen data.

The work could be extended by running the ensemble mean climate anomalies through the offline vegetation model BIOME4 and compare the resulting vegetation maps to that of BIOME 6000 as a further test of the models. This has not been done yet due to time constraints. It has been a priority to check that the climatic response to the mid-Holocene forcing is realistic before the more detailed biome counting. Running the results from the 6kyBP experiments with the ice sheet would be a natural extension of the model testing in ENA.

Searching for other paleo–constraints on climate sensitivity is another direction to extend this work. Less time has been spent on this exercise in this study as one might question the usefulness of climate sensitivity as a concept (see Allen and Frame (2007)).

Since the (hard) groundwork for four – phase distributions now has been made, it is possible to use the set–up for new distributions investigation other time–periods. It

could be particularly interesting to design an ensemble for the Last Glacial Maximum and see how the CPDN ensemble compares to the other LGM simulations already performed by other modelling groups (see e.g. Covey et al. (2001)).

A natural continuation of the project would be to use these paleo–tested models for future prediction efforts.

Finally the work presented here highlights the need for better synthesis of paleo-climate data.

Appendix A

Parameter Definitions

The following is a list of the parameters perturbed in the climate*prediction*.net ensemble and a description of them
(http://www.climateprediction.net/science/parameters.phpp, (July 2006)).

alpham and dtice: relates the albedo of the sea ice to temperature.

ct: rate of droplet conversion to rain.

cw_land and cw_sea: expresses how much water there is in a cloud when it starts to rain. A function of CCN, Cloud Condensation Nuclei, e.g the more CCN, the more and smaller raindrops.

entcoef: entrainment coefficient. Determines how fast the mixing rate is between convective clouds and ambient air.

vf1: ice fall speed. Important for cloud development and precipitation amounts.

ice_size: radius of ice crystal in clouds, assuming they are spherical. Important with regards to the reflective properties of clouds in the radiation scheme

eacf: Empirically Adjusted Cloud Fraction. Says how much cloud cover there will be when the air is saturated.

rhcrit: critical relative humidity. A relationship between the atmospheric humidity and cloud amount in a grid box.

Appendix B

Default Parameter Values

The table shows the default values for the parameters perturbed in the models.

Parameter	**Default value**
alpham	0.5
ct	1.0×10^{-4}
cw_land	2.0×10^{-4}
cw_sea	5.0×10^{-5}
entcoef	3.0
vf1	1.0
ice_size	3.0×10^{-5}
dtice	10
eacf	0.5 on all 19 vertical levels
rhcrit	0.95, 0.9, 0.85, then 0.7 on the top 16 levels

Appendix C

ENA ancillary file perturbations

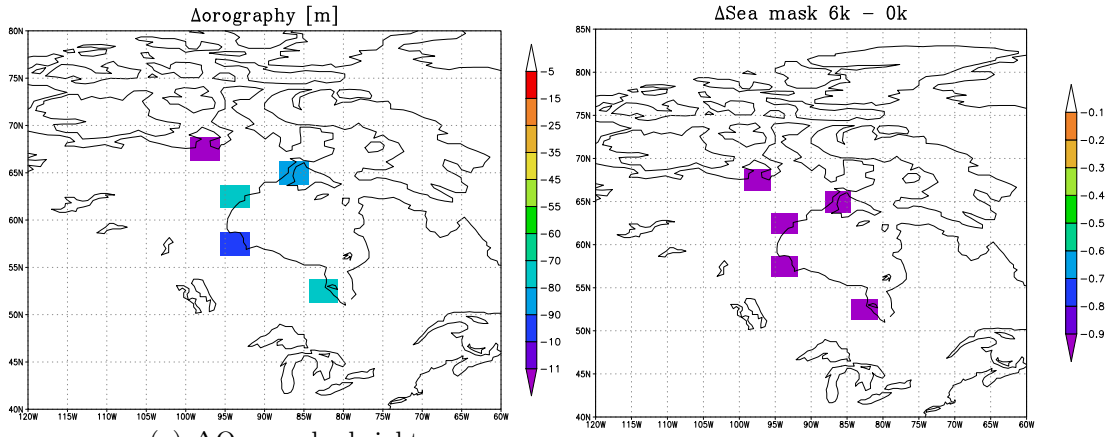

(a) ΔOrography height (b) ΔLand–sea–mask

Figure C.1: (a) The difference in orography height between the new and old ancillary files. (b) The difference in land–sea mask. These five grid boxes are changed from land to sea in the new and more refined boundary conditions.

This appendix covers the changes made to the vegetation ancillary file for the mid-Holocene simulations, as described in **Section 3.4.2**. The file contains ten fields that are all simultaneously changed; the root depth, snow–free surface albedo, surface resistance to evaporation, roughness length, surface capacity, vegetation fraction, infiltration factor, deep snow surface albedo, leaf area index and canopy height of vegetated fraction. The changes to the orography and land–sea–mask are also shown.

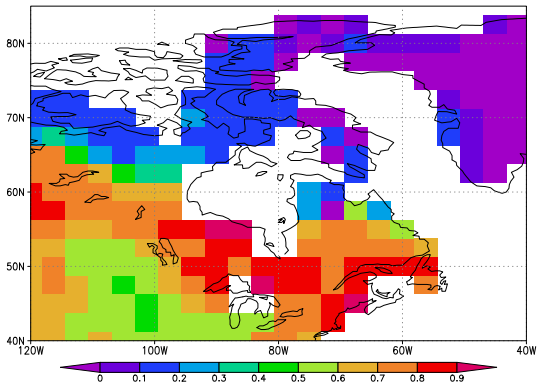

(a) Root depth (m)

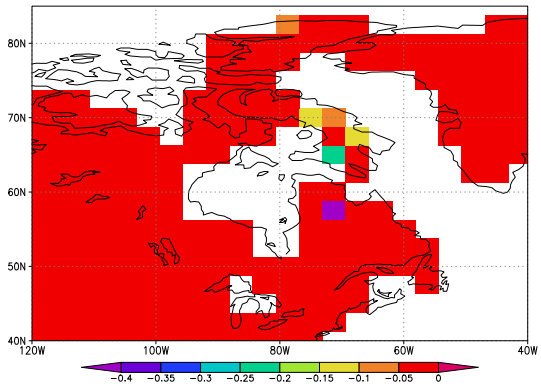

(b) ΔRoot depth (m)

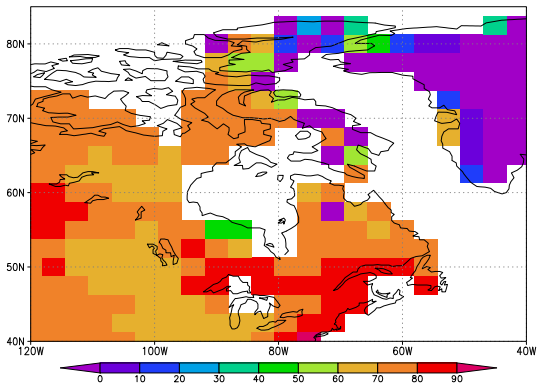

(c) Snow free surface albedo

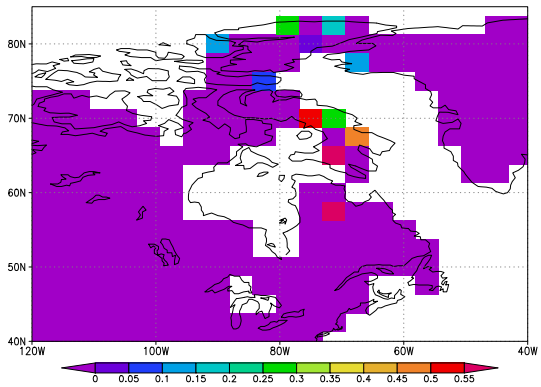

(d) ΔSnow free surface albedo

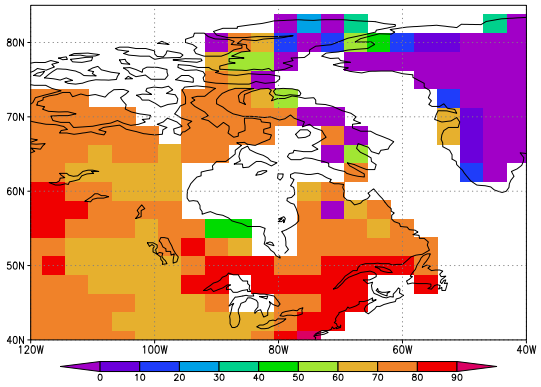

(e) Surface resistance to evaporation (sm^{-1})

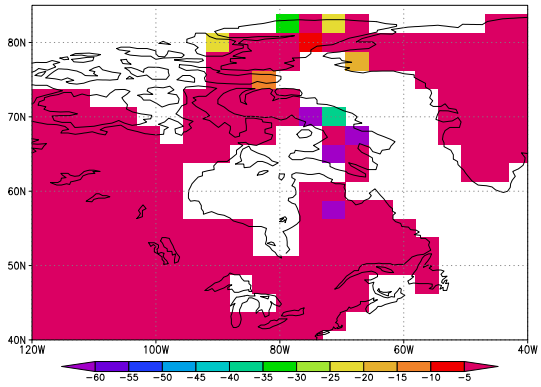

(f) ΔSurface resistance to evaporation (sm^{-1})

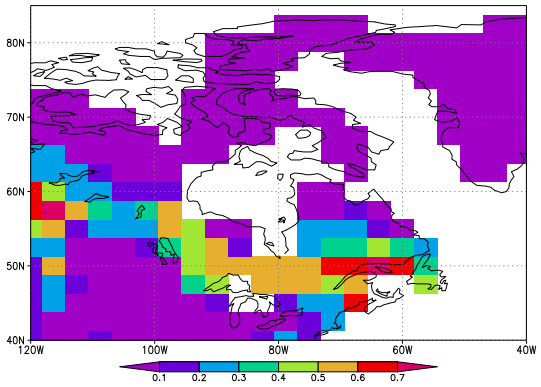

(g) Roughness Length (m)

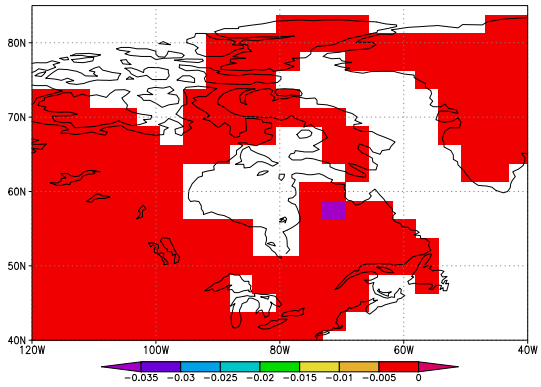

(h) ΔRoughness Length (m)

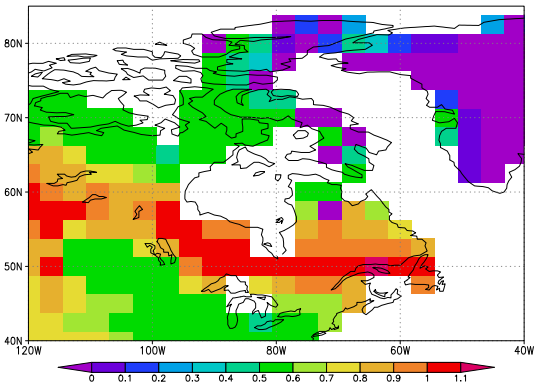

(i) Surface Capacity (kgm^{-2})

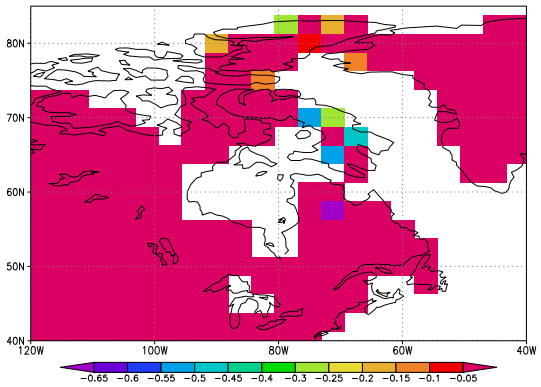

(j) ΔSurface Capacity (kgm^{-2})

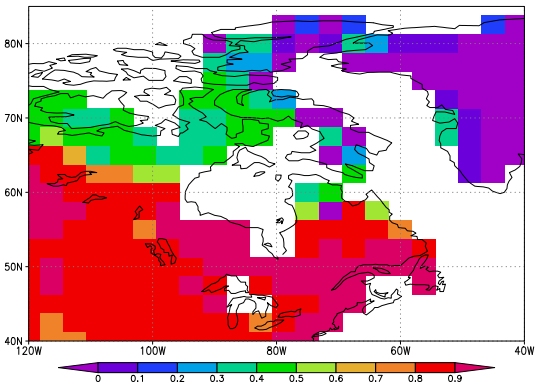

(k) Vegetation Fraction

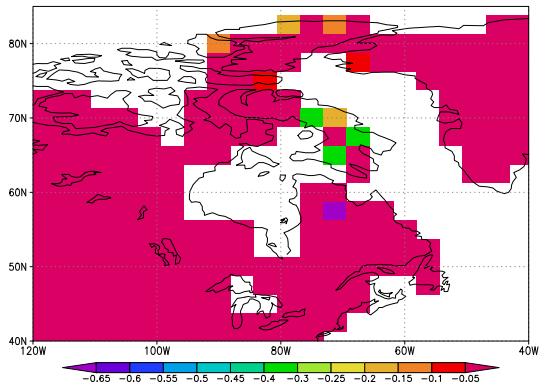

(l) ΔVegetation Fraction

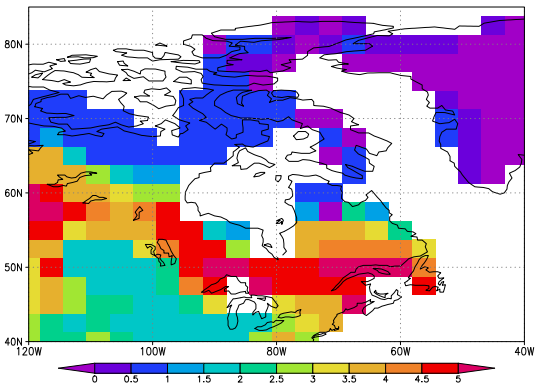

(m) Infiltration factor

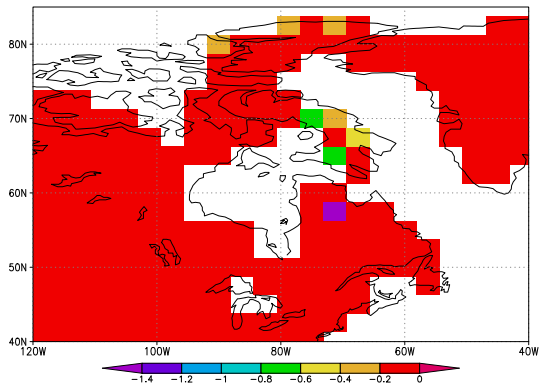

(n) ΔInfiltration factor

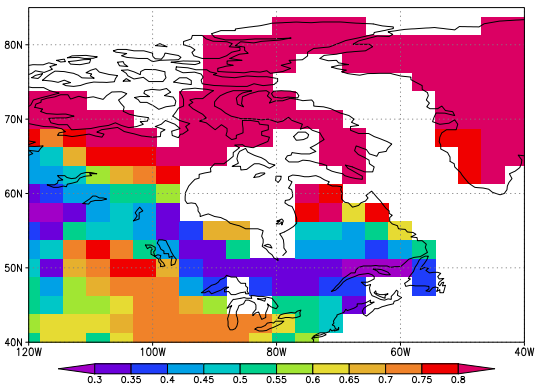

(o) Deep snow surface albedo

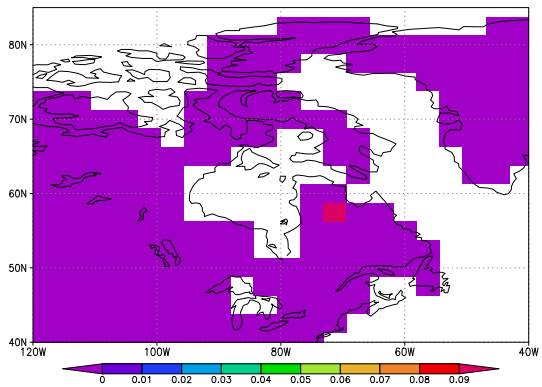

(p) ΔDeep snow surface albedo

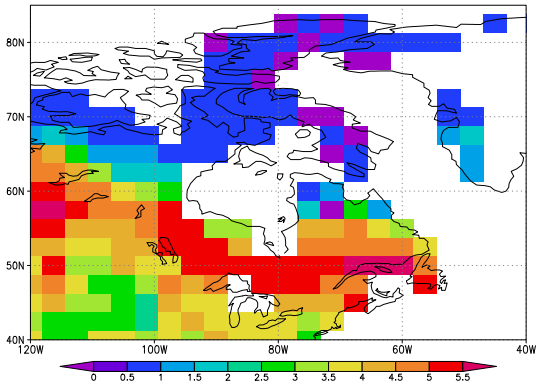

(q) Leaf Area Index

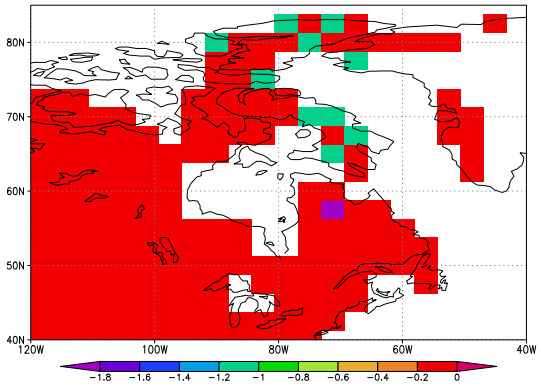

(r) ΔLeaf Area Index

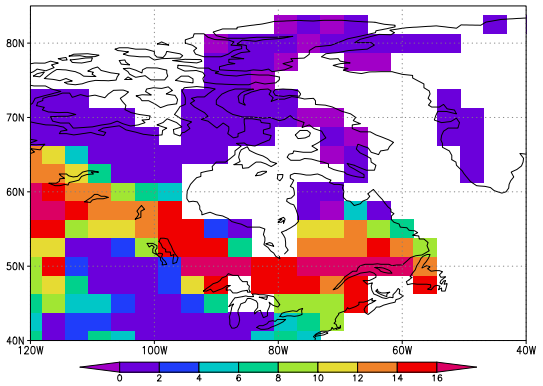

(s) Canopy height of vegetated fraction (m)

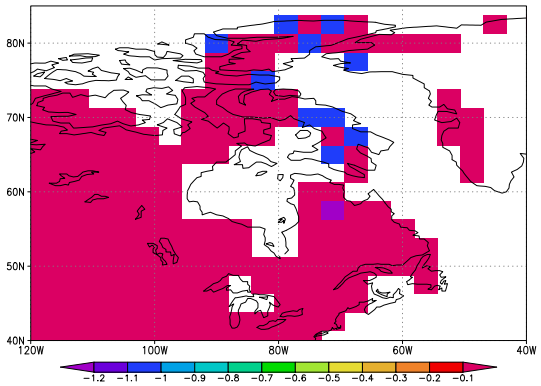

(t) ΔCanopy height of vegetated fraction (m)

Appendix D

North African vegetation changes

The following plots show the difference between the new and the old vegetation ancillary files in Africa and the Middle East in the right hand side column and the new vegetation fields in the left column.

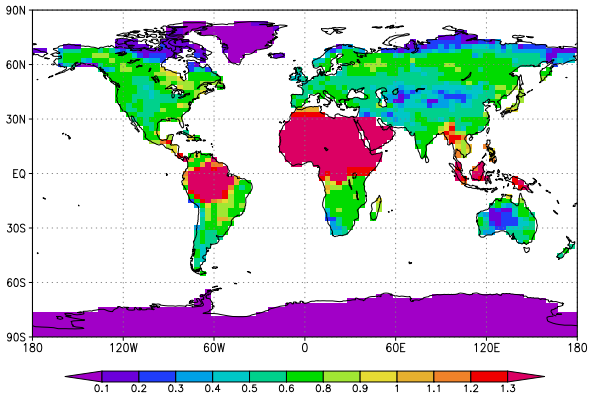

Root depth (m)

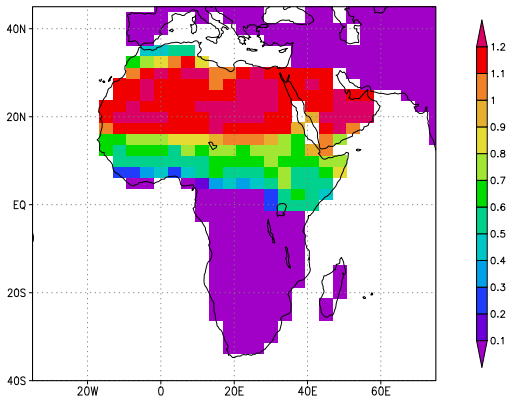

ΔRoot depth (m)

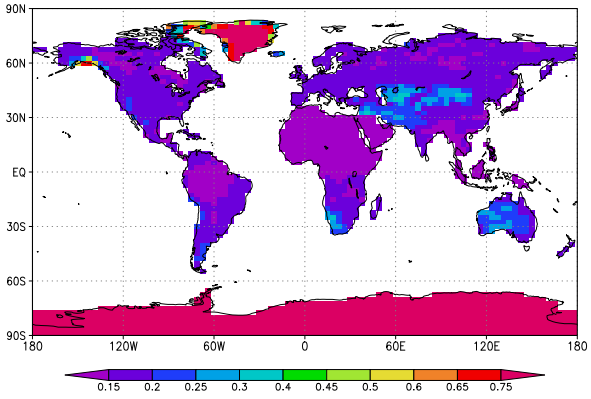

Snow free surface albedo

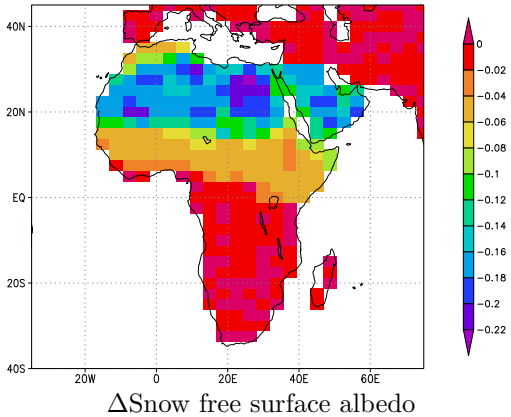

ΔSnow free surface albedo

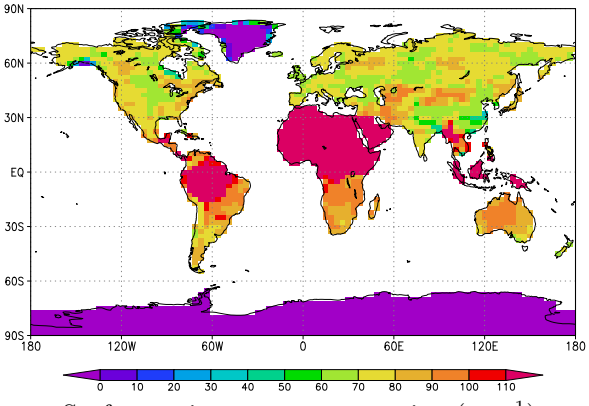

Surface resistance to evaporation (sm^{-1})

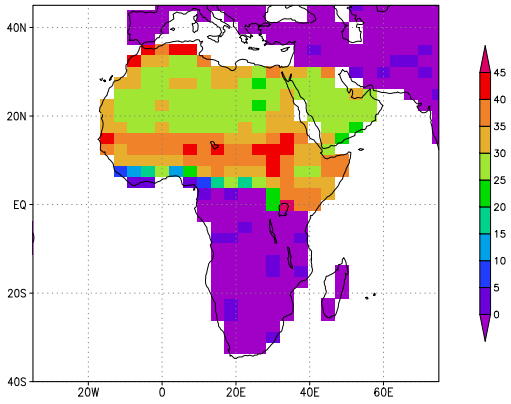

ΔSurface resistance to evaporation (sm^{-1})

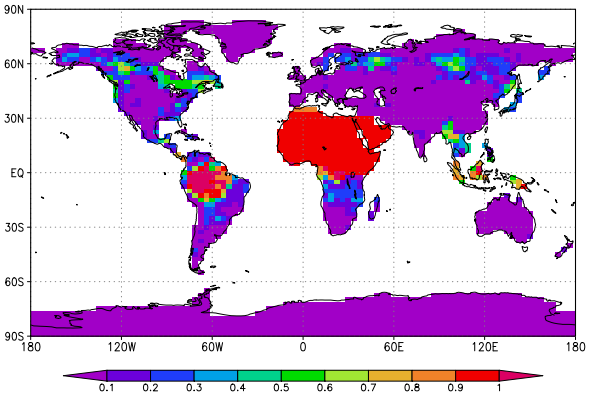

Roughness Length (m)

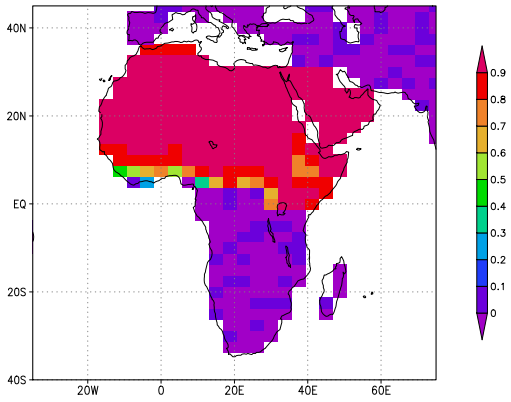

ΔRoughness Length (m)

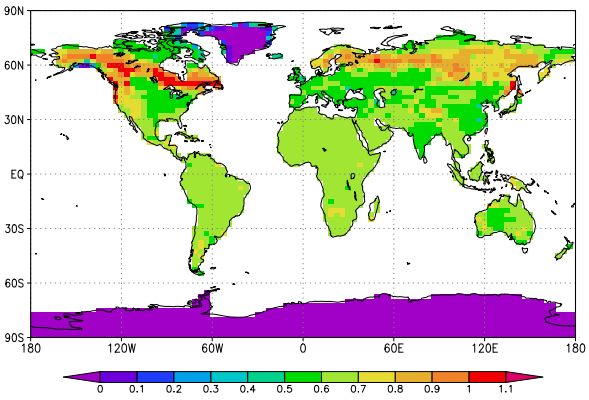

Surface Capacity (kgm^{-2})

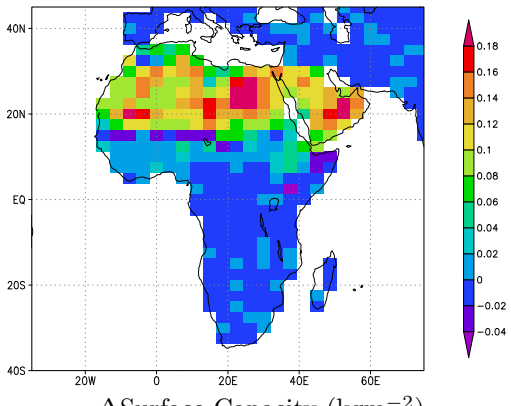

ΔSurface Capacity (kgm^{-2})

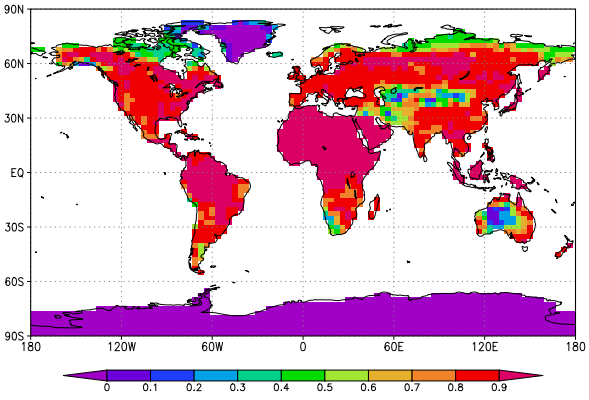

Vegetation Fraction

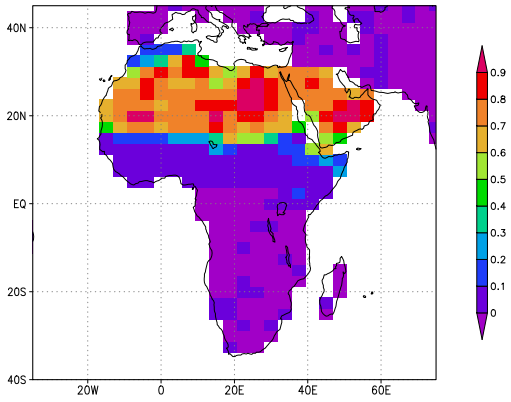

ΔVegetation Fraction

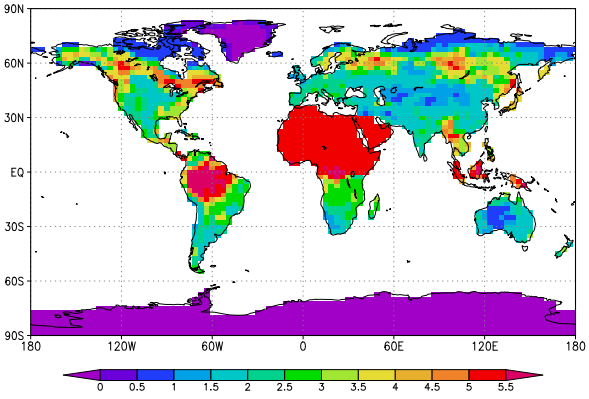

Infiltration factor

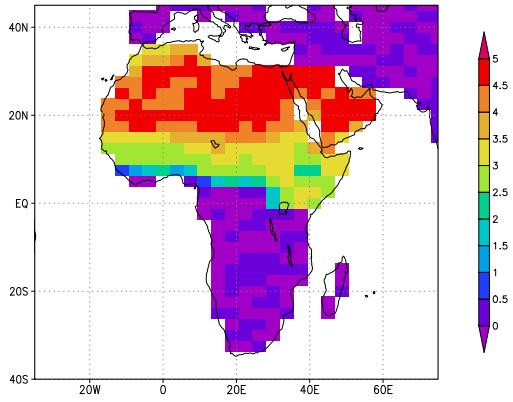

ΔInfiltration factor

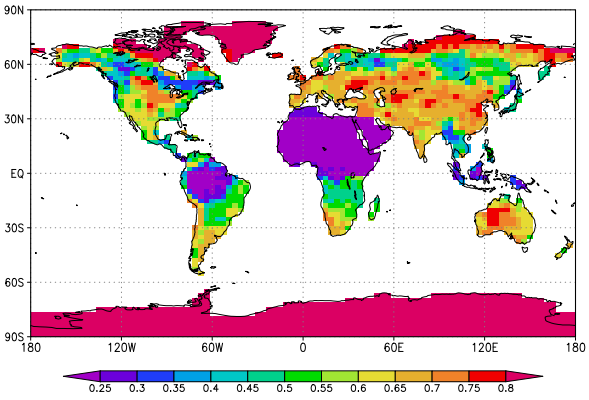

Deep snow surface albedo

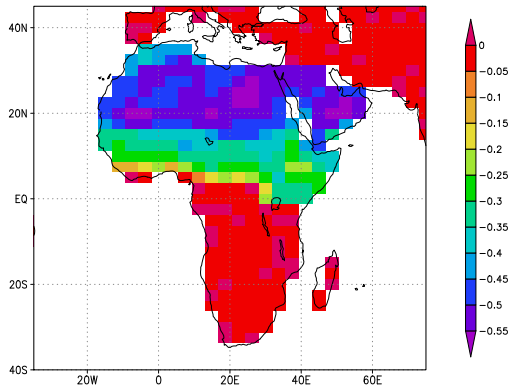

ΔDeep snow surface albedo

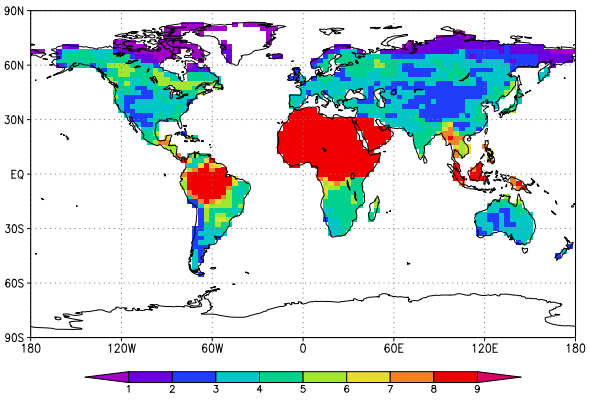

Leaf Area Index

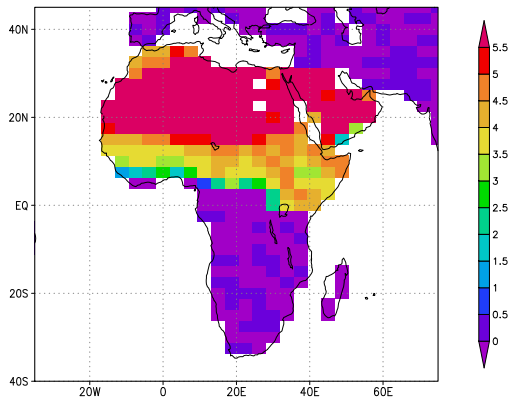

ΔLeaf Area Index

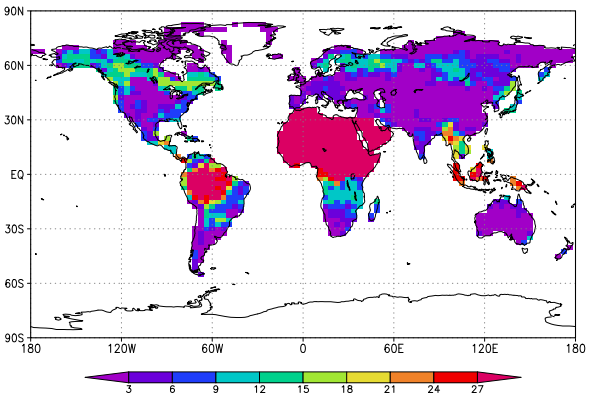

Canopy height of vegetated fraction (m)

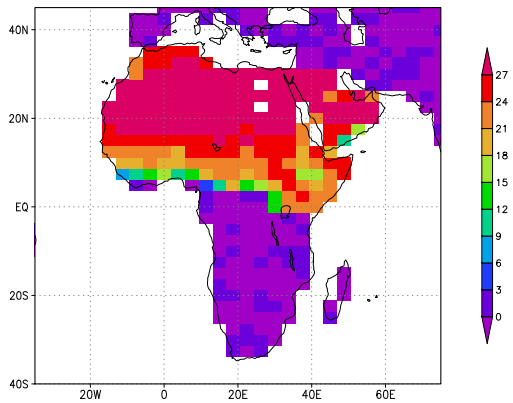

ΔCanopy height of vegetated fraction (m)

References

Allen, M. R. and Frame, D. J. (2007). Call off the quest. *Science*, 318:582–583.

Allen, M. R., Stott, P., Mitchell, J., Schnur, R., and Delworth, T. (2000). Quantifying the uncertainty in forecasts of anthropogenic climate change. *Nature*, 407(6804):617–620.

An, C. B., Feng, Z. D., and Barton, L. (2006). Dry or humid? Mid-Holocene humidity changes in arid and semi-arid China. *Quaternary Science Reviews*, 25:351–361.

An, Z. S., Porter, S. C., Kutzbach, J. E., Wu, X. H., Wang, S. M., and Liu, X. D. (2000). Asynchronous Holocene optimum of the East Asian Monsoon. *Quaternary Science Reviews*, 19:743–762.

Anderson, T., Charlson, R., Schwartz, S., Knutti, R., Boucher, O., Rohe, H., and Heintzenberg, J. (2003). Climate forcing by aerosols: a hazy picture. *Science*, 300:1103–1104.

Barker, P. A., Street-Perrott, F. A., Leng, M. J., Greenwood, P. B., Swain, D. L., Perrott, R. A., Telford, R. J., and Ficken, K. J. (2001). A 14,000–year oxygen isotope record from diatom silica in two alpine lakes on Mt. Kenya. *Science*, 292:2307–2310.

Behling, H. and Hooghiemstra, H. (2000). Holocene Amazon rainforest–savanna dynamics and climatic implications: high-resolution pollen record from Laguna Loma Linda in eastern Colombia. *Journal of Quaternary Sciences*, 15:687–695.

Behling, H. and Hooghiemstra, H. (2001). *Neotropical savanna environments in space and time: Late Quaternary interhemispheric comparisons.*, chapter Interhemispheric climate linkages. San Diego, CA: Academic.

Berger, A. (1978). Long term variations of daily insolation and Quaternary climatic changes. *Journal of Atmospheric Sciences*, 35(12):2362–2367.

Betts, R. (2001). Biogeophysical impacts of land use on present-day climate: near-surface temperature change and radiative forcing. *Atmospheric Science Letters*, 2(1–4):39–51.

Beuning, A. and Russell, J. M. (2004). Vegetation and sedimentation on the Lake Edward Basin, Uganda–Congo during the late Pleistocene and early Holocene. *J. Paleolimnol.*, 32:1–18.

Bigelow, N. H., Brubaker, L. B., Edwards, M. E., Harrison, S. P., Prentice, I. C., Anderson, P. M., Andreev, A. A., Bartlein, P. J., Christensen, T. R., Cramer, W., Kaplan, J. O., Lozhkin, A. V., Matveyeva, N. V., Murray, D. V., McGuire, A. D., Razzhivin, V. Y., Ritchie, J. C., Smith, B., Walker, D. A., Gajewski, K., Wolf, V., Holmqvist, B. H., Igarashi, Y., Kremenetskii, K., Paus, A., Pisaric, M. F. J., and Vokova, V. S. (2003). Climate change and Arctic ecosystems I. Vegetation changes north of 55°N between the Last Glacial Maximum, mid-Holocene and present. *Journal of Geophysical Research*, 108(D19):8170.

Boer, G. J. and Yu, B. (2003). Climate sensitivity and climate state. *Climate Dynamics*, 21:167–176.

Braconnot, P. and Harrison, S. P. (2008). PMIP (Paleoclimate Modelling Intercomparison Project). *PAGES News*, 16(2).

Braconnot, P., Loutre, M. F., Dong, B., Joussaume, S., Valdes, P., and PMIP-participants (2002). How the simulated change in monsoon at 6ka BP is related to the simulation of the modern climate: results from the Paleoclimate Modelling Intercomparison Project. *Climate Dynamics*, 19:107–121.

Braconnot, P., Marti, O., Joussaume, S., and Leclainche, Y. (2000). Ocean feedbacks from ocean and vegetation on the monsoon response to 6ky BP insolation. *Journal of Climate*, 13:1537–1553.

Braconnot, P., Otto-Bliesner, B., Harrison, S. P., Joussaume, S., Peterschmitt, J. Y., Abe-Ouchi, A., Crucifix, M., Driesschaert, E., Fichefet, T., Hewitt, C. D., Kageyama, M., Kitoh, A., Laîné, A., Loutre, M. F., Marti, O., Merkel, U., Ramstein, G., Valdes, P., Weber, S. L., Yu, Y., and Zhao, Y. (2007a). Results from PMIP2 coupled simulations of the Mid-Holocene and Last Glacial Maximum; Part 2: Feedbacks with emphasis on the location of the ITCZ and the mid– and high latitudes heat budget. *Climates of the Past*, 3(2):279–296.

Braconnot, P., Otto-Bliesner, B. L., Harrison, S. P., Joussaume, S., Peterschmitt, J. Y., Abe-Ouchi, A., Crucifix, M., Driesschaert, E., Fichefet, T., Hewitt, C. D., Kageyama, M., Kitoh, A., Laîné, A., Loutre, M. F., Marti, O., Merkel, U., Ramstein, G., Valdes, P., Weber, S. L., Yu, Y., and Zhao, Y. (2007b). Results from

PMIP2 coupled simulations of the Mid-Holocene and Last Glacial Maximum; Part 1: experiments and large-scale features. *Climates of the Past*, 3(2):261–277.

Bradley, R., editor (2006). *Future climate change: the need for a past perspective*. HOLIVAR2006 Abstracts.

Broström, A., Coe, M., Harrison, S. P., Gallimore, R., Kutzbach, J. E., Foley, J., Prentice, I. C., and Behling, P. (1998). Land surface feedbacks and paleomonsoons in northern Africa. *Geophysical Research Letters*, 25:3615–3618.

Burroughs, W. J. (1999). *The climate revealed (Insights on science)*. Cambridge University Press.

Cadet, D. L. and Houston, S. H. (1984). Precipitable water over Africa and the Eastern/Central Atlantic Ocean during the 1979 summer. *J. Meteor. Soc. Japan*, 62:761–774.

Cheddadi, R., Yu, G., Guiot, J., Harrison, S. P., and Prentice, C. (1997). The climate of Europe 6000 years ago. *Climate Dynamics*, 13:1–9.

Chen, C.-T., Lan, H.-C., Lou, J.-Y., and Chen, Y.-C. (2003). The dry Holocene Megathermal in Inner Mongolia. *Palaeogeogr. Palaeoclimatol. Palaeoecol.*, 193:181–200.

Claussen, M. (1994). On coupling global biome models with climate models. *Climate Research*, 4(203–221).

Claussen, M. (1997). Modelling bio-geophysical feedback in the African and Indian monsoon region. *Climate Dynamics*, 13(4):247–257.

Coe, M. T. and Bonan, G. B. (1997). Feedbacks between climate and surface waters in northern Africa during the middle Holocene. *Journal of Geophysical Research*, 102(D10):11,087–11,101.

Coe, M. T. and Harrison, S. P. (2002). The water balance of northern Africa during the middle-Holocene: an evaluation of the 6ka BP PMIP experiments. *Climate Dynamics*, 19:155–166.

Collins, M. and Allen, M. R. (2002). Assessing the relative roles of initial and boundary conditions in interannual to decadal climate predictability. *Journal of Climate*, 15(21):3104–3109.

Colman, R. (2003). A comparison of climate feedbacks in general circulation models. *Climate Dynamics*, 20(7–8):865–873.

Cook, K. H. (1998). Generation of the African Easterly Jet and its role in determining West African precipitation. *Journal of Climate*, 12(5):1165–1184.

Covey, C., Joussaume, S., Kattsov, V., Kitoh, A., Ogana, W., Pitman, A. J., Weaver, A. J., Wood, R. A., and Zhao, Z. C. (2001). *IPCC Third Assessment Report, Working Group 1.*, chapter Climate Change 2001: The Scientific Basis. Cambridge University Press.

Cox, P. M., Betts, R. A., Jones, C. D., Spall, S. A., and Totterdell, I. J. (2001). Modelling vegetation and the carbon cycle as interactive elements of the climate system. Technical Report 23, Met. Office.

Crowley, T. J. and North, G. R. (1991). *Palaeoclimatology*. Oxford University Press.

Crucifix, M., Braconnot, P., Harrison, S. P., and Otto-Bliesner, B. L. (2005). Second phase of Paleoclimate Modelling Intercomparison Project. *EOS*, 86:264.

Cruz Jr., F. W., Burns, S. J., Karmann, I., Sharp, W. D., Vuille, M., Cardoso, A. O., Ferrari, J. A., Dias, P. L. S., and Viana, O. (2005). Insolation–driven changes in atmospheric circulation over the past 116,000 years in subtropical Brazil. *Nature*, 434(7029):63–66.

Curry, J. A., Schramm, J. L., and Ebert, E. E. (1995). Sea ice–albedo climate feedback mechanism. *Journal of Climate*, 8(2):240–247.

Dean, W. E., Ahlbrandt, T. S., Anderson, R. Y., and Bradbury, J. P. (1996). Regional aridity in North America during the middle Holocene. *The Holocene*, 6(2):145–155.

Dong, B. and Valdes, P. (1998). Modelling Asian summer monsoon rainfall and Eurasian winter/spring snow. *Q. J. Royal Meteorological Society*, 124:2567–2596.

Dyke, A. S., England, E., Reimnitz, E., and Jette, H. (1997). Changes in drift-wood delivery to the Canadian Arctic Archepilago: The hypothesis of postglacial oscillations of the transpolar drift. *Arctic*, 50:1–16.

Dyke, A. S., Moore, A., and Robertson, L. (2003). Deglaciation of North America. *Geological Survey of Canada Open File Report 1574, 1 CD-ROM/ 2 map sheets.*

Edwards, T., Crucifix, M., and Harrison, S. P. (2008). Using the past to constrain the future: how the palaeorecord can improve estimates of global warming. *Progress in Physical Geography*, 31:481–500.

Essery, R. L. H., Best, M. J., Betts, R. A., Cox, P. M., and Taylor, C. M. (2003).

Explicit representation of subgrid heterogeneity in a GCM land-surface scheme. *Journal of Hydrometeorology*, 4(3):530–543.

Filby, S. K., Locke, S. M., Person, M. A., Winter, T. C., Rosenberry, D. O., Nieber, J. L., Gutowski, W. J., and Ito, E. (2002). Mid-Holocene Hydrologic model of the Shingobee Watershed, Minnesota. *Quaternary Research*, 58(3):246–254.

Fisher, D. A. (1982). Carbon-14 production compared to oxygen isotope records from Camp Century, Greenland and Devon Island, Canada. *Climatic Change*, 4:419–426.

Forster, P. e. a. (2007). *Climate Change 2007: The physical science basis.*, chapter Contribution of working group I to the Fourth Assessment Report of the Intergovernmental Panel on Climate Change., pages 129–234. Cambridge University Press.

Gordon, C., Cooper, C., Senior, C. A., Banks, H., Gregory, J. M., Johns, T. C., Mitchell, J. F. B., and Wood, R. A. (2000). The simulation of SST, sea ice extent and ocean heat transport in a version of the Hadley Centre coupled model without flux adjustments. *Climate Dynamics*, 16:147–168.

Guiot, J., Haibin, J., Wenying, J., and Yunli, L. (2008). East Asian Monsoon and paleoclimatic data analysis: a vegetation point of view. *Climate of the Past Discussions*, 4:137–145.

Haberzettl, T., Mayr, C., Wille, M., and Zolitschka, B. (2007). Linkages between Southern Hemisphere westerlies and hydrological changes in semi-arid Patagonia during the last 16,000 years. *PAGES Newsletter*, (2).

Hansen, J., Lacis, A., Rind, D., Russell, G., Stone, P., Fung, I., Ruedy, R., and Lerner, J. (1984). Analysis of feedback mechanisms. In Hansen, J. E. and Takahashi, T.,

editors, *Climate processes and climate sensitivity*, volume 5 of *AGU Geophysical Monograph*, pages 130–163. American Geophysical Union.

Hansen, J. and Nazarenko, L. (2004). Soot climate forcing via snow and ice albedos. *Proceedings of the National Academy of Sciences*, 101(2):423–428.

Hansen, J., Sato, M., Reudy, R., Nazarenko, L., Lacis, A., Schmidt, G. A., Russell, G., Aleinov, I., Bauer, M., Bauer, S., Bell, N., Cairns, B., Canuto, V., Chandler, M., Cheng, Y., Genio, A. D., Faluvegi, G., Fleming, E., Friend, A., Hall, T., Jackman, C., Kelley, M., Kiang, N., Koch, D., Lean, J., Lerner, J., Lo, K., Menon, S., Miller, R., Minnis, P., Novakov, T., Oinas, V., Perlwitz, J., Rind, D., Romanou, A., Shindell, D., Stone, P., Sun, P., Tausnev, T., Thresher, D., Wielicki, B., Wong, T., Yao, M., and Zhang, S. (2005). Efficiancy of climate forcings. *Journal of Geophysical Research*, 110(D18104). doi:10.1029/2005JD005776.

Hansen, J., Sato, M., and Ruedy, R. (1997). Radiative forcing and climate response. *Journal of Geophysical Research*, 102:6831–6864.

Hargreaves, J. C., Abe-Ouchi, A., and Annan, J. D. (2007). Linking glacial and future climates through an ensemble of GCM simulations. *Climates of the Past*, 3:77–87.

Harrison, S. P. (1989). Lake levels and climate change in eastern North America. *Climate Dynamics*, 3:157.

Harrison, S. P., Braconnot, P., Hewitt, C., and Stouffer, R. J. (2002). Fourth International Workshop of the Paleoclimate Modelling Intercomparison Project (PMIP): Launching PMIP Phase 2. *EOS*, 83:447.

Harrison, S. P., Jolly, D., Laarif, F., Abe-Ouchi, A., Dong, B., Herterich, K., Hewitt, C., Joussaume, S., Kutzbach, J. E., Mitchell, J., de Noblet, N., and Valdes, P.

(1998). Intercomparison of simulated global vegetation distributions in response to 6kyr BP orbital forcing. *Journal of Climate*, 11:2721–2742.

Harrison, S. P., Kutzbach, J. E., Liu, Z., Bartlein, P. J., Otto-Bliesner, B., Muhs, D., Prentice, I. C., and Thompson, R. S. (2003). Mid-Holocene climates of the Americas: a dynamical response to changed seasonality. *Climate Dynamics*, 20:663–688.

Harrison, S. P., Yu, G., Takahara, H., and Prentice, I. C. (2001). Palaeovegetation –Diversity of temperate plants in east Asia. *Nature*, 413:129–130.

Haug, G. H., Hughen, K. A., Sigman, D. M., Peterson, L. C., and Rohl, U. (2001). Southward Migration of the Intertropical Convergence Zone through the Holocene. *Science*, 293(5533):1304–1308.

Hays, J. D., Imbrie, J., and Shackleton, N. J. (1976). Variations in the Earth's Orbit: Pacemaker of the Ice Ages. *Science*, 194(4270):1121–1132.

Haywood, A. M. and Valdes, P. J. (2004). Modelling Pliocene warmth: Contribution of atmosphere, oceans and cryosphere. *Earth Planetary Science Letters*, 218:363–377.

Haywood, J., Farnborough, E., Boucher, O., and Atmosphérique, L. (2000). Estimates of the direct and indirect radiative forcing due to tropospheric aerosols: a review. *Reviews of Geophysics*, 38:513–543.

Hewitt, C. D. and Mitchell, J. F. B. (1998). A fully coupled GCM simulation of the climate of the mid-Holocene. *Geophysical Research Letters*, 25:361–364.

Hoelzmann, P., Jolly, D., Harrison, S. P., Laarif, F., Bonnefille, R., and Pachur, H. J. (1998). Mid-Holocene land-surface conditions in northern Africa and Arabian peninsula: a data set for AGCM sensitivity experiments. *Global Biogeochemical Cycles*, 12:35–52.

Houghton, J. T., Ding, Y., Griggs, D., Noguer, M., van der Linden, P. J., Dai, X., Maskell, K., and Johnson, C. A., editors (2001). *IPCC Report 2001:*, chapter Climate Change: The Scientific Basis. Cambridge University Press.

Hu, C., Henderson, G. M., Huang, J., Xie, S., Sun, Y., and Johnson, K. R. (2008). Quantification of Holocene Asian monsoon rainfall from spatially separated cave records. *Earth and Planetary Science Letters*, 266(3–4):221–232.

Huber, B. T., MacLeod, K. G., and Wing, S. L., editors (2001). *Warm climates in Earth history*, chapter Approaches to the study of paleo-climates. Cambridge University Press.

Huntley, B. and Prentice, I. C. (1993). *Global climates since the Last Glacial Maximum.*, chapter Holocene vegetation and climates of Europe, pages 136–168. University of Minnesota, Minneapolis.

Imbrie, J., Berger, A., Boyle, E. A., Clemens, S. C., Duffy, A., Howard, W. R., Kukla, G., Kutzbach, J., Martinson, D. G., McIntyre, A., Mix, A. C., Molfino, B., Morley, J. J., Peterson, L. C., Pisias, N. G., Prell, W. L., Raymo, M. E., Shackleton, N. J., and Toggweiler, J. R. (1993). On the structure and origin of major glaciation cycles 2. The 100,000-year cycle. *Paleoceanography*, 8(6):699–735.

Ingram, W. J., Wilson, C. A., and Mitchell, J. F. B. (1989). Modeling climate change:

An assessment of sea ice and surface albedo feedbacks. *Journal of Geophysical Research*, 94(D6):8609–8622.

Jackson, C. S. and Broccoli, A. J. (2003). Orbital forcing of Arctic climate: mechanisms of climate response and implications for continental glaciation. *Climate Dynamics*, 21:539–557.

Jiang, W. Y., Guo, Z. T., Sun, X. J., Wu, H. B., Chu, G. Q., Yuan, B. Y., Hatte, C., and Guiot, J. (2006). Reconstruction of climate and vegetation changes of Lake Bayanchagan (Inner Mongolia): Holocene variability of the East Asian Monsoon. *Quaternary Science Reviews*, 65:411 – 420.

Jiang, W. Y. and Liu, T. S. (2007). Timing and spatial distribution of mid-Holocene drying over northern China: Response to a southeastward retreat of the East Asian Monsoon. *Journal of Geophysical Research*, 112.

Jolly, D., Harrison, S. P., Damnati, D., and Bonnefille, R. (1998a). Simulated climate and biomes of Africa during the Late Quaternary: Comparison with pollen and lake status data. *Quaternary Science Reviews*, 17:629–657.

Jolly, D., Prentice, I. C., Bonnefille, R., Ballouche, A., Bengo, M., Brenac, P., Buchet, G., Burney, D., Cazet, J. P., Cheddadi, R., Edorh, T., Elenga, H., Elmoutaki, S., Guiot, J., Laarif, F., Lamb, H., Lezine, A. M., Maley, J., Mbenza, M., Peyron, O., Reille, M., Reynoud-Farrera, I., Riollet, G., Ritchie, J. C., Roche, E., Scott, L., Semmanda, I., Straka, H., Umer, M., Van Campo, E., Vilimumbalo, S., Vincens, A., and Waller, M. (1998b). Biome reconstruction from pollen and plant macrofossil data for Africa and the Arabian peninsula at 0 and 6000 years. *Journal of Biogeography*, 25:1007–1027.

Joshi, M., Shine, K., Ponater, M., Stuber, N., Sausen, R., and Li, L. (2003). A comparison of climate response to different radiative forcings in three general cirulation models: towards an improved metric of climate change. *Climate Dynamics*, 20:843–854.

Joussaume, S. and Taylor, K. (1995). Status of the Paleoclimate Modelling Intercomparison Project (PMIP). Proc. First In. AMIP Scientific Conf., pages 425–430, Monterey, CA. PCMDI.

Joussaume, S., Taylor, K. E., Braconnot, P., Mitchell, J. F. B., Kutzbach, J. E., Harrison, S. P., Prentice, I. C., Broccoli, A. J., Abe-Ouchi, A., Bartlein, P. J., Bonfils, C., Dong, B., Guiot, J., Herterich, K., Hewitt, C. D., Jolly, D., Kim, J. W., Kislov, A., Kitoh, A., Loutre, M. F., Masson, V., McAvaney, B., McFarlane, N., de Noblet, N., Peltier, W. R., Peterschmitt, J. Y., Pollard, D., Rind, D., Royer, J. F., Schlesinger, M. E., Syktus, J., Thompson, S., Valdes, P., Vettoretti, G., Webb, R. S., and Wyputta, U. (1999). Monsoon changes for 6000 years ago: results of 18 simulations from the Paleoclimate Modelling Intercomparison Project (PMIP). *Geophysical Research Letters*, 26:859–862.

Kaplan, J. O. (2001). Geophysical applications of vegetation modelling. In *Department of Ecology*, page 132. Lund University.

Kerwin, M. W., Overpeck, J. T., Webb, R. S., DeVernal, A., Rind, D. H., and Healy, R. J. (1999). The role of oceanic forcing in mid-Holocene Northern Hemisphere climatic change. *Paleoceanography*, 14:200–210.

Kiehl and Trenberth (1997). Earth's annual global mean energy budget. *Bulletin of the American Meteorological Society*, 78:197–208.

Kim, J.-H. and Schneider, R. R. (2004). GHOST global database for alkenone-derived 6ka sea-surface temperatures. http://www.pangaea.de/Projects/GHOST/. MOTIF6k data.

Kirby, M. E., Poulsen, C. J., Lund, S. P., Patterson, W. P., Reidy, L. H., and E., D. (2004). Late Holocene lake level dynamics inferred from magnetic susceptibility and stable oxygen isotope data: Lake Elsinore, southern California (USA). *Journal of Paleolimnology*, 31(3):275–293.

Knutti, R. and Hegerl, G. C. (2008). The equilibrium sensitivity of the Earth's temperature to radiation changes. *Nature Geoscience*, 1:735–743.

Kohfeld, K. E. and Harrison, S. P. (2000). How well can we simulate past climates? Evaluating the models using global palaeoenvironmental datasets. *Quaternary Science Reviews*, 19(1-5):321–346.

Kutzbach, J. E., Bonan, G., Foley, J., and Harrison, S. P. (1996). Vegetation and soil feedbacks on the response of the African monsoon to orbital forcing in the early to middle Holocene. *Nature*, 384:623–626.

Kutzbach, J. E., Guetter, P. J., Ruddiman, W. F., and Prell, W. L. (1989). Sensitivity of climate to late Cenozoic uplift in southern Asia and the American West. *Journal of Geophysical Research*, 94:18,393–18,407.

Kutzbach, J. E. and Liu, Z. (1997). Response of the African monsoon to orbital forcing and ocean feedbacks in the middle Holocene. *Science*, 278:440–443.

Larson, G. L., Collier, R., and Buktenica, M. W. (2007). Long-term limnological research and monitoring at Crater Lake, Oregon: a benchmark study of a deep and exceptionally clear montane caldera lake. *Developments in hydrobiology*, 191.

Liu, Z., Harrison, S. P., Kutzbach, J., and Otto-Bliesner, B. (2004). Global monsoons in the mid-Holocene and oceanic feedback. *Climate Dynamics*, 22:157–182.

Markgraf, V. (1991). Late Pleistocene environmental and climatic evolution in southern South America. *Bamberger Geograph Schrift*, 11:271–281.

Markgraf, V. (1993). *Global climates since the Last Glacial Maximum*, chapter Climatic history of Central and South America since 18,000 yr B.P., pages 357–385. University of Minnesota Press: Minneapolis.

Maslin, M. A. and Burns, S. J. (2000). Reconstruction of the Amazon basin effective moisture available over the past 14,000 years. *Science*, 290:2285–2287.

Mayle, F. (2007). personal communication.

Mayle, F., Burbridge, R., and Killeen, T. (2000). Millennial-scale dynamics of southern Amazonian rain forests. *Science*, 290:2291–2294.

Mayle, F. E., Beerling, D. J., Gosling, W. D., and Bush, M. B. (2004). Responses of Amazonian ecosystems to climatic and atmospheric carbon dioxide changes since the Last Glacial Maximum. *Philosophical Transactions of the Royal Society London: B Biological Science*, 359(1443):499–514.

Mayle, F. E. and Power, M. (2008). Impact of a drier Early Mid-Holocene climate upon Amazonian forests. *Philosophical Transactions of the Royal Society London*, 363:1829–1838.

Meehl, G. A. (2004). Combinations of natural and anthropogenic forcings in twentieth-century climate. *Journal of Climate*, 17:3721–3727.

Mitchell, J. F. B., Grahame, N. S., and Needham, K. J. (1988). Climate simulations for 9000 years before present: seasonal variations and effect of the Laurentide ice sheet. *J. Geophys. Res-Atmos.*, 93:8283–8303.

Morimoto, M., Kayanne, H., Abe, O., and McCulloch, M. T. (2007). Intensified mid-Holocene Asian monsoon recorded in corals from Kikai Island, subtropical northwestern Pacific. *Quaternary Research*, 67(2):204–214.

Murphy, J. M., Sexton, D. M. H., Barnett, D. N., Jones, G. S., Webb, M. J., Collins, M., and Stainforth, D. A. (2004). Quantification of modeling uncertainties in a large ensemble of climate change simulations. *Nature*, 430:768–772.

Palmer, T. N. (2000). Predicting uncertainty in forecasts of weather and climate. *Reports on Progress in Physics*, 63(2):71–116.

Patricola, C. M. and Cook, K. H. (2007). Dynamics of the West African Monsoon under Mid-Holocene precessional forcing: Regional climate model simulations. *Journal of Climate*, 20:694–716.

Peltier, W. R. (2004). Global glacial isostasy and the surface of the ice-age Earth: the ICE-5G (VM2 model and GRACE). *Annual Review of Earth and Planetary Sciences*, 32:111–149.

Peyron, O., Jolly, D., Braconnot, P., Bonnelfille, R., Guiot, J., Wirrmann, D., and Chalié, F. (2006). Quantitative reconstructions of annual rainfall in Africa 6000 years ago: Model-data comparison. *Journal of Geophysical Research*, 111.

Piani, C., Frame, D. J., Stainforth, D. A., and Allen, M. R. (2005). Constraints on climate change from a multi-thousand member ensemble of simulations. *Geophysical Research Letters*, 32.

Pickett, E., Harrison, S. P., Hope, G., Harle, K., Dodson, J. R., Kershaw, A. P., Prentice, I. C., Backhouse, J., Colhoun, E. A., D'Costa, D., Flenley, J., Grindrod, J., Haberle, S., Hassell, C., Kenyon, C., Macphail, M., Martin, H., Martin, A. H., McKenzie, M., Newsome, J. C., Penny, D., Powell, J., Raine, I., Southern, W., Sutra, J.-P., Thomas, I., van der Kaars, S., and Ward, J. (2004). Pollen-based reconstructions of biome distributions for Australia, South East Asia and the Pacific (SEAPAC region) at 0, 6000 and 18,000 14C yr B.P. *Journal of Biogeography*.

Pope, V. D., Gallani, M. L., Rowntree, P. R., and Stratton, R. A. (2000). The impact of new physical parametrisations in the Hadley Centre climate model – HadAM3. *Climate Dynamics*, 16:123–146.

Prentice, C. I., Guiot, J., Huntley, B., Jolly, D., and Cheddadi, R. (1996). Reconstructing biomes from palaeoecological data: a general method and its application to European pollen data at 0 and 6 ka. *Climate Dynamics*, 12:185–194.

Prentice, I. C., Jolly, D., and BIOME6000-participants. (2000). Mid-Holocene and glacial–maximum vegetation geography of the northern continents and Africa. *Journal of Biogeography*, 27:507–519.

Qin, B. Q., Harrison, S. P., and Kutzbach, J. E. (1998). Evaluation of modelled regional water balance using lake status data: a comparison of 6ka simulations with the NCAR CCM. *Quaternary Science Reviews*, 17:535–548.

Raghavan, K. (1973). Tibetan anticyclone and tropical easterly jet. *Pure and Applied Geophysics*, 110(1):2130–2142.

Rasmusson, E. M. and Carpenter, T. H. (1983). The relationship between eastern

equatorial Pacific sea surface temperatures and rainfall over India and Sri Lanka. *Monthly Weather Review*, 111:517–528.

Raynaud, D., Jouzel, J., Barnola, J. M., Chappelaz, J., Delmas, R., and Lorius, C. (1993). The ice record of greenhouse gases. *Science*, 259:926–934.

Rayner, N. A., Horton, E. B., Parker, D. E., Folland, C. K., and Hackett, R. B. (1996). Version 2.2 of the Global sea-Ice and Sea Surface Temperature data set, 1903-1994. CRTN 74, Hadley Centre, Met Office, UK.

Rayner, N. A., Parker, D. E., Horton, E. B., Folland, C. K., Alexander, L. V., Rowell, D. P., Kent, E. C., and Kaplan, A. (2003). Global analyses of sea surface temperature, sea ice, and night marine air temperature since the late nineteenth century. *Journal of Geophysical Research*, 108(D14):4407–4444.

Rind, D., Healey, R., Parkinson, C., and Martinson, D. (1995). The role of sea ice in $2\times CO_2$ climate model sensitivity. Part 1: The total influence of sea ice thickness and extent. *Journal of Climate*, 8(3):449–463.

Rodwell, M. R. and Hoskins, B. J. (1995). The Asian summer monsoon II: cross–equatorial flow and PV behaviour. *Journal of Atmospheric Sciences*, 52:1341–1356.

Rowe, H. D., Guilderson, T. P., Dunbar, R. B., Southon, J. R., Seltzer, G. O., Mucciarone, D. A., Fritz, S. C., and Baker, P. A. (2003). Late Quaternary lake-level changes constrained by radiocarbon and stable isotope studies on sediment cores from Lake Titicaca, South America. *Global and Planetary Change*, 38:273–290.

Sanderson, B., Knutti, R., Aina, T., Christensen, C., Faull, N., Frame, D. J., Ingram,

W. I., Piani, C., Stainforth, D. A., Stone, D. A., and Allen, M. R. (2008). Constraints on model response to greenhouse gas forcing and the role of sub-grid scale processes. *Journal of Science*, 21:2384–2400.

Sanderson, B., Piani, C., Ingram, W. J., Stoe, D. A., and Allen, M. R. (2007). Towards constraining climate sensitivity by linear analysis of feedback patterns in thousands of perturbed–physics GCM simulations. *Climate Dynamics*, 30:175–190.

Seltzer, G., Rodbell, D., and Burns, S. (2000). Isotopic evidence for late Quaternary climatic change in tropical South America. *Geology*, 28:35–38.

Senior, C. A. and Mitchell, J. F. B. (2000). The time–dependence of climate sensitivity. *Geophysical Research Letters*, 27:2685–2688.

Shine, K. P., Fouquart, Y., Solomon, S., and Srinavasan, J. (1995). Radiative forcing. *Climate change 1994, Radiative forcing of climate change. Cambridge University Press.*, 4:163–203.

Sjostrom, D. J., Hren, M. T., and Chamberlain, C. P. (2004). Oxygen isotope records of goethite from ferricrete deposits indicate regionally varying Holocene climate change in the Rocky Mountain region, USA. *Quaternary Research*, 61(1):64–71.

Smagorinsky, J., Manabe, S., and Holloway, J. L. (1965). Numerical results from a nine-level general circulation model of the atmosphere. *Monthly Weather Review*, 93.

Smith, G. and Street-Perrott, F. A. (1983). *Late Quaternary Environments of the United States*, chapter Pluvial lakes of the western United States., pages 190–212. Univ. Minnesota Press, Minneapolis.

Smith, L. (2002). What can we lear from climate forecasts? *Proceedings of the National Academy of Sciences*, 99:2487–2492.

Solomon, S., Qin, D., Manning, M., Marquis, M., Averyt, K., Tignor, M., Miller, H. L., and Chen, Z. (2007). *IPCC Fourth Assessment Report, Working Group 1.*, chapter Climate Change 2007: The physical science basis. Cambridge University Press.

Stainforth, D. A., Aina, T., Christensen, C., Collins, M., Faull, N., Frame, D., Kettleborough, J. A., Knight, S., Martin, A., Murphy, J. M., Piani, C., Sexton, D., Smith, L. A., Spicer, R. A., Thorpe, A. J., and Allen, M. R. (2005). Uncertainty in predictions of the climate response to rising levels of greenhouse gases. *Nature*, 433:403–406.

Stott, P. and Kettleborough, J. R. (2002). Origins and estimates of uncertainty in predictions of twenty-first century temperature rise. *Nature*, 416:723–725.

Stratton, R. A. (1999). A high resolution AMIP integration using the Hadley Centre model HadAM2b. *Climate Dynamics*, 15(1):9–28.

Street-Perrott, F. A. and Harrison, S. P. (1985). *Paleoclimate Analysis and Modeling*, chapter Lake levels and climate reconstruction., pages 291–340. John Wiley, New York.

Street-Perrott, F. A., Mitchell, J. F. B., Marchland, D. S., and Brunner, J. S. (1990). Milankovitch and albedo forcing of the tropical monsoons: A comparison of geological evidence and numerical simulations for 9000 yBP. *Trans. Roy. Soc. Edinburgh: Earth Sci.*, 81:407–427.

Tao, S. Y. and Chen, L. X. (1987). *Monsoon Meteorology*, chapter A review of recent research on the east Asian summer monsoon, pages 60–92. Oxford University Press.

Tarasov, P. E., Guiot, J., Cheddadi, R., Andreev, A. A., Bezusko, L. G., Blyakharchuk, T. A., Dorofeyuk, N. I., Filimonova, L. V., Volkova, V. S., and Zernitskaya, V. P. (1999). Climate in northern Eurasia 6000 years ago reconstructed from pollen data. *Earth and Planetary Science Letters*, 171:635–645.

Tarasov, P. E., Webb III, T., Andreev, A. A., Afanaseva, N. B., Berezina, N. A., Bezusko, L. G., Blyakhararchuk, T. A., Bolikhovskaya, N. S., Cheddadi, R., Chernavskaya, M. M., Chernova, G. M., Dorofeyuk, N. I., Dirksen, V. G., Elina, G. A., Filimonova, L. V., Glebov, F. Z., Guiot, J., Gunova, V. S., Harrison, S. P., Jolly, D., Khomutova, V. I., Kvavadze, E. V., Osipova, I. M., Panova, N. K., Prentice, I. C., Saarse, L., Sevastyanov, D. V., Volkova, V. S., and Zernitskaya, V. K. (1998). Present-day and mid-Holocene biomes reconstructed from pollen and plant macrofossil data from the former Soviet Union and Mongolia. *Journal of Biogeography*, 25:1029–1053.

Taylor, K. C., Mayewski, P. A., Alley, R. B., Brook, E. J., Gow, A. J. Grootes, P. M., Meese, D. A., Saltzmann, E. S., Severinghouse, J. P., Twickler, M. S., White, J. W. C., Whitlow, S., and Zielinski, G. A. (1997). The Holocene - Younger Dryas transition recorded at Summit, Greenland. *Science*, 278:825–827.

Texier, D., de Noblet, N., Harrison, S. P., Haxeltine, A., Jolly, D., Joussaume, S., Laarif, F., Prentice, I. C., and Tarasov, P. (1997). Quantifying the role of biosphere-atmosphere feedbacks in climate change: Coupled model simulation for 6000 years BP and comparison with palaeodata for northern Eurasia and northern Africa. *Climate Dynamics*, 13:865–882.

Thompson, L. G., Davis, M. E., Mosley-Thompson, E., Sowers, T. A., Henderson, K. A., Zagorodnov, V. S., Lin, P. N., Mikhalenko, V. N., Campen, R. K., Bolzan, J. F., Cole-Dai, J., and Francou, B. (1998). A 25,000-year tropical climate history from Bolivian ice cores. *Science*, 282:1858–1864.

Thompson, L. G., Mosley-Thompson, E., Davis, M. E., Henderson, K. A., Brecher, H. H., Zagorodnov, V. S., Mashiotta, T. A., Lin, P. N., Mikhalenko, V. N., Hardy, D. R., and Beer, J. (2002). Kilimanjaro ice core records: Evidence of Holocene climate change in tropical Africa. *Science*, 298:589–593.

Troccoli, A. and K*å*llberg, P. (2004). Precipitation correction in the ERA-40 Reanalysis. ERA-40 Project Report Series 13, ECMWF.

Turcq, B., Siffedine, A., Martin, L., Absy, M. L., Soubies, F., Suguio, K., and Volkmer-Ribeiro, C. (1998). Amazonia rainforest fires: A lacustrine record of 7000 years. *Ambio*, 27:139–142.

Uscinowicz, S., Kramarska, R., Tomczak, A., and Zachowicz, J. (2000). The radiocarbon age of marine and land deposits in the southern Baltic area. *Geologos*, 5:155–163.

Valdes, P. (2000). South American palaeoclimate models. *Journal of Quaternary Sciences*, 15(4):357–368.

Viau, A. E., Gajewski, K., Sawada, M. C., and Fines, P. (2006). Millennial-scale temperature variations in North America during the Holocene. *Journal of Geophysical Research*, 111.

Webb, R. S., Anderson, K. H., and Webb III, T. (1993). Surface estimates of late–

Quaternary changes in the moisture balance of the Northeastern United States. *Quaternary Research*, 40:213–227.

Weisse, R. and Oestreicher, R. (2001). Reconstruction of potential evaporation for water balance studies. *Climate Research*, 16:123–131.

Wigley, T. M. L., Ammann, C. M., Santer, B. D., and Raper, S. C. B. (2005). Effect of climate sensitivity on the response to volcanic forcing. *Journal of Geophysical Research*, 110(D09107).

Wohlfahrt, J., Harrison, S. P., Braconnot, P., Hewitt, C. D., Kitch, A., Mikolajewicz, U., Otto-Bliesner, B. L., and Weber, S. L. (2008). Evaluation of coupled ocean–atmosphere simulations of the mid-Holocene using palaeovegetation data from the northern hemisphere extratropics. *Climate Dynamics*, pages 871–890.

Wright, H. E., Kutzbach, J. E., Webb III, T., Ruddiman, W. F., Street-Perrott, F. A., and Bartlein, P. J. (1993). *Global climates since the Last Glacial Maximum*. University of Minnesota Press.

Yin, Q., Berger, A., Driesschaert, E., Goosse, H., Loutre, M. F., and Crucifix, M. (2008). The Eurasian ice sheet reinforces the East Asian summer monsoon during the interglacial 500 000 years ago. *Climate of the past*, 4:79–90.

Yu, G., Harrison, S. P., and Xue, B. (2001). Lake Status records from China: Data Base Documentation. *Technical Reports - Max-Planck-Institut for Biogeochemie*, 4:243.

Yu, H., Kaufman, Y., Chin, M., Feingold, G., Remer, L., Anderson, T., Balkanski, Y., Bellouin, N., Boucher, O., and Christopher, S. (2006). A review of measurement–

based assessments of the aerosol direct radiative effect and forcing. *Atmos. Chem. Phys.*, 6:613–666.

Zhao, Y., Braconnot, P., Harrison, S. P., Yiou, P., and Marti, O. (2007). Simulated changes in the relationship between tropical ocean temperatuers and the western African monsoon during the mid-Holocene. *Climate Dynamics*, 28:533–551.